EVALUATION OF ANALYTICAL METHODS TO INTERPRET GROUND DEFORMATIONS DUE TO SOFT GROUND TUNNELING

by

Despina M. Zymnis

B.A., MEng Civil Engineering (2007)

Trinity College, Cambridge University

Submitted to the Department of Civil and Environmental Engineering
in Partial Fulfillment of the requirements for the Degree of
Master of Science in Civil and Environmental Engineering

at the

Massachusetts Institute of Technology

February 2009

Signature of Author ……..
Department of Civil and Environmental Engineering
January 29, 2009

Certified by ……..
Andrew J. Whittle
Professor of Civil and Environmental Engineering
Thesis Supervisor

Accepted by ……..
Daniele Veneziano
Chairman, Departmental Committee for Graduate Students

EVALUATION OF ANALYTICAL METHODS TO INTERPRET GROUND DEFORMATIONS DUE TO SOFT GROUND TUNNELING

by

Despina M. Zymnis

Submitted to the Department of Civil and Environmental Engineering
on January 29, 2009 in Partial Fulfillment of the
Requirements for the Degree of Master of Science in
Civil and Environmental Engineering

ABSTRACT

An in depth study was undertaken to evaluate the effectiveness of analytical solutions in describing ground movements induced by soft ground tunneling. The analytical solutions that were examined consider both isotropic and anisotropic stiffness parameters and were proposed by Pinto and Whittle (1999) and Chatzigiannelis and Whittle (2001) respectively.

Computed ground movements were compared to field measurements from five published case studies of tunnels around the world that involved different excavation methods (open and closed face tunneling) and varying soil properties. A Least Squares Solution procedure has been employed in each case for selecting model input parameters that best describe the field data.

The control study of the thesis involves the westbound tunnel of the Jubilee Line Extension project in London. The use of anisotropic stiffness parameters improved significantly the agreement with surface and subsurface field measurements. Moreover, the volume loss computed by the analytical solutions is significantly reduced comparing with previous published interpretations of volume loss that were based on empirical methods.

The analytical solutions prove to be a very powerful tool for describing ground displacements induced by different methods of tunnel excavation through various soil types. They are practical, since they require minimal information on soil properties, while at the same provide a complete framework for understanding the relationships between the distribution of far-field deformations, construction methods and ground conditions. Pinto's proposed design method proved to be effective in selecting appropriate input parameters for most tunnel cases apart from the tunnels excavated in London Clay.

Thesis Supervisor: Andrew J. Whittle

Title: Professor of Civil and Environmental Engineering

Acknowledgements

I would like to thank Professor Whittle for his invaluable help and support throughout my studies at MIT. His unparalleled knowledge and in-depth understanding of the geotechnical engineering concepts have guided me through the difficulties of this undertaking. I would also like to thank Professor Veneziano for his idea to incorporate the Least Squares Solution error method in my work. I would like to thank Professor Kausel for his enthusiasm and passion towards Civil Engineering and for helping me believe in me. Last but not least I would like to thank Kris Kipp and Jeanette Marchocki for their invaluable help and support, when I needed it the most.

I would like to thank my friends from the Civil Engineering Department: Sinan, Sherif, Naeem, Maria, Nikos, Jaehoon, Ray, Julia, Eva, Dimitris, for making MIT a very happy place to work and hang out.

Christina, Shoshanna, Antonis, Nikolas, Andreas, Yiannis, Giorgos, Ruben, Kostas, Stavros, Spyros, Ana, you are true friends and you are the main reason why I am sad to leave MIT. I know that, no matter how far away we are, you will always have a very special place in my heart.

Finally, I would like to thank my family, my friends in Greece and especially Konstantinos for their strong love and for making my life the most fascinating journey. Being next to them gives me strength and inspiration to move on, but most importantly, it is these people who make my life worth living.

Table of Contents

List of Figures

List of Tables

Chapter 1
Introduction

Construction of tunnels in soft ground inevitably induces causes movements in the surrounding ground due to stress relief and ground loss at the tunnel cavity. This can potentially damage overlying buildings and services. The prediction of tunnel-induced ground deformations and assessment of their influence on the surrounding structures are crucial during design and construction, especially when tunneling takes place in urban environments.

Three main methods have been developed for the modeling and prediction of ground movements induced by tunneling: 1) empirical methods, 2) closed-form analytical solutions and 3) finite element analyses. The goal of this thesis is to evaluate the effectiveness of the analytical method in simulating ground deformations that were measured in the field. Initially, closed-form analytical solutions proposed by Pinto and Whittle (1999) will be studied. These solutions assume isotropic ground behavior and require minimal information on soil properties. Further analytical solutions that assume cross-anisotropic stiffness parameters, developed by Chatzigiannelis and Whittle (2001), will also be examined.

1.1 Thesis Outline

Chapter 2 presents a literature review with background information on the three methods for describing soil displacements induced by tunneling.

Chapters 3, 4 and 5 apply the proposed analytical solutions are applied to five published case studies of tunnels around the world that involve different excavation methods (open and closed face tunneling) and varying soil properties. A Least Squares Solution procedure has been employed in each analysis to evaluate the performance of the analytical solutions and to select appropriate model input parameters that best describe the field data. Chapter 3 presents the main control study of the thesis, which involves the construction of the westbound tunnel of the Jubilee Line Extension project in London, at a heavily instrumented site in St James's Park. Chapter 4 shows similar analyses undertaken for the Heathrow Express trial tunnel in London. Finally, Chapter 5 includes further illustrative examples of tunnels, namely the Madrid Metro extension project, a sewer-line tunnel in Mexico City and the N-2 contract tunnel for the San Francisco clean water project.

Chapter 6 provides a summary and presents the main conclusions of the study, and also includes recommendations for future work.

Chapter 2
Literature Review

2.1 Introduction

Ground displacements induced by the boring of tunnels have several sources, such as deformation of the ground due to stress relief induced by the excavation of the tunnel, radial ground displacements associated with the passage of the shield and the gap between the shield and the lining, and also due to deformation of the lining as the loads in the overhead ground change. Finally, long-term ground movements can also be induced due to consolidation.

Three main methods have been developed for the modeling and prediction of ground movements induced by tunneling: 1) empirical methods, 2) closed form analytical solutions and 3) finite element analysis. The goal of this chapter is to present these methods and discuss the advantages and disadvantages of each.

2.2 Empirical Method

The empirical method proposed by Peck (1969) and Schmidt (1969) is the most commonly used in the engineering practice. This method suggests that the *transverse settlement trough* induced at the surface, immediately after tunnel construction, is well fitted by a Gaussian distribution curve (see Figure 2.1):

$$u_y = u_y{}^0 \exp\left(-\frac{x^2}{2x_i{}^2}\right) \qquad (2.1)$$

where u_y = settlement

$S_y{}^0$ = maximum settlement on the tunnel centerline

x = horizontal distance from the tunnel centerline

x_i = horizontal distance from the tunnel centerline to the point of inflexion of the settlement trough

The volume of the surface settlement trough (per meter length of tunnel), ΔV_s per unit length of tunnel can be obtained by integrating equation (2.1) to give:

$$\Delta V_s = \sqrt{2\pi}\, x_i\, u_y{}^0 \qquad (2.2)$$

The *volume loss* ΔV_L, which represents the ground lost in the region close to the tunnel, is equal to:

$$\Delta V_L = \Delta V_s + \Delta V_g \qquad (2.3)$$

where D is the diameter of the circular tunnel.

When tunneling under drained conditions, for example in dense sands, ΔV_s is less than ΔV_L because of dilation (Cording and Hansmire,1975). When tunneling in clays, ground movements usually occur under undrained (constant volume) conditions, in which case $\Delta V_s = \Delta V_L$ (i.e. $\Delta V_g \approx 0$) (Mair and Taylor, 1997).

A linear relationship has also been proposed (Mair and Taylor, 1997) between the inflection point parameter, x_i and the depth of the tunnel springline, H:

$$x_i = KH \qquad (2.4)$$

where K is a trough width parameter determined by empirical means based on surface settlement troughs induced by previous tunnel constructions around the world. From Figure 2.2 we deduce that K is equal to 0.5 for tunnels in clays and 0.35 for tunnels in sands. Note the considerable scatter in the field measurements of parameter x_i (Figure 2.2).

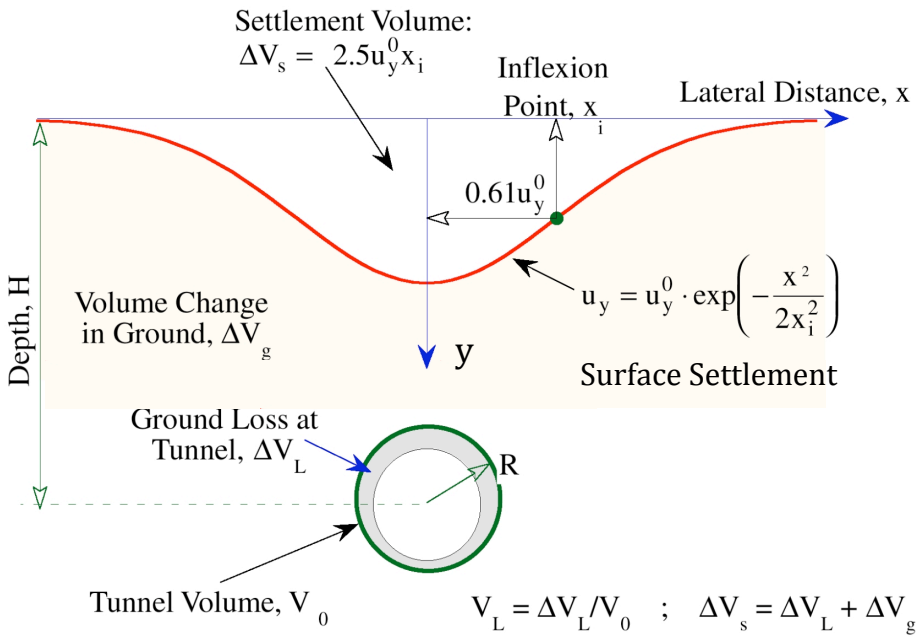

Figure 2.1: Empirical function for transversal surface settlement trough (after Peck, 1969 and Schmidt, 1969)

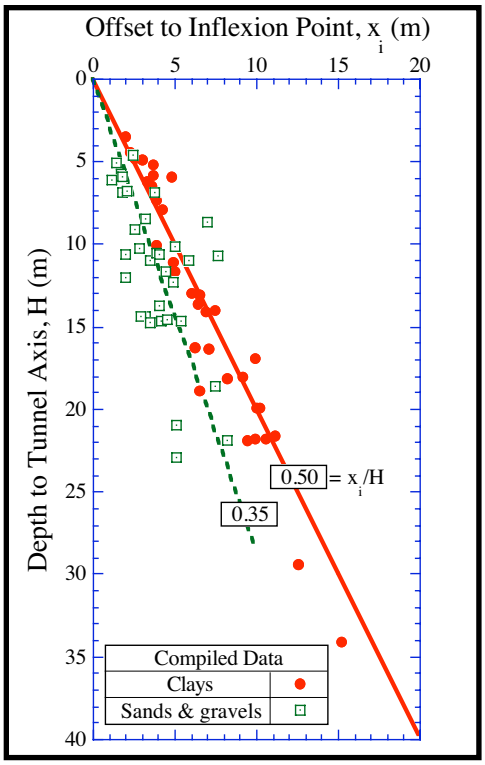

Figure 2.2: Variation in surface settlement trough width parameter x_i with tunnel depth for soft ground tunneling (Mair & Taylor, 1997)

Mair et al (1993) showed through empirical means that the *subsurface settlements* can also be modeled with Gaussian distribution curves using equation (2.1). However, for subsurface settlements at a depth y below the ground surface and with the tunnel springline being at a depth H, the trough width parameter x_i is equal to:

$$x_i = K\,(H - y) \tag{2.5}$$

where K increases with depth (see Fig. 2.3) and for tunnels in clays can be expressed by

$$K = \frac{0.175 + 0.325\left(1 - \frac{y}{H}\right)}{1 - \frac{y}{H}} \tag{2.6}$$

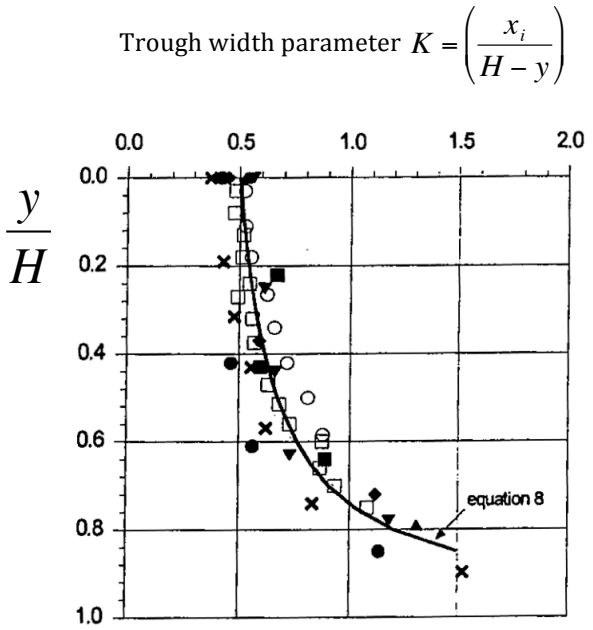

Figure 2.3: Variation of Trough width parameter K with normalized depth (y/H) for tunnels in clay (after Mair et al, 1993)

Attewell (1978) and O'Reilly and New (1982) suggested empirical expressions for the *horizontal ground displacements* based on the assumption that the ground displacement vectors are directed towards the center of the tunnel, for tunnels in clays. According to this assumption, the horizontal ground displacements can be simply expressed by:

$$u_x = \left(\frac{x}{H}\right) u_y \qquad (2.7)$$

where x is the offset from the centerline, H is the depth to tunnel springline and u_y is the settlement.

The empirical method represents a simple practical way of modeling ground movements induced by the construction of tunnels. Particularly when there are

previous cases of tunnels being excavated in comparable ground conditions and with similar construction techniques, the empirical method works very well since the parameters of the model can be derived based on the previous case histories. However, there are several limitations related to the empirical method, since it can only be applied to single tunnels or tunnels that don't have significant interaction. Moreover, the empirical methods only represent ground displacements that are generated immediately after the construction of the tunnel and don't provide any insight in the long-term ground movements caused due to consolidation. Empirical methods strictly apply to greenfield conditions, as there is no attempt to model soil-structure interaction and most of the data are from sites with few near-by structures. It is hard to find an accurate value for the volume loss ΔV_L induced by tunneling works, since this parameter depends on several factors such as the geometry of the tunnel, the construction method used and the groundwater and soil conditions. Finally, although the empirical method is practical and easy to use, it is based on field observations and lacks of a rigid theoretical framework to support it. The fact that the conventional method is not based on physically meaningful equations can lead to inaccurate estimates of subsurface ground movements, especially in the horizontal direction.

2.3 Analytical Solutions

Simplified closed-form analytical solutions can offer an attractive alternative to the empirical method for simulating the ground movements induced by tunnel construction in soft ground conditions. These analyses, requiring a small number of physically meaningful input parameters, make gross approximations of real soil behavior by assuming linear, elastic soil properties. However, they fulfill the principles of continuum mechanics and provide a complete framework for understanding the relationships between the distribution of far-field deformations, construction methods and ground conditions. The analytical solutions described in this section relate ground displacements to a prescribed set of displacements around the tunnel cavity and can be expressed as the summation of three basic modes of deformation: 1) uniform convergence u_ε, 2) ovalization u_δ and 3) vertical translation Δu_y (see Figure 2.4a). The convergence component u_ε is the only one related to volume loss ΔV_L, by:

$$-\frac{2u_\varepsilon}{R} = \frac{\Delta V_L}{V_0} \tag{2.8a}$$

where $V_0 = \pi R^2$ and is the volume of the tunnel cavity per unit length.

Hence $$-u_\varepsilon = \Delta V_L \frac{R}{2\pi R^2} = \frac{\Delta V_L}{2\pi R} \Rightarrow \Delta V_L = -2\pi R u_\varepsilon \tag{2.8b}$$

The analytical solutions presented in this section are a result of ongoing research. Sagaseta (1987) proposed analytical solutions based on the superposition of singularity solutions to represent the uniform convergence and pure ovalization modes of a tunnel cavity in an elastic half-plane. In his analysis, the tunnel cavity is represented by a line-sink and the physical dimension of the tunnel (radius R) is not taken into account. These solutions, which were subsequently refined by Verruijt and Booker (1996) and Pinto (1999), can also address partially the effects of soil plasticity and dilation (Sagaseta & González, 1999; Pinto & Whittle, 2001) and are readily extended to 3-D conditions (Pinto, 1999).

Alternative analytical formulations have been proposed by Verruijt (1997) and refined by Pinto (1999) to represent the ground distortions generated by uniform convergence and pure distortion of a tunnel cavity in a planar-elastic soil. Although these formulations are more accurate ('exact') since they represent the physical dimensions of the tunnel cavity, the results are inconveniently derived in an infinite series form and can therefore most easily be evaluated in graphical form (Whittle and Sagaseta, 2001). Pinto and Whittle (2001) proved that the two sets of analytical solutions ('approximate' and 'exact') produce very similar results for tunnels with radius-embedment ratios $R/H < 0.5$, over the full range of expected elastic Poisson's ratios.

Figure 2.5 compares analytical solutions of ground movements (horizontal, u_x/u_ε; and vertical, u_y/u_ε) around a very shallow tunnel with $R/H = 0.45$ (and assumed

values $\rho = -\frac{u_\delta}{u_\varepsilon} = 0.5$ and $\nu = 0.25$) using the exact (complex variable) and approximate (superposition of line sources) methods. The agreement is surprisingly close between these two solutions (differences are within 10% above the crown and indistinguishable in most of the soil mass), especially considering this is such a shallow tunnel. Hence, the results confirm the efficacy of using approximate superposition methods for shallow tunnels (Whittle and Sagaseta, 2001).

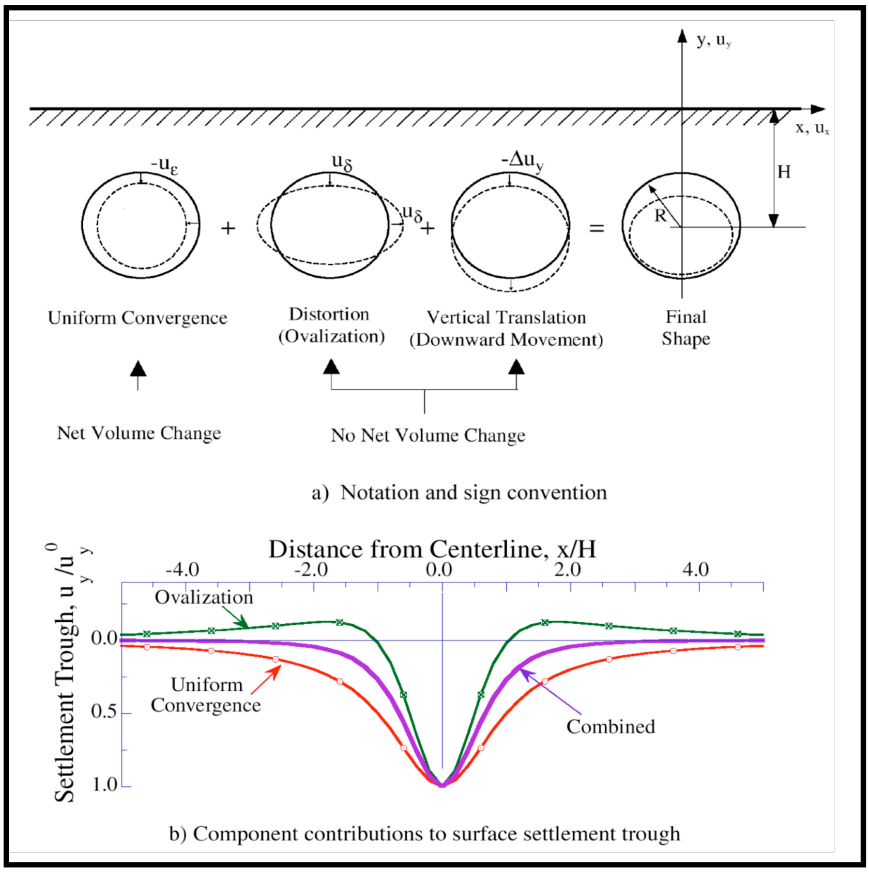

Figure 2.4: Deformation modes around tunnel cavity (Whittle & Sagaseta, 2001)

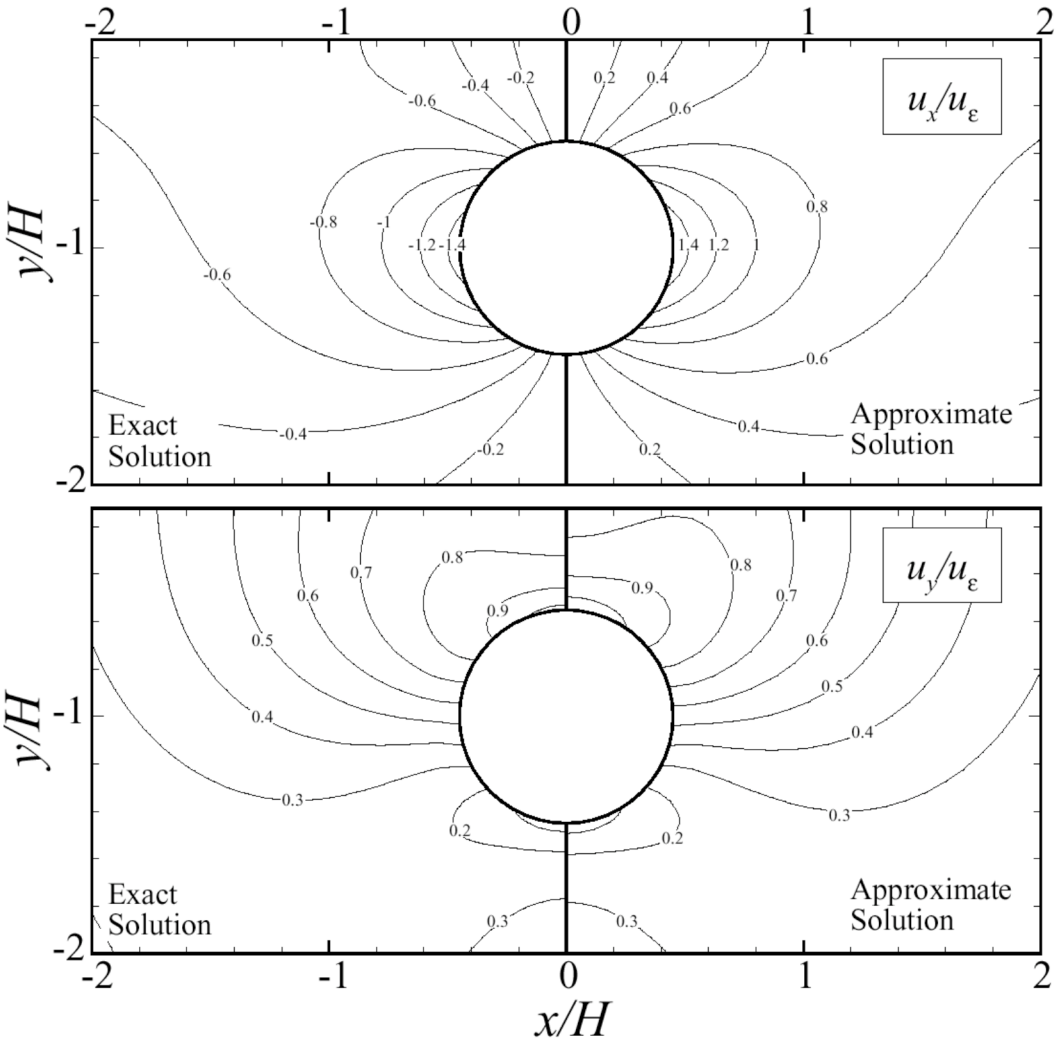

Figure 2.5: Comparison of elastic solutions for shallow tunnel (R/H = 0.45, $\rho = -\frac{u_\delta}{u_\varepsilon}$ = -0.5, ν = 0.25), (Whittle and Sagaseta, 2001)

The complete solutions proposed by Pinto (1999) for ground movements (u_x, u_y; in an elastic half-plane), which were derived using the approximate (superposition of line sources) method, are shown below. It should be noted that both the uniform convergence and ovalization modes induce vertical translation of the tunnel cavity (Δu_y; Fig. 2.4a, eqns. 2.9c and 2.10c).

1. Uniform Convergence Mode

$$\frac{u_x}{u_\varepsilon} = x \cdot R \cdot \left\{ \frac{1}{x^2 + (y+H)^2} - \frac{1}{x^2 + (y-H)^2} + \frac{4 \cdot (1-\nu)}{x^2 + (y-H)^2} - \frac{4 \cdot (y-H) \cdot y}{\left[x^2 + (y-H)^2\right]^2} \right\} \qquad (2.9a)$$

$$\frac{u_y}{u_\varepsilon} = R \cdot \left\{ \begin{array}{l} \dfrac{(y+H)}{x^2 + (y+H)^2} - \dfrac{(y-H)}{x^2 + (y-H)^2} + \dfrac{4 \cdot (y-H) \cdot x^2 + 2 \cdot H \cdot \left[x^2 - (y-H)^2\right]}{\left[x^2 + (y-H)^2\right]^2} - \\ \ldots - \dfrac{4 \cdot (1-\nu) \cdot (y-H)}{x^2 + (y-H)^2} \end{array} \right\} \qquad (2.9b)$$

Associated vertical translation of tunnel springline

$$\frac{\Delta u_y}{u_\varepsilon} = 4 \cdot \frac{R}{H} \cdot \frac{8 \cdot (1-\nu) - (1-2\nu) \cdot \left(\frac{R}{H}\right)^2}{\left[4 + \left(\frac{R}{H}\right)^2\right]^2} \qquad (2.9c)$$

2. Ovalization Mode

$$\frac{u_x}{u_\delta}=\frac{R\cdot x}{3-4\nu}\cdot\left\{\begin{array}{l}\dfrac{(3-4\nu)\cdot\left[x^2+(y+H)^2\right]^2-\left[3(y+H)^2-x^2\right]\cdot\left[x^2+(y+H)^2-R^2\right]}{\left[x^2+(y+H)^2\right]^3}-\\ \ldots-\dfrac{(3-4\nu)\cdot\left[x^2+(y-H)^2\right]^2-\left[3(y-H)^2-x^2\right]\cdot\left[x^2+(y-H)^2-R^2\right]}{\left[x^2+(y-H)^2\right]^3}+\\ \ldots+\dfrac{x^2+y^2-H^2}{\left[x^2+(y-H)^2\right]^2}\cdot 8(1-\nu)-8y\cdot\dfrac{y\cdot(x^2+y^2)+2H\cdot(H^2-x^2)-3\cdot y\cdot H^2}{\left[x^2+(y-H)^2\right]^3}\end{array}\right\} \tag{2.10a}$$

$$\frac{u_y}{u_\delta}=\frac{R}{3-4\nu}\cdot\left\{\begin{array}{l}(y-H)\cdot\dfrac{(3-4\nu)\cdot\left[x^2+(y-H)^2\right]^2-\left[3x^2-(y-H)^2\right]\cdot\left[x^2+(y-H)^2-R^2\right]}{\left[x^2+(y-H)^2\right]^3}-\\ \ldots-(y+H)\cdot\dfrac{(3-4\nu)\cdot\left[x^2+(y+H)^2\right]^2-\left[3x^2-(y+H)^2\right]\cdot\left[x^2+(y+H)^2-R^2\right]}{\left[x^2+(y+H)^2\right]^3}+\\ \ldots+\dfrac{x^2\cdot(2H-y)-y\cdot(y-H)^2}{\left[x^2+(y-H)^2\right]^2}\cdot 8(1-\nu)-\\ \ldots-\dfrac{8(y-H)\cdot\left\{H\cdot y\cdot(y-H)^2-x^2\cdot\left[(x^2+y^2)+H\cdot(y+H)\right]\right\}}{\left[x^2+(y-H)^2\right]^3}\end{array}\right\} \tag{2.10b}$$

Associated vertical translation of tunnel springline:

$$\frac{\Delta u_y}{u_\delta}=\frac{2}{3-4\nu}\cdot\frac{R}{H}\cdot\frac{(1-8\nu)\cdot\left(\frac{R}{H}\right)^4-4(11-8\nu)\cdot\left(\frac{R}{H}\right)^2-32}{\left[4+\left(\frac{R}{H}\right)^2\right]^3} \tag{2.10c}$$

The notation and sign convention used in the analytical solutions are shown in Figure 2.4a. A complete derivation of these equations is included in Pinto (1999). The input parameters used in the analytical model are: the radius of the tunnel *R*, the depth to the tunnel springline *H*, the poisson's ratio *ν*, the uniform convergence u_ε and the ovalization of the tunnel cavity u_δ.

Figure 2.4b illustrates the distribution of surface settlements for the uniform convergence and ovalization modes. It is clear that the resulting trough shape is controlled primarily by the ratio of the two modes, $\rho = -\frac{u_\delta}{u_\varepsilon}$, which is subsequently referred to as the 'relative distortion' parameter. Pinto and Whittle (2001) suggest that the typical range for the relative distortion is $-0.5 \leq \rho \leq 3$.

Figures 2.6 a and b compare analytical solutions of ground movements (horizontal, u_x/u_ε; and vertical, u_y/u_ε) around a tunnel with R/H = 0.3 (and assumed Poisson's ratio $\nu = 0.5$) using $\rho = 0.5$ and 2. It is deduced that the solutions with $\rho = 2$ produce much larger displacements throughout the soil (as twice as large) and at the same time generate much narrower settlement troughs.

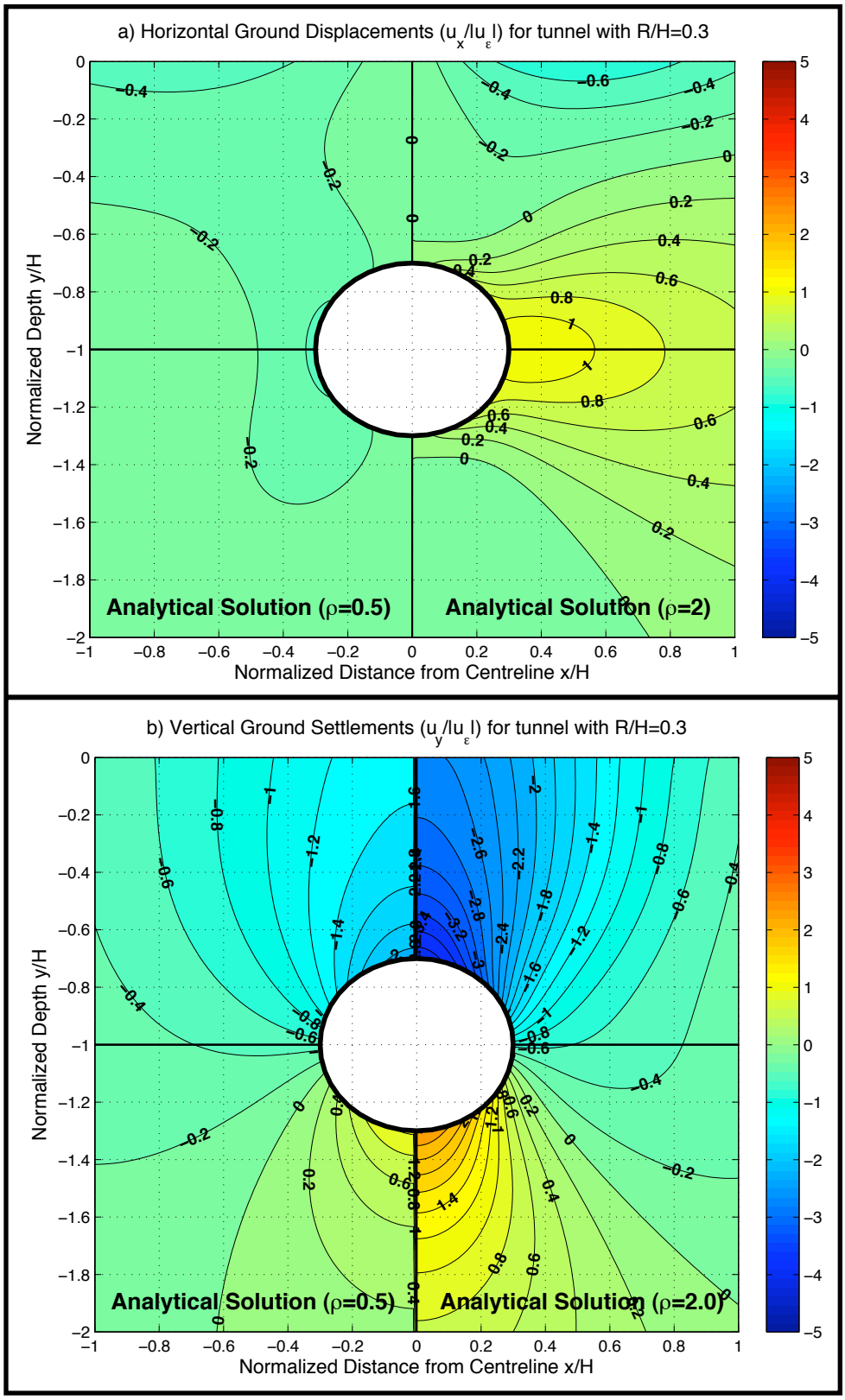

Figure 2.6: Comparison of elastic solutions with ρ=0.5 and 2 (R/H=0.3, ν=0.25)

2.3.1 Plasticity induced by tunneling

One of the key limitations of the proposed analysis is the assumption that the soil behavior can be approximated by linear elasticity. In practice, the zone of soil close to the tunnel cavity may experience significant shearing that may be accompanied by irrecoverable volume expansion creating a plastic zone. For a deep tunnel this can be represented by a concentric annulus around the tunnel (Sagaseta, 2001). In Figure 2.7 we observe the case of a circular tunnel of radius a and of infinite length, in a soil initially subjected to a uniform isotropic compression, p_0 (i.e. with $K_0 = 1$). Following Peck (1969) the overload factor N can be defined as follows:

$$N = \frac{(p_0 - p_i)}{s_u} \tag{2.11}$$

where p_i ($p_i \leq p_0$) is a uniform pressure that acts at the tunnel wall (see Figure 2.7) and s_u is the undrained shear strength of the soil. The factor N has been universally adopted in tunnel design as a qualitative measure of the mobilized soil strength. Following Sagaseta (2001) and Pinto and Whittle (2007) the radius of the plastic zone R_p is equal to:

$$\frac{R_p}{a} = \exp\left(\frac{N-1}{2}\right), \quad (N \geq 1) \tag{2.12}$$

For $N \leq 1$, the soil remains in the elastic range. For N between 1 and 3 the plastic zone is moderate and it becomes very large for N approaching 5 - 6.

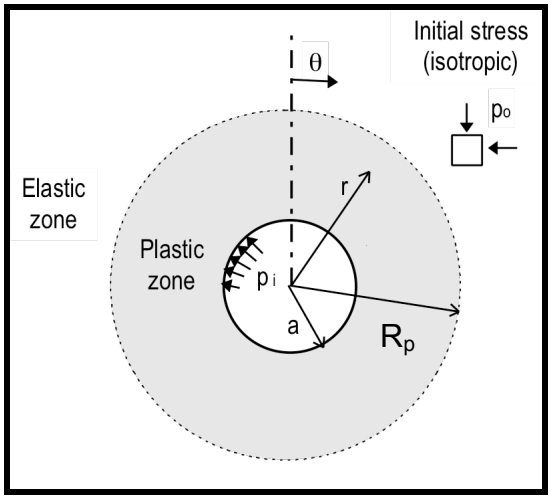

Figure 2.7: Plastic zone around deep tunnel in clay (Sagaseta, 2001)

Apart from linear elasticity, analytical solutions for ground movements can also partially address the effects of soil plasticity and dilation under the assumption of a constant flow rule: $\varepsilon_{vol} = -\sin\psi \cdot \gamma_{\max}$, where ε_{vol} is the volumetric strain, γ_{max} the maximum shear strain, and ψ an average angle of dilation. Under this assumption (and neglecting elastic strains), Sagaseta (1987) suggested that the radial displacements around a line source attenuate according to $u_r \sim 1/r^{\beta}$, where $\beta = (1+\sin\psi)/(1-\sin\psi)$.

For soils where there is no dilation (e.g. undrained shearing of clays), $\beta = 1$ and the displacement field, $u_r \sim 1/r$ (identical to elastic case with $\nu = 0.5$). Sagaseta and González (1999) and Pinto (1999) subsequently presented analytical solutions for the uniform convergence and ovalization deformation modes in terms of $\alpha=(1+\beta)/2=1/(1-\sin\psi)$. Assuming a maximum dilation angle, $\psi = 30°$, then $1 \leq \alpha \leq 2.0$.

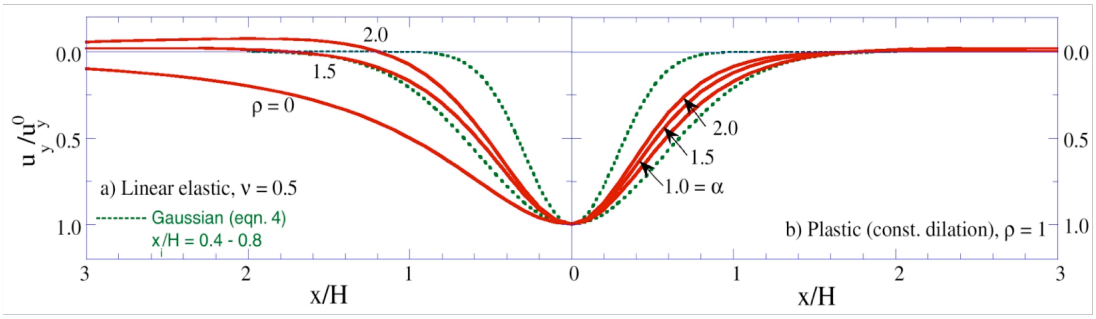

Figure 2.8: Effect of input parameters on surface settlement distribution (Whittle and Sagaseta, 2001)

Figures 2.8 a and b compare the surface settlement distributions (u_y/u_y^0) obtained analytically by assumptions of linear elastic (ρ, ν) and constant dilation plastic (ρ, α) material behavior, respectively, with the empirical relations (eqn. 2.1) assuming $x_i/H = K = 0.4 – 0.8$. It is clear that the parameters ρ and α control the predicted settlement trough shape (ν plays only a secondary role) and can match a large fraction of the empirically observed settlement distributions (Whittle and Sagaseta, 2001).

2.3.2 Interpretation of Field Monitoring Data as proposed by Pinto & Whittle (2001)

For a given tunnel (of radius *R* and depth to springline *H*) the analytical solutions described require three input parameters: 1) ν, ρ and u_ε for the linear elastic soil; or 2) α, ρ and u_ε for the case of constant dilation plasticity. These parameters can be derived from a set of three independent field measurements. In practice, it is common to measure the surface settlement above the crown of the tunnel. However,

the location and scope of other field data varies significantly from one project to another. In order to illustrate the design capability and to evaluate the analytical solutions Pinto and Whittle (2001) proposed a reference measuring system that uses 3 pre-defined measurements to interpret the model parameters as shown in Figure 2.9:

1) the centerline surface settlement, u_y^0;

2) the surface settlement offset at a distance H from the centerline of the tunnel, u_y^1; and

3) the horizontal displacement measured at the springline elevation (i.e., at depth H) in an inclinometer located 2R from the center of the tunnel, u_x^0.

Figures 2.10 a, b and c illustrate the design charts developed by Pinto and Whittle (2001) for a tunnel with R/H = 0.2. The interpretation procedure recommended by the authors first uses the measured ratios, u_x^0 / u_y^0 and u_y^1 /u_y^0 to estimate parameter sets (ρ, ν) or (α, ρ) (e.g., Fig. 2.10a). These parameters are then used to find the ground loss ratio u_y^0 /u_ε from either Fig 2.10b or 2.10c (under the preferred assumption of soil model).

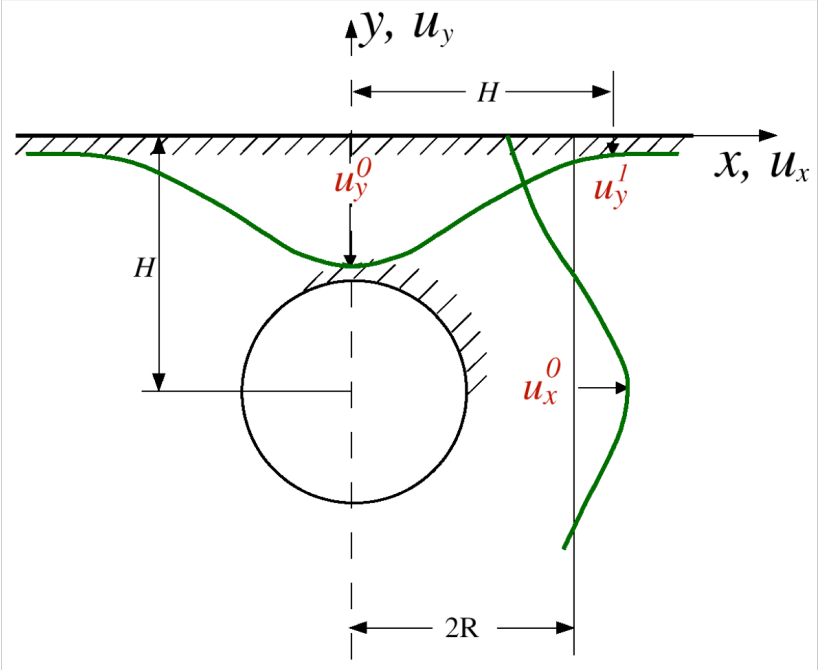

Figure 2.9: Reference field measurements for proposed design method (Pinto, 1999)

The N-2 contract tunnel for the San Francisco clean water project described by Clough et al. (1983) is used as an example to illustrate the design method suggested by Pinto and Whittle (2001) and to evaluate the effectiveness of the proposed method in selecting appropriate input parameters for the analytical solutions.

Figure 2.12 shows a typical cross-section of the tunnel with radius, R = 1.78m located at a depth, H = 9.6m (R/H = 0.185). The soil profile comprises 6.6m of rubble fill underlain by a 7.1m layer of Recent Bay Mud, containing the tunnel and underlain by colluvium and residual sandy clay. The measured settlements and lateral deflections shown in Figure 2.11 were measured at one line of instrumentation (line 4; Clough et al., 1983) 15 days after the passage of the tunnel shield. The surface settlements were only measured over a width -0.5 < x/H < 0.5, from which u_y^0 = -30.6mm is well defined while u_y^1 is not measured. An

inclinometer installed at x = 3.6m (x/R ≈ 2.0), enables direct evaluation of u_x^0 = 23.5mm. Given that the soil is a soft clay, the analyses can be applied under the assumption of incompressible behavior (ν = 0.5). Table 2.1 summarizes the model parameters derived from these data (based on design charts at R/H = 0.15, 0.20).

The proposed method for choosing analytic input parameters identify a relatively large distortion parameter, ρ = 2.15. Figure 2.11 shows that the measured surface settlements are in very good agreement with the analytically computed surface settlement trough. It should be noted that these same data were also well matched by Clough et al. (1983) using the empirical Gaussian curve with x_i/H = 0.42. The analytical solutions also give very reasonable estimates of the outward lateral deflections measured in inclinometers located 3.6m and 5.6m (data for two inclinometers are combined in the figure) from the tunnel centerline, Figure 2.11. The analyses predict maximum lateral movements at the springline elevation, while the measured maxima occur between the crown and springline.

The good agreement between the ground displacements generated by the analytical solution and the field data recorder in the N-2 contract tunnel for the San Francisco clean water project suggests that the proposed design procedure was effective in choosing appropriate model input parameters. However, Pinto (1999) discovered that the proposed design scheme failed to produce a good match to the ground deformations induced by the Heathrow Express trial tunnel in London. He suggested that this could be due to limitations of the isotropic analytical model for heavily overconsolidated and highly fissured soils (like London Clay).

u_x^0/u_y^0 = -0.77	R / H (from design charts)		
ν = 0.5	0.15	0.2	**R/H = 0.18**
P	1.7	2.5	**2.15**
u_y^0/u_ε	1.30	2.30	**1.86**
u_ε [mm] ($\Delta V_L/V_0$ x 100%)	-24	-13	**-19 (2.15%)**
u_δ [mm]	--	--	
Δu_y [mm]	Eqn. 2.9c $\Delta u_y/u_\varepsilon$ = 0.175 Δu_y = -3.5mm	Eqn. 2.10c $\Delta u_y/u_\varepsilon$ = -0.170 Δu_y = -5.6mm	**-9**
Crown settlement [mm]: $uc = u_\varepsilon - u_\delta + \Delta u_y$			**-69**

Table 2.1: Interpretation of tunnel deformation parameters, N-2 water tunnel, San Francisco (Whittle and Sagaseta, 2001)

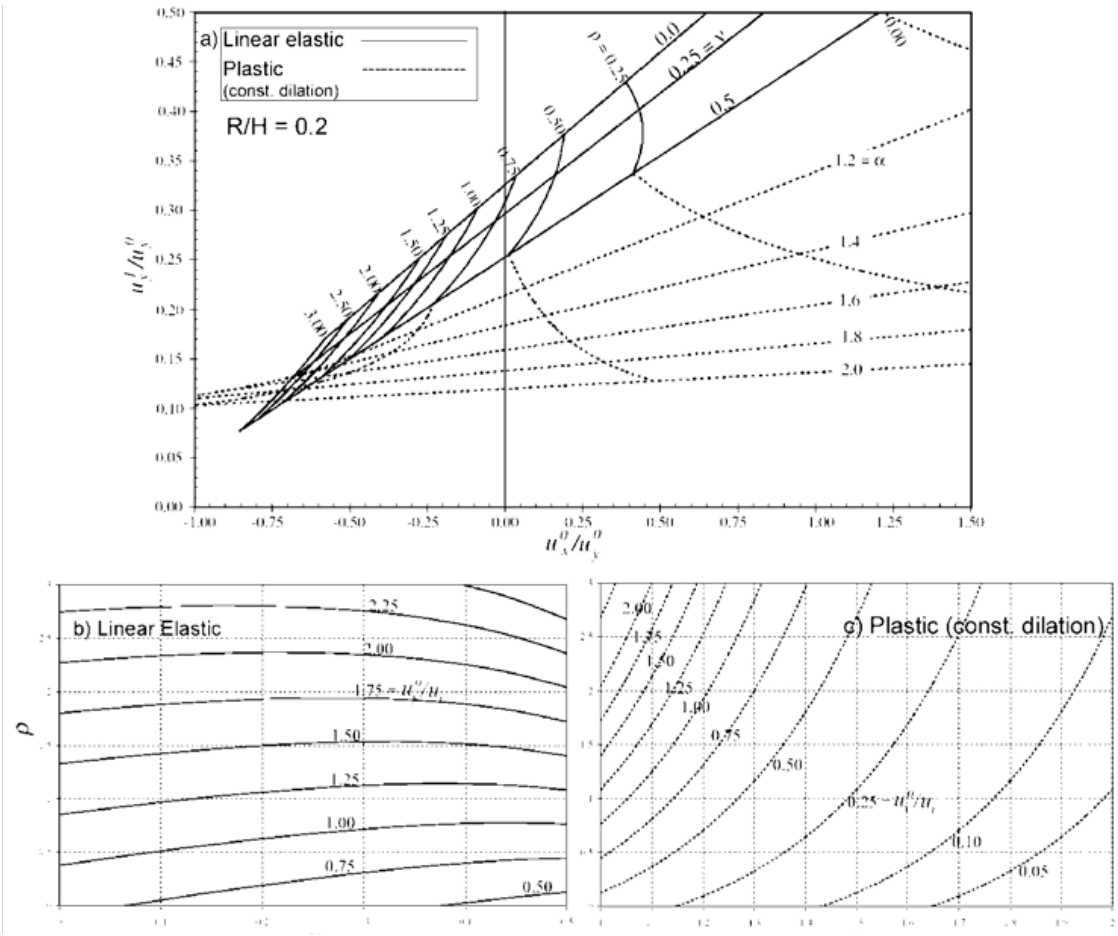

Figure 2.10: Example design charts for interpreting analytical model input parameters (Pinto and Whittle, 2001)

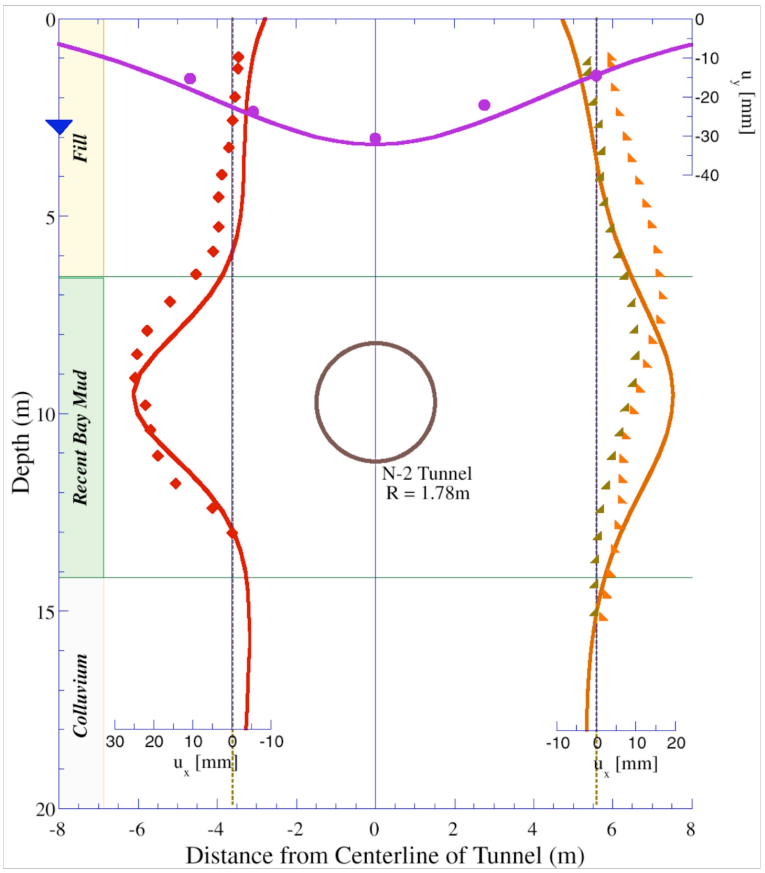

Figure 2.11: Comparison of computed (solid lines) and measured deformations, N-2 tunnel project (after Whittle and Sagaseta, 2001)

2.3.3 Analytical Solutions with cross-anisotropic stiffness

Further analytical solutions have been reported by Chatzigiannelis and Whittle (2001) for *cross-anisotropic*, elastic soils. These solutions were derived for cases where the observed settlement trough was far too narrow to be predicted by an isotropic elastic solution (ex. the Heathrow Express trial tunnel in London). Chatzigiannelis and Whittle (2001) concluded that the ground movements generated by the Heathrow Express trial were better described by the anisotropic

solutions than the isotropic formulations. Simpson et al (1995), using finite element analysis, concluded that effects of anisotropy are significant on both the magnitude of the surface settlements and also the shape of the surface settlement trough, while non-linear behavior has only subtle effects. Lee and Rowe (1983) have also shown that while elastic cross-anisotropy does not greatly change the results of surface loading problems, it has a significant effect on the computed settlements above the tunnel.

This section starts with some background information on cross-anisotropy in soils, moves on to present the analytical solutions derived for the cases of uniform convergence and pure distortion of a circular tunnel in a cross-anisotropic half-plane and concludes with a comparison of the isotropic and anisotropic analytical models. Appendix I presents complete derivations of the cross-anisotropic analytical solutions written by Chatzigiannelis and Whittle (2001).

2.3.3.1 Cross-Anisotropy in a Soil

Geotechnical properties of a soil depend primarily on the arrangement of its particles. Therefore any anisotropy in the fabric leads to directional dependence of the engineering properties of the soil. Natural soils almost always possess some degree of anisotropy and also any load can cause their anisotropy to change. There are three types of soil anisotropy: 1) structural or inherent, 2) strain-induced and 3) stress-induced. The inherent anisotropy arouses from the soil's way of formation,

while the strain-induced anisotropy can be produced by dominant shear strain in a certain direction. Finally, stress-induced anisotropy develops as the stress state of a soil becomes anisotropic. Uniform clay deposits often have inherent anisotropy, since they were formed by sedimentation, followed by 1D consolidation over long periods of time. The particles are often horizontally layered and are characterized by cross-anisotropic behavior, i.e. with a vertical axis of symmetry and horizontal planes of isotropy. It can be generally expected for normally or slightly overconsolidated clays to be fairly isotropic, while heavily overconsolidated clays (like London Clay) usually exhibit high degrees of anisotropy, with the horizontal stiffness being greater than the vertical. Figure 2.12 defines the stresses and displacements in the x, y and z directions and also states the sign convention used in the analytical solutions.

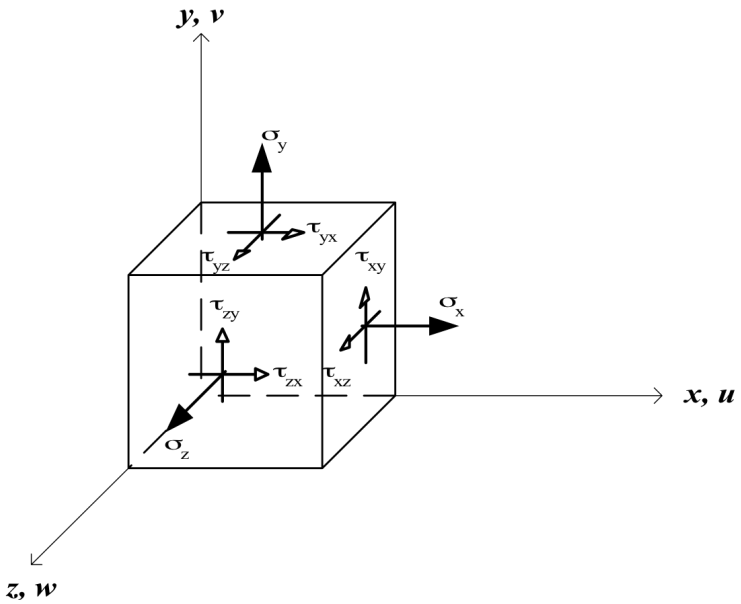

Figure 2.12: Definition of notation and sign convention used in the analysis

In cross-anisotropic media, with x-y being the plane of anisotropy, the linear relation between strains and stresses (commonly known as Hooke Law) is:

$$\begin{Bmatrix} \varepsilon_x \\ \varepsilon_y \\ \varepsilon_z \\ \gamma_{yz} \\ \gamma_{zx} \\ \gamma_{xy} \end{Bmatrix} = \begin{bmatrix} \frac{1}{E_h} & -\frac{\nu_{hh}}{E_h} & -\frac{\nu_{vh}}{E_v} & 0 & 0 & 0 \\ -\frac{\nu_{hh}}{E_h} & \frac{1}{E_h} & -\frac{\nu_{vh}}{E_v} & 0 & 0 & 0 \\ -\frac{\nu_{hv}}{E_h} & -\frac{\nu_{hv}}{E_h} & \frac{1}{E_v} & 0 & 0 & 0 \\ 0 & 0 & 0 & \frac{1}{G_{vh}} & 0 & 0 \\ 0 & 0 & 0 & 0 & \frac{1}{G_{vh}} & 0 \\ 0 & 0 & 0 & 0 & 0 & \frac{1}{G_{hh}} \end{bmatrix} \begin{Bmatrix} \sigma_x \\ \sigma_y \\ \sigma_z \\ \tau_{yz} \\ \tau_{zx} \\ \tau_{xy} \end{Bmatrix} \qquad (2.13)$$

where

E_v Young's modulus in the vertical direction

E_h Young's modulus in (any) horizontal direction

ν_{vh} Poisson's ratio for the effect of vertical strain on horizontal strain

ν_{hh} Poisson's ratio for the effect of horizontal strain on complementary horizontal strain

ν_{hv} Poisson's ratio for the effect of horizontal on vertical strain

$G_{vh}= G_{hv}$ Shear modulus for strain in (any) vertical plane (planes of anisotropy)

G_{hh} Shear modulus for strain in the horizontal plane (plane of isotropy)

Of these 7 engineering properties only 5 are independent for an elastic body: E_v, E_h, ν_{vh}, ν_{hh} and G_{vh}. For the remaining 2 the following relations are valid:

$$\nu_{hv} = \nu_{vh} \frac{E_h}{E_v}$$

$$G_{hh} = \frac{E_h}{2(1+\nu_{hh})}$$

Two commonly used ratios that measure the degree of anisotropy of a soil are:

$$n = \frac{E_h}{E_v}; \quad m = \frac{G_{vh}}{E_v}$$

For prescribed tunnel wall displacements (u_ε, u_δ) the displacement field around a circular tunnel cavity in a cross-anisotropic half-plane can be determined. The input parameters of the anisotropic analytical equations are the parameters of the isotropic analytical model: R, H, u_ε and u_δ defined earlier and also the 5 anisotropic stiffness parameters introduced earlier: E_v', $n = \frac{E_h}{E_v}$, $m = \frac{G_{vh}}{E_v}$, ν_{vh}' and ν_{hh}'.

For both modes of deformation of the tunnel cavity (uniform convergence and pure distortion) the general solutions to the displacement field [u(x,y), v(x, y)] were derived based on the superposition principle by combining fundamental solutions for: 1) a line sink in a full plane [$u^+(x, y)$, $v^+(x, y)$], 2) an image source of equal strength located equidistant (depth, H) above the plane of the ground surface (which cancels the normal stress component along the surface) [$u^-(x, y)$ & $v^-(x, y)$]

and 3) a distribution of corrective shear tractions along the bisecting line (simulating a traction-free ground surface) [$u^c(x,y)$, $v^-(x,y)$], as shown below:

$$u(x,y) = u^+(x,y) + u^-(x,y) + u^c(x,y) \quad (2.14a)$$

$$v(x,y) = v^+(x,y) + v^-(x,y) + v^c(x,y) \quad (2.14b)$$

The complete solutions proposed by Chatzigiannelis and Whittle (2001) for ground movements (u_x, u_y; in a cross-anisotropic half-plane), are shown in the following pages. Complete derivations of these analytical solutions can be found in Appendix I. Note that the sign convention used is the same as the one used in the isotropic analysis (see Figure 2.4a).

1) Uniform convergence case:

Horizontal displacements: $u_\varepsilon(x,y) = u^+(x,y) + u^-(x,y) + u^c(x,y)$ (2.15a)

$$u^+(x,y) = U(x,y+H) = 2\mathrm{Re}\left\{\frac{u_\varepsilon}{2}\,p_1\frac{q_2-ip_2}{p_1q_2-q_1p_2}\cdot\frac{1}{\zeta_1(x,y+H)} + \frac{u_\varepsilon}{2}\,p_2\frac{-q_1+ip_1}{p_1q_2-q_1p_2}\cdot\frac{1}{\zeta_2(x,y+H)}\right\}$$

$$u^-(x,y) = -U(x,y-H) = -2\mathrm{Re}\left\{\frac{u_\varepsilon}{2}\,p_1\frac{q_2-ip_2}{p_1q_2-q_1p_2}\cdot\frac{1}{\zeta_1(x,y-H)} + \frac{u_\varepsilon}{2}\,p_2\frac{-q_1+ip_1}{p_1q_2-q_1p_2}\cdot\frac{1}{\zeta_2(x,y-H)}\right\}$$

$$u^c(x,y) = 2\mathrm{Re}\left\{p_1\Phi_1^{\,c}(z_1) - p_2\Phi_1^{\,c}(z_2)\right\}$$

$$= 2\mathrm{Re}\left\{\frac{u_\varepsilon}{(\lambda_1-\lambda_2)\cdot(p_1q_2-q_1p_2)}\cdot\left[\begin{array}{l}\dfrac{p_1\lambda_1R(1-i\lambda_1)\cdot(q_2-ip_2)}{z_1-\lambda_1H+\sqrt{\left[(z_1-\lambda_1H)^2-R^2\left(1+\lambda_1^{\,2}\right)\right]}} + \dfrac{p_1\lambda_2R(1-i\lambda_2)\cdot(-q_1+ip_1)}{z_1-\lambda_2H+\sqrt{\left[(z_1-\lambda_2H)^2-R^2\left(1+\lambda_2^{\,2}\right)\right]}} - \\ \ldots - \dfrac{p_2\lambda_1R(1-i\lambda_1)\cdot(q_2-ip_2)}{z_2-\lambda_1H+\sqrt{\left[(z_2-\lambda_1H)^2-R^2\left(1+\lambda_1^{\,2}\right)\right]}} - \dfrac{p_2\lambda_2R(1-i\lambda_2)\cdot(-q_1+ip_1)}{z_2-\lambda_2H+\sqrt{\left[(z_2-\lambda_2H)^2-R^2\left(1+\lambda_2^{\,2}\right)\right]}}\end{array}\right]\right\}$$

Vertical settlements: $v_\varepsilon(x,y) = v^+(x,y) + v^-(x,y) + v^c(x,y)$ (2.15b)

$$v^+(x,y) = V(x,y+H) = 2\mathrm{Re}\left\{\frac{u_\varepsilon}{2}\,q_1\frac{q_2-ip_2}{p_1q_2-q_1p_2}\cdot\frac{1}{\zeta_1(x,y+H)} + \frac{u_\varepsilon}{2}\,q_2\frac{-q_1+ip_1}{p_1q_2-q_1p_2}\cdot\frac{1}{\zeta_2(x,y+H)}\right\}$$

$$v^-(x,y) = -V(x,y-H) = -2\mathrm{Re}\left\{\frac{u_\varepsilon}{2}\,q_1\frac{q_2-ip_2}{p_1q_2-q_1p_2}\cdot\frac{1}{\zeta_1(x,y-H)} + \frac{u_\varepsilon}{2}\,q_2\frac{-q_1+ip_1}{p_1q_2-q_1p_2}\cdot\frac{1}{\zeta_2(x,y-H)}\right\}$$

$$v^c(x,y) = 2\mathrm{Re}\left\{q_1\Phi_1^{\,c}(z_1) - q_2\Phi_1^{\,c}(z_2)\right\}$$

$$= 2\mathrm{Re}\left\{\frac{u_\varepsilon}{(\lambda_1-\lambda_2)\cdot(p_1q_2-q_1p_2)}\cdot\left[\begin{array}{l}\dfrac{q_1\lambda_1R(1-i\lambda_1)\cdot(q_2-ip_2)}{z_1-\lambda_1H+\sqrt{\left[(z_1-\lambda_1H)^2-R^2\left(1+\lambda_1^{\,2}\right)\right]}} + \dfrac{q_1\lambda_2R(1-i\lambda_2)\cdot(-q_1+ip_1)}{z_1-\lambda_2H+\sqrt{\left[(z_1-\lambda_2H)^2-R^2\left(1+\lambda_2^{\,2}\right)\right]}} - \\ \ldots - \dfrac{q_2\lambda_1R(1-i\lambda_1)\cdot(q_2-ip_2)}{z_2-\lambda_1H+\sqrt{\left[(z_2-\lambda_1H)^2-R^2\left(1+\lambda_1^{\,2}\right)\right]}} - \dfrac{q_2\lambda_2R(1-i\lambda_2)\cdot(-q_1+ip_1)}{z_2-\lambda_2H+\sqrt{\left[(z_2-\lambda_2H)^2-R^2\left(1+\lambda_2^{\,2}\right)\right]}}\end{array}\right]\right\}$$

2) Pure distortion case:

Horizontal displacements: $u_\delta(x,y) = u^+(x,y) + u^-(x,y) + u^c(x,y)$ (2.16a)

$$u^+(x,y) = U(x,y+H) = 2\mathrm{Re}\left\{\frac{u_\delta}{2}\,p_1\frac{q_2+ip_2}{p_1q_2-q_1p_2}\cdot\frac{1}{\zeta_1(x,y+H)} + \frac{u_\delta}{2}\,p_2\frac{-q_1-ip_1}{p_1q_2-q_1p_2}\cdot\frac{1}{\zeta_2(x,y+H)}\right\}$$

$$u^-(x,y) = -U(x,y-H) = -2\mathrm{Re}\left\{\frac{u_\delta}{2}\,p_1\frac{q_2+ip_2}{p_1q_2-q_1p_2}\cdot\frac{1}{\zeta_1(x,y-H)} + \frac{u_\delta}{2}\,p_2\frac{-q_1-ip_1}{p_1q_2-q_1p_2}\cdot\frac{1}{\zeta_2(x,y-H)}\right\}$$

$$u^c(x,y) = 2\mathrm{Re}\left\{p_1\Phi_1^{\,c}(z_1) - p_2\Phi_1^{\,c}(z_2)\right\}$$
$$= 2\mathrm{Re}\left\{\frac{u_\delta}{(\lambda_1-\lambda_2)\cdot(p_1q_2-q_1p_2)}\cdot\left[\begin{array}{l}\dfrac{p_1\lambda_1R(1-i\lambda_1)\cdot(q_2+ip_2)}{z_1-\lambda_1H+\sqrt{\left[(z_1-\lambda_1H)^2-R^2(1+\lambda_1^{\,2})\right]}} + \dfrac{p_1\lambda_2R(1-i\lambda_2)\cdot(-q_1-ip_1)}{z_1-\lambda_2H+\sqrt{\left[(z_1-\lambda_2H)^2-R^2(1+\lambda_2^{\,2})\right]}} - \\ \ldots - \dfrac{p_2\lambda_1R(1-i\lambda_1)\cdot(q_2+ip_2)}{z_2-\lambda_1H+\sqrt{\left[(z_2-\lambda_1H)^2-R^2(1+\lambda_1^{\,2})\right]}} - \dfrac{p_2\lambda_2R(1-i\lambda_2)\cdot(-q_1-ip_1)}{z_2-\lambda_2H+\sqrt{\left[(z_2-\lambda_2H)^2-R^2(1+\lambda_2^{\,2})\right]}}\end{array}\right]\right\}$$

Vertical settlements: $v_\delta(x,y) = v^+(x,y) + v^-(x,y) + v^c(x,y)$ (2.16b)

$$v^+(x,y) = V(x,y+H) = 2\mathrm{Re}\left\{\frac{u_\delta}{2}\,q_1\frac{q_2+ip_2}{p_1q_2-q_1p_2}\cdot\frac{1}{\zeta_1(x,y+H)} + \frac{u_\delta}{2}\,q_2\frac{-q_1-ip_1}{p_1q_2-q_1p_2}\cdot\frac{1}{\zeta_2(x,y+H)}\right\}$$

$$v^-(x,y) = -V(x,y-H) = -2\mathrm{Re}\left\{\frac{u_\delta}{2}\,q_1\frac{q_2+ip_2}{p_1q_2-q_1p_2}\cdot\frac{1}{\zeta_1(x,y-H)} + \frac{u_\delta}{2}\,q_2\frac{-q_1-ip_1}{p_1q_2-q_1p_2}\cdot\frac{1}{\zeta_2(x,y-H)}\right\}$$

$$v^c(x,y) = 2\mathrm{Re}\left\{q_1\Phi_1^{\,c}(z_1) - q_2\Phi_1^{\,c}(z_2)\right\}$$
$$= 2\mathrm{Re}\left\{\frac{u_\delta}{(\lambda_1-\lambda_2)\cdot(p_1q_2-q_1p_2)}\cdot\left[\begin{array}{l}\dfrac{q_1\lambda_1R(1-i\lambda_1)\cdot(q_2+ip_2)}{z_1-\lambda_1H+\sqrt{\left[(z_1-\lambda_1H)^2-R^2(1+\lambda_1^{\,2})\right]}} + \dfrac{q_1\lambda_2R(1-i\lambda_2)\cdot(-q_1-ip_1)}{z_1-\lambda_2H+\sqrt{\left[(z_1-\lambda_2H)^2-R^2(1+\lambda_2^{\,2})\right]}} - \\ \ldots - \dfrac{q_2\lambda_1R(1-i\lambda_1)\cdot(q_2+ip_2)}{z_2-\lambda_1H+\sqrt{\left[(z_2-\lambda_1H)^2-R^2(1+\lambda_1^{\,2})\right]}} - \dfrac{q_2\lambda_2R(1-i\lambda_2)\cdot(-q_1-ip_1)}{z_2-\lambda_2H+\sqrt{\left[(z_2-\lambda_2H)^2-R^2(1+\lambda_2^{\,2})\right]}}\end{array}\right]\right\}$$

where

- $$\begin{Bmatrix} z_k = x + \lambda_k y \\ p_k = \beta_{12} + \beta_{11}\lambda_k^{\,2} \\ q_k = \frac{\beta_{22}}{\lambda_k} + \beta_{12}\lambda_k \end{Bmatrix} \qquad k = 1, 2$$

- $\lambda_k, \overline{\lambda_k} \quad k = 1, 2$ are roots of the characteristic equation

  $f(\lambda) = \beta_{11}\lambda^4 + (2\beta_{12} + \beta_{66})\lambda^2 + \beta_{22}$

  where

$$\beta_{11} = a_{11} - \frac{a_{13}^{\,2}}{a_{33}} = \frac{1}{E_h} - \frac{\nu_{vh}^{\,2}}{E_v}$$

$$\beta_{12} = a_{12} - \frac{a_{13}a_{23}}{a_{33}} = -\frac{\nu_{hh}}{E_h} - \frac{\nu_{vh}^{\,2}}{E_v}$$

$$\beta_{22} = a_{22} - \frac{a_{23}^{\,2}}{a_{33}} = \frac{1}{E_h} - \frac{\nu_{vh}^{\,2}}{E_v}$$

$$\beta_{66} = a_{66} = \frac{1}{G_{vh}} \ (in\ plane - strain\ conditions)$$

- The conformed variables ζ_k, k=1, 2 are analytical functions that are used as transformations from an ellipse to a circle of unit radius and are equal to:

$$\zeta_k = \frac{z_k + \left\{ z_k^{\,2} - R^2\left(1 + \lambda_k^{\,2}\right)\right\}^{1/2}}{R\left(1 - i\lambda_k\right)}, \quad k = 1, 2$$

The total displacements are the sum of the displacements generated due to uniform convergence and pure distortion (given in eq. 2.15 and 2.16) and are equal to:

$$u_{tot}(x,y) = u_{\varepsilon}(x,y) + u_{\delta}(x,y) \quad (2.17a)$$

$$v_{tot}(x,y) = v_{\varepsilon}(x,y) + v_{\delta}(x,y) \quad (2.17b)$$

2.3.4 Comparison of isotropic and anisotropic analytical solutions

Figures 2.13 a and b compare distributions of ground movements (horizontal, $u_x/|u_\varepsilon|$; and vertical, $u_y/|u_\varepsilon|$) around a tunnel with R/H = 0.3 and assumed ρ = 0.5, using the isotropic model (with ν=0.5) and the anisotropic model with stiffness parameters that correspond to isotropic conditions: E_v'=100MPa, $n = \frac{E_h'}{E_v'} = 1.001$, ν_{vh}= ν_{hh}=0.5, $m = \frac{G_{vh}}{E_v'} = \frac{0.5}{1+\nu_{hh}} = 0.333$. The agreement is excellent between the two solutions and any differences are indistinguishable in most of the soil mass (the maximum difference is 5.6% and was found in the horizontal displacements at the surface at a distance x/H=0.41 from the tunnel centerline). Hence, the results confirm that the anisotropic solutions converge to the isotropic case for appropriate stiffness parameters.

Figure 2.14 shows a vector diagram of normalized field displacements (horizontal, $u_x/|u_\varepsilon|$; and vertical, $u_y/|u_\varepsilon|$) for a tunnel with R/H=0.3 and assumed ρ = 2, using the isotropic model (with ν=0.5) and the anisotropic model with stiffness parameters that were reported by Gasparre et al (2007) for London Clay at strain levels < 0.001% (E_v'=100MPa, n=2, m=0.6 ν_{vh}= 0.25 and ν_{hh}=-0.2). It is interesting to note

that the displacement vectors are not all directed towards the same point (for example the center of the tunnel, as was suggested by Attewell (1978) and O'Reilly and New (1982) for the computation of the horizontal displacements in the empirical method). For both models the displacement vectors along the surface are directed towards the centre of the tunnel. The anisotropic models seems to be predicting larger surface settlements. At a zone along the tunnel springline, the isotropic model predicts nearly purely horizontal outward displacements, while the anisotropic model predicts much smaller horizontal movements and larger vertical settlements. At a zone along the tunnel centerline, both models predict nearly purely vertical settlements, with the anisotropic model predicting slightly higher values. Finally, below the tunnel, both models predict very small ground distortions.

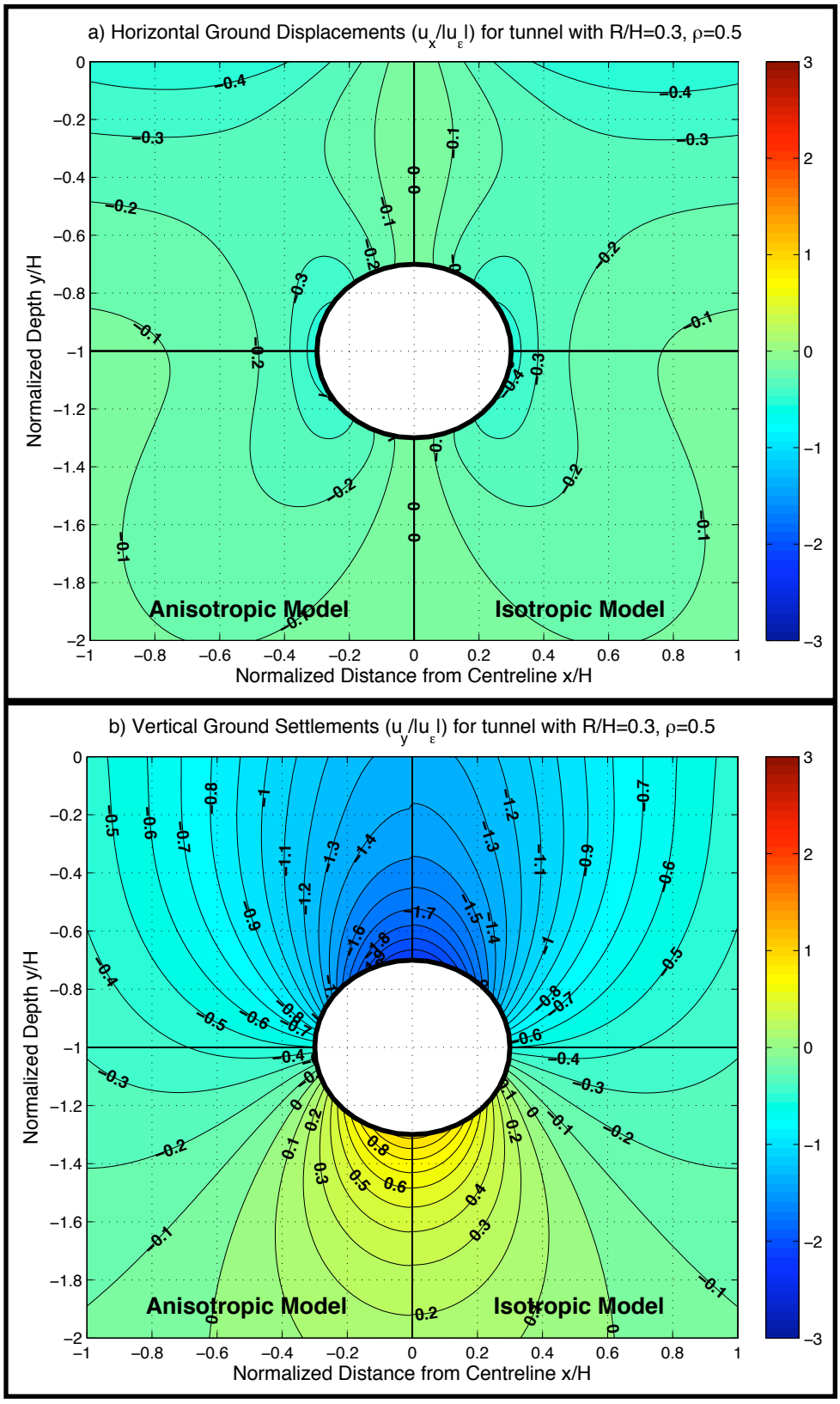

Figure 2.13: Comparison of displacement fields computed by Isotropic and Anisotropic models with isotropic stiffness parameters

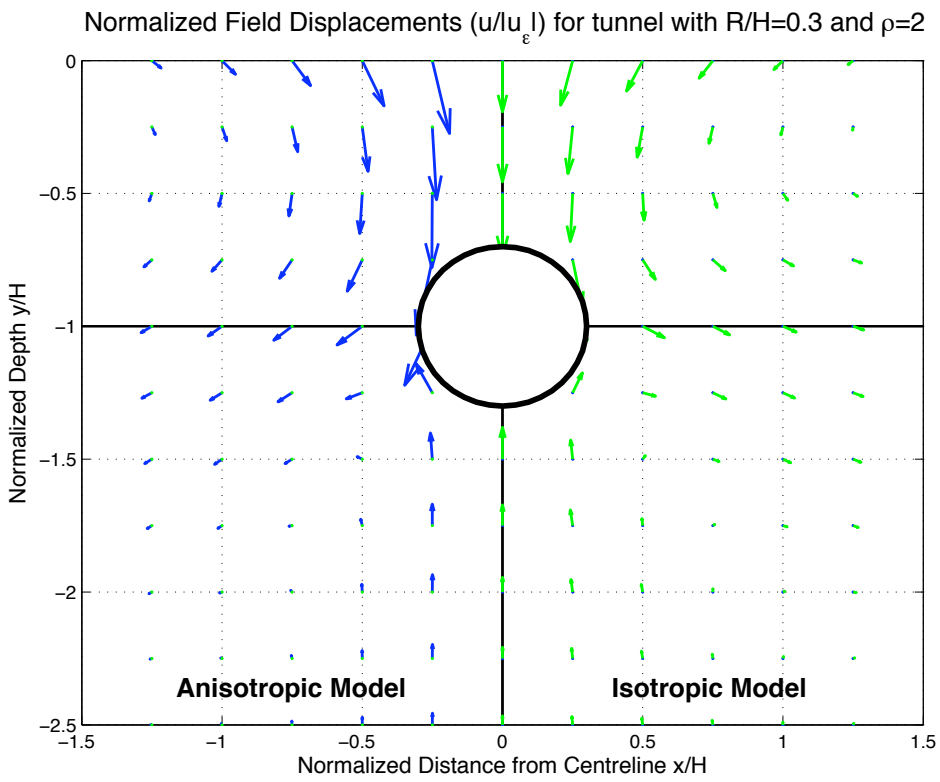

Figure 2.14: Comparison of field displacement vector diagrams computed by Isotropic and Anisotropic models with London Clay stiffness parameters

Figures 2.15 a and b compare surface ground movements (horizontal, $u_x/|u_\varepsilon|$; and vertical, $u_y/|u_\varepsilon|$) around a tunnel with R/H = 0.3 and assumed ρ = 1.5, using the isotropic model (with ν=0.5) and the anisotropic model with London Clay stiffness parameters (E_v'=100MPa, n=2, m=0.6 ν_{vh}= 0.25 and ν_{hh}=-0.2). The surface horizontal displacements predicted by the two analytical solutions are very similar in the range -0.8 < x/H < 0.8, with the isotropic model predicting slightly larger maximum horizontal displacement, but at the same position as the anisotropic model. However, further away from the tunnel the two models predict very different horizontal movements, with the isotropic model converging to $u_x/|u_\varepsilon|$=0.25 in the

far field instead of converging to zero horizontal displacements as would be expected and also as is predicted by the anisotropic analytical solutions. On the other hand, the surface settlements predicted by the two models are very similar. The maximum settlement at the centreline $u_y^0/|u_\varepsilon|$ predicted by the anisotropic model is slightly higher than the corresponding isotropic value. Also, the surface settlement trough predicted by the isotropic analytical solutions converges to $u_y^0/|u_\varepsilon| \approx 0.1$ in the far field as opposed to the anisotropic case that converges to zero at x/H=2.5.

Chatzigiannelis and Whittle (2001) undertook an extensive study on elastic anisotropic parameters reported from laboratory tests in the literature for various types of soils. Their results are summarized in Table 2.2 (the table also includes anisotropic parameters reported by Gasparre et al in 2007 for London Clay at strain level < 0.001%). Figure 2.16 presents design charts similar to those produced by Pinto (1999) for R/H=0.3 that incorporate the anisotropic parameters of Table 2.2 and also show the isotropic solution (assuming ν=0.3). Anisotropy has a significant effect in the relation of u_y^1/u_y^0 vs u_x^0/u_y^0 (i.e. in the gradient of the design line). The isotropic solution coincides with the 'Normally consolidated and soft clays' line which has n=0.86 and m=0.33. For the soils that have n > 1 (ex London Clay), the gradient of the design line becomes smaller than the isotropic line, while for soils with n < 1 (ex sands and gravels) the gradient becomes larger. The design charts show that incorporating anisotropy enable the analytical solutions describe a larger range of soil responses.

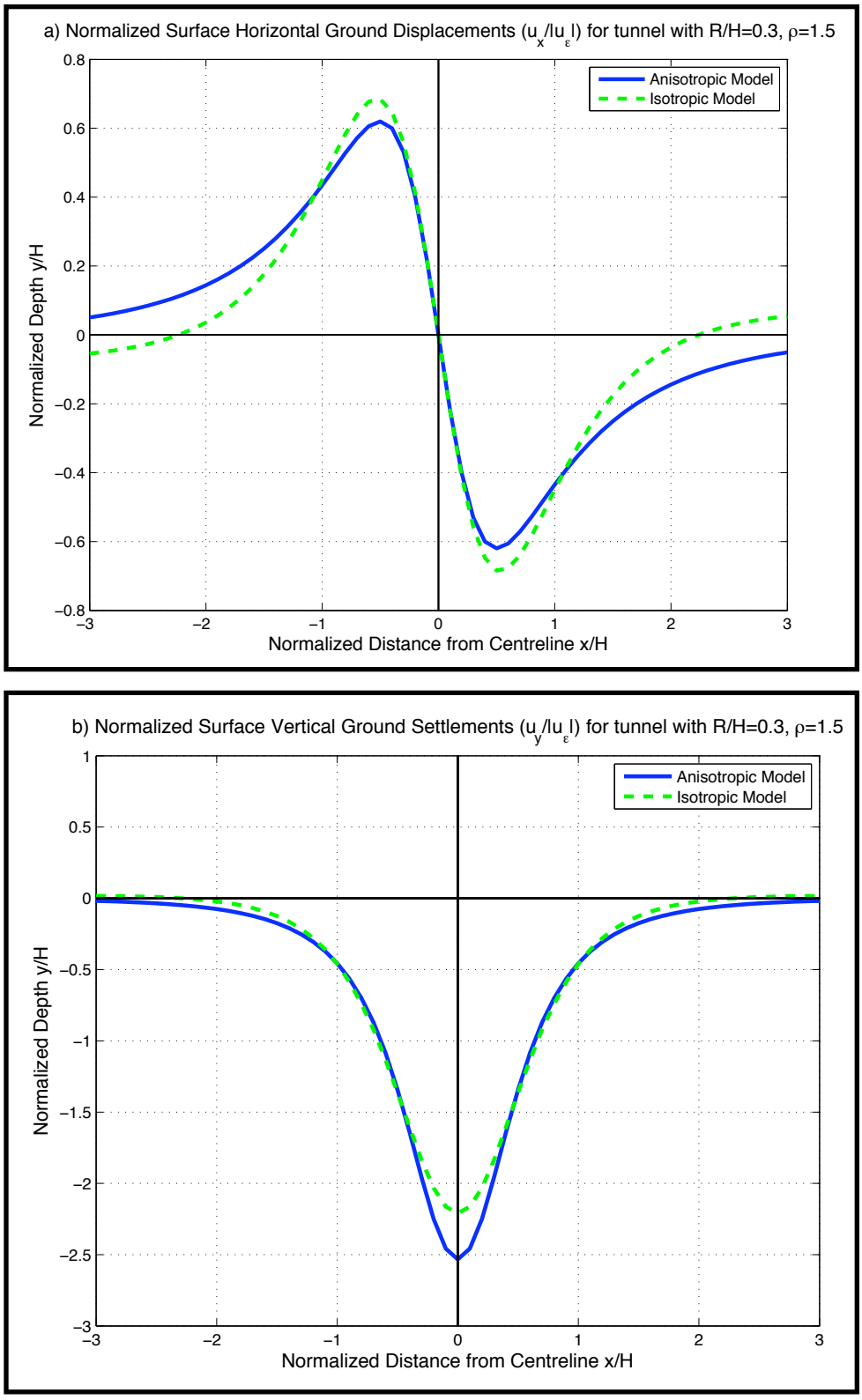

Figure 2.15: Comparison of surface displacements computed by Isotropic and Anisotropic models for tunnel with R/H = 0.3 and ρ = 1.5

Soil Type	E_v (MPa)	$n=E_h/E_v$	$m=G_{vh}/E_v$	ν_{vh}'	ν_{hh}'
London Clay*	112	2.11	0.64	0.25	-0.19
Gravel	305	0.51	0.3	0.25	0.18
Sand	330	0.94	0.4	0.15	0.17
Silts	300	0.79	0.78	0.06	0.29
NC & Soft Clays	80	0.86	0.33	0.34	0.3
Varved Clays	20	1.11	0.3	0.19	0.23
Clays	100	1.46	0.44	0.34	0.27
OC & Stiff Clays	110	1.23	0.46	0.28	0.13
* Measured by HCA tests at strain level < 0.001% (Gasparre et al, 2007)					

Table 2.2: Average values of elastic anisotropic stiffness parameters found in literature (Chatzigiannelis and Whittle, 2001)

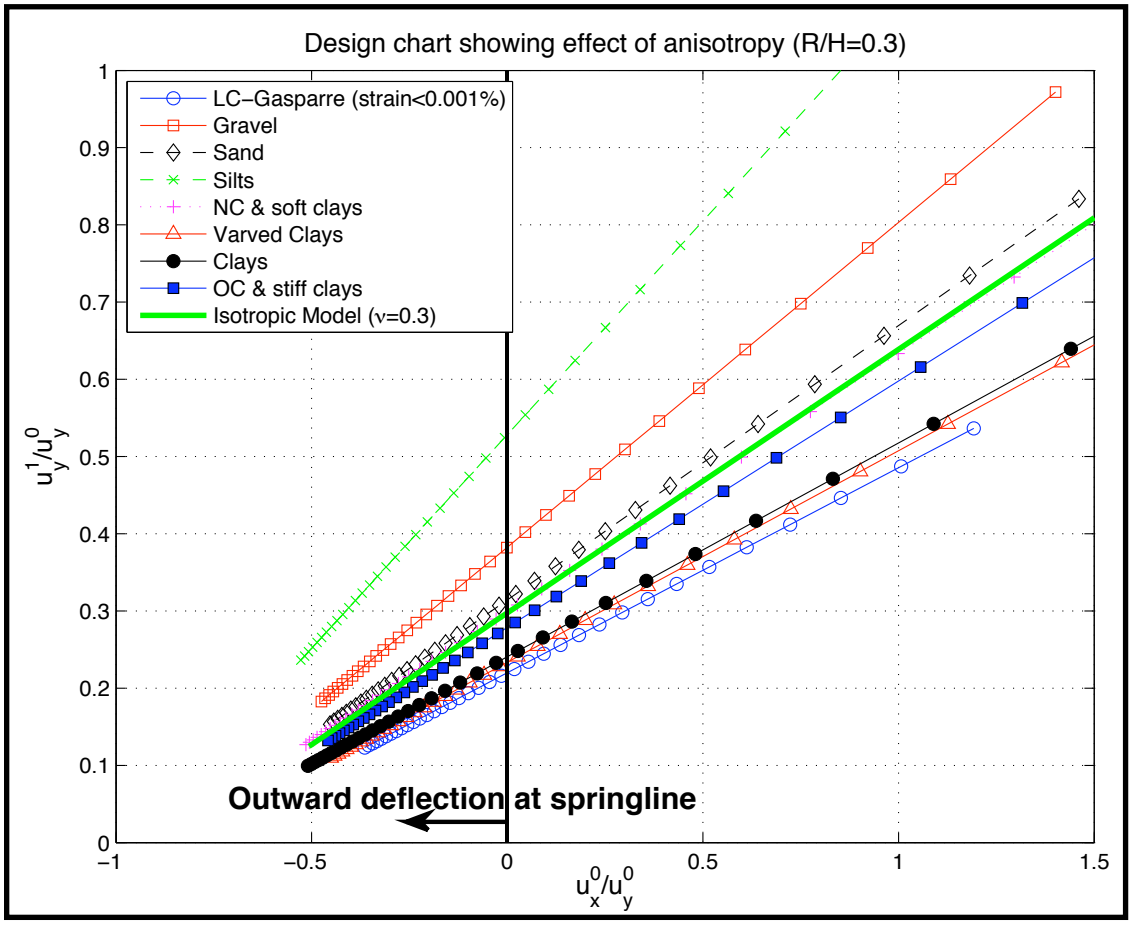

Figure 2.16: Design chart for R/H=0.3 showing effect of anisotropy in the gradient of the design line (u_y^1/u_y^0 vs u_x^0/u_y^0)

2.3.5 Summary of analytical solutions

Analytical solutions provide a useful framework for understanding the distributions of ground movements caused by the construction of tunnels. The isotropic analytical formulations require minimal information on soil properties and therefore make gross approximations of real soil behavior (i.e. constitutive equations), but otherwise are based on a rigid theoretical framework. Having the choice between linear elastic (ρ, ν) or constant dilation plastic (ρ, α) material behavior the analytical solutions can match a large fraction of the empirically observed settlement distributions (Figure 2.8).

The reference field measurements and the design charts proposed by Pinto and Whittle (2001) were effective in selecting appropriate input parameters for several tunnels such as the N-2 contract tunnel for the San Francisco clean water project and for other tunnels. However, the proposed design charts failed to select appropriate input parameters for the case of the Heathrow Express trial tunnel in London and thus the analytically computed ground displacements deviated significantly from the measured data (Pinto, 1999). The proposed reference scheme is very restricted to the three particular field measurements, especially considering that the location and scope of field measurements varies significantly from one project to another. Also, by not taking into account more field data, the proposed reference scheme is prone to measurement errors that might have taken place in measuring the three field parameters.

Analytical solutions that accounted for cross-anisotropy were subsequently developed by Chatzigiannelis and Whittle (2001). These anisotropic analytical solutions require more information on soil stiffness properties (5 stiffness properties vs. 2 for isotropic solutions). However, in cases where soils are highly overconsolidated and fissured (ex London Clay), the anisotropic solutions can produce better fits to the measured data. This is illustrated extensively in Chapters 3 and 4. The anisotropic solutions produce similar vertical settlements with the isotropic solutions. However, the anisotropic solutions with $n > 1$ seem to produce smaller horizontal ground movements than the isotropic model.

2.4 Finite Element Analysis

Non-linear Finite Element methods are powerful numerical analyses that can simulate various forms of tunnel construction. For simplicity reasons, two-dimensional (2D) FE analyses remain more widely used than 3D models, though the latter are clearly preferable for modeling tunnel construction. When using 2D FE analysis, it has proven difficult to reproduce the Gaussian distribution curve presented in equation (1) for modeling the transverse surface settlement trough. Clough and Leca (1989) suggested that one of the reasons for the shape of the surface settlement trough not being well predicted is the use of 2D analyses to represent a setup which is, by its nature, three-dimensional (see Figure 2.17). Furthermore, sophisticated soil models are necessary to produce a realistic surface

settlement trough using 2D FE analyses, particularly for tunnels in heavily overconsolidated clays, since isotropic linear elastic-perfectly plastic soil models lead to wider surface settlement troughs than the observed Gaussian distribution (Mair et al, 1981). Other factors such as the radial stress field can also significantly affect the shape of the surface settlement trough. In addition, the degree of anisotropy used in the soil model plays an important role in the ground movement predictions.

Lee and Rowe (1989) suggest that introducing anisotropic elastic soil properties can significantly improve the FE analysis results. Finally, the tunnel construction process is very hard to model, with shield tunneling posing more problems for 3D FE analysis than NATM, which is less complex (Moeller, 2006). Figures 2.17 and 2.18 illustrate proposed installation procedures, to simulate construction of open face NATM tunnels and closed face shield tunnels.

Although considerable progress has been made in finite element analysis in recent years, problems in FE modeling still exist. First, FE analyses that use non-linear constitutive soil models are expensive and their high cost is not justified for the majority of tunneling projects. Furthermore, other parameters, such as the geometry of the tunnel lining and dimensions of the tail void, are often very hard to define or represent in FE models. A third drawback of the FE method is that multiple analyses are required for different sections of the tunnel due to usual change in tunnel elevation and soil stratigraphy. Finally, a constitutive soil model that is successful at modeling all aspects of soil behavior related to tunnel construction has

not yet been developed. These limitations are further illustrated by the case study presented in Chapter 3.

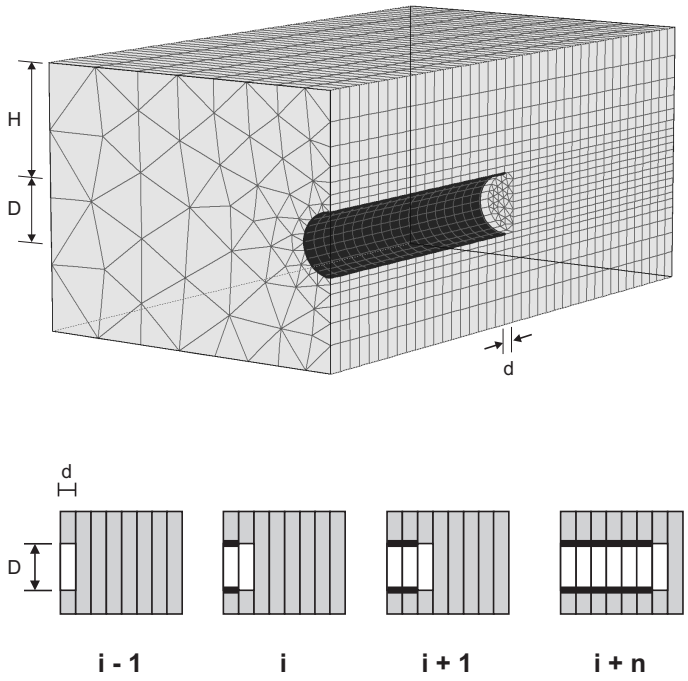

Figure 2.17: Step-by-step simulation of open face, NATM tunneling (Moeller, 2006)

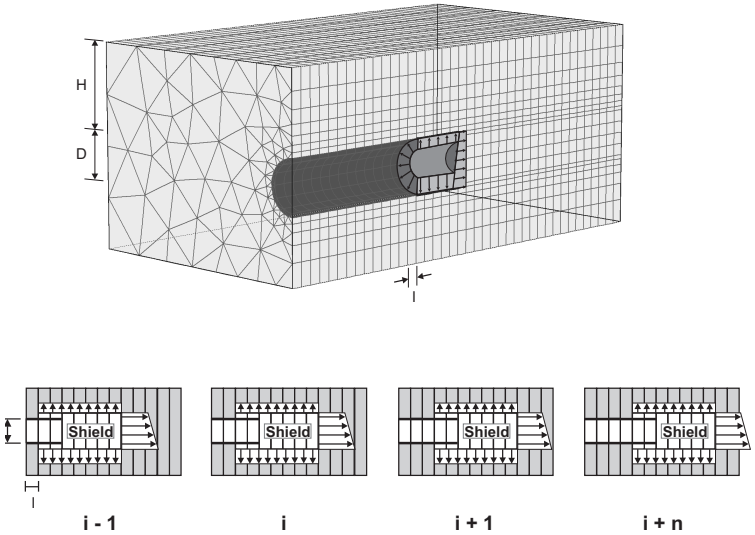

Figure 2.18: Step-by-step simulation of closed face, shield tunneling (Moeller, 2006)

2.4.5 Conclusions

Assessment of the ground movements induced by the construction of a tunnel is crucial, especially when tunneling takes place in an urban environment, since these ground movements can cause extensive damage to overlying structures. Three main methods exist for describing ground movements. Empirical methods are the most widely used in the engineering practice, they are simple and effective in modeling surface ground settlements. However, they lack of a theoretical framework to support them and also are not very successful in modeling horizontal and subsurface ground settlements. Isotropic analytical closed form solutions provide a more consistent framework for interpreting the ground movements induced by tunneling than conventional empirical models and require minimal information on soil properties. They also provide a useful basis for evaluating the performance of numerical analyses. The reference scheme suggested by Pinto and Whittle (2001) proved to be effective in selecting appropriate model parameters for several tunnels (Pinto, 1999). However, the proposed design method is very restricted to the predefined field data and makes the analysis prone to measurements errors. Also, the suggested design scheme failed to generate a good fit to the ground movements measured at the Heathrow Express trial tunnel (Pinto, 1999).

Cross-anisotropic analytical solutions have been developed by Chatzigiannelis and Whittle (2001). These solutions manage to better describe the field data at the Heathrow Express trial tunnel. At the same time incorporating anisotropy enables the analytical solutions to match a larger number of soil types. However, they

require more information on soil properties and thus their application is more complex than the simple closed-form analytical solutions proposed by Pinto and Whittle (2001).

Non-linear Finite Element analyses are capable of modeling a wide range of tunnel construction methods. However, this requires modeling details of the construction process and appropriate constitutive model parameters, which are very hard to select. Prior studies (e.g. Mair et al, 1981) have shown that FE analyses tend to produce wider settlement troughs than those measured for tunnels in highly over-consolidated clays, such as London Clay.

Chapter 3
St James's Park Tunnel

3.1 Introduction

Construction for the Jubilee Line Extension (JLE, 1994-1999) included 15km of twin, 4.85m diameter, bored tunnels from Green Park and St. James's Park to Westminster, Waterloo and into London's East End The tunneling was carried out using open-face shields and mechanical backhoes for excavation. The ground displacements caused by the construction of the tunnels were measured at a well instrumented greenfield site situated at St. James's Park, shown in Figure 3.1, and were analyzed in great depth by Nyren (1998). The Westbound (WB) tunnel passed underneath the instrumentation site in April 1995 and the Eastbound (EB) tunnel in January 1996. The monitoring data includes surface and subsurface ground movements in three dimensions, pore water pressures and total stress changes in the ground above the two tunnels.

The main purpose of the study described here is to evaluate the effectiveness of analytical solutions proposed by Pinto and Whittle (1999) and Chatzigiannelis and Whittle (2000) in simulating the ground deformations generated by open face tunnel construction in London Clay. The focus is on the WB tunnel since it was built first, with a time lag of nine months prior to the construction of the EB tunnel and therefore can be treated as a single tunnel cavity. Chapter 3 begins with a detailed description of the St James's test site conditions, the instrumentation used and a summary of previous interpretations of the measurements undertaken by Nyren et

al (1998). The Chapter moves on to present the application of the proposed analytical solutions and evaluate their effectiveness in predicting surface and subsurface movements, in the vertical and horizontal directions. The Chapter ends with the application of further analytical solutions that incorporate cross-anisotropic stiffness parameters and provides an assessment of their performance in describing the ground movements that were generated by the construction of the JLE WB tunnel.

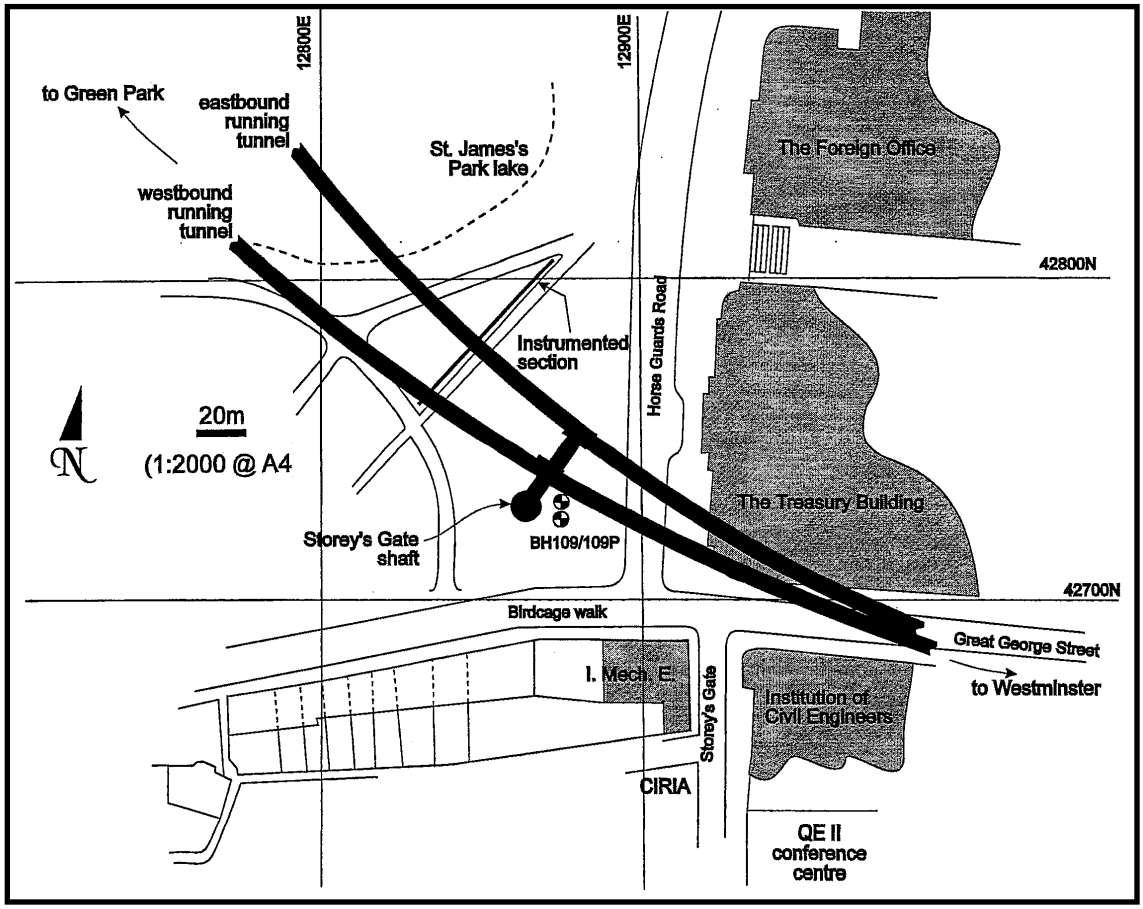

Figure 3.1: Plan of St James's area showing running tunnels for JLE project

3.2 Site Conditions

The stratigraphy, groundwater and physical properties of the soils have been evaluated in detail by Nyren et al (1998) and later by Standing and Burland (2006). Figure 3.2 shows a cross-section of the ground conditions at St James's Park. Note that elevations are given as 'above Project Datum' (aPD), which was set by Standing and Burland (2006) at 100m below Ordnance Datum. In addition, boreholes 1 and 2 (Bh1 and Bh2) are placed south of the lake, while boreholes 3, 4 and 5 (Bh3 – Bh5) are placed north of the lake. The instrumented control section is at the ground surface (~103m aPD) south of the lake.

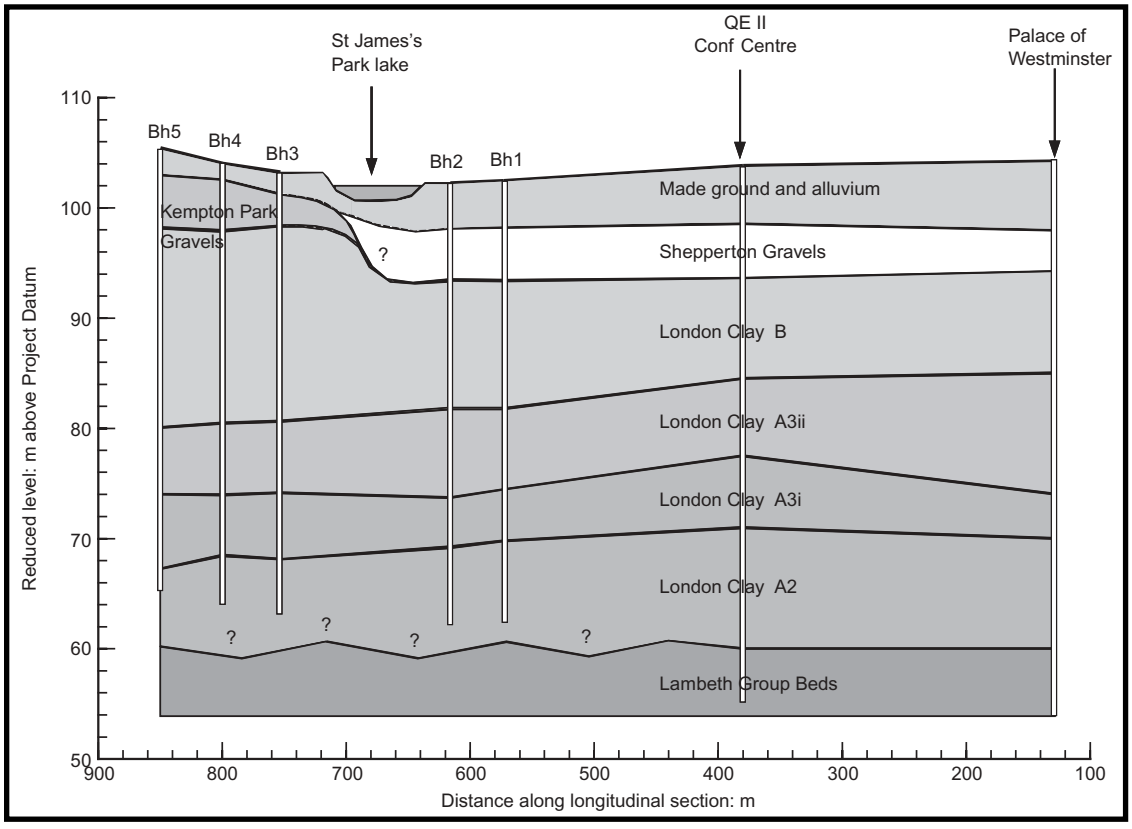

Figure 3.2: Longitudinal section across St James's Park and Westminster showing ground conditions (Standing and Burland, 2006)

The soil profile comprises the following units:

1-2m of sandy man-made fill that contained debris and brick pieces was present along most of the length of the JLE tunnels except for St. James's Park.

5m of alluvium deposits, which cover the whole test site, are mainly a sandy silt. Alluvium deposits originate from the end of glaciation and were probably formed recently (within the last 10000 years) by glacial run-off carried locally by the River Thames or other rivers that existed previously in the area. Alluvium soils are very common across the London Basin. They are mostly sandy but can often vary laterally and vertically in composition, containing layers of soft, compressible and highly variable clays, silts, gravels and organics (Nyren, 1998).

5m of dense terrace gravel, which are also very common in the London area and were developed as part of an ancient flood plain that was produced in response to seasonal snow-melt run-off during cold climatic periods of the Pleistocene (Nyren, 1998). The resulting deposits are generally well-graded and contain sand and gravel with some silt and silty sand partings. Specifically in the test site, Terrace Gravels were described as 'orange brown, very sandy (medium to coarse), sub-angular to sub-rounded, well graded (fine to coarse), flint gravel with occasional cobbles. The material state was estimated as medium to dense, from SPT 'N' values.' (Nyren, 1998).

Approximately 40m of London Clay, which is a marine clay, deposited in a quiet offshore environment during the Eocene and Palaeocene age. Most of the overlying

deposits, which are estimated to have been about 200m thick from the base of the London Clay (Skempton and Henkel, 1957), were removed by erosion during the later Tertiary and Pleistocene periods, leaving most of the unit in an overconsolidated state. Four distinct layers were identified within the London Clay (Standing and Burland, 2006). The divisions are based on the examination of split samples from the test site and are shown in Figure 3.2. Starting from the top:

1. **Division B** represents a stiff to very stiff, thinly laminated, silty to very silty clay, of dark grey brown colour that contains large vertical fissures towards the base.
2. **Division A3ii** is a very stiff thinly laminated very silty to silty clay, of dark grey brown colour that contains silt/sand partings, dustings, pockets and lenses and occasional fissures.
3. **Division A3i** is an often heavily fissured, thinly laminated silty clay of dark grey brown colour.
4. **Division A2** is a very stiff becoming very stiff to hard interbedded, fine sandy and very silty clay, of dark grey brown and in zones dark brown grey colour, with little visible fabric (strongly bioturbated). This horizon corresponds to the basal beds, is up to 10m thick and lies between 2m and 4m above the top of the Lambeth Group.

The base of B is easily identified by the sudden appearance of sand and silt partings. The boundary between A3ii and A3i is not so apparent, as it corresponds to the disappearance of sand and silt partings. Finally, the boundary between A3i and A2

was evident by the presence of bedding planes and the appearance of strongly bioturbated, amorphous, slightly sandy clay (Standing and Burland, 2006). The WB tunnel was entirely excavated within the London Clay *A3* unit at a depth to springline H = 31m, while the EB tunnel was bored within the London Clay *B* unit at a depth to springline H = 20.5m.

It is interesting to note in Figure 3.2 the significant reduction in elevation (about 4.5m) of the top of the London Clay layer, from north to south of the lake. This represents a terrace feature that caused a total of about 9.5m of material to be unloaded from the London Clay in the area south of the lake that was subsequently replaced by 4.5-5m of Shepperton gravels (Standing and Burland, 2006). The terrace feature and the unloading of the London Clay in the area south of the lake have direct implications for the engineering characteristics of the clay.

Beneath the London Clay formation exist the Lambeth Group deposits, the Thanet Sand Formation and Chalk Group of considerable thickness.

Two aquifers exist in the London Basin: 1) a deep aquifer at lower granular units of the Lambeth Group, Thanet sands and Chalk capped by the London Clay or the clays contained in the Lambeth Group and 2) a water table in the Terrace Gravels on top of the London Clay. During the JLE site investigation the water table of the upper aquifer was found at 3m below ground surface and observations from piezometers installed in the London Clay Formation showed a near-hydrostatic water pressure distribution from the top of the Terrace Gravel deposits.

3.2.1 Properties of London Clay

Standing and Burland (2006) undertook some extensive review of the soil properties at the test site. They focused on basic traditional sampling and testing methods similar to those used by Nyren et al (1998) for the original JLE site investigation, in order to be able to make comparisons with the existing data. Five pairs of boreholes were drilled to 40m depth across the park (see Bh1-Bh5, Figure 3.2). Continuous open-driven 100mm diameter samples were taken in one borehole and in the other SPT tests at 4m intervals were undertaken at intermediate depths for laboratory testing. Standpipe piezometers were also intalled at each of the five locations to measure pore pressures and to establish the in situ permeability across the site. Table 3.1 summarizes engineering properties of London Clay as recommended by Nyren et al (1998) and from the more recent study by Standing and Burland (2006).

London Clay Parameters	Nyren et al (1998)		Standing & Burland (2006)	
	Best Estimate	Possible Range	Best Estimate	Possible Range
γ_t (kN/m^3)	19.5	18.5 - 20.5	19.5	19.0 - 20.0
s_u (kPa)	115	80 – 150	228	95 – 360
k (m/s)	1×10^{-9}	1×10^{-8}-1×10^{-6}	7.9×10^{-9}	7.3×10^{-9}-8.4×10^{-9}
K_0	1.5	0.8 – 2	No reported values for these parameters by Standing & Burland (2006)	
c' (kPa)	10	0 – 12		
ϕ'	21°	14° - 28°		
E_u (MPa)	80.5	17 – 144		
E' (MPa) [+]	64.4	14 – 115		
[+] $E'=0.8E_u$ assuming Poisson's ratio $\nu=0.5$				

Table 3.1: London Clay Parameters (Nyren et al,1998 and Standing & Burland, 2006)

From Table 3.1 we deduce that the more recent study by Burland and Standing shows same values for unit weight γ_t, but a significantly higher undrained shear strength s_u (nearly twice the value proposed by Nyren et al, 1998). Furthermore, the coefficient of permeability k was found significantly lower. In fact, Nyren et al (1998) quotes a range of values with an average $k=10^{-7}$m/s, while Standing and Burland (2006) quote a range that is 100 times lower ($k=10^{-9}$m/s). These very low values of k suggest that the behavior of the soil after the excavation of the tunnels is likely to be undrained. Finally, another important point to note is the high coefficient of lateral earth pressure at rest (K_0=1.5) quoted by Nyren (1998), which is typically found in the London Basin.

An extensive study recently undertaken by Gasparre et al (2007) has led to further improvements in understanding the anisotropic stiffness of natural London Clay. Triaxial and Hollow Cylinder Apparatus (HCA) experiments were undertaken on high quality samples taken from continuously sampled rotary boreholes and from blocks cut by hand in excavations at the Heathrow Terminal 5 (T5) site. Note that the stratigraphy of the T5 area is similar to St James's Park and it comprises 6m of gravel overlying about 52m of London Clay.

The hybrid triaxial cells employed to test 100mm diameter, 200mm high intact samples were fitted with the high-resolution axial and radial strain Linear Variable Differential Transformer (LVDT) sensors described by Cuccovillo and Coop (1997) and laterally mounted bender elements to measure G_{hh} and G_{hv}, the shear moduli associated with horizontally propagating shear waves that are polarized in the

horizontal and vertical planes respectively (Pennington et al, 1997), as shown in Figure 3.3. The LVDT devices allowed strain increments around $\pm 3 \times 10^{-5}$ % to be resolved, and the overall system (including the stress sensors) allowed the elastic stiffness of the samples to be measured with an accuracy of around ±3%. Conventional pressure transducers and load cells were used for the cell pressure, pore pressure and deviatoric load, along with a miniature mid-height pore pressure probe to monitor local pressures and drainage conditions.

Two different HCAs were employed in the study undertaken by Gasparre et al (2007): 1) the Imperial College Mark II HCA (ICHCA II) and 2) the hybrid Imperial College Resonant Column HCA (ICRCHCA). The nominal inner diameters, outer diameters and heights of specimens were 60mm, 100mm and 200mm respectively for the ICHCA II, and 38mm, 70mm and 170-190mm respectively in the ICRCHCA. Local strain sensors were deployed in the reported ICHCA II tests. The axial and torsional shear strains were measured with an enhanced electrolevel system, and radial and circumferential strains were calculated from the outer and inner diameter changes monitored with a set of three proximity transducers and a laterally mounted LVDT respectively. Taking multiple readings and using an averaging routine allowed strains to be resolved down to around 0.0003%. The ICRCHCA was equipped with a Hardin oscillator and accelerometer assembly with which torsional resonant column tests were performed to obtain the dynamic shear modulus G_{vh} down to very small strains (less than 10^{-6} %).

Following sample setting-up, an undrained cell pressure was applied to the specimens that exceeded the in situ mean stress in all cases, leading to measurable positive initial pore water pressures, which made initial effective stresses computable. Samples in both the triaxial and the HCA tests were then reconsolidated following the scheme shown in Figure 3.4 designed to match the in situ stress paths. Static tests undertaken in the ICHCA II were also performed on block samples. Over 30 small-strain drained probing experiments were conducted in which only one stress component was changed under drained conditions, while the others were held constant. Complete suites of such tests were performed on four specimens, at three effective stress states, in which individual samples were subjected to successive slow probing cycles involving changes in the σ_α, σ_θ and $\tau_{\alpha\theta}$ components of around 2kPa over a 1 h period (corresponding to principal strain rates of the order of 0.001-0.002%/h), one at a time, with a 2-day ageing period between each probing cycle. The five anisotropic parameters E_v', E_h', G_{vh}, ν_{vh}' and ν_{hh}' were subsequently obtained.

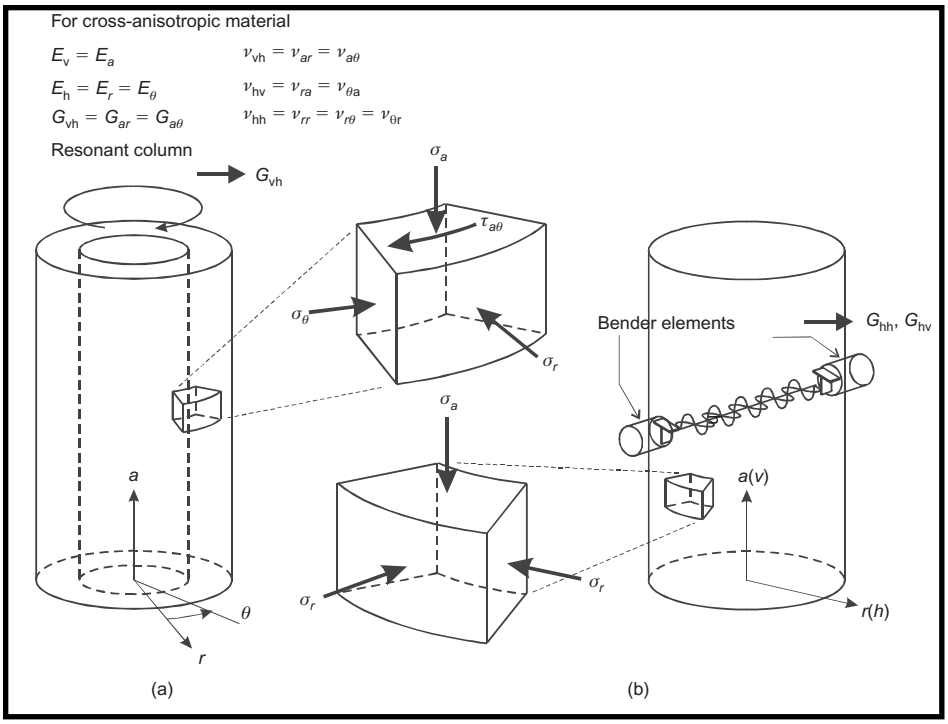

Figure 3.3: Coordinate systems in (a) HCA and (b) triaxial tests (Gasparre et al, 2007)

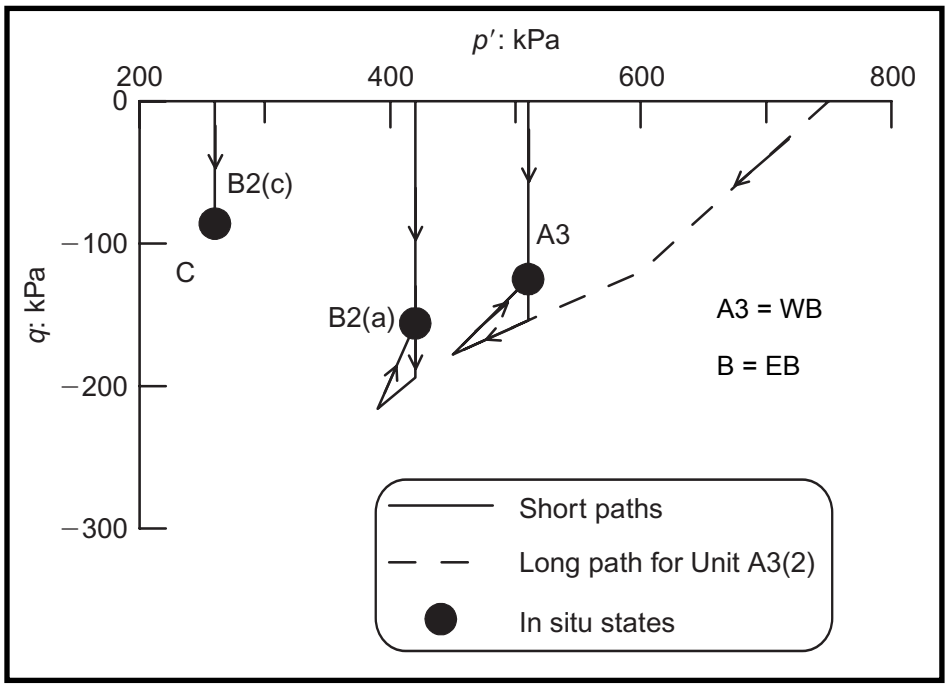

Figure 3.4: Stress paths imposed in triaxial and HCA samples (Gasparre et al, 2007)

Figure 3.5 shows 3 independent secant modulus measurements as functions of strain level. The measurements were taken from HCA tests on block samples from 5.2m depth from the top of the London Clay, with an initial mean normal effective stress p_0'=280kPa. Strong stiffness anisotropy is observed in the samples, with E_h' being significantly larger that E_v'. At very small strain we get stiffness parameters that would control the elastic wave propagation. An average strain level of 3% was deduced from the field data obtained at the St James's Park test site.

From Figure 3.5 we subsequently obtain stiffness parameters at 4 characteristic strain levels that are summarized in Table 3.2. Note that ν_{vh}' and ν_{hh}' are not reported as functions of strain and therefore are assumed constant.

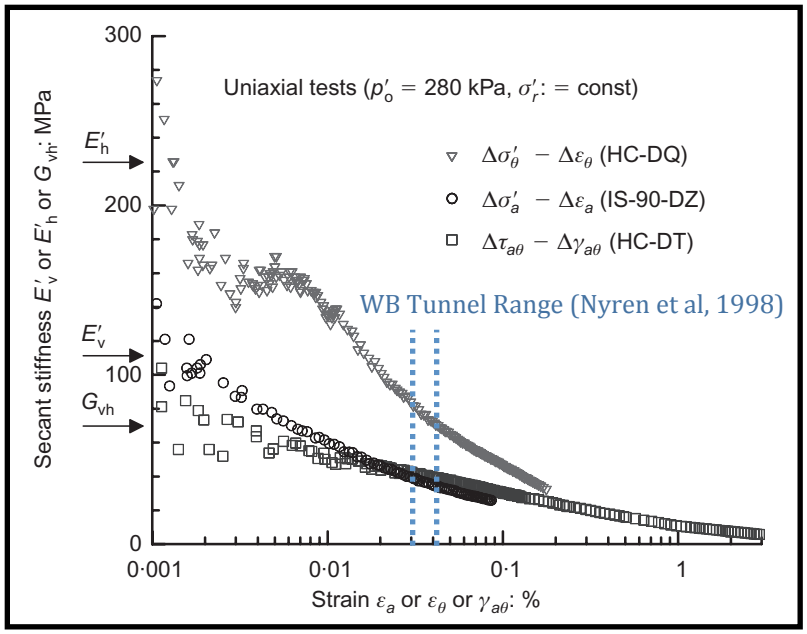

Figure 3.5: Secant moduli-strain relationships in drained HCA uniaxial loading tests (Gasparre et al, 2007)

Cross-Anisotropic Stiffness Parameters	Strain Level (%)			
	<0.001	0.01	0.03	0.1
E_v' (MPa)	112	65	40	26
E_h' (MPa)	236	136	85	49
G_{vh} (MPa)	72	50	45	30
v_{vh}' *	0.25	0.25	0.25	0.25
v_{hh}' *	-0.19	-0.19	-0.19	-0.19
* Not reported as functions of strain, assumed constant				

Table 3.2: Comparison between stiffness parameters obtained in HCA tests at different strain levels (values obtained from Fig. 3.5)

The anisotropic stiffness parameters for London Clay that correspond to the strain levels obtained by the WB tunnel construction (ε_α=0.03%) are:

1) E_v'=40MPa
2) $n = E_h'/E_v' = 85/40 = 2.125$
3) $m = G_{vh}/ E_v'=45/40 = 1.125$
4) $\nu_{vh}'= 0.25$
5) $\nu_{hh}'= -0.19$

3.3 Instrumentation at test site

The instrumentation installed by Nyren et al (1998) at the St James's Park test site is summarized in Figures 3.6 and 3.7 and drawing schematics of the different apparatus are included in Appendix II. The instrumentation comprised:

- 24 surface monitoring points (SMPs) for surface displacements measurements. The vertical displacements were measured using precision leveling while the transverse horizontal displacements were measured using a micrometer stick. For both sets of instruments a general accuracy of ±0.2mm was achieved. Figure 3.8 summarizes survey timings as well as the position of the WB tunnel face relative to the SMP line when the measurements were made during the construction period of the WB tunnel (called Period 2 by Nyren et al, 1998).
- 9 electrolevel inclinometers to measure subsurface horizontal displacements. The electrolevel inclinometers were auto-logged using a computer at 15-minute intervals. The digital reading (in bits) obtained from these instruments can be nearly linearly calibrated against tilt, for constant temperature conditions. The assumption of linear approximations generates an error of ±8% in the measured rotation. The largest rotation that was found during the monitoring at St. James's Park was about 7.5mm/m tilt, which yields a maximum potential error of 0.6mm/m. It was also noted by Nyren et al (1998) that in the inclinometer holes temperatures are generally constant and the error produced due to the slight temperature difference is negligible (±0.02mm/m tilt). Another important point related to the subsurface horizontal movements is that for deep inclinometers below the WB tunnel axis (A_i, C_i and D_i) the bottom of each inclinometer borehole was assumed stable (i.e. no displacement at the bottom), while for shallow inclinometers (D_i – H_i) movements at the top of the tubings were estimated

from the surface displacement measurements obtained by the micrometer stick.

- 11 rod extensometers for subsurface vertical displacements measurements, with an accuracy of ±0.2mm. Figure 3.9 summarizes the extensometer survey timings in relation to the position relative to the WB tunnel face. The figure shows that 10 sets of measurements were taken in 1 day (April 27th to 28th, 1995).
- Pneumatic Piezometers and 4 combined pneumatic piezometers/spade cells (see Figure 3.6 and 3.7) were installed at St James's Park to monitor the pore pressure changes above the WB tunnel. For the range of pressures measured at the test site, the piezometer as well as the combined spade cell/piezometer measurement accuracy is likely to lie between ±5kPa and ±10kPa. Around 15 measurements were completed at each instrument prior to the WB tunnel drive.

The WB tunnel advanced beneath the site at a depth to springline, H=-31m in April 1995 while the eastbound tunnel was built at a depth, H = -20.5m, 9 months later, in January 1996. At the line of SMPs, the two tunnels are 21.5m apart in plan and diverge towards Green Park. The WB tunnel intersects the instrumentation line at 80° while the EB tunnel is perpendicular. Both tunnels were excavated from the east to the west (i.e. from Waterloo, and through Westminster, to Green Park), at average rates of advance equal to 45.5 m/day (i.e. 1.9 m/hr).

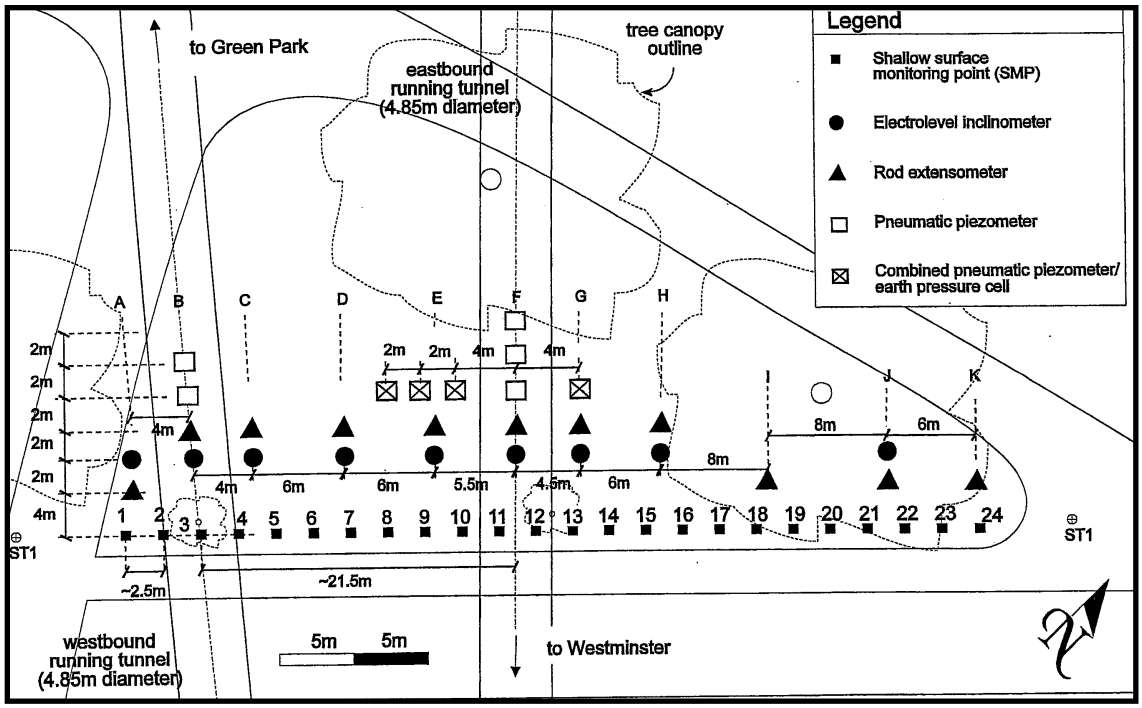

Figure 3.6: Instrumentation Layout at St James's Park (Nyren, 1998)

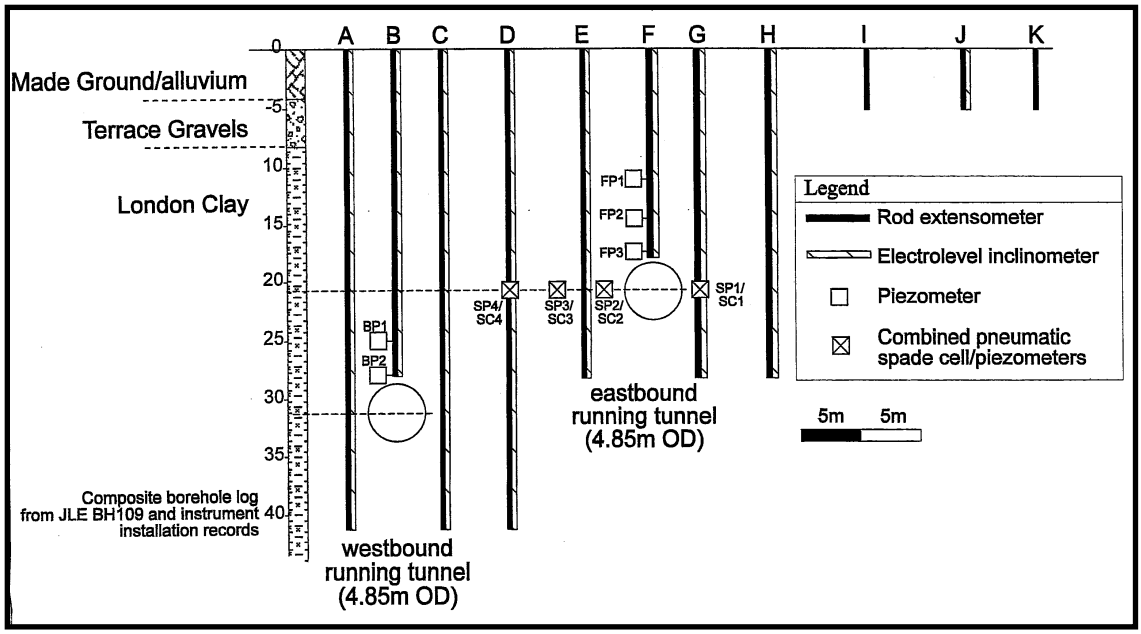

Figure 3.7: Cross-section of instrumentation at St James's Park (Nyren, 1998)

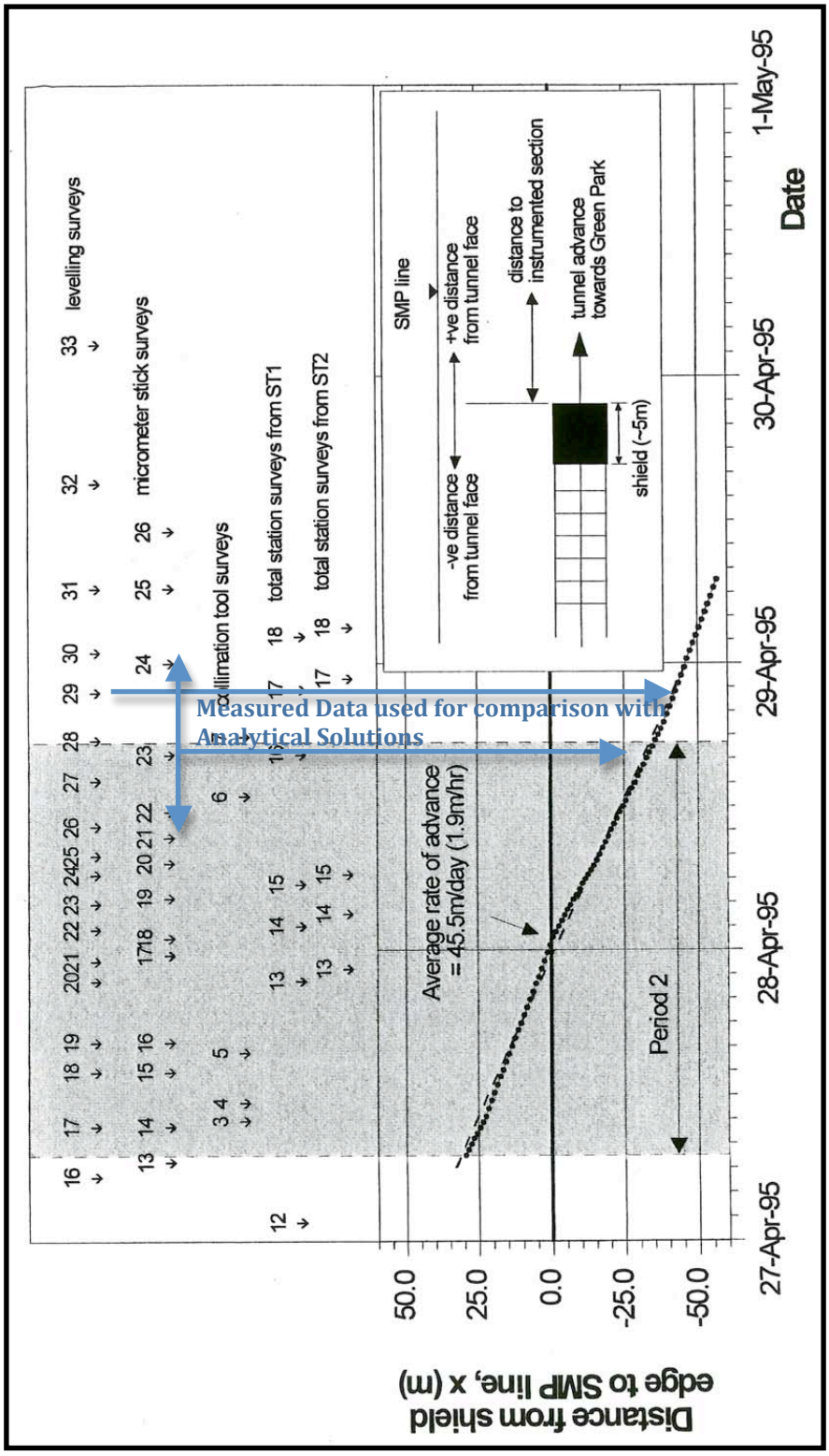

Figure 3.8: Timings of surface measurements in relation to WB face position

(Nyren, 1998)

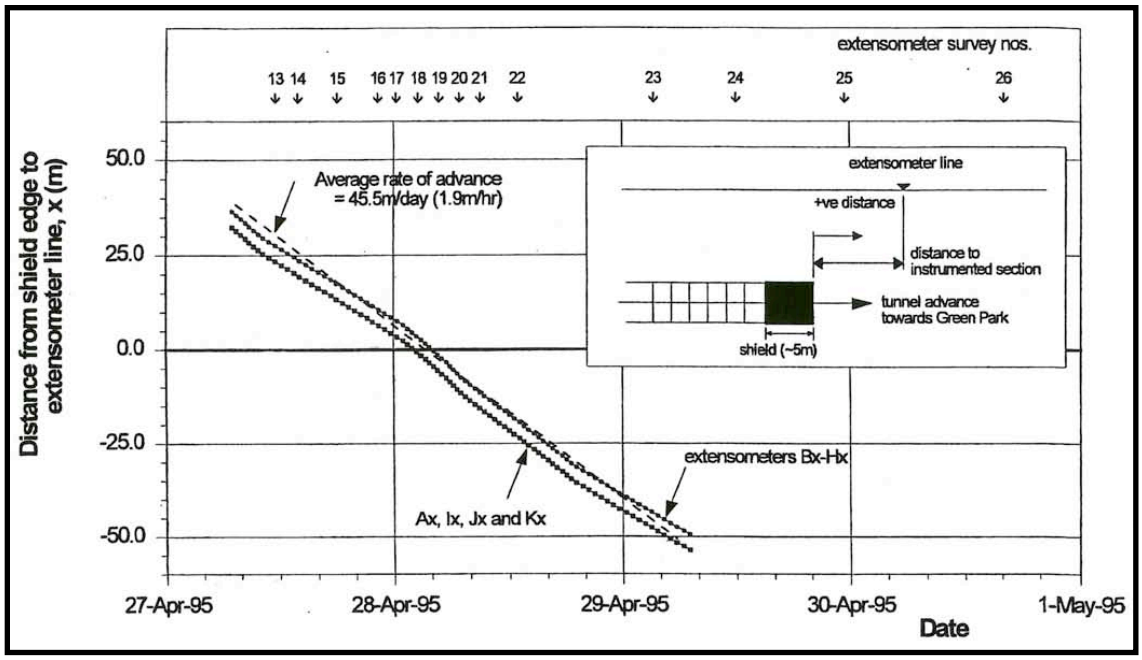

Figure 3.9: Extensometer survey timings in relation to WB tunnel face position (Nyren,1998)

3.4 Surface Displacements

Figures 3.10 and 3.11 summarize the vertical and horizontal surface displacement profiles. These are well defined to the east of the WB tunnel (see Fig. 3.6). The surface settlement data shown in Figure 3.10 come from levelling survey 29 and were collected from a distance of -40m from the WB tunnel face on April 29th 1995, 1 day after the WB tunnel face crossed the instrumentation line (see Figure 3.8). The horizontal surface ground movements shown in Figure 3.11 represent average values from micrometer stick surveys 21-24, which were collected from an average distance of -30m from the WB tunnel face (from -15m to -45m distance from the WB face) on the same day the WB tunnel crossed the SMP line (April 28th 1995). This

short time lag between the boring of the WB tunnel beneath the instrumentation line and the collection time (i.e. 1 day) in combination with the fact that London Clay is highly impermeable ($k \approx 10^{-9}$ m/s) suggest that the soil most likely experiences an undrained behavior when the measurements were taken by Nyren et al (1998) and therefore the settlements produced in the field are not caused by consolidation within the clay.

The vertical settlement profile appears to be symmetric, with a maximum settlement above the crown, $u_y^0 \approx 20$mm. Using the empirical Gaussian fit to model the surface settlements with the trough width parameter K = 0.43 ($x_i = K \times H = 0.43 \times 31\text{m} = 13.3\text{m}$) suggested by Standing and Burland (2006) we obtain the curve shown in Figure 3.10. The volume loss ratio implied using the conventional interpretation of ground movements is $\Delta V_L/V_0 = 3.7\%$ as shown:

From equation (2.2) $$V_s = u_y^{\,0}\, x_i \sqrt{2\pi} = 0.0204 \times 13.3 \times \sqrt{2\pi} = 0.68\,\text{m}^2$$

From equation (2.3) $$\frac{\Delta V_L}{V_0} = \frac{\Delta V_s}{\pi R^2} \times 100\% = \frac{0.68}{\pi \times 2.425^2} = 3.7\%$$

This volume loss is significantly higher than found from previous tunnel constructions in London Clay (Standing and Burland, 2006).

A maximum surface horizontal movement $u_x \approx 5.7$mm (towards the tunnel centreline) was measured at $x \approx 14$m east of the centreline (see Figure 3.12). However, there is also a point 3m to the west, with $u_x \approx -6$mm. Indeed, the profile

shows $u_x \neq 0$ at x = 0, and hence there is a loss of anti-symmetry in the measured horizontal displacements. The apparent centre-point ($u_x = 0$) occurs 2m to the east of the WB tunnel centreline. According to Nyren (1998) one possible reason for this asymmetry is the existence of far-field horizontal stresses, which vary with direction (i.e. the principal directions of the stresses in the horizontal plane do not coincide with the alignment of the tunnel). These in situ stress field will then influence horizontal ground deformations according to the trajectory of the tunnel alignment (see Fig. 3.6), i.e. even if the principal axes of stresses are initially aligned with the tunnel, deviations in the path can produce asymmetry in the horizontal displacements. Nyren et al (1998) recommend that in situ stress measurements should be obtained (e.g. using earth pressure cells, Fig. 3.6) across the site in order to measure the horizontal stress field prior to construction and also to identify any stress changes that occur during construction. However, Nyren et al used earth pressure cells to measure the total horizontal stress changes around only the EB tunnel, which do not provide any explanation to the asymmetry observed at the WB tunnel, since the EB tunnel generated symmetric ground response along the EB tunnel centerline.

Figure 3.11 also shows the empirical expression (eqn. 2.7) suggested by Attewell (1978) and O'Reilly and New (1982) for horizontal ground displacements, based on the assumption that the ground displacement vectors are directed towards the center of the tunnel, for tunnels in clays. We observe a very good fit between the

field measurements and the horizontal displacement profile generated by this simple empirical expression.

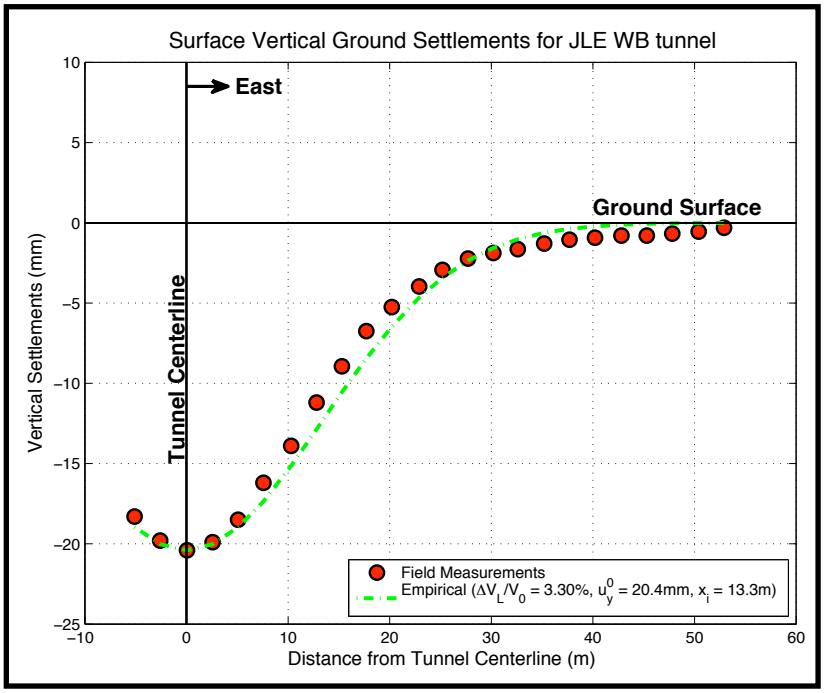

Figure 3.10: Surface vertical settlement profile at St James's Park WB tunnel (Nyren et al, 1998)

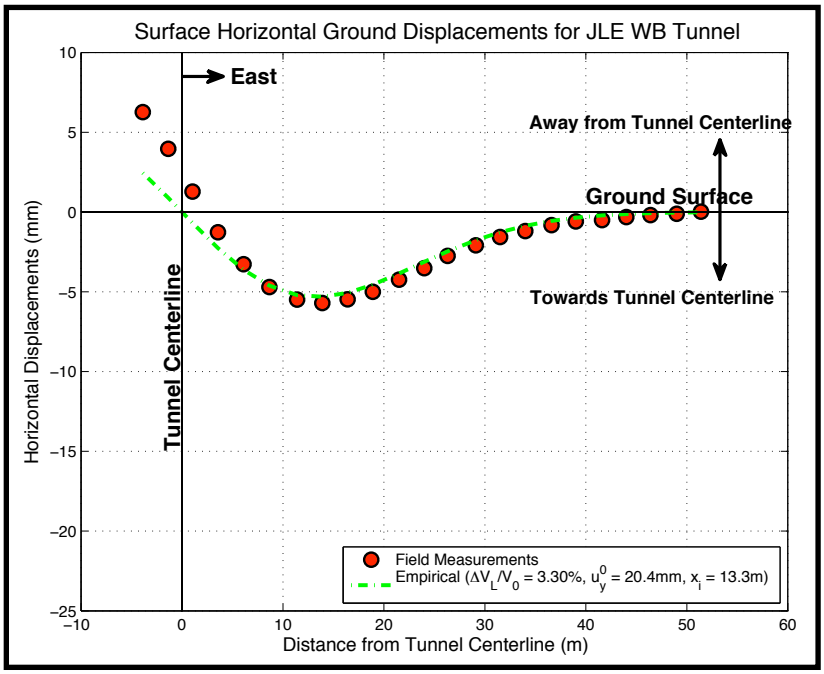

Figure 3.11: Transverse surface horizontal displacements at JLE WB tunnel (Nyren et al, 1998)

3.5 Evaluation of ground movements at test site

Prior to the construction of the JLE tunnels through St James's Park, the maximum volume loss that was expected to occur was $\Delta V_L/V_0$ = 2% (Standing & Burland, 2006). In fact this value seemed conservative when comparing to volume losses that had occurred in previous tunnel constructions in London Clay. For example $\Delta V_L/V_0$ of 1.3% - 1.4% was caused by construction of the Jubilee Line (originally called Fleet Line) under Regent's Park, where soil conditions are very similar to St James's Park and the construction method used was the same.

Standing & Burland (2006) concluded, using conventional assumptions, that the volume loss for the WB tunnel was $\Delta V_L/V_0$ = 3.3% at the test section. Hence, an extended study was undertaken to investigate possible reasons for this unexpectedly large volume loss. Their studies suggest two main causes: 1) construction method and 2) local ground conditions (in the area south of St James's Park lake). Standing and Burland (2006) estimated that 50% of the volume loss was induced in front of the shield, due to the fact that 1.9m of WB tunnel heading was excavated and left unsupported ahead of the shield. Their studies regarding the geology of the site showed that the undrained shear strength of the London Clay south of the lake was generally lower than north of the lake. Finally, south of the lake, the London Clay subdivision A3ii, which is above the WB tunnel and below the EB tunnel (see Figure 3.12), is more permeable than the other London Clay units, since it contains frequent silt/sand partings, pockets and lenses and therefore retains water. This water-bearing layer (A3ii), in combination with the unsupported

tunnel heading ahead of the shield that took place during construction, could have resulted in loosening and softening of the ground and therefore might have caused larger than expected volume losses.

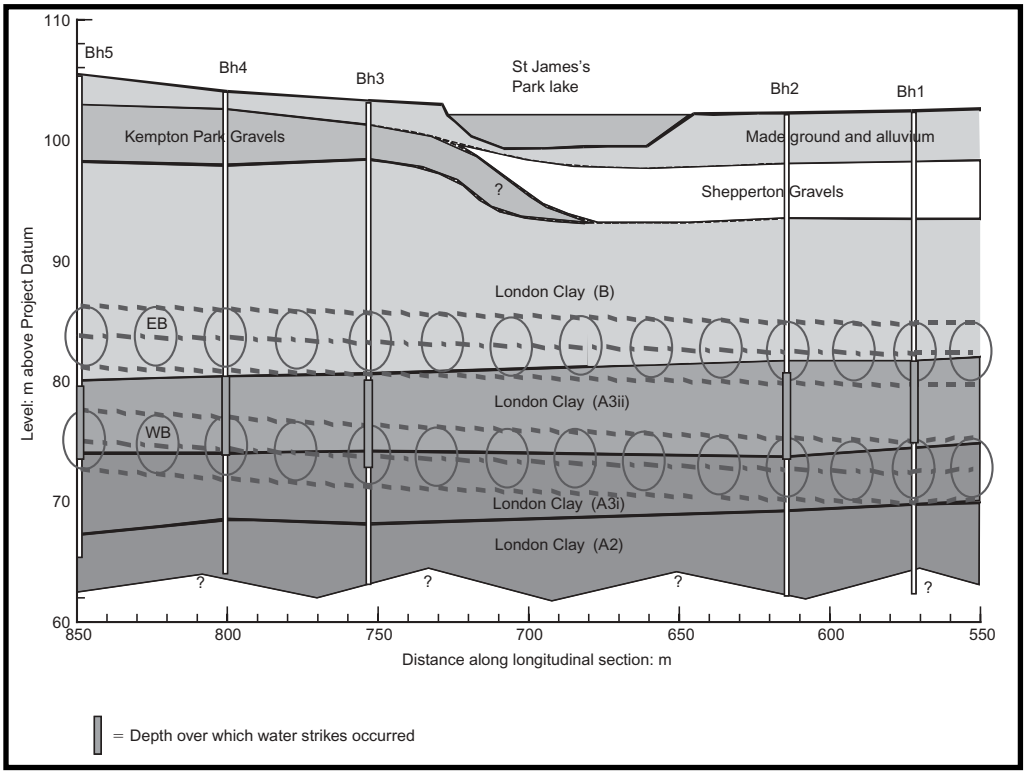

Figure 3.12: Longitudinal section across St James's Park site showing location of water bearing layer (A3ii) and tunnel alignments (Standing & Burland, 2006)

Franzius et al (2005) published results from analyses that were performed to evaluate capabilities of numerical analyses for describing the measured ground movements reported by Nyren et al (1998). The Authors compare 2D and 3D analyses, using different coefficients of lateral earth pressure at rest (K_0) and various constitutive models for simulating the construction of the JLE WB tunnel. Their base case scenario used a non-linear, elasto-plastic, isotropic model with

K_0=1.5. Figure 3.13 summarizes the transverse normalized surface settlement troughs produced by isotropic 2D and 3D numerical analysis and compares them with field measurements undertaken by Nyren et al (1998). Clearly, the basic soil model used in the analyses resulted in a transverse surface settlement trough that was too wide comparing to the field measurements and underestimated the maximum surface settlement. For example the 2D, incl. 12 FE analysis (see Figure 3.13) predicted a maximum surface settlement u_y^0 = 10mm, while the value measured in the field was u_y^0 = 20mm. However, the volume loss predicted by the same FE analysis was $\Delta V_L/V_0$ = 3.3% which is the same as the volume loss calculated by empirical means by Standing and Burland (2006). Subsequent 3D analyses produced very similar results and therefore more refined modeling of the tunnel heading didn't improve the performance of the FE model (see Figure 3.13).

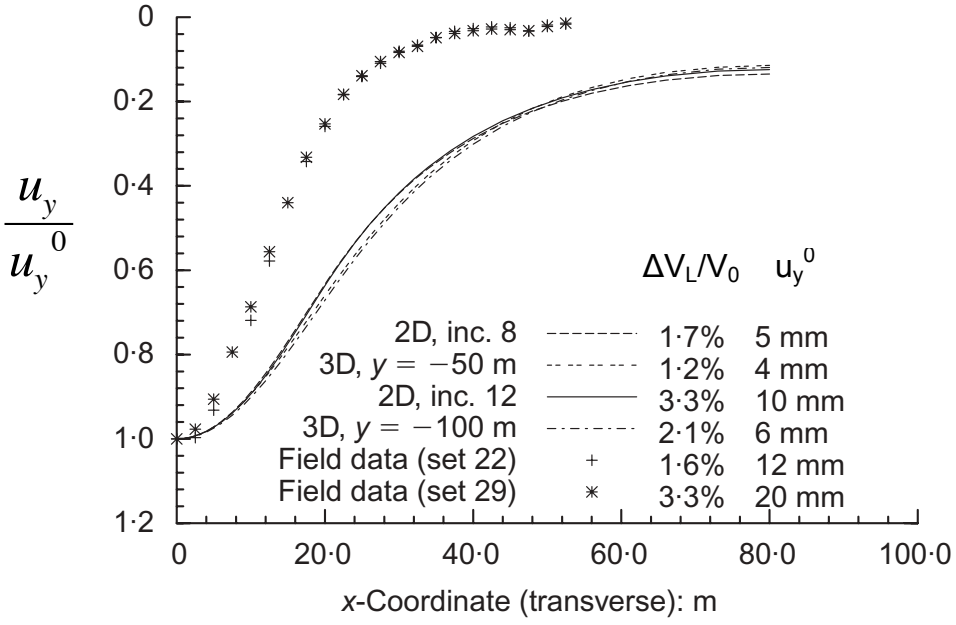

Figure 3.13: Transverse normalized settlement profiles for different stages of isotropic 2D and 3D FE analyses together with field data (Franzius et al, 2005)

The authors also introduced the transversely anisotropic stiffness formulation of Graham & Houlsby (1983) within their previous non-linear soil model. Two parameter sets referred to as 'set 1' and 'set 2' were applied to the anisotropic model and are summarized in Table 3.3. They were calculated for small strains (i.e. shear strain $E_d < E_{d,min} = 8.66\times10^{-4}$ %). Of the two parameter sets, the first one represents a degree of anisotropy that is appropriate for London Clay. In contrast, the second set incorporates extremely high degree of anisotropy (n' = 6.25) and is therefore more of academic interest than for use in engineering practice. (Note that a further set '2v' was also considered which assumes variable relationship between the stiffness parameters, i. e. variable m and n).

	Stiffness Parameters	Isotropic Model	Anisotropic Model	
			Set 1	Set 2
Drained Behavior	E_v' (MPa)	5.56	5.56	5.56
	$n' = E_h'/Ev'$	1.00	1.60	6.25
	$m' = G_{vh}/Ev'$	0.55	1.18	1.14
	ν_{vh}'	0.5	0.32	0.04
	ν_{hh}'	0.5	0.40	0.10
Undrained Behavior	E_v (MPa)	5.56	5.56	5.56
	$n = E_h/Ev$	1.00	1.18	1.66
	$m = G_{vh}/Ev$	0.33	0.33	0.28
	ν_{vh}	0.5	0.32	0.04
	ν_{hh}	0.5	0.40	0.10

Table 3.3: Soil model parameters used in FE analyses (Franzius et al, 2005)

Initially, realistic levels of anisotropy for London Clay were assumed (Set 1) which did not significantly affect the previous results (see Figure 3.14). Franzius et al (2005) were only able to achieve reasonable agreement with the settlement trough shape using unrealistically high degree of anisotropy (Set 2) in combination with a very low, K_0=0.5. However, as shown in Figure 3.15, these parameters generated a maximum surface settlement of 85mm (more that four times the maximum settlement that was reported by Nyren, 1998) and a volume loss $\Delta V_L/V_0$ = 18% (six times that quoted by Standing & Burland, 2006).

Overall, the non - linear FE analyses undertaken by Franzius, Potts & Burland (2005) showed that numerical analyses produce much wider transverse surface settlement troughs, when dealing with soils that have high K_0 values, such as London Clay. Moreover, it was concluded that 3D analysis and also the introduction of realistic degrees of anisotropy and K_0 values do not significantly improve the performance of FE models.

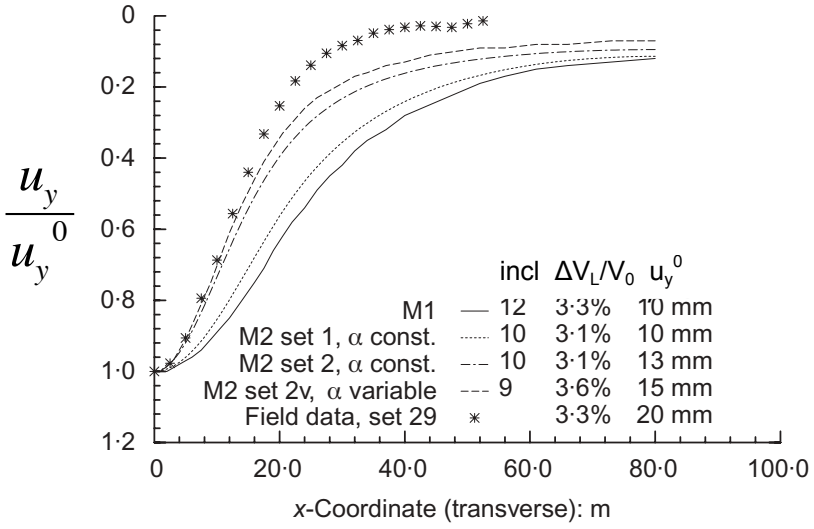

Figure 3.14: Transverse normalized settlement profiles for isotropic (M1) and anisotropic (M2) soil models (Franzius et al, 2005)

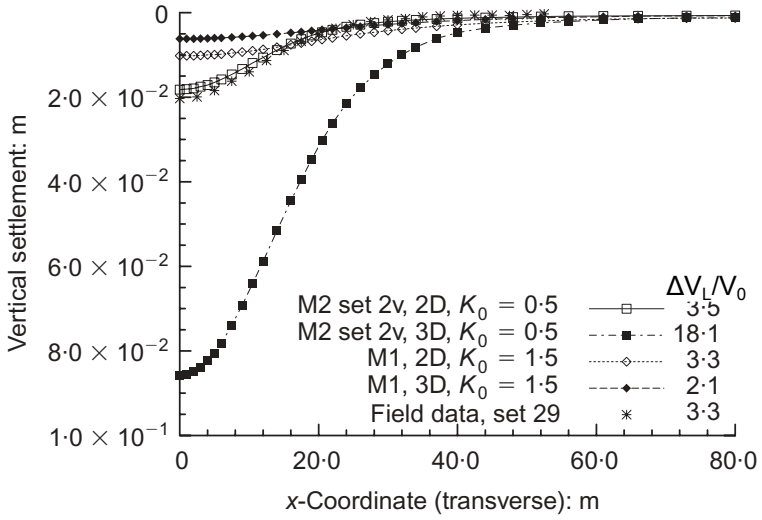

Figure 3.15: Transverse settlement profiles of isotropic (M1) and anisotropic (M2) 2D and 3D analyses compared with field data (Franzius et al, 2005)

Wongsaroj (2005) carried out an in depth FE analyses to evaluate the short and long-term tunneling induced ground response at the St James's Park test site. The Author compared 3D analyses, using different coefficients of lateral earth pressure at rest (K_0) and various constitutive models for simulating vertical and horizontal, surface and subsurface ground movements, generated by the construction of the JLE WB tunnel.

For the scope of this thesis, Wongsaroj's predictions of short-term ground deformations are presented. Two elasto-plastic soil models[1], one isotropic and one anisotropic, with a London Clay K_0 = 1.5, were initially employed. Details of the soil parameters used in each soil model are shown in Tables 3.4 - 3.6 (Appendix II

[1] Wongsaroj (2005) developed an 'advanced critical state elastoplastic soil model' to describe the behavior of London Clay. Details of the formulation are beyond the scope of the current review.

provides an explanation of what each model parameter represents). Figure 3.16 summarizes the computed and measured transverse settlement profiles at various depths, when the tunnel face is 60m beyond the instrument plane. Both the isotropic and anisotropic models give settlement troughs that are wider than the monitoring data and also predict smaller maximum surface settlement u_y^0 than the value measured by Nyren (1998). The anisotropic model generates slightly narrower settlement troughs compared to the isotropic model. The magnitudes of volume loss computed for these simulations are $\Delta V_L/V_0$ = 6.08% for the isotropic case and $\Delta V_L/V_0$ = 5.6% for the anisotropic case, which are both unrealistically large.

Figure 3.17 summarizes the computed and measured horizontal displacements at the inclinometer positions C_i to H_i (see Figure 3.7) when the tunnel face was 60m beyond the instrumentation line. It should be noted that the field measurement data presented in Figure 3.17 were adjusted such that the magnitude of surface horizontal displacements interpreted from the inclinometers was the same as the measurements obtained from the micrometer stick. The different scale in the horizontal ground movement axes for the different inclinometers should also be considered. The FE analysis predicted horizontal movements of larger magnitude than the field data measured by Nyren (1998), with the anisotropic model predicting slightly lower values than the isotropic case. In inclinometers Ci and Di the FE analysis predict significantly higher horizontal movements in the zone around the springline (difference of ~15mm). The discrepancy between the computed and measured displacements increases with increasing distance from the

tunnel centerline (note discrepancy of ~7mm at the ground surface at inclinometer Hi). However, the computed profiles of horizontal displacement have similar shape to the adjusted field measurements.

The effect of K_0 on the ground deformations predicted by the anisotropic model was subsequently studied, by considering values of K_0 = 1.5, 1.2 and 1.0. Figure 3.18 summarizes the computed transverse settlement profiles at the surface and subsurface predicted by the three anisotropic models, along with the field measurements reported by Nyren (1998). The decrease in K_0 increases the settlement of the centerline for all depths. The settlement troughs predicted by the numerical analyses are again wider than the troughs measured in the field.

However, the normalized transverse surface settlement trough shown in Figure 3.20 suggests that as K_0 is reduced from 1.5 to 1.2, the settlement trough becomes narrower. The volume losses generated by the three FE models, when the tunnel face is 60m beyond the instrumentation line are: $\Delta V_L/V_0$ = 5.6% for K_0 = 1.5, $\Delta V_L/V_0$ = 5.1% for K_0 = 1.2 and $\Delta V_L/V_0$ = 5.4% for K_0 = 1.0. Again, the values of $\Delta V_L/V_0$ predicted by the FE models are unrealistically high. The horizontal ground displacements predicted by the three anisotropic FE models of different K_0 are very similar to the movements previously computed by the anisotropic (K_0 = 1.5) and isotropic models.

A ratio of G_{hh}/G_{vh} =1.5 was used for the FE simulations presented up to now, the ratio G_{hh}/G_{vh} =1.5 was used. Further simulations were conducted by Wongsaroj

(2005) incorporating G_{hh}/G_{vh} = 2 and 5 in the anisotropic soil model with a K_0 = 1.2. Figure 3.19 summarizes the computed settlement profiles with depth and the corresponding field measurements reported by Nyren et al (1998). The simulation with ratio G_{hh}/G_{vh} = 2 underpredicted the magnitude of maximum settlement u_y^0, while assuming G_{hh}/G_{vh} = 5 resulted in overprediction of u_y^0. The normalized transverse surface settlement trough (Figure 3.21) shows that, as the ratio G_{hh}/G_{vh} increases, the trough becomes narrower, with G_{hh}/G_{vh} = 5 underpredicting the width of the trough. This suggests that G_{hh}/G_{vh} = 3 - 4 would give a good matching transverse settlement for tunneling in London Clay. However, there is limited data to justify such high G_{hh}/G_{vh} ratios. Even the anisotropic stiffness data that were reported by Gasparre et al (2007) and shown in Figure 3.5, after the study by Wongsaroj was completed, gave G_{hh}/G_{vh} ratios around 2. The volume losses predicted by these analyses were $\Delta V_L/V_0$ = 3.93% and 3.16%, when the value of G_{hh}/G_{vh} was 2 and 5 respectively, which are lower than $\Delta V_L/V_0$ generated by the previous simulations but are still large comparing to volume losses generally induced by open-face tunneling in London Clay.

A 2D simulation was finally undertaken, using an anisotropic soil model with K_0 = 1.5. Figure 3.22 suggests that modeling the 3D effect of the tunnel excavation makes negligible improvement on the surface settlement trough produced by the 2D analysis. Figure 3.23, shows that the normalized horizontal displacements predicted by the 2D and 3D simulations are also similar. Note that for comparison purposes the horizontal displacements were normalized by the volume losses generated by

each model $\Delta V_L/V_0$ = 5.3% for the 2D model while $\Delta V_L/V_0$ = 5.6% for the 3D model). This similarity in results produced by the 2D and 3D FE analyses suggests that 3D stress at the tunnel heading has little influence on the displacement field in the transverse plane, a conclusion also reached by Franzius et al (2005).

To summarize, the analysis undertaken by Wongsaroj (2005) showed that 3D FE analyses produced transverse settlement troughs that were wider compared to those monitored in the field by Nyren et al (1998). The computed settlement profiles became narrower when soil stiffness anisotropy and lower K_0 values were assumed. However, the width of the settlement troughs was still overpredicted. The settlement troughs became narrower when higher G_{hh}/G_{vh} ratios were considered. The horizontal displacements computed by the different simulations were higher than those measured in the field. However, the shape of the horizontal displacement profiles was similar to the adjusted field data. Finally, it was deduced that for same volume losses, 2D and 3D FE analyses produce very similar results, both in the horizontal and vertical directions.

STRATA	Bulk Density, γ (kN/m^3)	Critical Angle Of Shearing Resistance, ϕ'_{cv} (Degree)	Coefficient of Earth Pressure at Rest, K_0	Poisson's Ratio, ν	Permeability, k (m/s)
Made Ground	20.0	25.0	0.6	0.2	1×10^{-7}
Terrace Gravel	20.0	35.0	0.4	0.2	5×10^{-4}
London Clay	20.0	21.0	1.5	-	1×10^{-9}
Woolwich and Reading Beds Clay	20.0	27.0	1.5	0.2	0.5×10^{-11}

Table 3.4: Soil Properties adopted in FE simulations (Wongsaroj, 2005)

Soil model	ν'_{vh}	ν'_{hv}	ν'_{hh}	G_{hh}/G_{vh}
isotropic	0.15			1.0
anisotropic	0.07	0.16	0.12	1.5

Table 3.5: Poisson's Ratios for the isotropic and anisotropic soil models (Wongsaroj, 2005)

STRATA	M	e_0	u_1	m	C_b	ω_s	λ	ρ_c	p'_c	D	r
Made Ground	0.984	0.65	100	0.1	100	15	0.1	0.2476	vary*	-	-
Terrace Gravel	1.418	0.5	100	0.1	400	15	0.1	0.556	vary*	-	-
London Clay	0.814	0.7	300	0.2	200	20	-	0.3	vary*	0.05	2
Woolwich and Reading Beds Clay	1.07	0.65	100	0.1	900	50	0.15	0.37	vary*	0.05	2

Table 3.6: Model parameters assumed for each soil using advanced soil model (Wongsaroj, 2005)

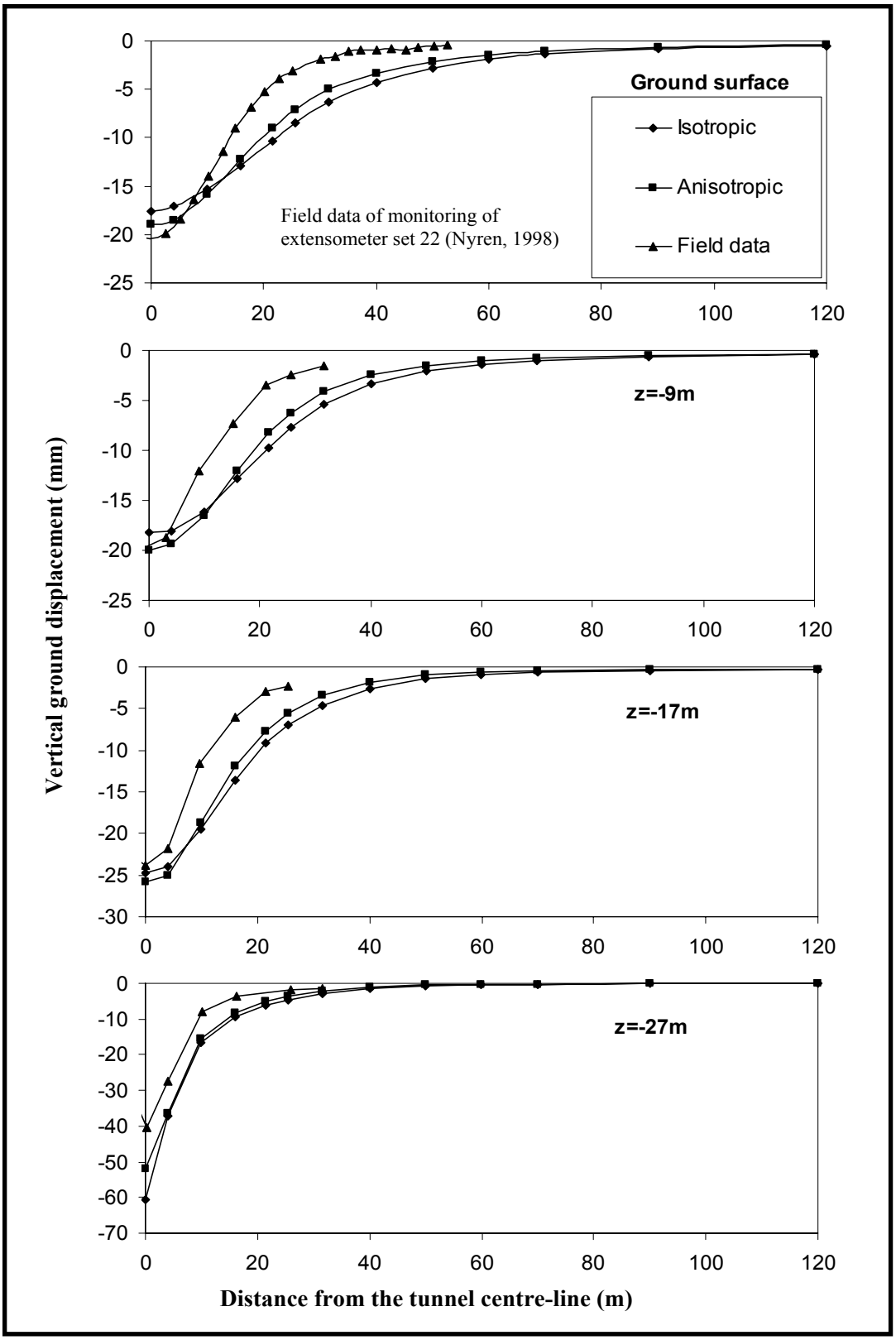

Figure 3.16: Vertical Movements predicted by isotropic and anisotropic 3D FE analyses and comparison with field data above WB tunnel (Wongsaroj, 2005)

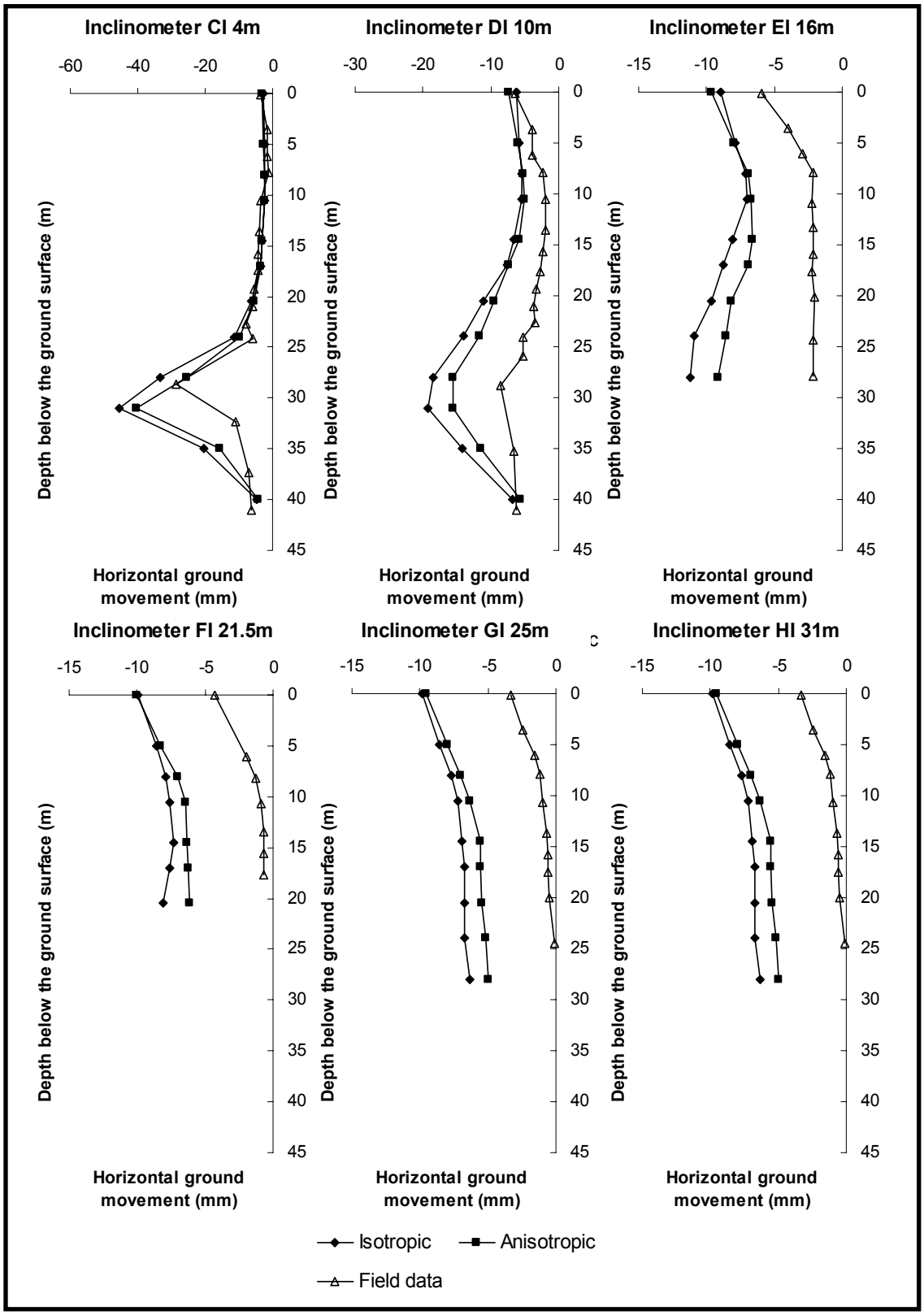

Figure 3.17: Subsurface horizontal displacements predicted by isotropic and anisotropic 3D FE analyses and adjusted field measurements (Wongsaroj, 2005)

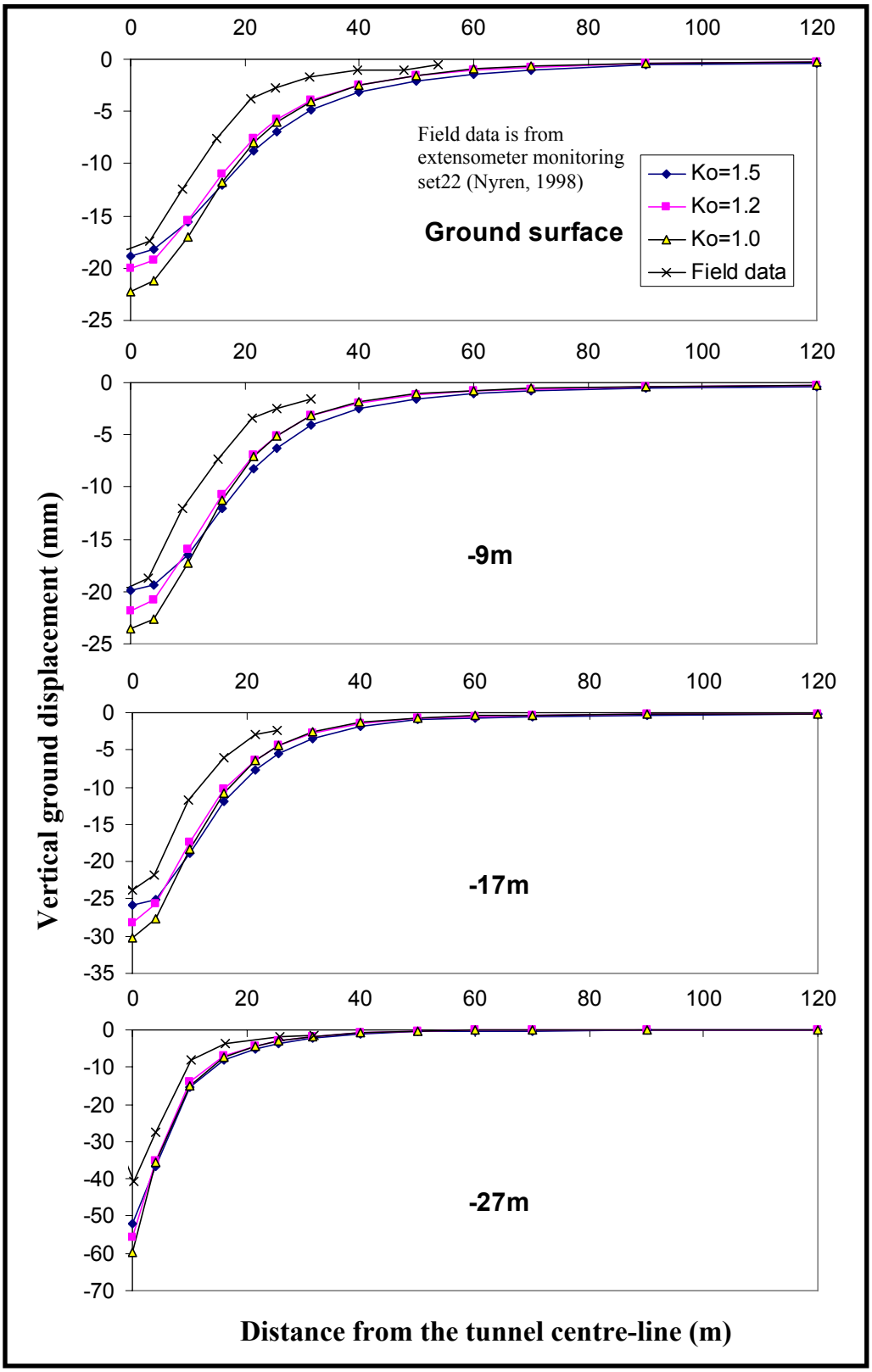

Figure 3.18: Vertical Movements predicted by anisotropic 3D FE analyses of different K_0 and comparison with field data above JLE WB tunnel (Wongsaroj, 2005)

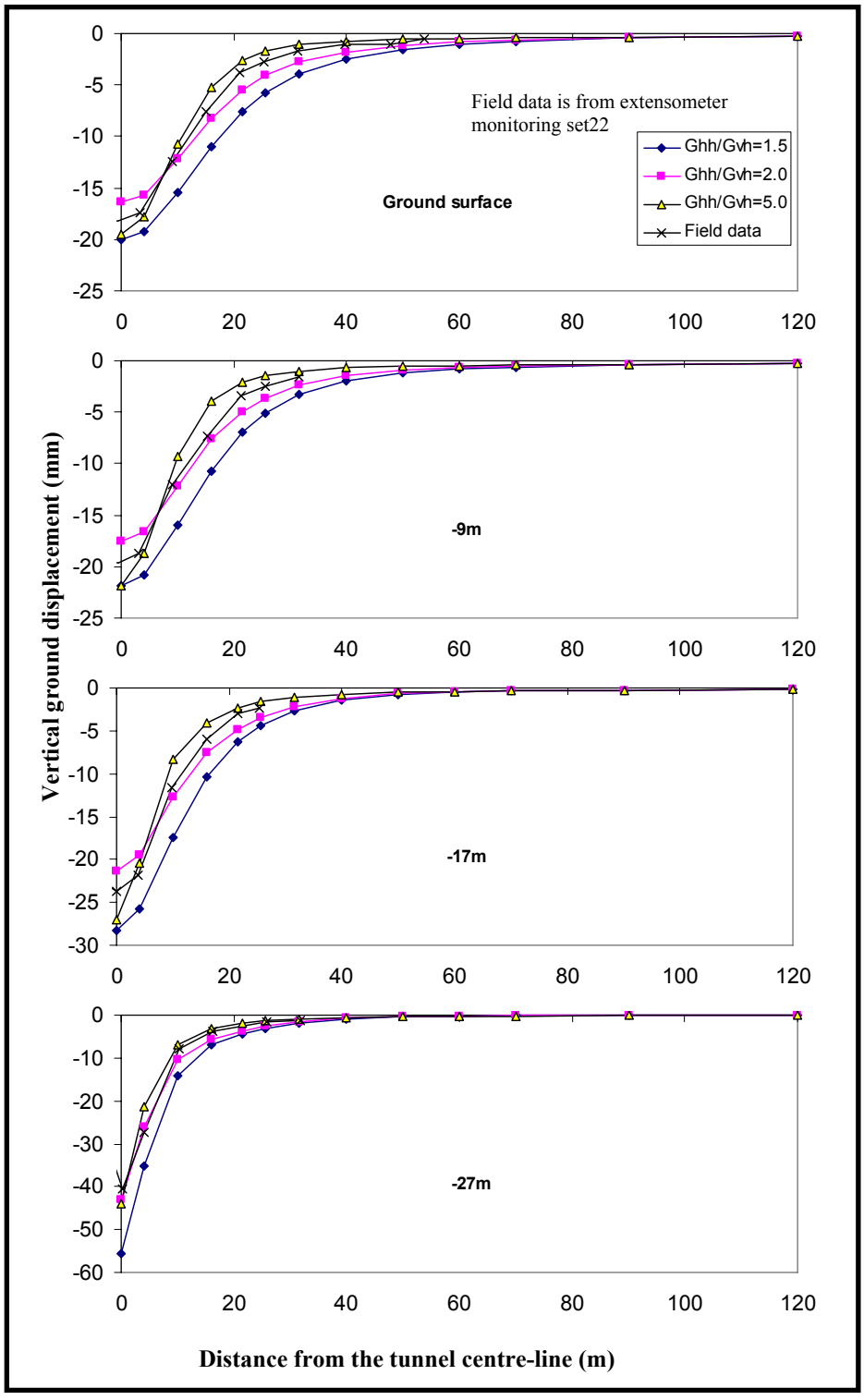

Figure 3.19: Vertical Movements predicted by 3D FE anisotropic analyses of different G_{hh}/G_{vh} ratios and comparison with field data above JLE WB tunnel (Wongsaroj, 2005)

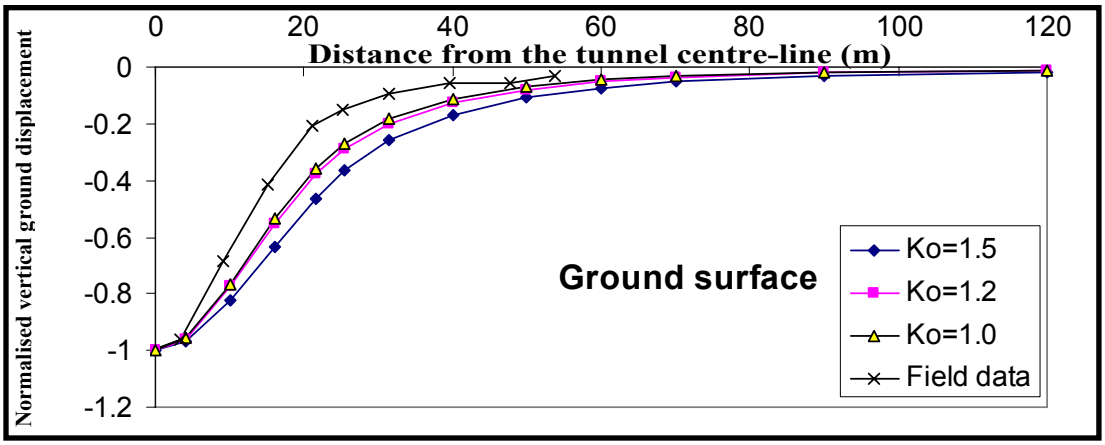

Figure 3.20: Normalized settlements predicted by anisotropic 3D FE analyses of different K_0 and comparison with JLE WB field data (Wongsaroj, 2005)

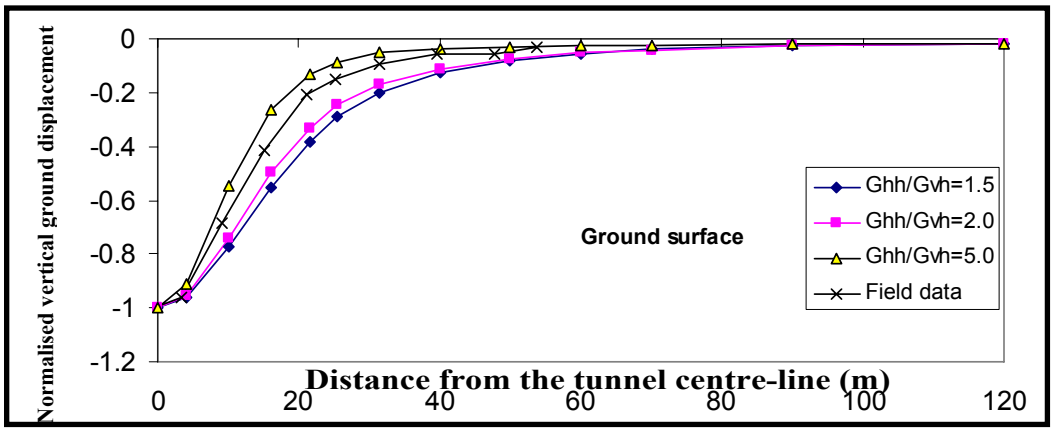

Figure 3.21: Normalized settlements predicted by 3D FE anisotropic analyses of different G_{hh}/G_{vh} ratios and comparison with JLE WB field data (Wongsaroj, 2005)

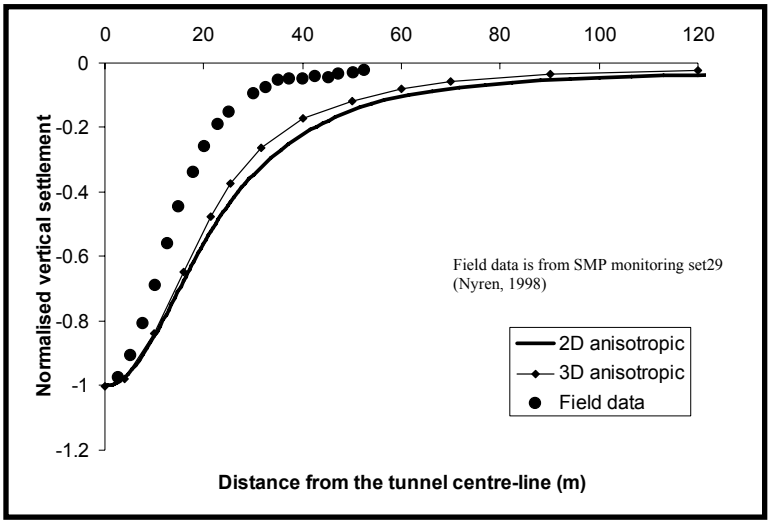

Figure 3.22: Comparison between the normalized surface settlement trough produced by 2D and 3D FE anisotropic analyses and field data (Wongsaroj, 2005)

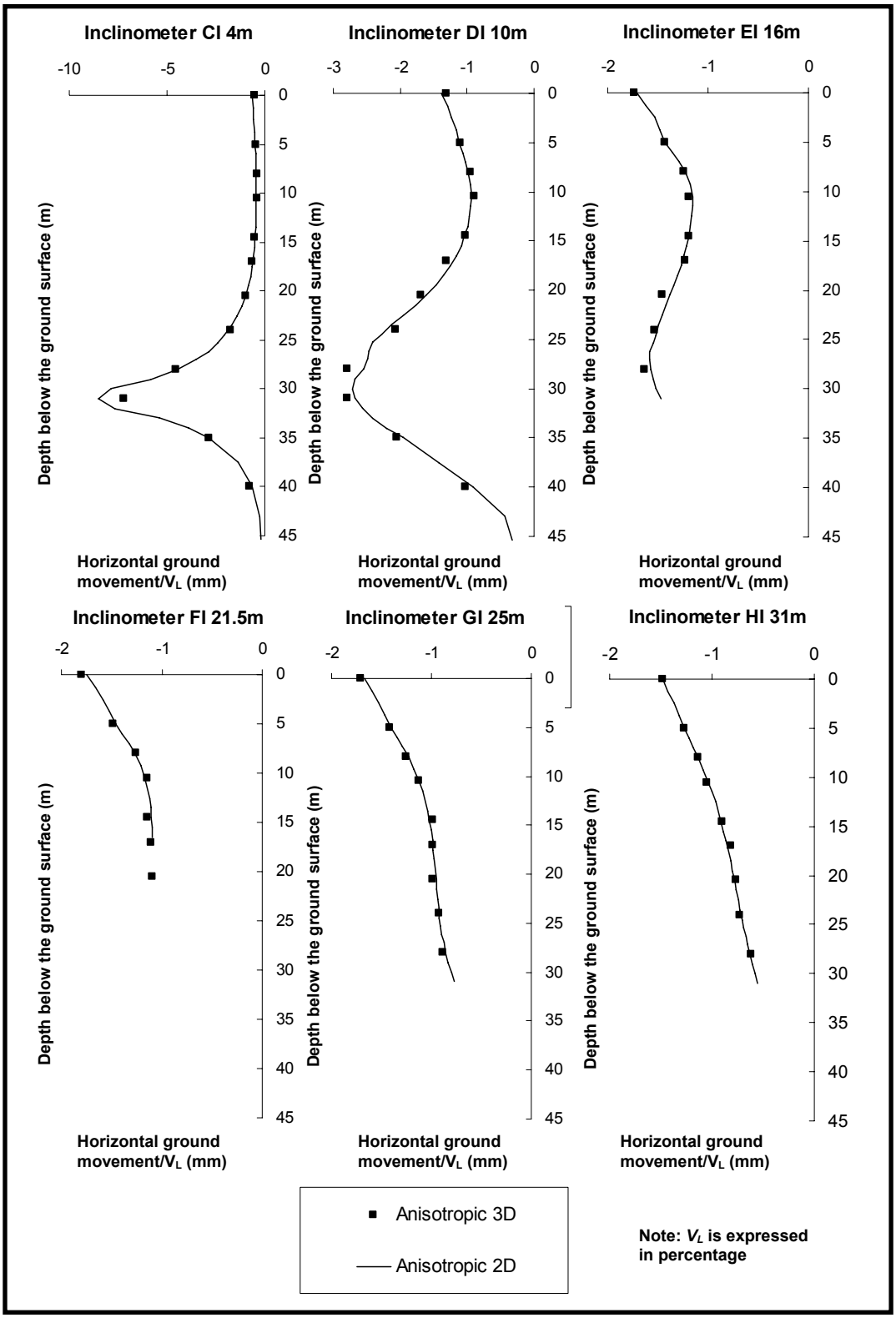

Figure 3.23: Comparison between normalized horizontal displacements produced by 2D and 3D anisotropic FE analysis for JLE WB tunnel (Wongsaroj, 2005)

3.6 Application of proposed analytical solutions

The analytical framework introduced in Chapter 2 can be used to interpret the ground movements caused by the construction of a single tunnel in soft ground conditions. Therefore, for the case of the JLE project, the analytical model was used for the prediction of the ground movements induced by the WB tunnel, since it was built first, with a time lag of nine months before the construction of the second, EB tunnel. The key geometric parameters for the WB tunnel are:

- ⇒ Depth to springline H = 31m
- ⇒ Diameter 2R = 4.85m ➔ Radius R = 2.425m
- ⇒ Ratio R/H = 0.0782

Assuming that ground movements are controlled by the low permeability London Clay, the initial assumption is that the ground should be treated as incompressible with Poisson's ratio $\nu = 0.5$.

Following Sagaseta (2001) and Pinto and Whittle (2007), it is important to assess the potential zone of plastic deformation around the tunnel bore. For the case of St James's Park WB tunnel:

The overburden pressure: $p_o = \gamma_{clay} \times H = 19.5 \times 31 kN/m^2 = 605 kN/m^2$. The undrained shear strength at depth H=-31m ranges from s_u = 150 – 350 kPa. Hence assuming a best estimate, s_u = 225kPa. The overload factor $N = p_o/s_u = 604.5/225 = 2.69$. For a deep tunnel, the estimated radius of plastic zone is then

$\frac{R_p}{a}\exp\left(\frac{N-1}{2}\right) = 2.32 \Rightarrow R_p = 2.32 \times 2.425 \approx 5.7\,\text{m}$. (Note that it could be as high as 10.6m for s_u = 150).

Having estimated the Plastic Zone, the subsequent analyses focus on measurements of surface and subsurface, horizontal and vertical displacements, which are outside the plastic zone. This measurement 'grid' is shown schematically in Figure 3.24 and uses data from 8 inclinometers (Ai-Hi) and 8 extensometers (Ax-Hx), with data at depths from the surface, y = 0m, to a depth, y = -27m. For comparison purposes, the analytical model is set to calculate ground movements at the points of the measurement grid shown below, which coincide with the points where field measurements have been undertaken.

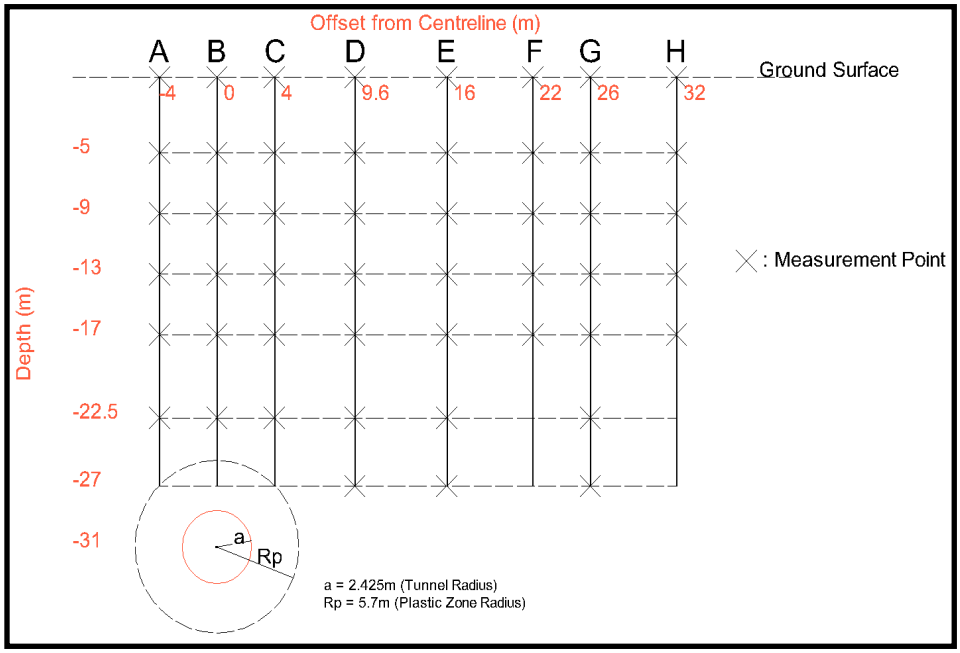

Figure 3.24: Grid of Measurement Points from St James's test site

Figures 3.25 and 3.26 show the position of the WB tunnel face relative to the instrumentation line when vertical and horizontal subsurface measurements were taken. The vertical measurements used in the analytical solutions are obtained from survey number 23, 26 hours after the passage of the WB tunnel and 50m behind the WB tunnel face. These settlement measurements match the field data used in previous studies by Wongsaroj (2005), for comparison purposes. The horizontal subsurface measurements used in the analysis are represented by an 'x' in Figure 3.26 and were obtained at a distance x = -18.5m from the WB shield. Although the horizontal displacements used in the analysis were recorded from much closer to the WB shield comparing with the settlement measurements, the position x = -18.5m is the maximum distance of subsurface horizontal deflection measurement reported by Nyren et al (1998) for Period 2, which corresponds to the period right after the WB shield passed.

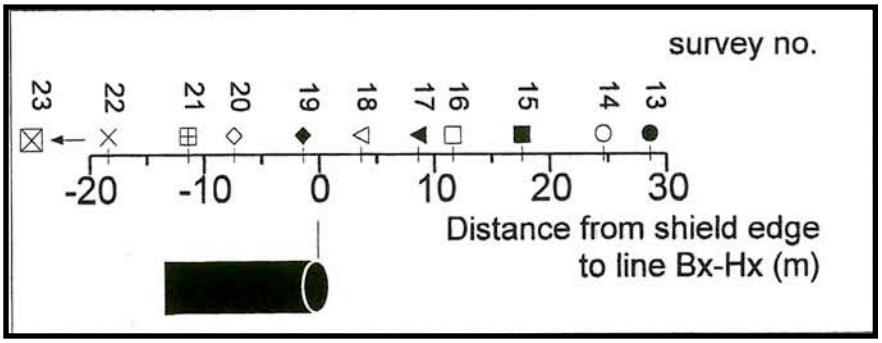

Figure 3.25: Position of WB tunnel face relative to instrumentation line for different extensometer surveys (Nyren, 1998)

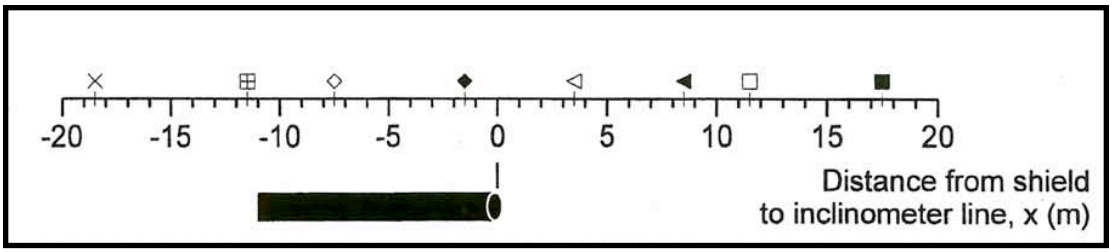

Figure 3.26: Position of WB tunnel face relative to instrumentation line for different inclinometer surveys (Nyren, 1998)

3.6.1 Computed and measured ground movements, isotropic model

From the Surface settlements in Figure 3.10, the two key measurements suggested by Pinto (1999) are:

Centreline: $u_y^0 = 20.4mm$

Offset at x/H=1: $u_y^1 = 1.70mm$

Two different sets of input parameters were selected to model the field measurements for the WB tunnel. The first set of parameters (Case 1) result in a volume loss of $\Delta V_L/V_0 = 1.8\%$ while the second set of parameters (Case 2) result in a volume loss of $\Delta V_L/V_0 = 3.3\%$. The parameters used in each model are shown in the Table 3.7.

Parameter	Case 1	Case 2
Poisson's Ratio, v	0.50	0.50
Radius, R (m)	2.425	2.425
Depth to springline, H (m)	31.00	31.00
Uniform Convergence, u_ε (mm)	-21.73	-40.01
Ovalization, u_δ (mm)	54.50	45.33
Relative Distortion, ρ	2.508	1.133
Volume Loss, $\Delta V_L/V_0$ (%)	1.80	3.30

Table 3.7: Parameters used in analytical solutions

The parameters of **Case 1** were derived by matching the surface vertical settlements at the centerline, u_y^0 and at an offset x = 31m (x/H=1), u_y^1. This method resulted in a uniform convergence, u_ε = -21.73mm, (which is equivalent to a volume loss $\Delta V_L/V_0$ = 1.8%) and an ovalization component, u_δ = 54.50mm.

The parameters of **Case 2** were derived by assuming a volume loss $\Delta V_L/V_0$ = 3.3%, based on the reported empirical fit by Standing & Burland (2002). From the volume loss the convergence parameter u_ε is obtained directly,

$$\Delta V_L/V_0 = (2u_\varepsilon)/R \rightarrow u_\varepsilon = (2.425\times3.3\%)/2 = 0.04001\text{m} = 40.01\text{mm}$$

while the ovalization, u_δ is chosen to match the surface vertical settlement at the centerline, u_y^0 (using eqn. 2.9b and 2.10b), hence u_δ = 45.33mm.

3.6.1.1 Surface Displacements

Figure 3.27 compares the computed and measured surface settlements for the WB tunnel with the empirical Gaussian distribution used by Standing and Burland (2006). We observe that Case 1 is in closer agreement with the field measurements than Case 2 (for $x \leq 40$m). The Case 2 analysis produces differences up to 3.5mm with the measured data and overestimates the width of the settlement trough. Case 1 and the conventional Gaussian curve produce very similar results with a maximum deviation less than 2mm from the measured data. However, Case 1 predicts a small heave in the far field (for $x \approx 50$m, $u_y \approx 1$ - 2mm) that is not found in the measured data.

Figure 3.28 compares the analytical model with empirical solutions (eqn. 2.7) for the measured horizontal surface displacement profiles. As expected, both analytical and also the empirical solution preserve the antisymmetry in horizontal displacements (i.e. $u_x = 0$ at $x = 0$). The Case 1 analysis matches closely the maximum horizontal displacement measured east of the centerline ($u_{x,max} \approx$ -5.7mm), while Case 2 computes slightly higher movement and the empirical curve slightly underestimates the maximum displacement. Case 1 is in very good agreement with the field measurements for $x \leq 34$m, but tends to diverge in the far field where small outward movements ($u_x > 0$; for $x > 40$m) are predicted. The empirical solution on the other hand successfully fits the shape of the surface horizontal displacement profile.

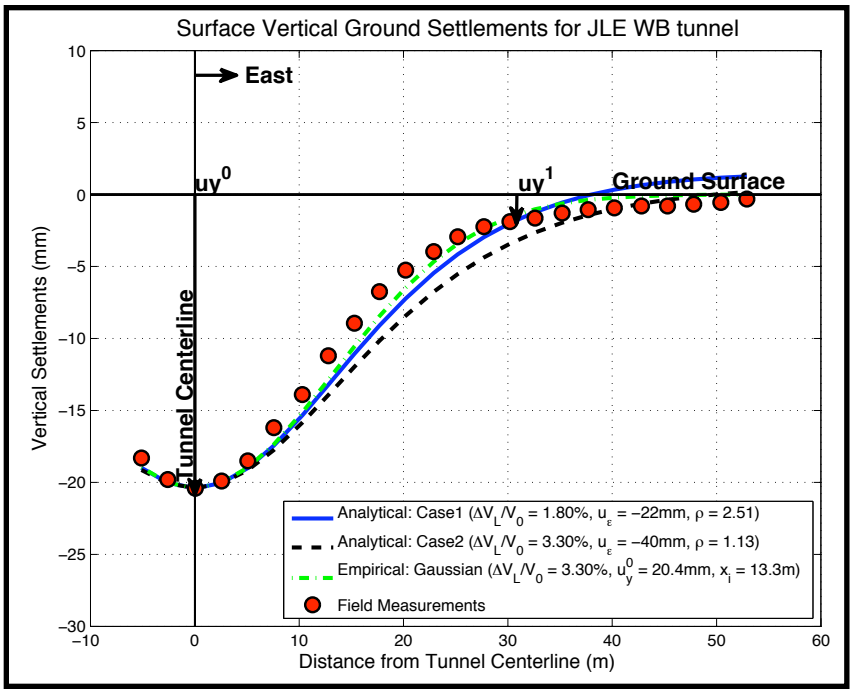

Figure 3.27: Vertical Ground Displacements at Surface, St James's Park WB Tunnel

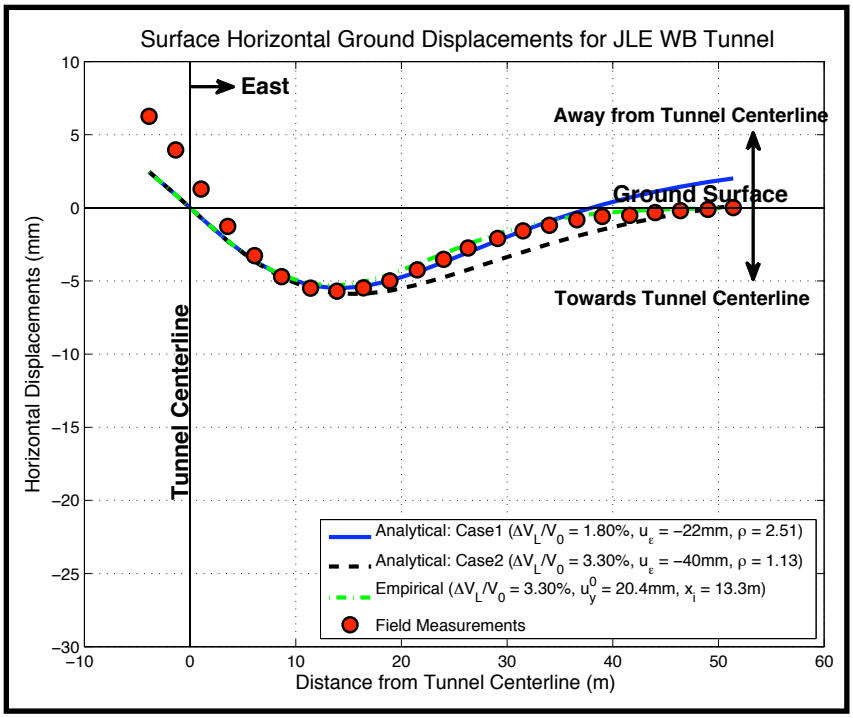

Figure 3.28: Surface Horizontal Displacements for St James's Park WB Tunnel

3.6.1.2 Subsurface Displacements

Figures 3.29 and 3.30 summarize the computed distribution of vertical and horizontal soil displacements for the WB tunnel using analytical Cases 1 and 2. Both Cases predict very similar vertical displacement profiles above the tunnel springline, with Case 2 generating slightly higher movements than Case 1. Moreover, along the centerline and above the tunnel we observe that the two models predict exactly the same displacements, while below the tunnel, Case 1 predicts larger displacements than Case 2.

Above the tunnel springline, the two models predict very similar horizontal ground displacements. However, along the surface elevation Case 1 predicts larger ground displacements than Case 2. Moreover, both models predict ground movements away from the tunnel, for the soil along the tunnel springline. Finally, below the tunnel cavity, the two cases predict very similar ground displacement patterns.

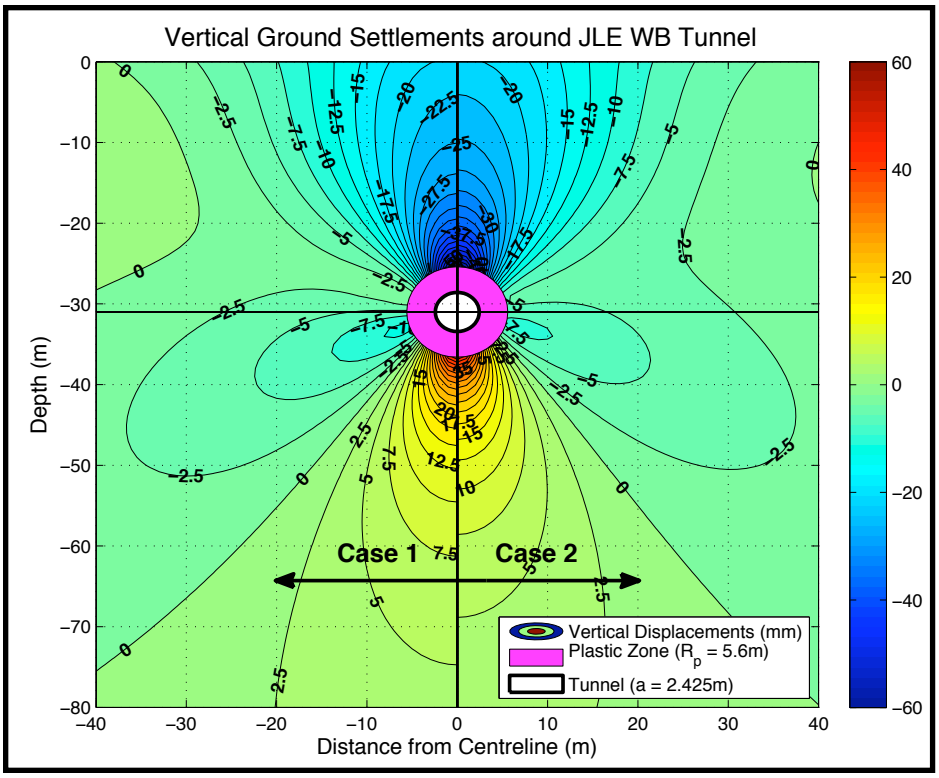

Figure 3.29: Contour Diagram of Vertical Displacements (mm) for JLE WB tunnel

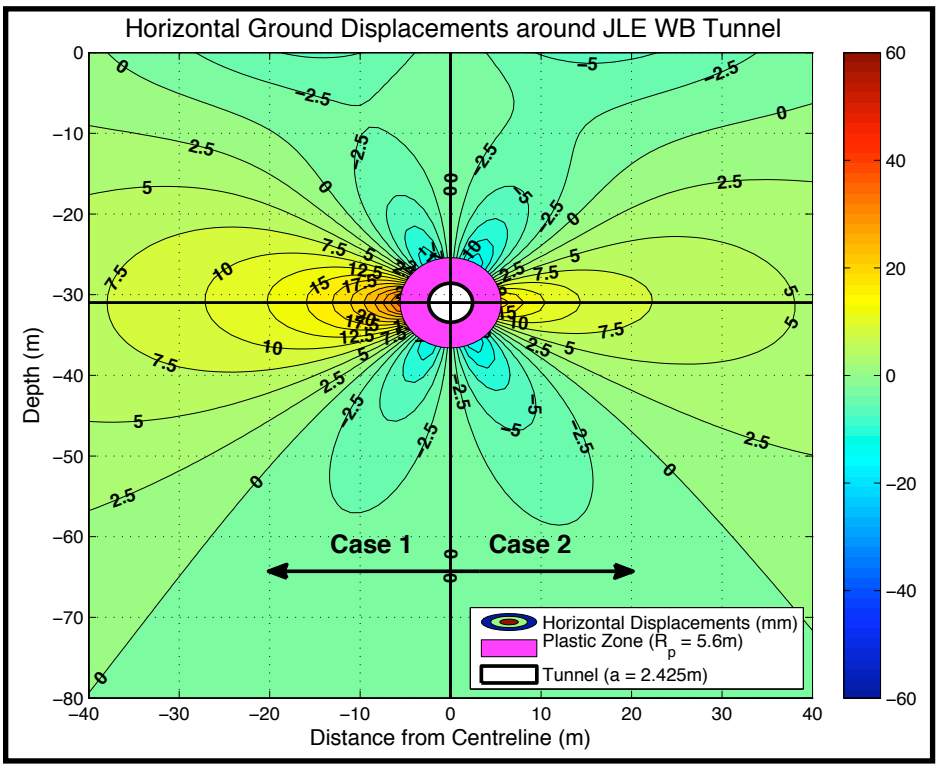

Figure 3.30: Contour Diagram of Horizontal Displacements (mm) for JLE WB tunnel

Figure 3.31 compares the analytically computed and measured subsurface vertical settlements for the WB tunnel. The measurements are based on 8 arrays of extensometers (A – H). There is very good overall agreement between the predicted and measured settlements and also there is very little difference between Cases 1 and 2. The analytical solutions predict well the increase in vertical displacements towards the tunnel in extensometers A and C but overestimate settlement immediately above the crown in B (at depth y = -22.5m, measurements show u_y = -29.8mm vs the analytical values from Cases 1 and 2, u_y = -43.4mm). Regarding extensometers A and C, symmetry is observed in the field measurements, something we would expect from a theoretical point of view, since they both have an offset of 4m from the centerline.

Regarding extensometer D, the models overpredict the settlements from right below the surface to a depth of y = -19m, and then the field measurements become higher than the predicted values. The displacements of extensometer E are well modeled from the surface until a depth y = -17m, where the model underpredicts the settlements. Finally, extensometers F to H show an excellent match between the field measurements and the model predictions.

Figure 3.32 shows a similar set of comparisons for the horizontal displacements. Here the measured data are obtained from in-place inclinometers (A_i through H_i). The results show more discrepancies between computed and measured behavior (although the difference in plotting scales between Figures 3.31 and 3.32 should be noted. In general, the analytical models are in better agreement with the movements

measured by inclinometers E_i to H_i, which are further away from the tunnel, than the movements measured by inclinometers A_i to D_i, closer to the tunnel. It is interesting to notice than inclinometer B_i, which lies along the centerline, shows some subsurface horizontal ground movements taking place. Furthermore, the displacements measured by inclinometers A_i and C_i, which have the same offset from the centerline, are not anti-symmetric (mirror images). The analytical models fit the measurements for A_i better than for C_i (where the measurements show subsurface movements away from the tunnel). The analytical solutions show small deformations towards the centerline in the shallow subsurface, while net outward movements occur below a transition depth marked in Figure 3.32.

For comparison purposes, a similar procedure is undertaken to evaluate the effectiveness of the empirical solutions proposed by Mair et al (1993) in predicting subsurface ground movements. Figure 3.33 compares the empirically computed and measured subsurface vertical settlements for the WB tunnel. Although there is a good overall agreement between the predicted and measured settlements from the ground surface to a depth y = -12m, the empirical method underpredicts the vertical settlements at larger depths. The conventional solutions fail to describe the increase in vertical displacements towards the tunnel in extensometers A to C. The displacements of extensometers D-H are not well predicted by the empirical expressions, with discrepancies as large as 10mm from the measured vertical movements. Figure 3.34 compares the empirically computed and measured subsurface horizontal displacements for the WB tunnel. The results show very large

discrepancies between the computed and measured behavior (although the difference in plotting scales between Figures 3.33 and 3.34 should be noted). The empirical method only matches the horizontal displacements measured at the surface and fails to fit any of the subsurface horizontal displacements that were recorded by Nyren et al (1998).

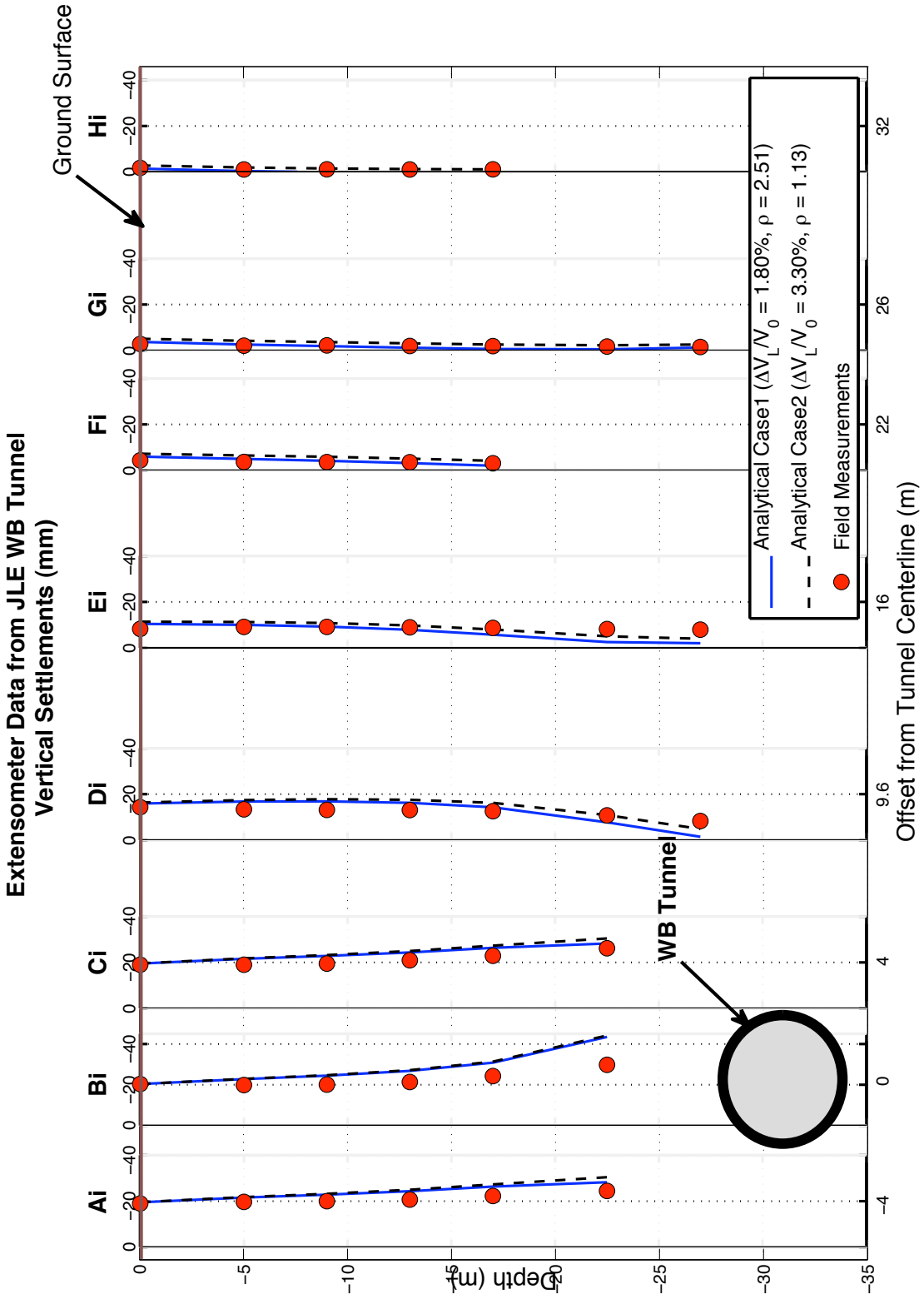

Figure 3.31: Subsurface vertical ground settlements as measured by Extensometers A to H and also as predicted by Analytical Models

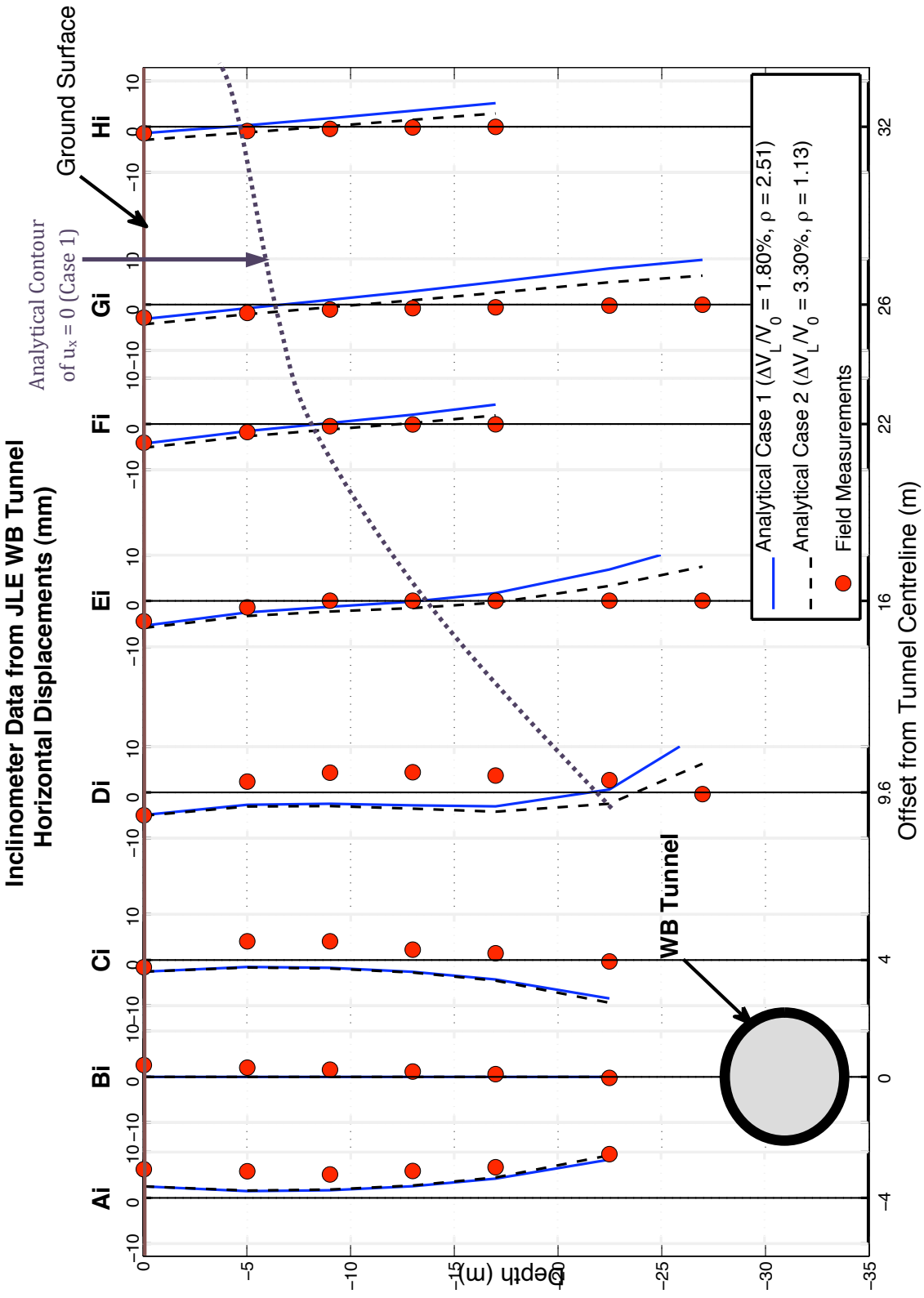

Figure 3.32: Subsurface horizontal ground displacements as measured by Inclinometers A to H and also as predicted by Analytical Models

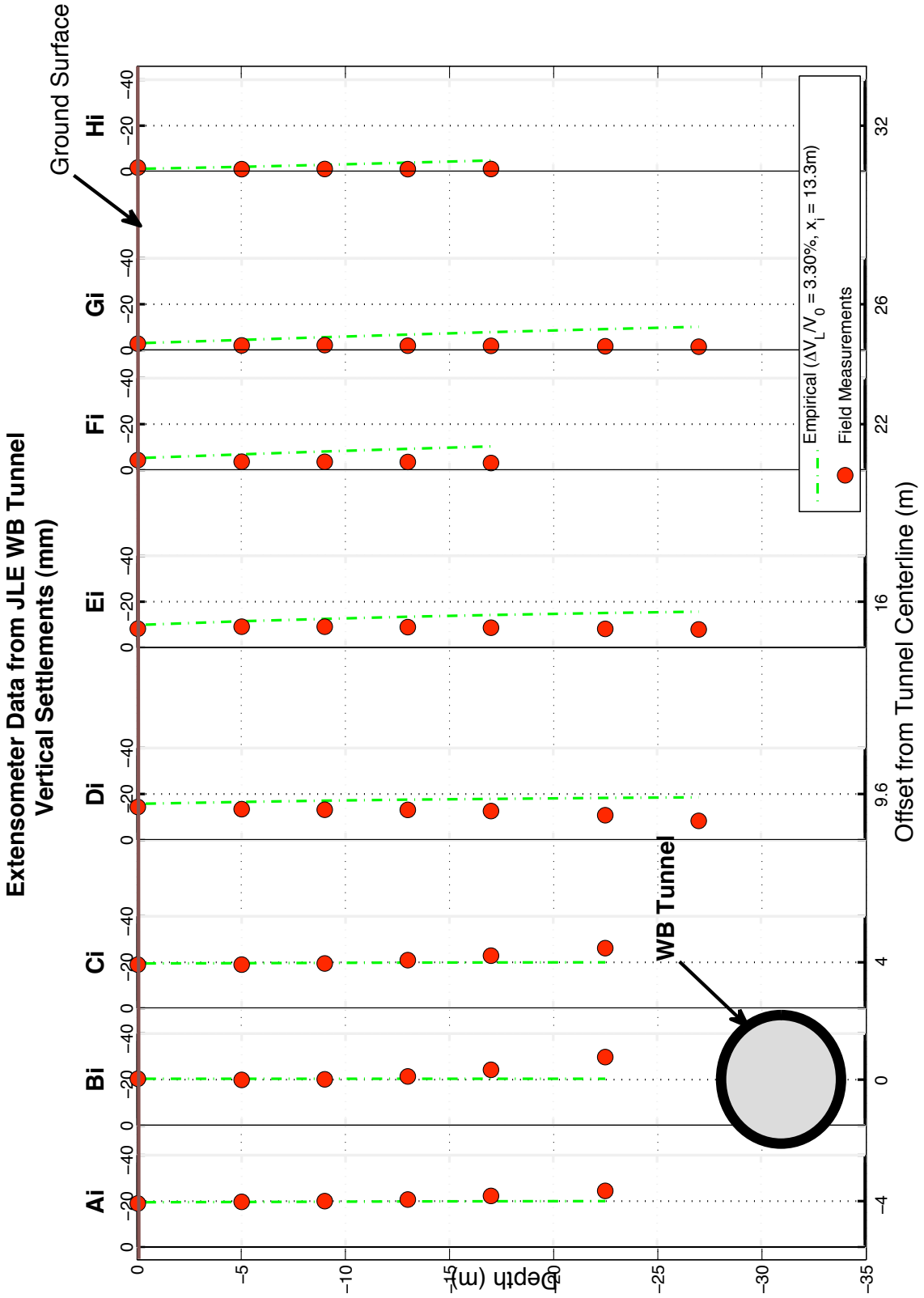

Figure 3.33: Subsurface vertical ground settlements as measured by Extensometers A to H and also as predicted by Empirical Method

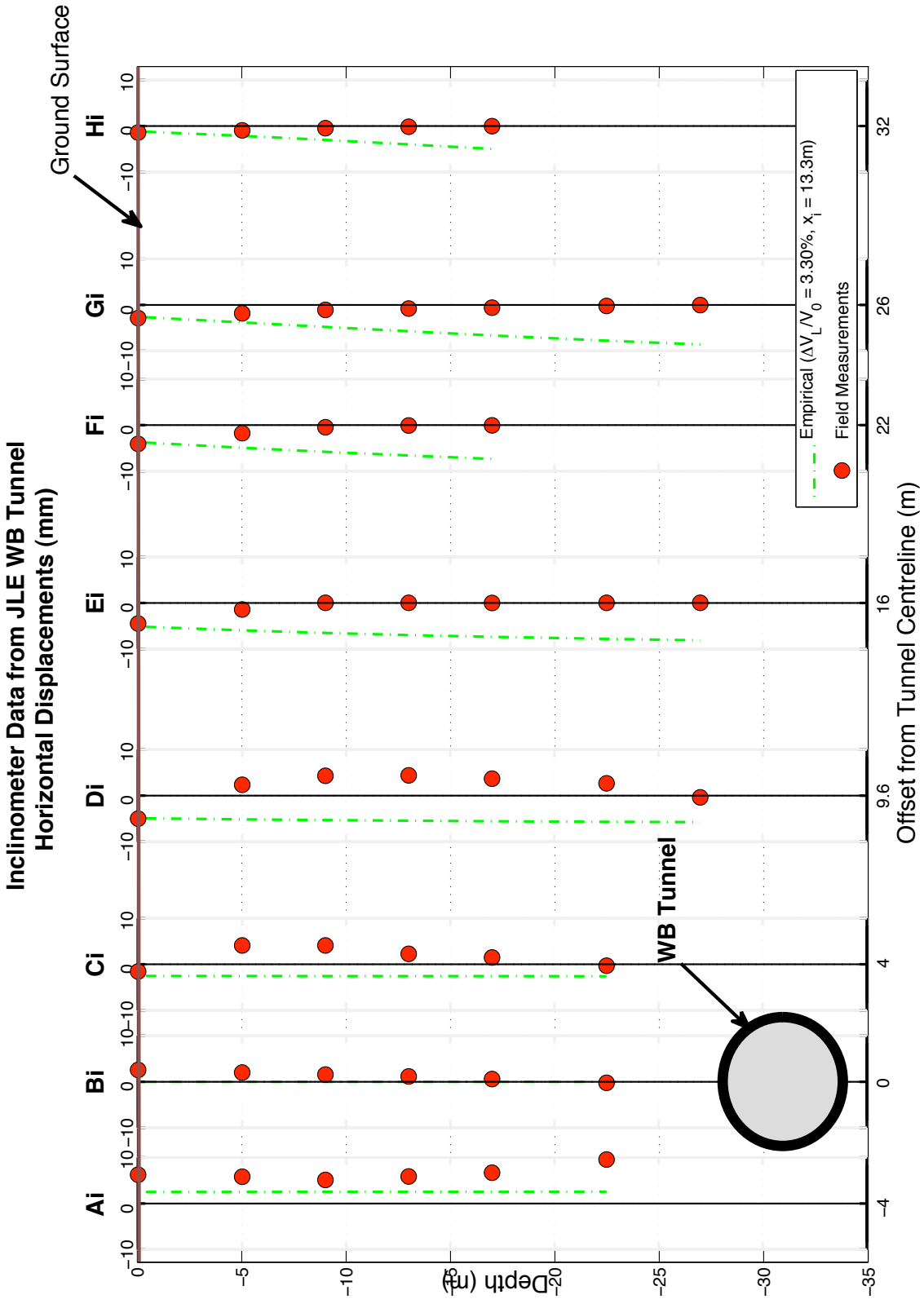

Figure 3.34: Subsurface horizontal ground displacements as measured by Inclinometers A to H and also as predicted by Empirical Method

3.6.1.3 Evaluation of effectiveness of analytical solutions

In order to evaluate the effectiveness of the two analyses in describing the measured ground movements on the reference grid (Fig. 3.24), a least squares error method has been employed. For different sets of u_ε and u_δ, a Square Solution (SS) is obtained, which is equal to:

$$SS = \sum (u_{meas,i} - u_{analytical,i})^2, \text{ for given set } (u_\varepsilon, u_\delta) \quad (3.1)$$

This method is applied in both the horizontal and vertical directions independently, thus obtaining parameters SS_H and SS_V. The total square solution is then equal to:

$$SS_T = SS_H + SS_V \quad (3.2)$$

Contour plots of these Square Solutions have been prepared covering the full range of the state space (u_ε,u_δ).

Assuming that all analyses will fit the centerline settlement, u_y^0, a line has been added to the figure corresponding to the (u_ε, u_δ) sets that fit the centerline surface settlement. The optimum solution is the one that produces the minimum SS error and is called Least Square Solution (LSS). In our analysis, we consider two LSSs: a **global LSS** that corresponds to the overall minimum SS, and a **surface LSS** that corresponds to the combination of (u_ε, u_δ) that produces the minimum SS while at the same time fits the centerline surface settlement u_y^0 (i.e. the point on the surface settlement line with the minimum SS).

Figures 3.35, 3.36 and 3.37 show the state space square solutions for vertical, horizontal and total displacements, and Table 3.8 summarizes the results of the LSS error method. There is a very close agreement between LSS surface and LSS global solutions for the vertical displacement components in Figure 3.35. Case 1 lies very close to the LSS surface solution and thus appears to be a better fit to the data. The lack of anti-symmetry in measured horizontal displacement components caused a significant difference in the surface and global LSS solutions. Case 2 lies closer to the LSS surface solution for horizontal displacements and therefore provides a better match to the measured inclinometer data (Fig. 3.36). In fact, Case 1 generates a very large LSS error in the horizontal displacements (LSS_1=1112 mm^2 while LSS_2=744, see Table 3.8), which can be explained by the large discrepancies observed in Figure 3.32, at depths larger than 20m. Figure 3.37 suggests that Case 2 overall performs better than Case 1, since it coincides with the LSS surface solution for total displacements.

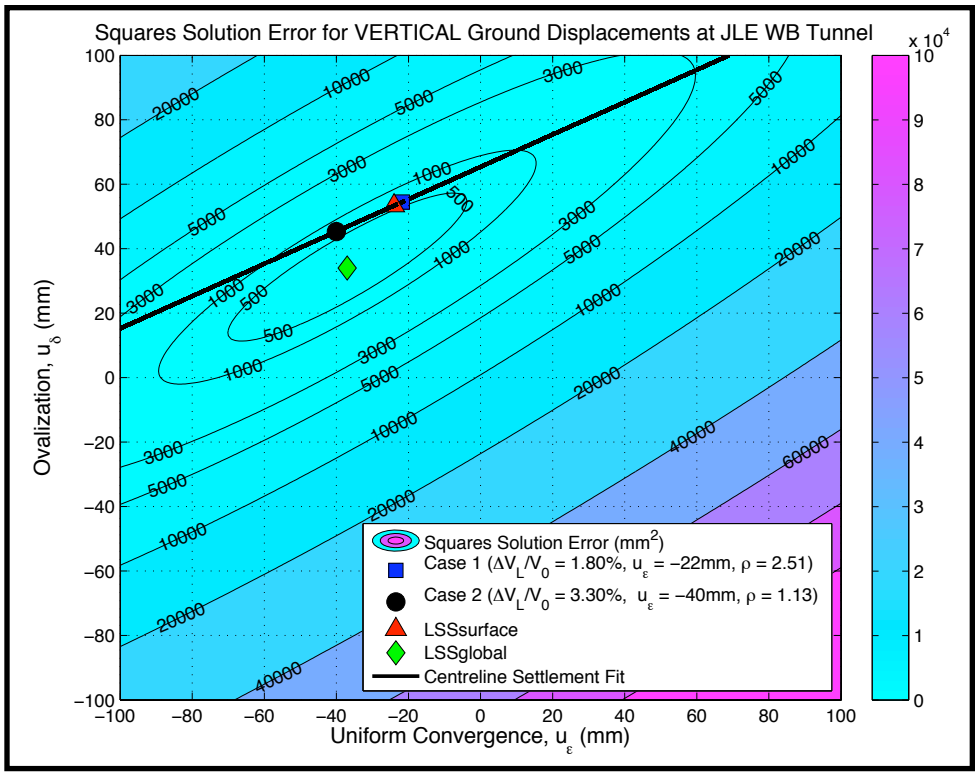

Figure 3.35: Squares Solution Error for Vertical Ground Displacements

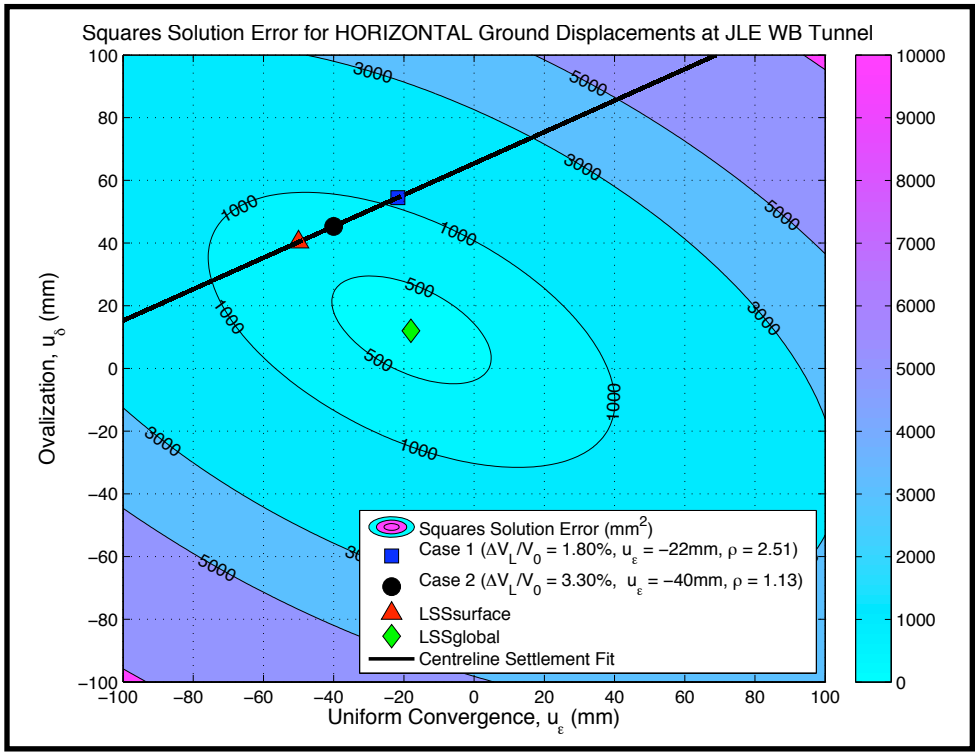

Figure 3.36: Squares Solution Error for Horizontal Ground Displacements

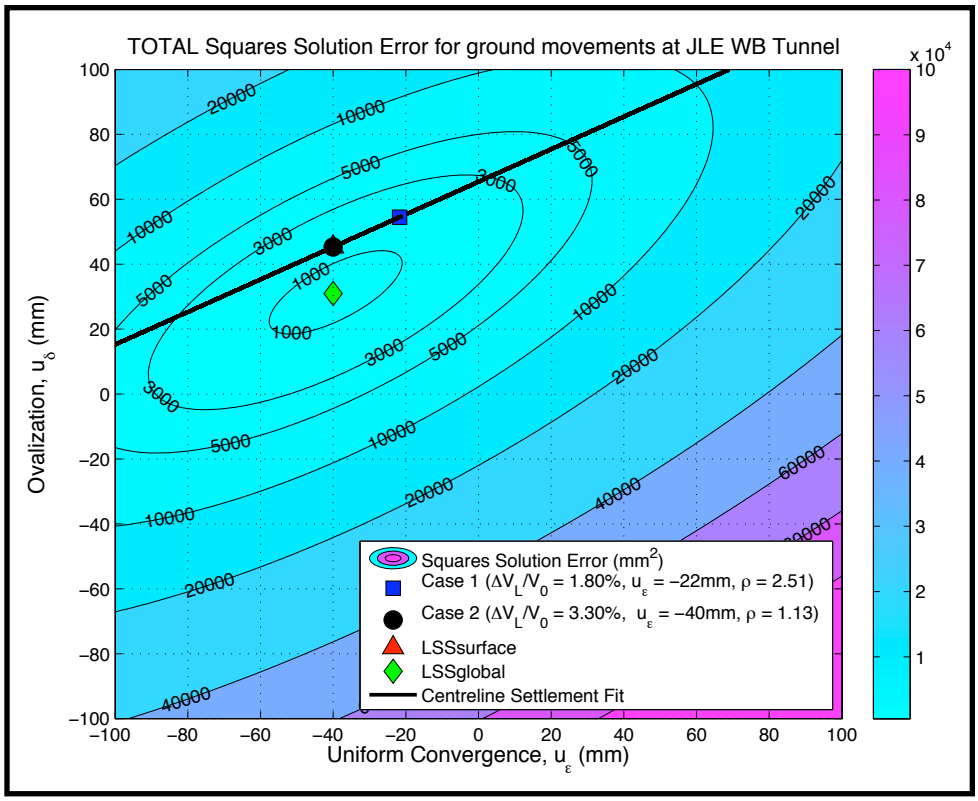

Figure 3.37: Squares Solution Error for both Horizontal and Vertical Ground Displacements

	Surface Solution			Global Solution		
	u_ε (mm)	u_δ (mm)	LSS (mm²)	u_ε (mm)	u_δ (mm)	LSS (mm²)
Vertical	-24	53	585	-37	34	166
Horizontal	-50	40	690	-18	12	409
Total	-40	45	1412	-40	31	712
	Analytical Case 1 (u_ε=-22mm, u_δ=55mm)			**Analytical Case 2** (u_ε=-40mm, u_δ=45mm)		
	LSS (mm²)			LSS (mm²)		
Vertical	588			668		
Horizontal	1112			744		
Total	1700			1412		

Table 3.8: Summary of results of LSS Error Method (full grid)

A further LSS error analysis was undertaken, but this time omitting the three measurement points that are at depth y = -27m (lowest measurement points of inclinometers and extensometers D, E and G, see 'Measurement Grid', Fig. 3.24), since these three points appeared to produce disproportionately high horizontal LSS errors, thus significantly affecting the overall results of the LSS error analysis. Table 3.9 summarizes the results of the revised LSS Error Method and Figures 3.38, 3.39 and 3.40 show the revised state space SS solutions for vertical, horizontal and total displacements. Again, there is a very close agreement between LSS surface and LSS global solutions for the vertical displacement components in Figure 3.38, with Case 1 being a better fit to the data. Case 2 lies closer to the LSS surface solution for horizontal displacements and therefore provides a better match to the measured inclinometer data (Fig. 3.39). However, the revised measurement grid resulted in Case 1 generating a much lower LSS error in the horizontal displacements (revised LSS_1 = 678 mm^2 as opposed to LSS_1 = 1112 mm^2 previously measured), which is significantly closer to LSS_2 = 604 mm^2 generated by Case 2. Figure 3.40 suggests that Case 1 overall performs better than Case 2, since it is closer to the LSS surface solution for total displacements. The LSS error analysis suggests that the optimum parameter sets (represented by the LSS surface solution for total displacements) is:

$(u_\varepsilon, u_\delta)$ = (-28 , 51) mm ➔ $\Delta V_L/V_0$ = <u>2.31%</u> and ρ = <u>1.82</u>

	Surface Solution			Global Solution		
	u_ε (mm)	u_δ (mm)	LSS (mm²)	u_ε (mm)	u_δ (mm)	LSS (mm²)
Vertical	-18	56	502	-33	37	130
Horizontal	-38	46	603	-17	16	403
Total	-28	51	1162	-33	36	630
	Analytical Case 1 (u_ε=-22mm, u_δ=55mm)			**Analytical Case 2** (u_ε=-40mm, u_δ=45mm)		
	LSS (mm²)			LSS (mm²)		
Vertical	506			639		
Horizontal	678			604		
Total	1184			1243		

Table 3.9: Summary of results of revised LSS Error Method (reduced grid)

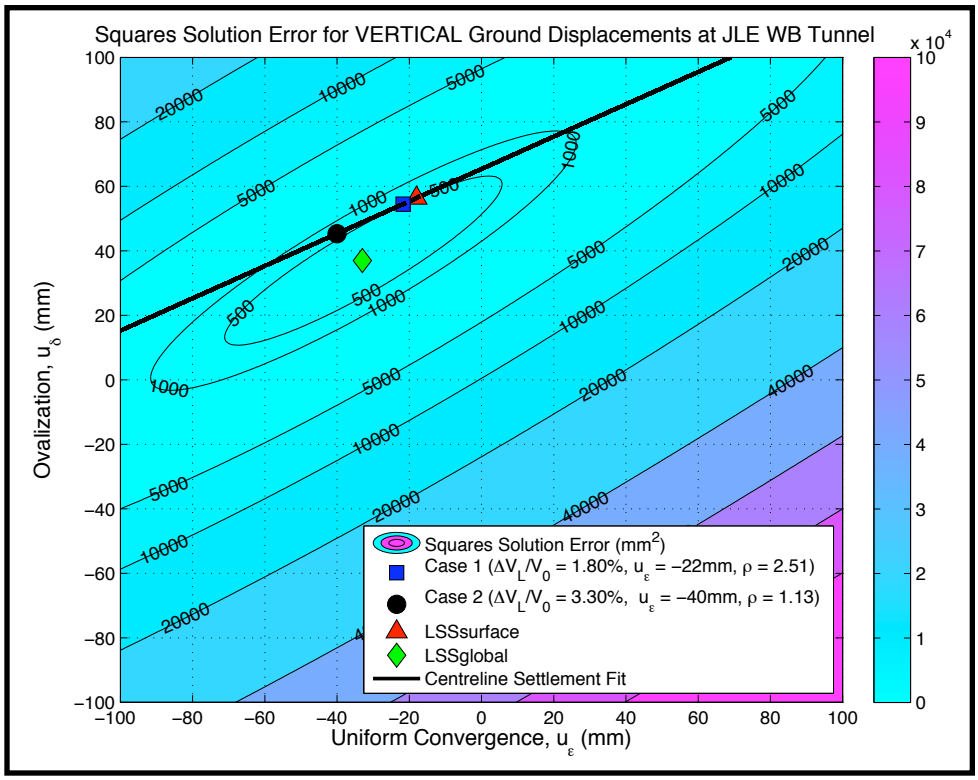

Figure 3.38: Squares Solution Error for Vertical Ground Displacements of revised 'measurement grid'

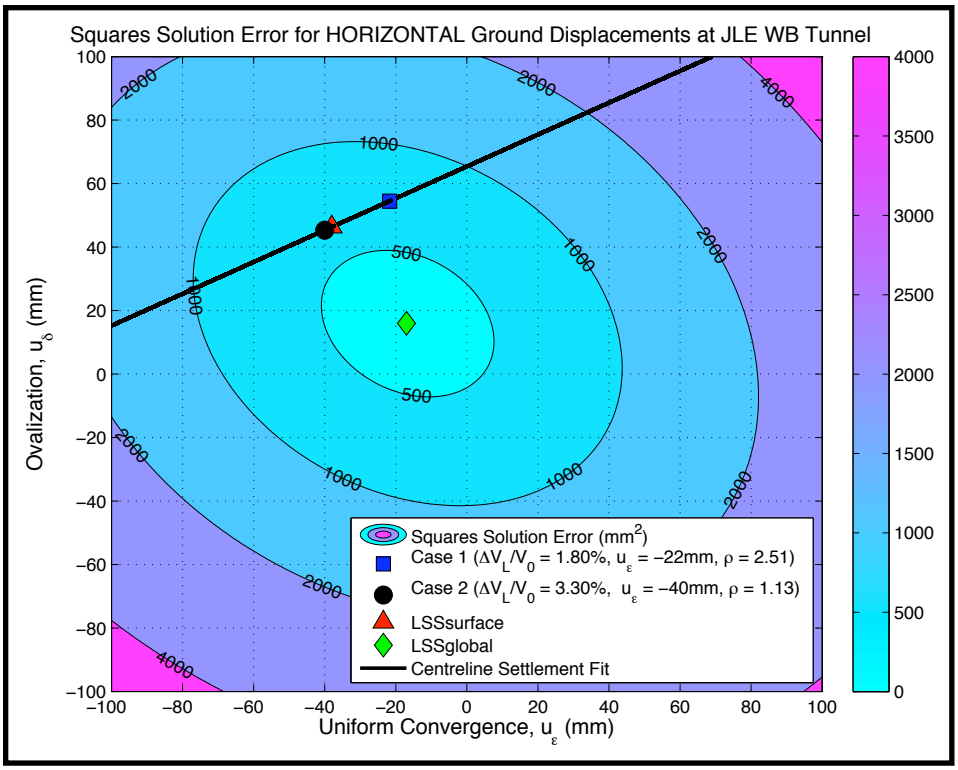

Figure 3.39: Squares Solution Error for Horizontal Ground Displacements of revised 'measurement grid'

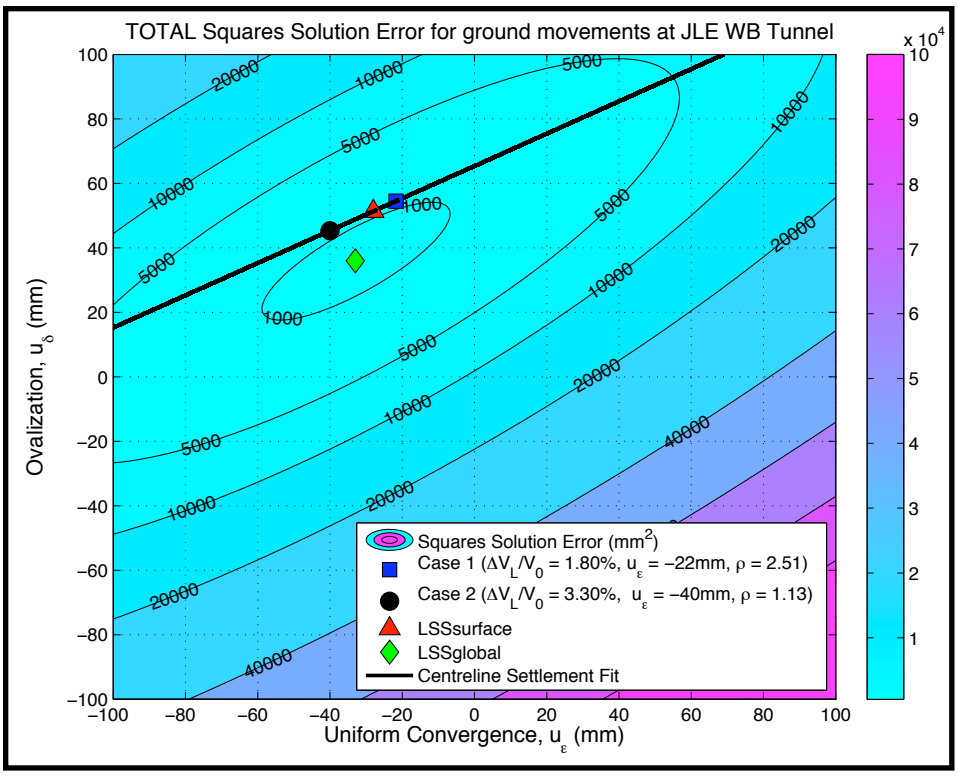

Figure 3.40: Squares Solution Error of both Horizontal and Vertical Ground Displacements of revised 'measurement grid'

3.7 Analytical Solutions with anisotropic stiffness

This section presents further analytical solutions of ground deformations around the WB tunnel, incorporating cross-anisotropic stiffness parameters. The analyses are based on solutions obtained by Chatzigiannelis (2000) while stiffness parameters are based on lab test data from Heathrow T5 reported by Gasparre et al (2007). The anisotropic solutions depend principally on two modulus ratios, $n = E'_h/E'_v$ and $m = G_{vh}/E'_v$, as well as ν_{vh} and ν_{hh}. Table 3.10 shows that n and m vary markedly with strain level while ν_{vh} and ν_{hh} were not reported as functions of strain and are assumed constant. The first set of analysis consider small strain stiffness parameters ($\varepsilon_\alpha < 0.001\%$) approximately corresponding to the elastic behavior of London Clay. The other three set of parameters consider larger strain levels, at the order of 0.01%, 0.03% (which represents the average strain level measured at the St James's test site) and 0.1%.

		Strain Level (%)			
		<0.001	**0.01**	**0.03**	**0.1**
Measured Data (Gasparre, 2007)	E_v' (MPa)	112	65	40	26
	E_h' (MPa)	236	136	85	49
	G_{vh} (MPa)	72	50	45	30
	ν_{vh}' *	0.25	0.25	0.25	0.25
	ν_{hh}' *	-0.19	-0.19	-0.19	-0.19
Model Parameters+	$n = E_h'/E_v'$	2.11	2.09	2.13	1.86
	$m = G_{vh}/E_v'$	0.64	0.77	1.13	1.14
	* Not reported as functions of strain, assumed constant				
	+ E_v', ν_{vh}', ν_{hh}': used in analytical solutions				

Table 3.10: Anisotropic stiffness parameters at four characteristic strain levels

A Least Squares error method is used in order to optimize the cavity parameters (u_ε,u_δ). As in the preceding section, the optimum can either be a **global LSS** or a **surface LSS** that corresponds to the (u_ε, u_δ) set that produces the minimum squares solution (SS) while at the same time fits the centerline surface settlement u_y^0. Contour plots of the SS error for vertical, horizontal and total ground displacements were produced for all four cross-anisotropic stiffness parameter sets and the results from this procedure (based on LSS surface solutions) are summarized in Table 3.11. Note that the reduced measurement grid, discussed in the previous section, was used in the analysis, since it proved to produce more reasonable. We conclude that the minimum LSS error is generated by the parameter set corresponding to the nearly elastic behavior of London Clay ($\varepsilon_\alpha < 0.001\%$) and thus this parameter set is chosen for further discussion. Figures II.8 and II.9 in Appendix II summarize the vertical and horizontal displacements at the surface, for all 4 sets of anisotropic stiffness parameters (and the isotropic Case 1).

	$\varepsilon_\alpha < 0.001\%$			$\varepsilon_\alpha = 0.01\%$		
	u_ε (mm)	u_δ (mm)	LSS (mm^2)	u_ε (mm)	u_δ (mm)	LSS (mm^2)
Vertical	-18	60	107	-14	69	109
Horizontal	-28	46	394	-28	48	406
Total	-25	50	520	-23	56	555
	$\varepsilon_\alpha = 0.03\%$			$\varepsilon_\alpha = 0.1\%$		
	u_ε (mm)	u_δ (mm)	LSS (mm^2)	u_ε (mm)	u_δ (mm)	LSS (mm^2)
Vertical	-9	83	146	-8	87	168
Horizontal	-26	56	438	-26	57	456
Total	-21	64	678	-19	69	747

Table 3.11: Results of LSS Error Method based on LSS Surface Solution for four cross-anisotropic stiffness parameter sets (reduced grid)

The contour plots of the SS error for horizontal, vertical and total ground displacements corresponding to the cross-anisotropic stiffness parameter at small strain level ($\varepsilon_\alpha < 0.001\%$) are shown in Figures 3.41-3.43. From Figure 3.43 we select the values of (u_ε, u_δ) that correspond to the surface LSS condition:

Anisotropic Model: (u_ε, u_δ) = (-25, 50) in mm, $\Delta V_L/V_0 = 2.06\%$, $\rho = 2.0$

It is very interesting to notice that the global and surface LSS solutions overlap for both vertical and 'total' displacements (Figures 3.41 and 3.43) and are very similar for the horizontal displacements (Figure 3.42). This observation suggests that the anisotropic model will generate an overall very good fit to the field measurements reported by Nyren et al (1998).

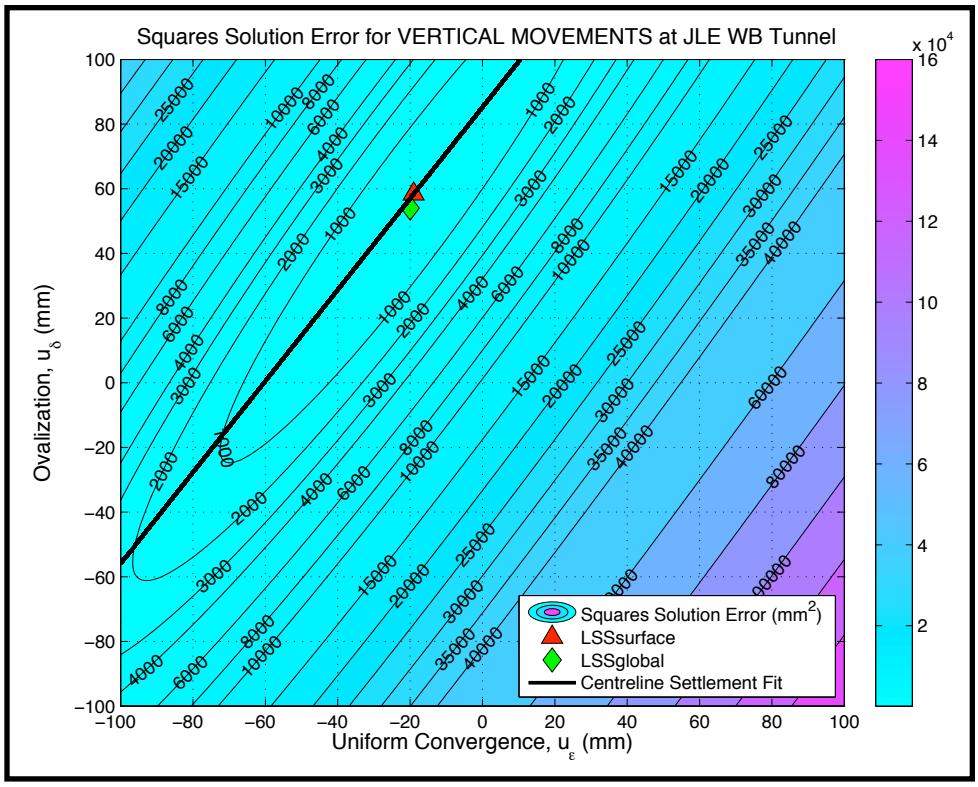

Figure 3.41: SS Error for Vertical Displacements (Anisotropic Model, reduced grid)

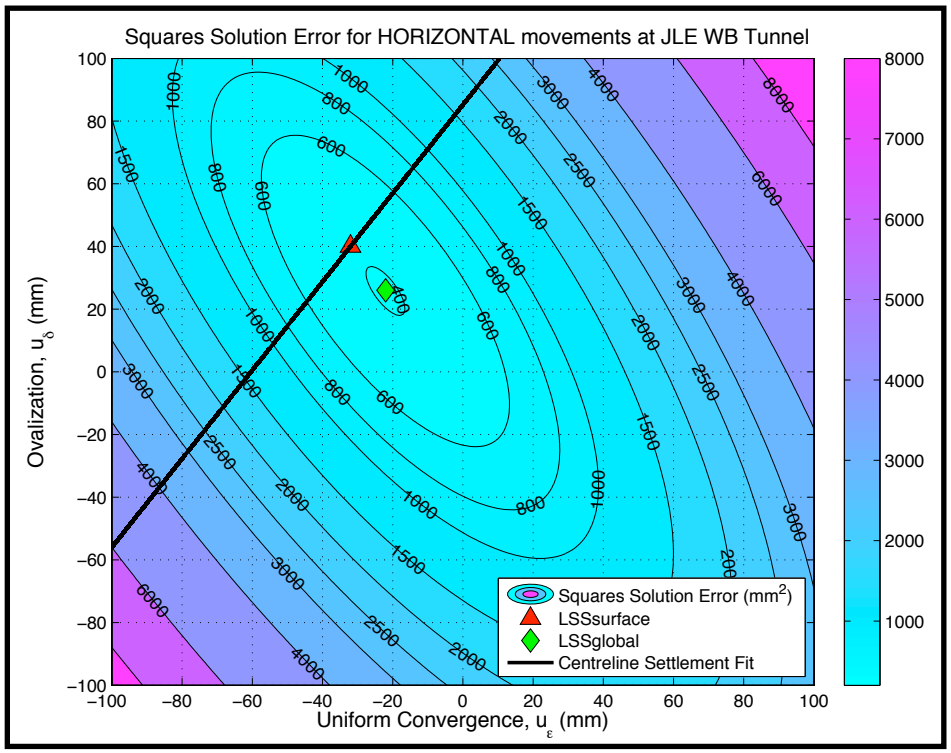

Figure 3.42: SS Error for Horizontal Displacements
(Anisotropic Model, reduced grid)

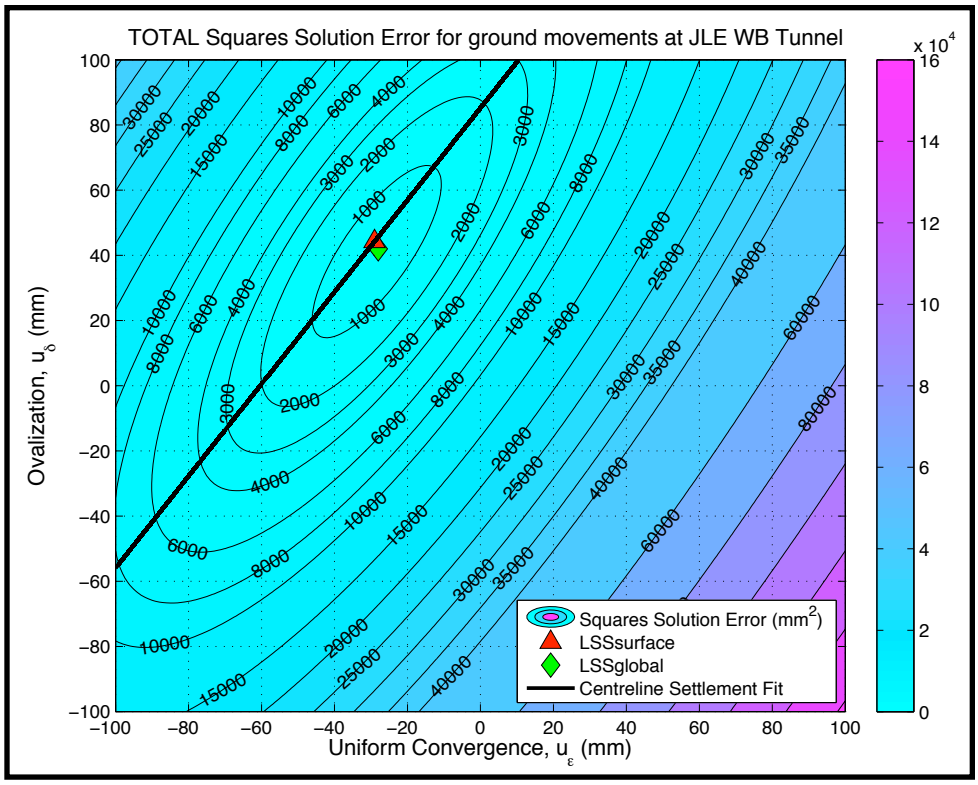

Figure 3.43: SS Error for ' total' displacements (Anisotropic Model, reduced grid)

The following paragraphs summarize observations on the surface and subsurface movements using analytical solutions with anisotropic and isotropic stiffness parameters for London Clay. The Case 1 isotropic solution was chosen as a reference, since the LSS error analysis on the revised measurement 'grid' showed that Case 1 produced the minimum error (see Figure 3.40). The cavity parameters used for the isotropic model are (u_ε, u_δ) = (-21.73, 54.5) mm, which are the parameters used in isotropic Case 1, while the cavity parameters used for the anisotropic case are (u_ε, u_δ) = (-25, 50) mm that correspong to the surface LSS solution computed in the previous section (for strain level <0.001%).

3.7.1 Effect of anisotropic stiffness on computed distribution of subsurface ground movements

Figures 3.44 and 3.45 compare the distributions of vertical and horizontal displacements respectively, for the WB tunnel, as predicted by the anisotropic and isotropic models (both using surface LSS solutions).

Both models predict very similar vertical displacement profiles above the tunnel springline, with the isotropic model generating slightly higher movements than the isotropic model and thus predicting slightly wider settlement troughs. Moreover, along the centreline and also at a zone below the tunnel springline the isotropic model predicts slightly higher displacements than the anisotropic model.

Figure 3.45 shows that the anisotropic model overall generates smaller horizontal ground deformations than the isotropic model. Above the tunnel springline the two models predict similar movements, with the anisotropic model predicting slightly smaller displacements. However, along the tunnel elevation the isotropic model predicts significantly larger outward movements (difference ≈ 15mm). Finally, below the tunnel springline, both models produce very small displacements, with the anisotropic model again predicting smaller values than the isotropic case.

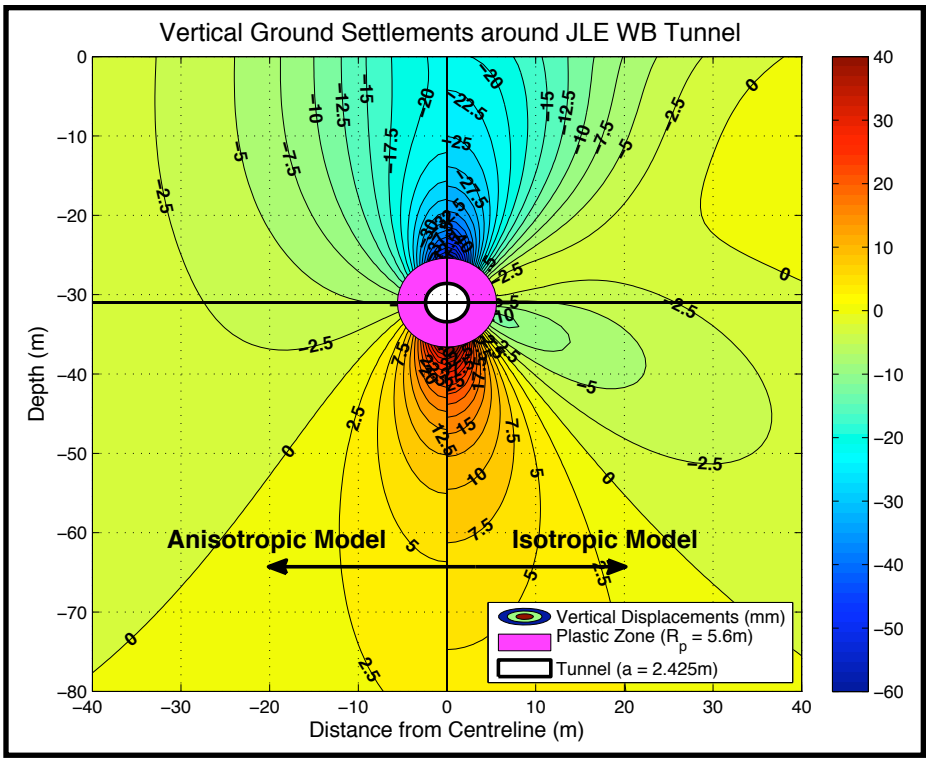

Figure 3.44: Contour Diagram of Vertical Displacements as predicted by Anisotropic and Isotropic Analytical Models (reduced grid)

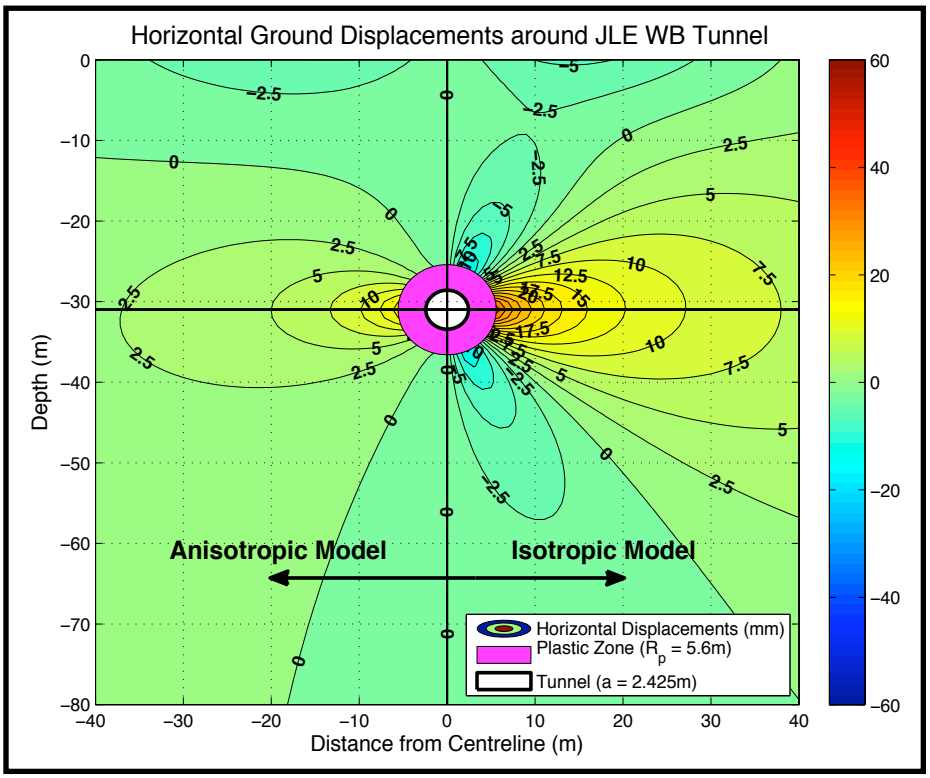

Figure 3.45: Contour Diagram of Horizontal Displacements as predicted by Anisotropic and Isotropic Analytical Models (reduced grid)

3.7.2. Computed and measured surface displacements

Figure 3.46 compares the measured surface settlements with analytical solutions by assuming isotropic and anisotropic stiffness parameters. We observe that the anisotropic model is in closer agreement with the field measurements than the isotropic model. In fact, the anisotropic model produces excellent fit to the field measurements, from x = 0 -15m from the tunnel centreline. The surface settlements generated by the anisotropic model for x > 15m are still more accurate than the predictions of the isotropic model, with differences from the field measurements up to 1.8mm. Finally, the anisotropic model produces surface settlements that converge to zero at x ≈ 50m (similar to the field data) while the isotropic model predicts a small heave in the far field ($u_y \approx$ 1-2mm) that is not seen in the measured data.

Figure 3.47 compares the measured surface horizontal displacements with analytical solutions by assuming isotropic and anisotropic stiffness parameters. As expected, both analytical solutions preserve the antisymmetry in horizontal displacements (i.e. $u_x = 0$ at x = 0). The isotropic model produces a better fit to the measured data than the anisotropic model, which generates differences up to 1.2mm. Also, the isotropic model matches very well the field data for x ≤ 34m but tends to diverge in the far field where small movements are predicted. The anisotropic model slightly underpredicts the maximum horizontal displacement but seem to converge to the measured data in the far field, although a slight inward movement ($u_x \approx$ 1mm) is still predicted at x = 50m when the field data show $u_x \approx 0$.

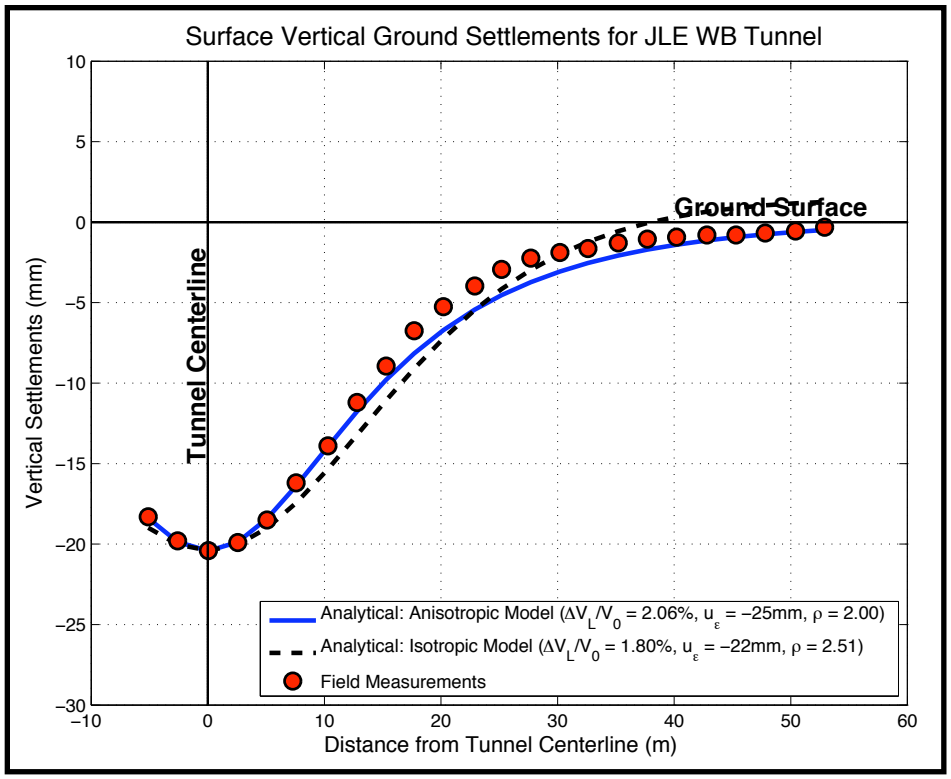

Figure 3.46: Vertical Ground Displacements at Surface, St James's Park Tunnel

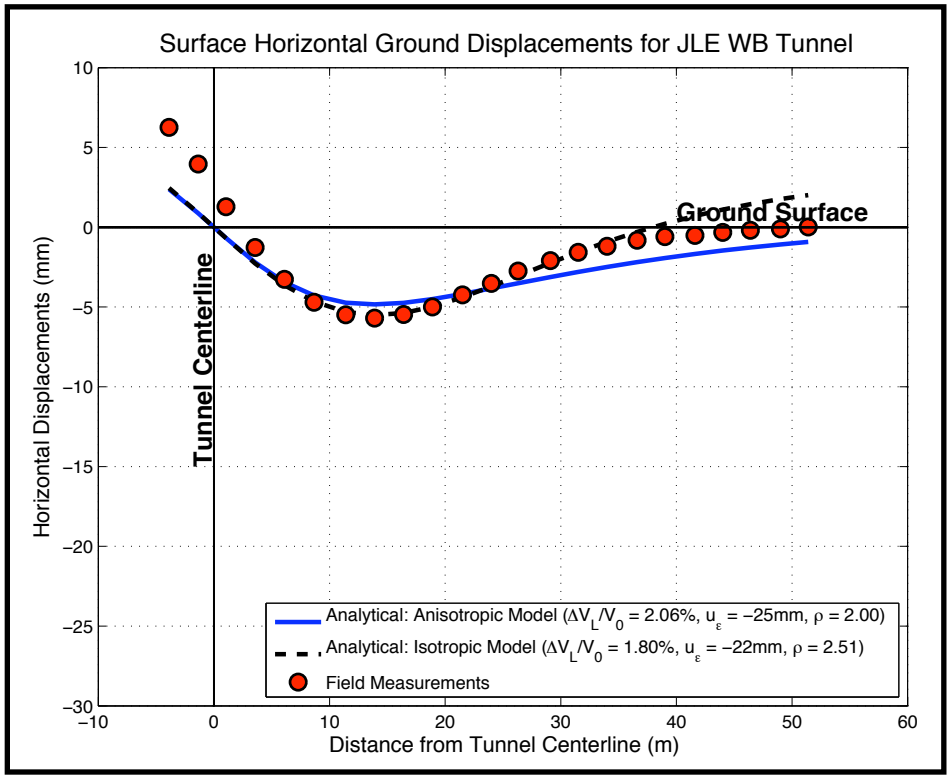

Figure 3.47: Surface Horizontal Ground Displacements for St James's Park Tunnel

3.7.3. Computed and measured subsurface displacements

Figure 3.48 compares the analytically computed (using anisotropic and isotropic models) and measured subsurface vertical settlements for the WB tunnel. There is very good agreement between the predicted and measured settlements, with the anisotropic model generating an overall excellent fit. Furthermore, the anisotropic model only slightly overestimates settlement immediately above the crown in extensometer B, where the isotropic model generates unrealistically large vertical settlements (at depth y = -22.5m, measurements show u_y = 30mm vs anisotropic model's prediction u_y= 35mm and isotropic model's prediction u_y = 43.4mm).

Figure 3.49 shows a similar set of comparisons for the horizontal displacements. The results show more discrepancies between the computed and measured behavior (although the difference in plotting scales between Figs 3.48 and 3.49 should be noted). The analytical models better match the movements measured by inclinometers E_i to H_i, which are further away from the tunnel than the movements measured by inclinometers A_i to D_i, which are closer to the tunnel. The isotropic model provides a better fit to the measurements of Ai while the anisotropic model better matches the measurements of Ci. Both analytical solutions show small deformations towards the centreline in the shallow subsurface, net outward movements occur below a transition depth (marked by contour line u_x = 0 in Figure 3.45). Note that the anisotropic model generates much smaller displacements below this transition depth, which closer match the field measurements that show u_x=0 for depth y < -9m at inclinometers E_i to H_i.

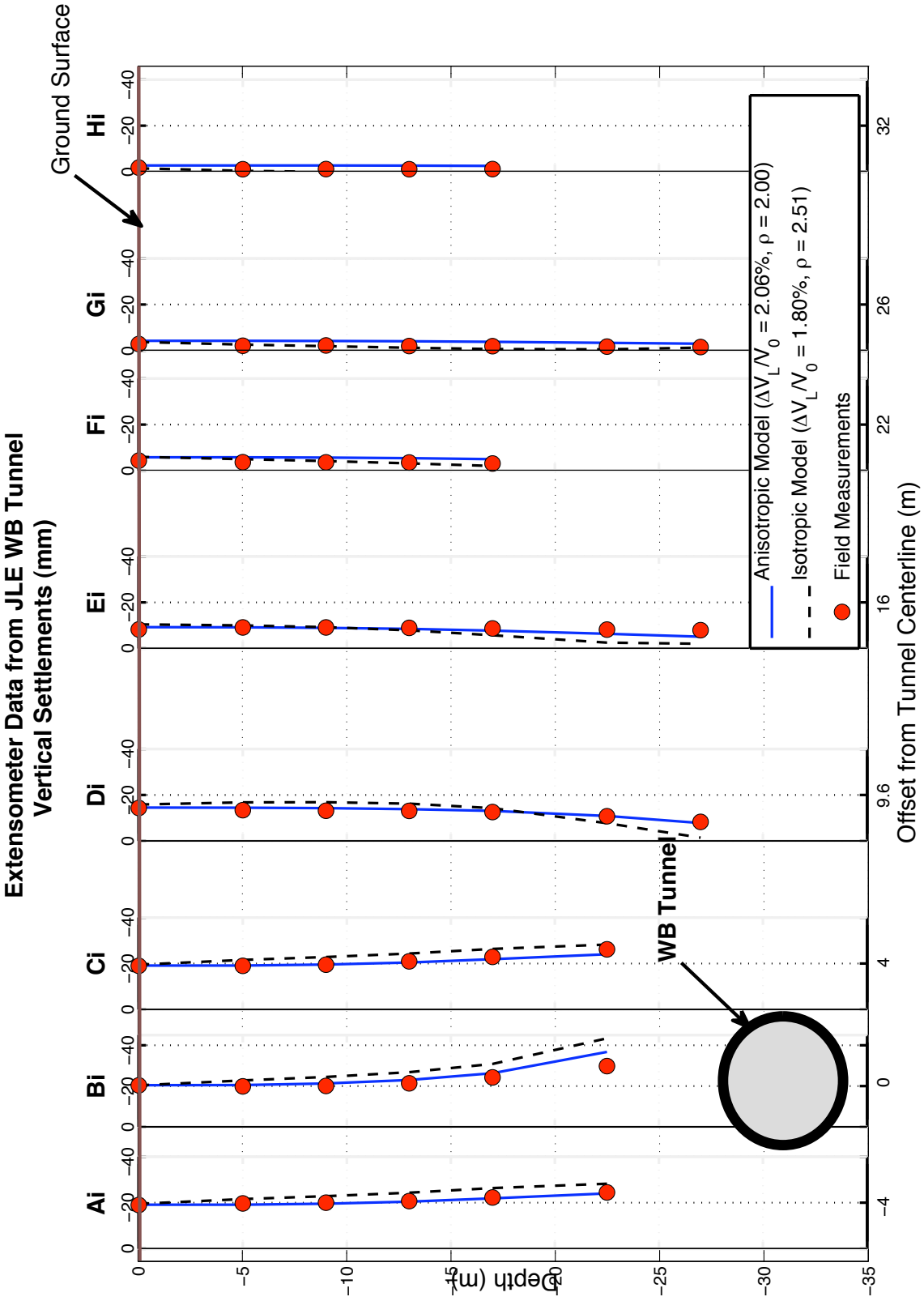

Figure 3.48: Subsurface vertical ground settlements as measured by Extensometers A to H and also as predicted by Anisotropic and Isotropic Models

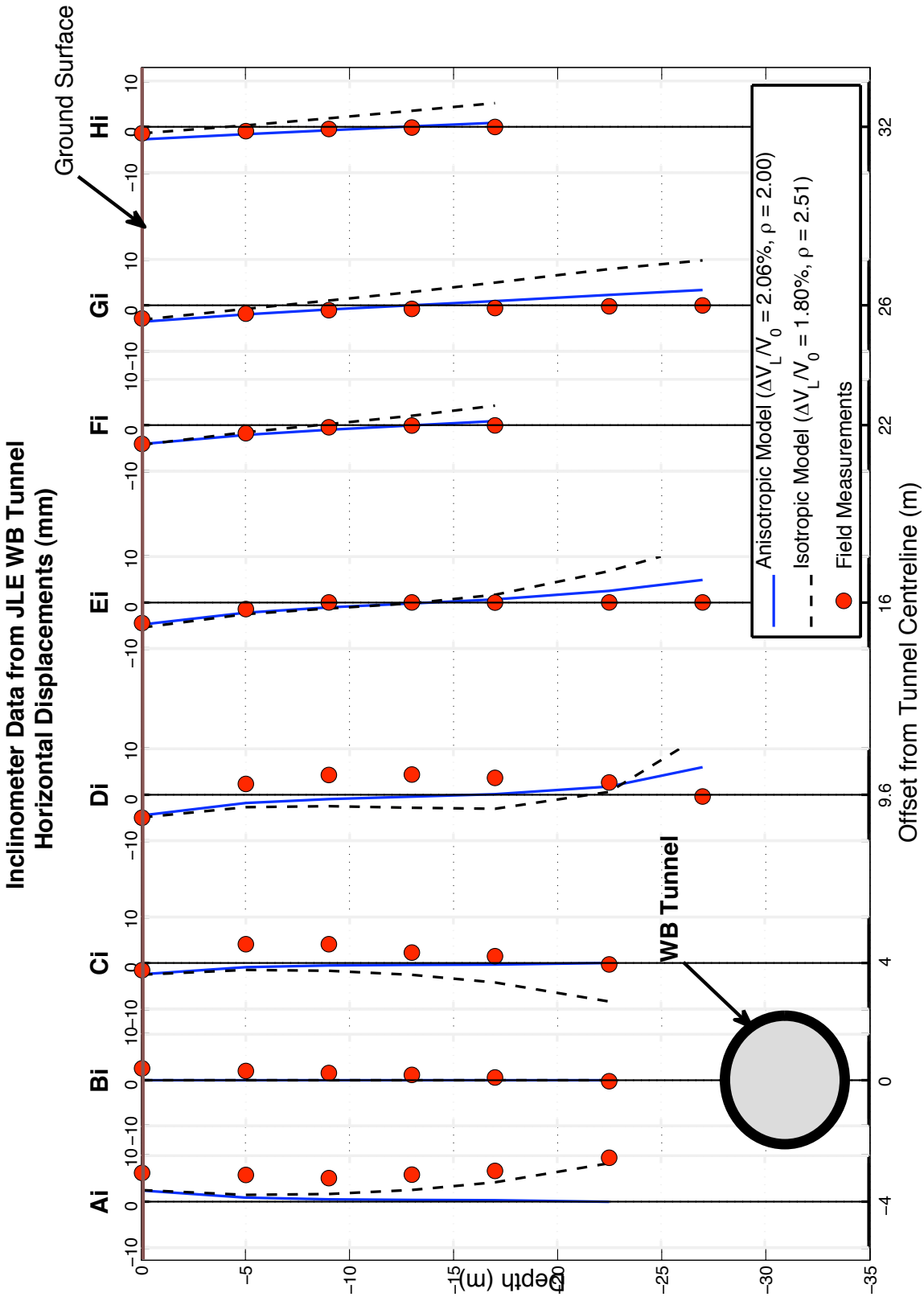

Figure 3.49: Subsurface horizontal ground displacements as measured by Inclinometers A to H and also as predicted by Anisotropic and Isotropic Models

3.8 Conclusions

Extensive measurements of ground deformations from the St James's Park test site (Nyren et al, 1998) provide a useful opportunity to evaluate the effectiveness of analytical solutions in describing the ground displacements induced by open face tunnel construction in London Clay.

Initially, analytical solutions that assume two isotropic stiffness parameters sets (Cases 1 and 2) were employed and the computed vertical and horizontal displacement profiles, at the surface and subsurface, were compared to reference grid of measured vertical and horizontal displacements (Figure 3.24). Overall Case 1 performed better than Case 2, as suggested by the proposed LSS error method (see Figure 3.40). Figure 3.27 shows that Case 1 produces a very good fit to the surface settlements measured in the field, but predicts a small heave in the far field that is not seen in the recorded data. Figure 3.28 suggests that Case 1 generates horizontal displacements that are very close to the field measurements for $x \leq 34$m, but tends to diverge in the far field, where small outward movements are predicted, which were not measured by Nyren et al (1998).

Figure 3.31 shows a very good agreement between the predicted and measured settlements in the subsurface, but the isotropic analytical solutions tend to overestimate the settlement measured immediately above the crown in extensometer B. Figure 3.32 shows more discrepancies between the computed and measured horizontal displacements in the subsurface. The analytical solutions

better match the movements measured by inclinometers E_i to H_i, which are further away from the tunnel. Furthermore, the analytical solutions preserve the antisymmetry in horizontal displacements (i.e. $u_x = 0$ at $x = 0$), which is not observed in the measured data, since inclinometer B_i, which lies along the centerline, shows some horizontal movements taking place. Furthermore, the displacements measured by inclinometers A_i and C_i, which have the same offset from the centerline, are not mirror images, as expected.

Further analytical solutions that incorporate cross-anisotropic stiffness parameters were employed for describing the ground deformations generated around the WB tunnel. Four different cross-anisotropic stiffness parameter sets corresponding to characteristic strain levels were considered. The anisotropic stiffness parameters incorporated in the analysis significantly reduced the LSS error and thus improved the overall fit. The LSS error method showed that the optimum solution corresponded to the nearly elastic behavior of London Clay ($\varepsilon_\alpha < 0.001\%$). Comparing to the isotropic Case 1, the anisotropic solutions appear to produce an excellent fit to the vertical displacements at the surface and subsurface. Incorporating anisotropy in the analytical solutions resulted in a narrower surface settlement trough (Figure 3.46) and also in convergence with the measured movements in the far field. Furthermore, as Figure 3.48 suggests, the anisotropic model generates vertical settlements above the crown in extensometer B, which are much closer to the field data than the isotropic model.

The anisotropic model generally predicts smaller horizontal displacements in the

subsurface and therefore produces profiles that are in most cases closer to the field measurements than the isotropic solutions.

It is interesting to notice that both isotropic and anisotropic solutions suggest volume losses that are lower than $\Delta V_L/V_0$ = 3.3% calculated by Standing and Burland (2006) using empirical means. The isotropic Case 1 suggests that $\Delta V_L/V_0$ = 1.80% while the anisotropic case results in $\Delta V_L/V_0$ = 2.06%. Both $\Delta V_L/V_0$ values are closer to the volume loss anticipated prior to the construction of the JLE WB tunnel ($\Delta V_L/V_0 \approx 2\%$), which was based on volume losses that had occurred in previous tunnel constructions in London Clay (Standing and Burland, 2006).

Finally, the empirical method seems to produce very good fits for surface ground movements, in the vertical and horizontal directions (Figures 3.27 and 3.28). However, the empirical method performs very poorly when predicting ground displacements in the subsurface (Figures 3.33 and 3.34). Although it generates settlements in the shallow subsurface (y < -12m) that are in good agreement with the field measurements, it significantly underpredicts the settlements measured at larger depths. Moreover, the empirical solutions fail to fit any of the subsurface horizontal displacements that were recorded by Nyren et al (1998), suggesting that the assumption that all ground displacements are directed towards the center of the tunnel does not apply to the case of St James's Park WB tunnel.

Chapter 4
The Heathrow Express trial tunnel

4.1 Introduction

Heathrow Express (HEX) is a high-speed rail link from central London to Heathrow Airport. As with any tunneling works taking place in an urban environment, one of the primary concerns prior to its construction were the ground movements that would be induced and could potentially damage important structures at the ground surface above the HEX tunnels, such as multi-storey car parks and the London Underground Piccadilly Line running tunnels. Therefore, it was decided that a trial tunnel would be built prior to the main works, in order to examine the ground response to different tunneling methods. Deane and Bassett (1995) provided a detailed description of the trial tunnel design characteristics and site conditions.

The trial tunnel was built on the line of the running tunnel from the central terminal area to the Terminal 4 station. Construction works began in February 1992 and were completed in early June 1992. Figure 4.1 shows the three excavation sequences that were employed, each using different versions of the New Austrian Tunneling Method (NATM) over a length of 30m (the trial tunnel was 100m long in total, with domed shotcrete headwalls separating subsequent tunnel types, to minimize interaction effects). The first tunneling method (Type 1) involved the excavation of the two side drifts followed by the removal of the central core of the tunnel, and was considered the most conservative. In Type 2, one side of the tunnel

was excavated first and was then enlarged to its full size. Type 3 involved a top heading and bench sequence with the bottom of the shotcrete arch of the heading supported on inverted shotcrete arches to limit excess settlement. For all three types, the first excavation phase that included the construction of the side headings or crown and bench were completed for the full 30m length of each construction sequence before the remainder of the tunnel was excavated and lined.

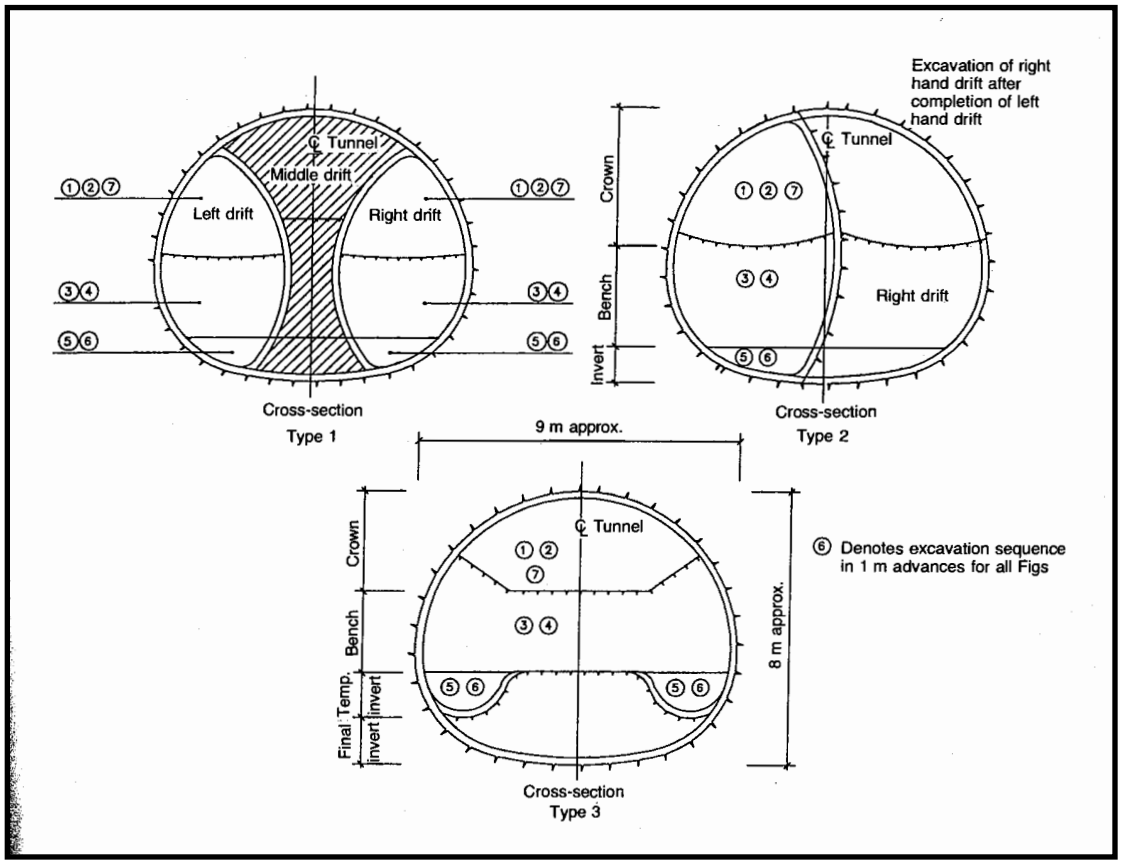

Figure 4.1: Cross-sections of NATM trial tunnel showing construction sequences (Deane and Bassett, 1995)

4.2 Site Conditions

The local stratigraphy is very similar to the ground conditions at St James's Park test site (Section 3.2) The soil profile comprises the following units:

- 1-2m of made ground
- 2-4m of dense terrace gravels
- Approximately 45m of London Clay
- Deeper still lays the Woolwich and Reading Beds and then the chalk aquifer

The trial tunnel was entirely excavated within the London Clay, at a depth to springline[1], H = 19m. Based on the division of London Clay undertaken by Standing and Burland (2006) for the St James's test site, the HEX tunnel was driven through the London Clay B unit, which is generally a very stiff, thinly-laminated, silty clay that contains large vertical fissures. Moreover, it is reasonably strong, has a good 'stand-up time' of at least 18h and also a very low permeability that provides a relatively dry tunnelling environment (Deane and Bassett, 1995).

[1] Springline is defined as the bench elevation of a central point midway between the crown and the bottom of the tunnel.

4.3 Instrumentation at test site

The ground movements induced by the HEX trial tunnel were measured from a virtually greenfield site with no significant structures in the zone of influence. The instrumentation used is summarized in Figure 4.2 and comprised:

- **59 levelling pins** that were placed just below the sub-base of the road, along the line of the tunnel and at 3 transverse sections, for surface displacement measurements. The vertical movements were measured using precise leveling and the horizontal movements using an EDM theodolite.
- **11 magnetic rod extensometers** that were positioned at transverse sections of Types 2 and 3, for subsurface settlement measurements.
- **8 ring inclinometers** that were placed at transverse sections of Types 2 and 3 to measure subsurface horizontal movements.
- **Piezometers and pressure cells** that were installed in parallel holes to the inclinometers and extensometers, for pore water pressure measurements.

It should be pointed out that Deane and Bassett (1995) have reported vertical displacements at the surface for all tunnel types, and horizontal and vertical displacements in the subsurface for tunnel Types 2 and 3 (through vector diagrams). Additional subsurface horizontal movements have been reported for tunnel Type 3, at four inclinometer positions.

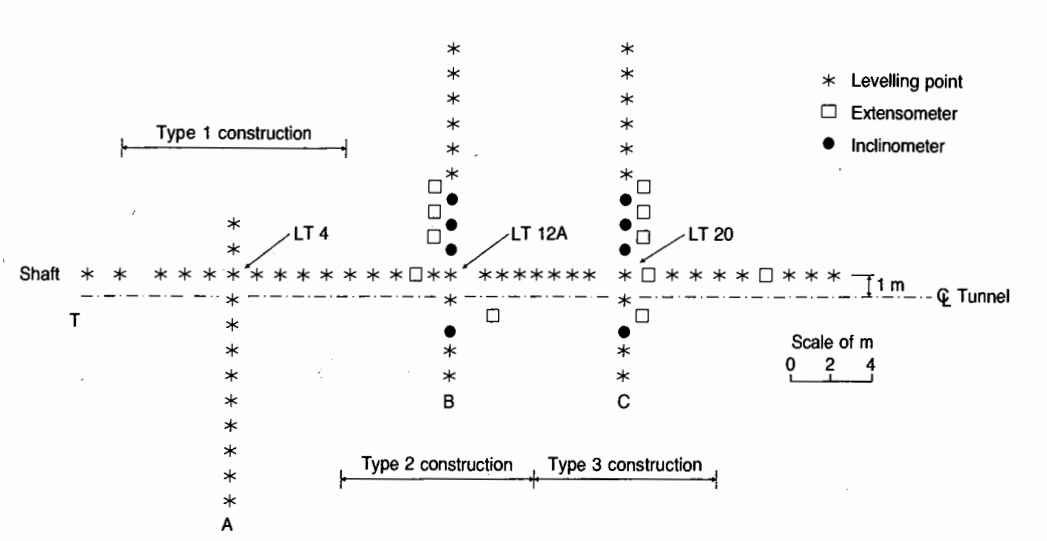

Figure 4.2: Instrumentation Layout at HEX test site (Deane and Bassett, 1995)

4.4 Surface Displacements

Figures 4.3 to 4.5 summarize the vertical settlements generated by the three tunnelling sequences[2]. Figure 4.3 shows that the surface settlement trough of Type 1 appears to be symmetric, with a maximum settlement above the crown $u_y^0 \approx 28$mm. It is interesting to note that most of the settlement (67% of the total settlement) was induced during the construction of the two side drifts. Figure 4.4 clearly demonstrates that the asymmetry involved in the construction method of Type 2 (the left drift area was excavated prior to the right) caused the asymmetry of the surface settlement profile. The maximum settlement that was recorded for Type 2 was above the crown and was $u_y^0 \approx 25$mm. Figure 4.5 shows that the settlement trough of Type 3 is also asymmetric along the tunnel centreline, although the construction method was symmetrical (top heading and bench sequence). The

[2] Note that Deane and Bassett (1995) have not published any horizontal surface measurement data.

apparent centrepoint $u_y^0 \approx 39$mm occurs 1m to the west of Type 3 tunnel centreline. Deane and Bassett (1995) suggest that this might be due to the tunnel excavation systematically taking place from left to right, with the left wall standing unsupported for a longer time than the right. The apparent centrepoint $u_y^0 \approx 39$mm was recorded 1m to the west of Type 3 tunnel centreline. It should be pointed out that the invert was closed 4 - 15 days after the crown and sides were completed and Deane and Bassett (1995) suspect that if there hadn't been a delay in closing the invert the vertical settlement would have been significantly reduced (possibly to $u_y^0 \approx 30$mm shown as point Q in Figure 4.5). Figure 4.6 summarizes the settlement profiles for all tunnel types about the trough centreline (not the tunnel centreline, since for the asymmetric trough of Types 3 the trough and tunnel centrelines do not coincide). Deane and Bassett (1995) used the empirical method to model the surface settlements induced by the 3 HEX tunnel sequences and the results of their analysis (inflection point x_i and volume loss $\Delta V_L/V_0$) are summarized in Table 4.1.

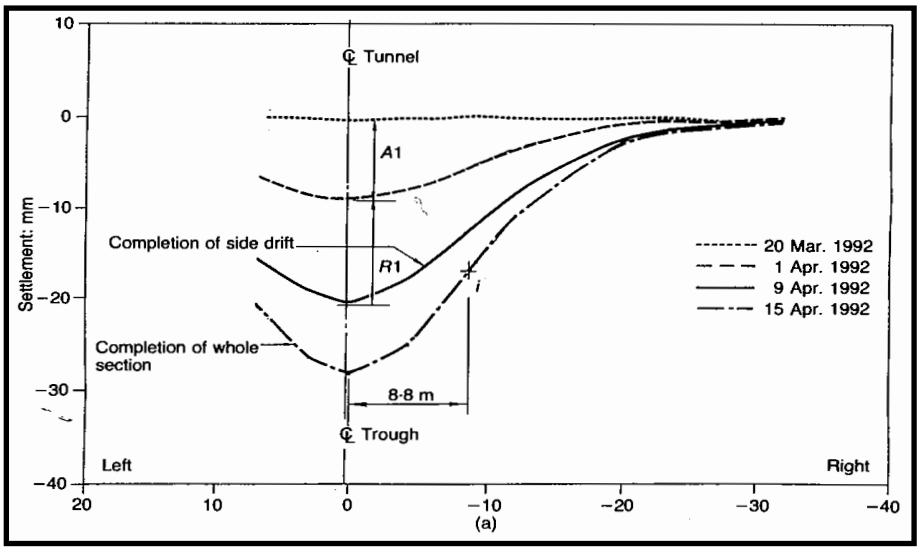

Figure 4.3: Transverse settlement profile of HEX Type 1 (Deane and Bassett, 1995)

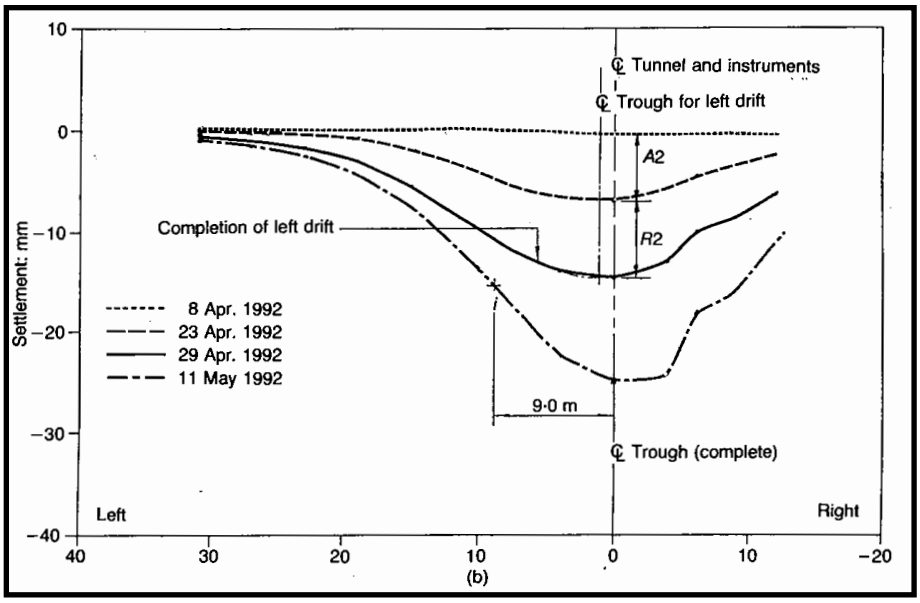

Figure 4.4: Transverse settlement profile of HEX Type 2 (Deane and Bassett, 1995)

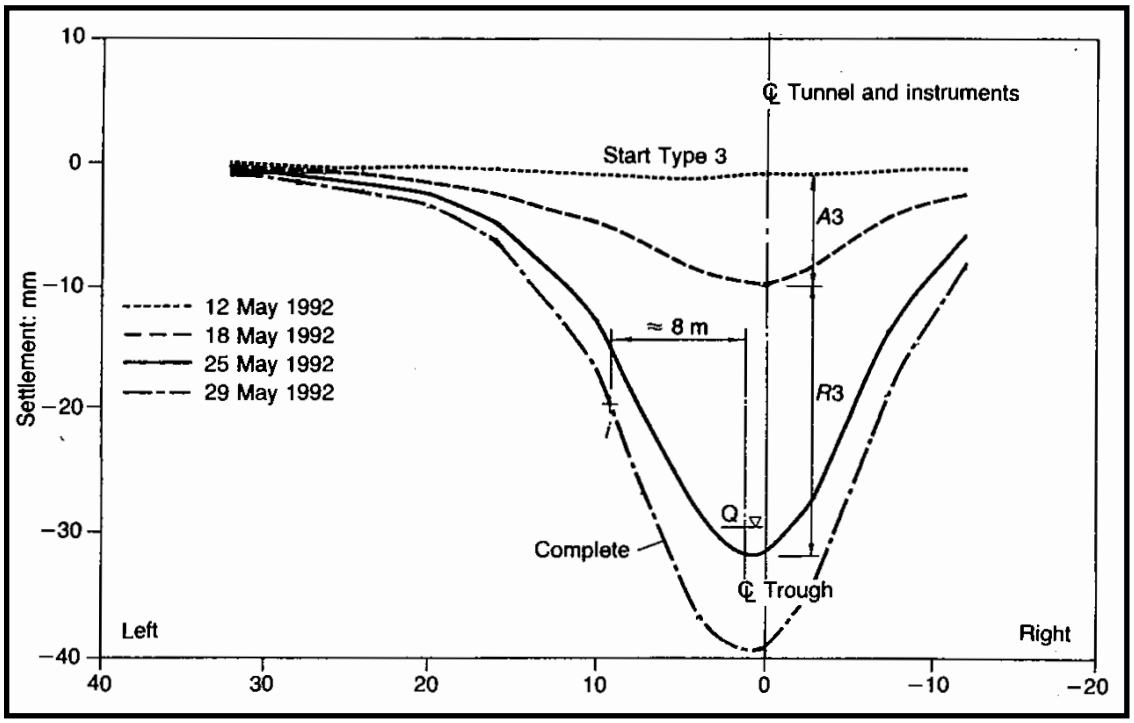

Figure 4.5: Transverse settlement profile of HEX Type 3 (Deane and Bassett, 1995)

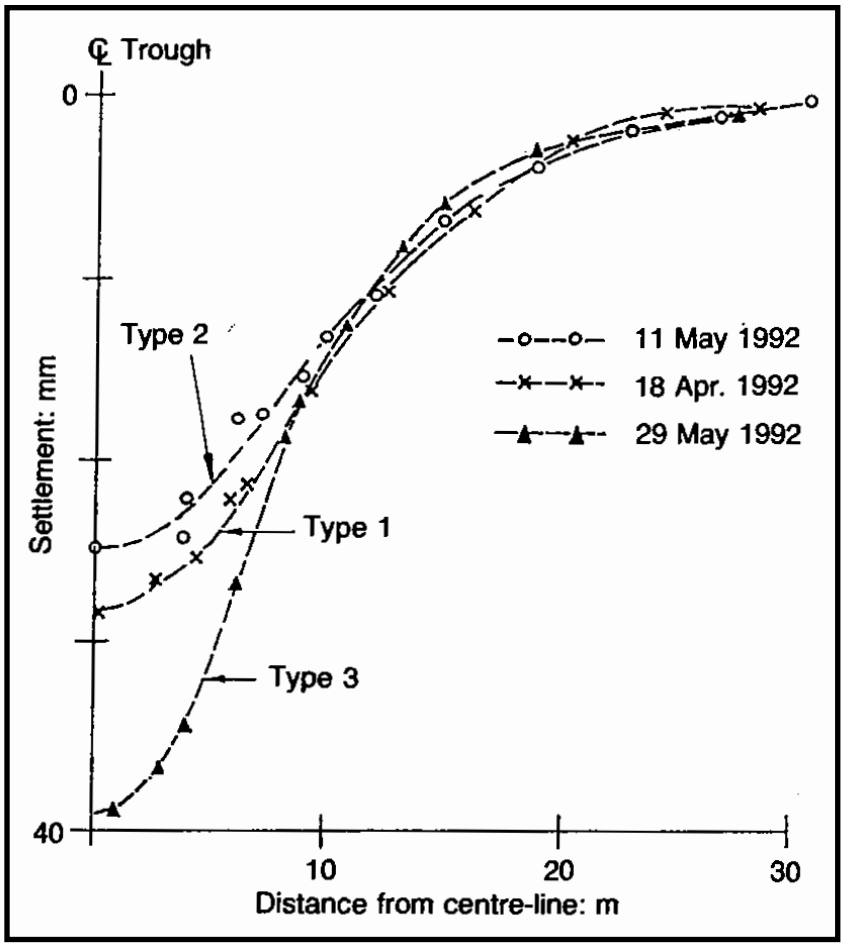

Figure 4.6: Settlement Profile for all HEX tunnels about trough centreline (Deane and Bassett, 1995)

HEX Trial Tunnel Type	Empirical Method Parameters (Deane & Bassett, 1995)		Key Deformation Parameters for Analytical Solutions (Pinto, 1999)	
	$\Delta V_L / V_0$ (%)	x_i (m)	u_y^0 (mm)	u_y^1 (mm)
1	1.13	8.8	28.1	3.57
2	1.06	9.0	24.6	3.89
3 (25 May)	1.36	9.7	31.6	3.05
3 (29 May)	1.33	8.2	38.9	4.60

Table 4.1: Summary of key parameters of empirical method and analytical solutions for all 3 HEX tunnels

Table 4.1 also summarizes the two key parameters suggested by Pinto (1999): 1) the maximum surface settlement, u_y^0 and 2) the surface settlement at an offset x/H = 1, u_y^1. The type 3 tunnel is analyzed for two different phases of the construction sequence: 1) May 25th, corresponding to the completion of the full face; and 2) May 29th, corresponding to the completion of the invert. The reason why Type 3 is analyzed for two points in time is because, as it was already stated, there was significant delay between the two phases and the invert was not closed quickly to form a full ring, causing excess settlement in the Type 3 (29 May) case. Deane and Bassett conclude in their paper that the centreline surface settlement (u_y^0) would have been reduced to approximately 30mm, had the delay been avoided, which is very close to u_y^0 induced by Type 3 (25 May). Most of the values shown in Table 4.1 are based on the half-troughs shown in Figure 4.6 (the values for Type 3, 25 May, were derived from the half trough from Figure 4.5). It is deduced that the maximum u_y^0 and $\Delta V_L/V_0$ (according to the Gaussian Fit parameters proposed by Deane and Bassett, 1995) are generated by tunnel Type 3, while Type 2 have the smallest values of u_y^0 and $\Delta V_L/V_0$.

4.5 Application of proposed analytical solutions

The analytical framework introduced in Chapter 2 can be used to interpret the ground movements caused by the construction of the three trial tunnels. The key geometric parameters are:

⇒ Depth to springline H = 19m

⇒ Equivalent diameter 2R = 8-9m ➔ Radius R = 4.25m

⇒ Ratio: R/H = 0.22

⇒ Poisson's Ratio: $\nu = 0.3$

Following Sagaseta (2001) and Pinto and Whittle (2007), it is important to assess the potential zone of plastic deformation around the tunnel bore. For the case of the HEX trial tunnel:

The overburden pressure $p_o = \gamma_{clay} \times H = 19.5 \times 19 kN/m^2 = 370.5 kN/m^2$. The undrained shear strength of London Clay at depth H=19m is $s_u \cong 200$ kPa. The overload factor N $= p_o/s_u = 370.5/200 = 1.85$. For a deep tunnel the radius of the plastic zone is then $R_p/a = \exp[(N-1)/2] = 1.532$ ➔ $\underline{R_p} = 1.53 \times 4.25 = \underline{6.51m}$

Having estimated the plastic zone, the subsequent analysis will focus on measurements of surface settlements for all three tunnel types and subsurface displacements for Types 2 and 3, extracted from the ground movement vector diagrams shown in Figure 4.7. Additional horizontal displacements, recorded by 4 inclinometers (IC1-IC4), have been used in the analysis of the Type 3 tunnel, which are outside the plastic zone. This 'measurement grid' is shown schematically in Figure 4.8 and shows the 4 inclinometer positions, with data at depths from the surface (y=0m) to a depth y=-30m. Deane and Bassett (1995) present continuous displacement profiles and don't specify the measurement points. For comparison purposes, the analytical model is set to calculate ground movements at the points of

the measurement grid shown below (i.e. every 5m), which coincide with the points where field measurements have been assumed to be undertaken.

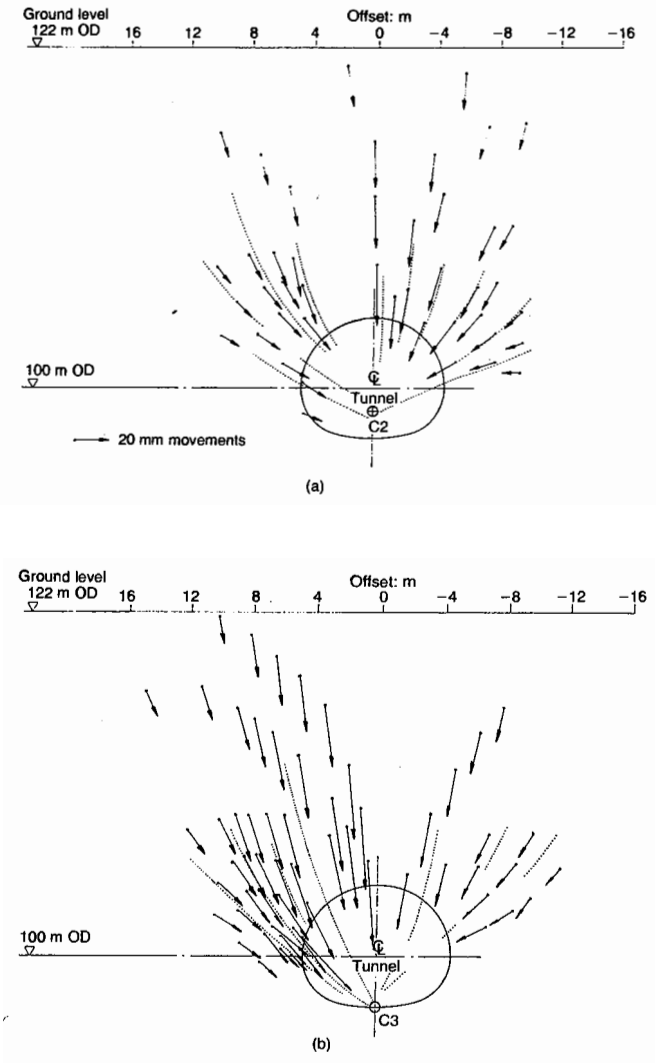

Figure 4.7: Ground movement vector digram for HEX trial tunnels: a)Type 2 (11 May) tunnel; and b)Type 3 (29 May), (Deane and Bassett, 1995)

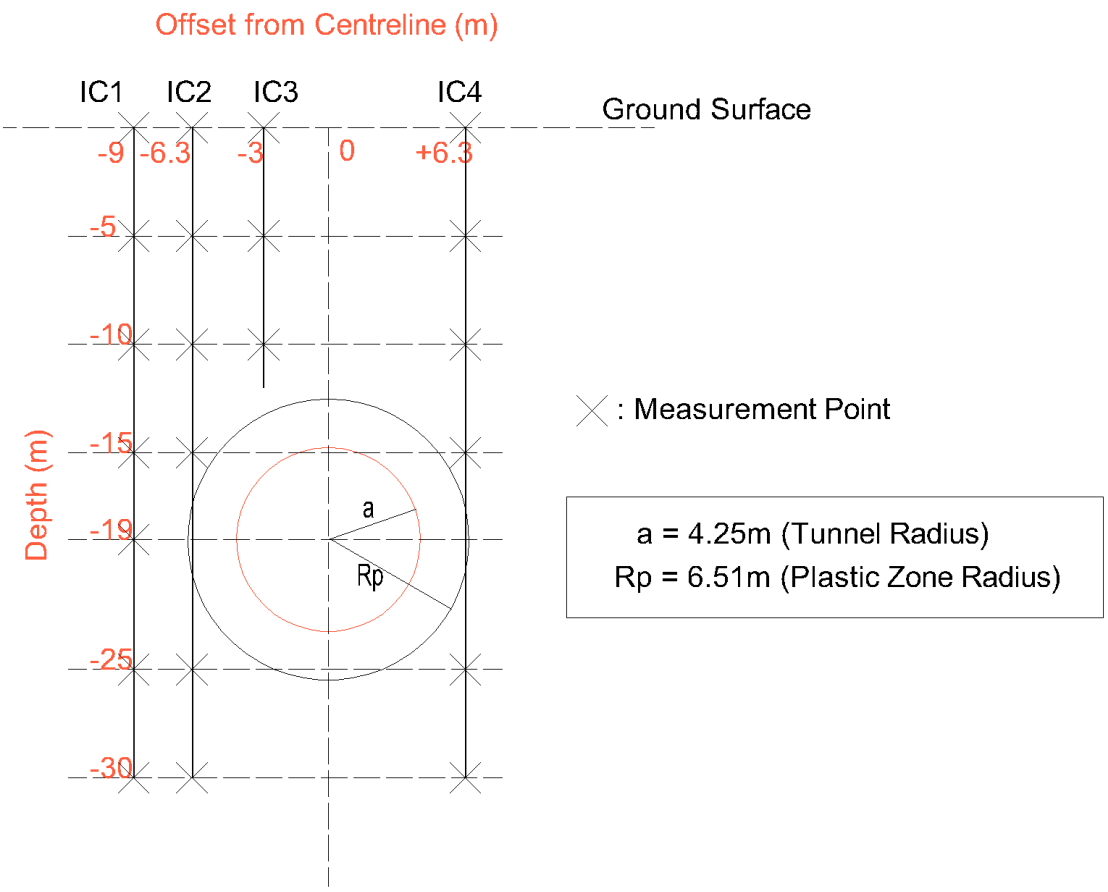

Figure 4.8: Grid of assumed measurement points for HEX Type 3 tunnel

4.5.1 Computed and Measured ground movements, isotropic model

Two different sets of input parameters were selected to model the field measurements of each tunnel type. Table 4.2 summarizes the parameters (u_ε, u_δ) used in the analysis as well as the corresponding ρ and $\Delta V_L/V_0$ values.

Tunnel Type	Case 1 Parameters				Case 2 Parameters			
	u_ε(mm)	u_δ(mm)	ρ	$\Delta V_L/V_0$ (%)	u_ε(mm)	u_δ(mm)	ρ	$\Delta V_L/V_0$ (%)
1	-11.40	30.67	2.69	0.54	-24.01	19.11	0.80	1.13
2	-12.42	24.61	1.98	0.58	-22.53	15.35	0.68	1.06
3(25May)	-9.74	37.31	3.83	0.46	-28.90	19.75	0.68	1.36
3(29May)	-14.69	43.45	2.96	0.69	-28.26	31.02	1.10	1.33

Table 4.2: Parameters used in analytical solutions

The parameters of **Case 1** were derived by matching the surface vertical settlements at the centreline, u_y^0 and at an offset x = 19m (x/H=1), u_y^1 (where u_y^0 and u_y^1 for each tunnel type are shown in Table 4.1).

The parameters of **Case 2** were derived by assuming a volume loss, $\Delta V_L/V_0$ for each tunnel type equal to that estimated by the empirical method (see Table 4.1). From ΔV_L the convergence parameter u_ε is obtained directly,

$$\frac{\Delta V_L}{V_0} = \frac{2u_\varepsilon}{R} \Rightarrow u_\varepsilon = \frac{\Delta V_L}{V_0} \cdot \frac{R}{2}$$

while the ovalization u_δ is chosen to match the surface vertical displacement at the centreline, u_y^0 (using eqn. 2.9b and 2.10b).

4.5.1.1 Surface Displacements

Figures 4.9 to 4.12 compare the computed and measured surface settlements for all three tunnel types with empirical Gaussian distribution curves used by Deane and Bassett (1995). We observe that Case 1 is in closer agreement with the field measurements than Case 2 for all tunnels. The Case 2 analysis produces differences up to 7mm with the measured data (see Figure 4.12) and overestimates the width of all settlement troughs. Case 1 and the conventional Gaussian curve generally produce similar results. Figures 4.9 and 4.10 show an excellent agreement between the computed Case 1 results and the field measurements for tunnel types 1 and 2, with a maximum deviation less than 1mm. On the other hand the computed troughs for types 3 (25 May) and (29 May) have larger differences with the measured displacements but are still less than 5mm.

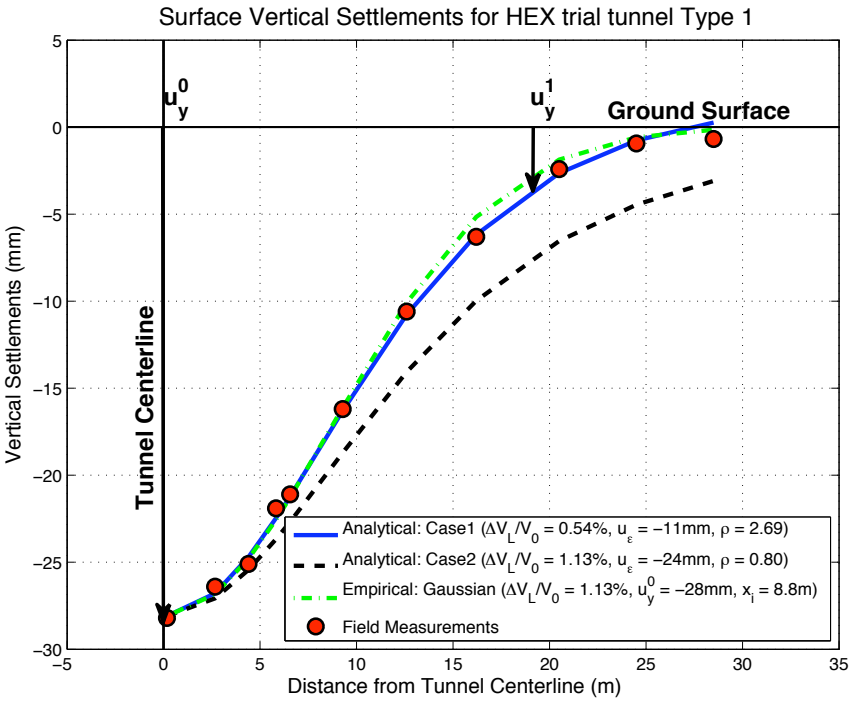

Figure 4.9: Surface Settlements for HEX Type 1 tunnel

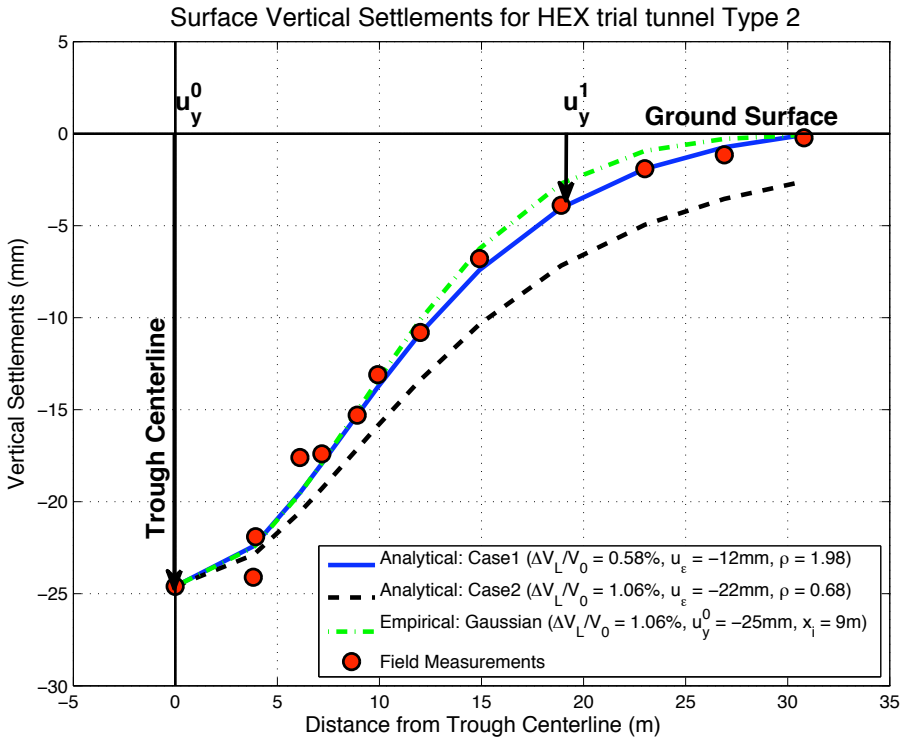

Figure 4.10: Surface Settlements for HEX Type 2 tunnel

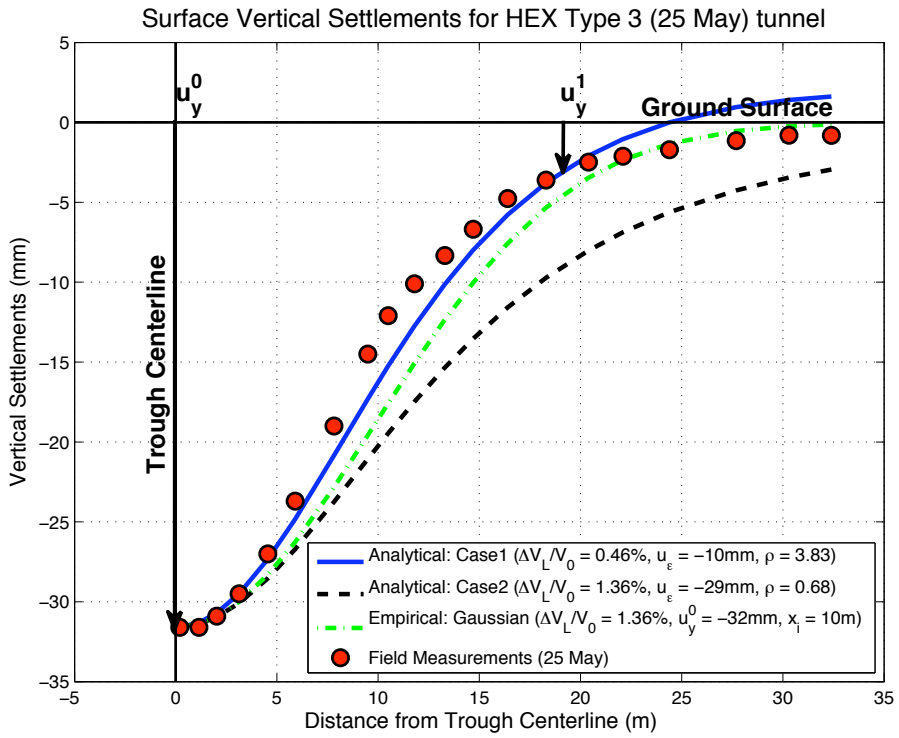

Figure 4.11: Surface Settlements about trough centreline for HEX Type 3 (25 May) tunnel

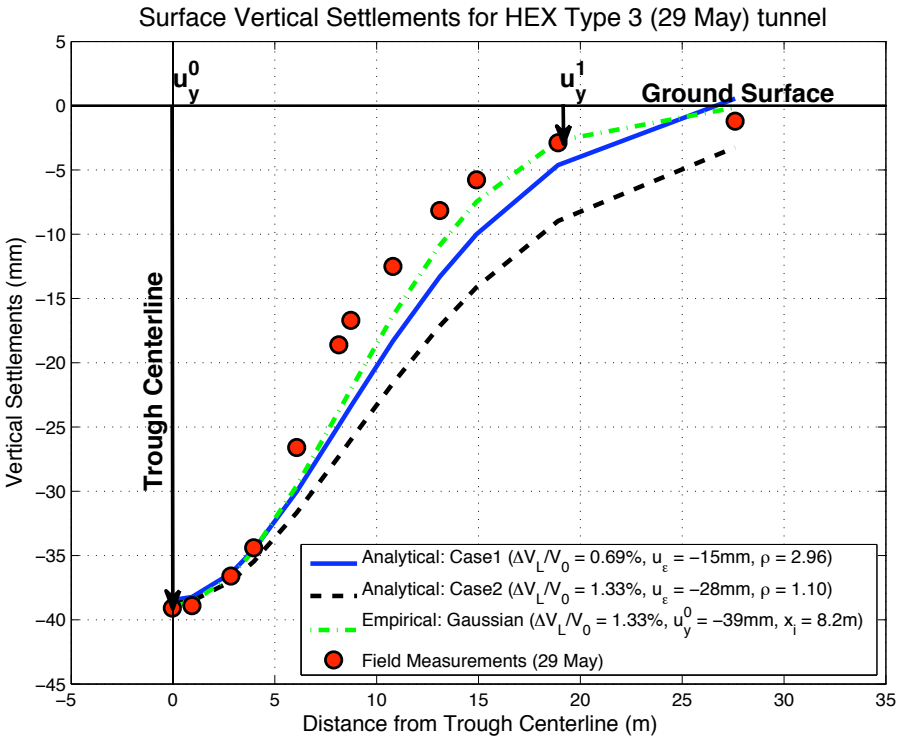

Figure 4.12: Surface Settlements about trough centreline for HEX Type 3 (29 May) tunnel

4.5.1.2 Subsurface Displacements

In this section, computed subsurface displacements for tunnel Types 2 and 3 are presented, since no subsurface measurements have been recorded for Type 1. Figures 4.13 and 4.14 summarize the computed distribution of vertical and horizontal soil movements for tunnel Type 2 using analytical Cases 1 and 2, while Figures 4.15 to 4.18 summarize the computed distribution of ground displacements for tunnel Types 3 (25 and 29 May). Note that the actual horseshoe shaped cross-section of the HEX trial tunnel is represented by a circular cross-section of equivalent diameter, for consistency, since the circular shape is what was used in the analysis. The observations discussed below apply to both tunnel Types 2 and 3. Cases 1 and 2 predict very similar vertical displacement profiles above the tunnel springline, with Case 2 generating wider settlement troughs than Case 1. Moreover, along the centreline and above the tunnel we observe that the two cases predict exactly the same displacements, while below the tunnel, Case 1 predicts larger displacements than Case 2 (especially for type 3, 29 May, Case 1 predicts vertical movements up to 5mm larger than Case 2).

Around the surface elevation, the two cases predict similar horizontal ground displacements, with Case 2 predicting slightly larger movements than Case 1. However, along the tunnel springline, Case 1 predicts significantly larger horizontal displacements than Case 2 (differences up to 20mm for the Type 3, 25 May case and up to 12.5mm for the Type 2 and Type 3, 29 May tunnels). Moreover, both analytical solutions predict movements away from the tunnel, for the soil along the tunnel

elevation (note that Case 2 predicts negligible horizontal displacements along the tunnel springline for Types 2 and 3 (25May) tunnels). Finally, below the tunnel cavity the two cases predict very small horizontal distortions, with Case 2 predicting slightly higher values.

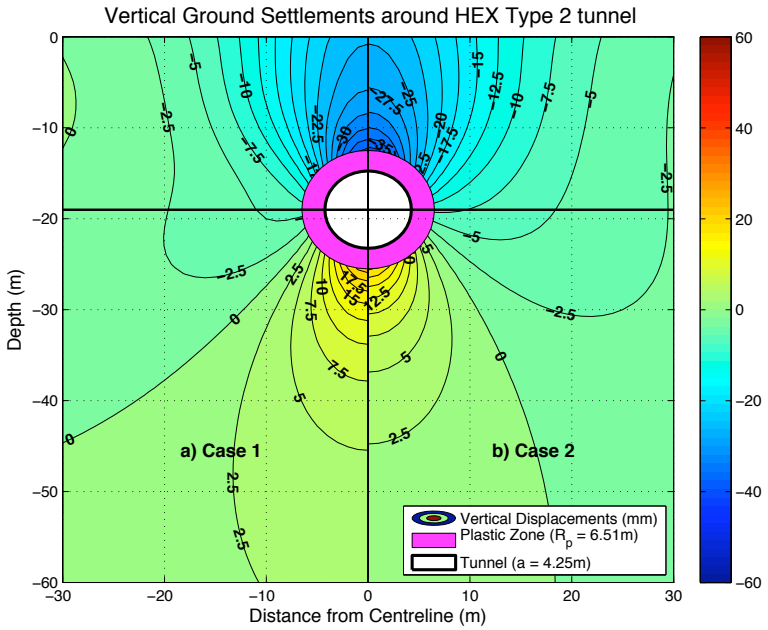

Figure 4.13: Distribution of Vertical Displacements for HEX Type 2 tunnel

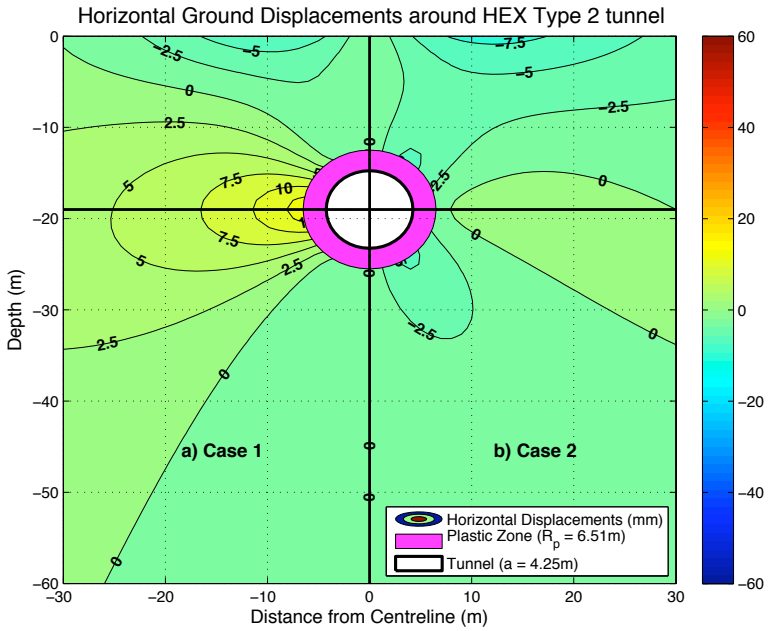

Figure 4.14: Distribution of Horizontal Displacements for HEX Type 2 tunnel

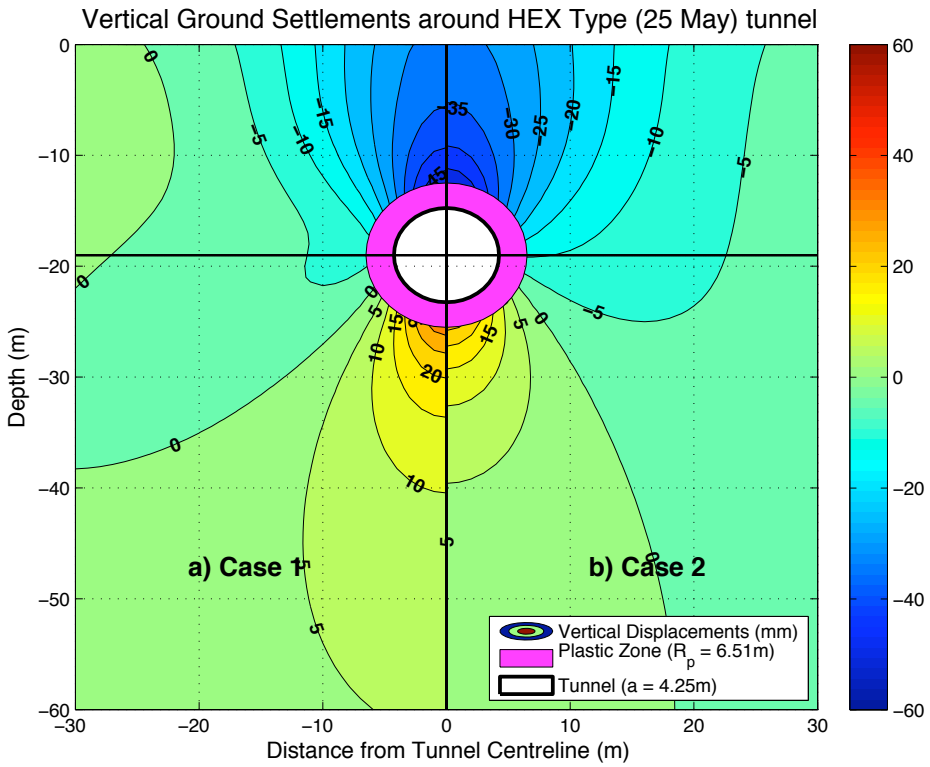

Figure 4.15: Distribution of Vertical Displacements for HEX Type 3 (25 May) tunnel

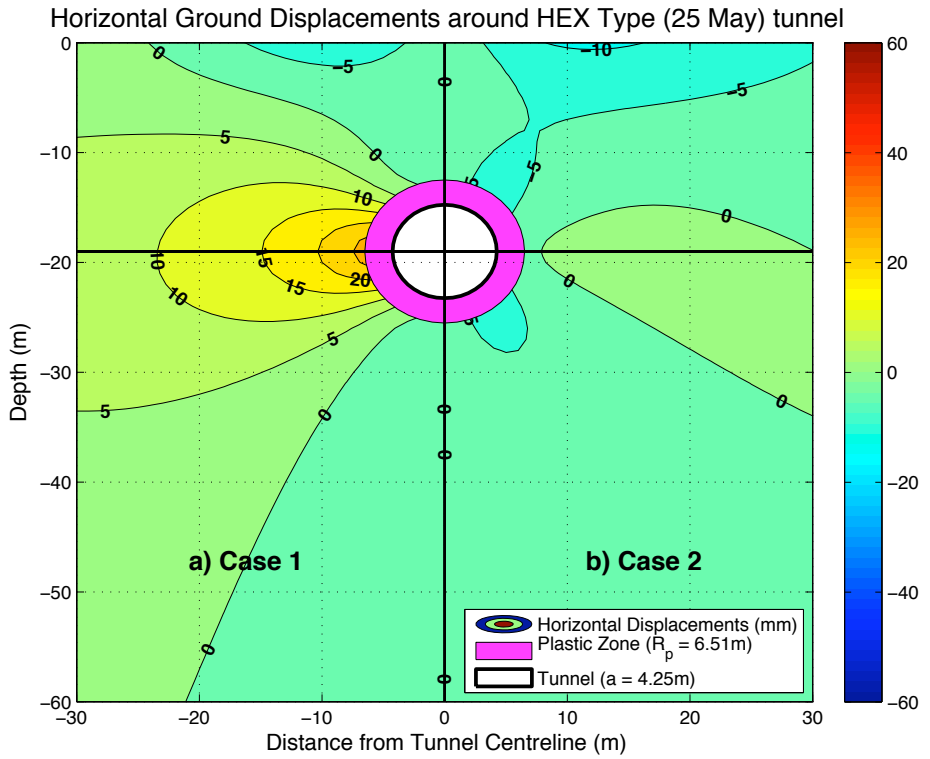

Figure 4.16: Distribution of Horizontal Displacements for HEX Type 3 (25 May) tunnel

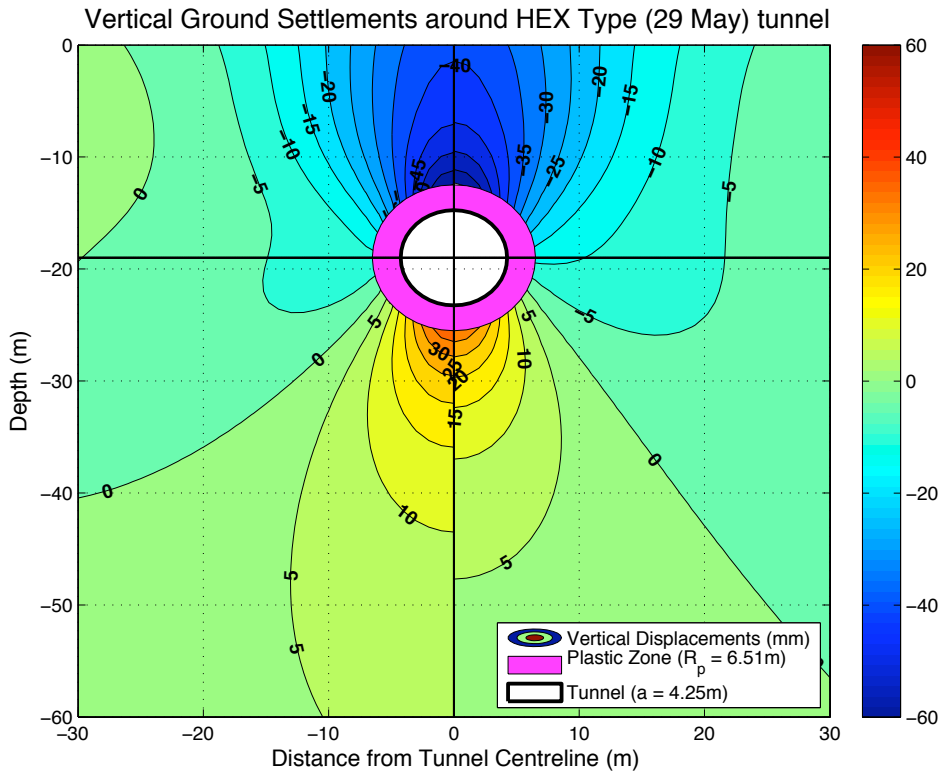

Figure 4.17: Distribution of Vertical Displacements for HEX Type 3 (29 May) tunnel

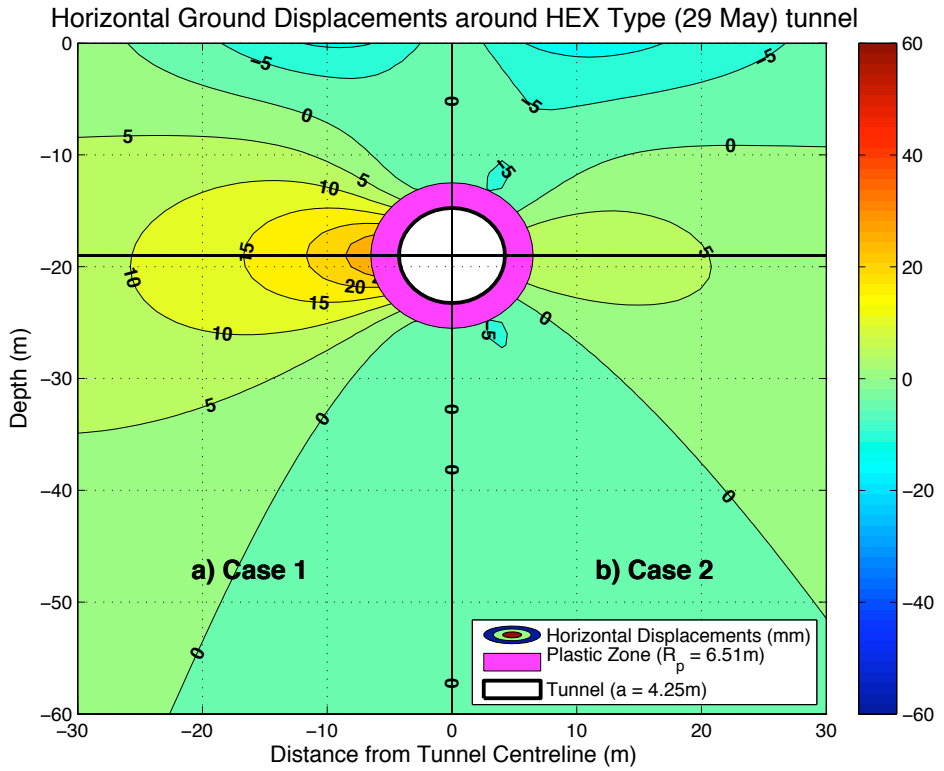

Figure 4.18: Distribution of Horizontal Displacements for HEX Type 3 (29 May) tunnel

Figures 4.19 and 4.20 compare the analytically computed and measured subsurface horizontal displacements for Type 3 (25 and 29 May) tunnels. The measurements are based on 4 arrays of inclinometers (IC1 - IC4). The results show large discrepancies between computed and measured behavior. Case 2 is in closer agreement with the field measurements than Case 1. In fact Case 2 produces very good fits to all the measured data that lie outside the zone $-25m \leq y \leq -10m$ (i.e. zone parallel to the tunnel springline). Case 1 does not generate realistic subsurface horizontal displacements for most of the soil mass apart from the shallow subsurface ($y \geq 5m$) and predicts outward movements along the tunnel springline instead of inward displacements that were recorded at the test site. Inclinometer IC3, which lies along the tunnel centerline, shows some subsurface horizontal ground movements taking place ($u_x \neq 0$ at $x = 0$) and hence there is a loss of anti-symmetry in the measured horizontal displacements (similar to the JLE tunnel case in Chapter 3).

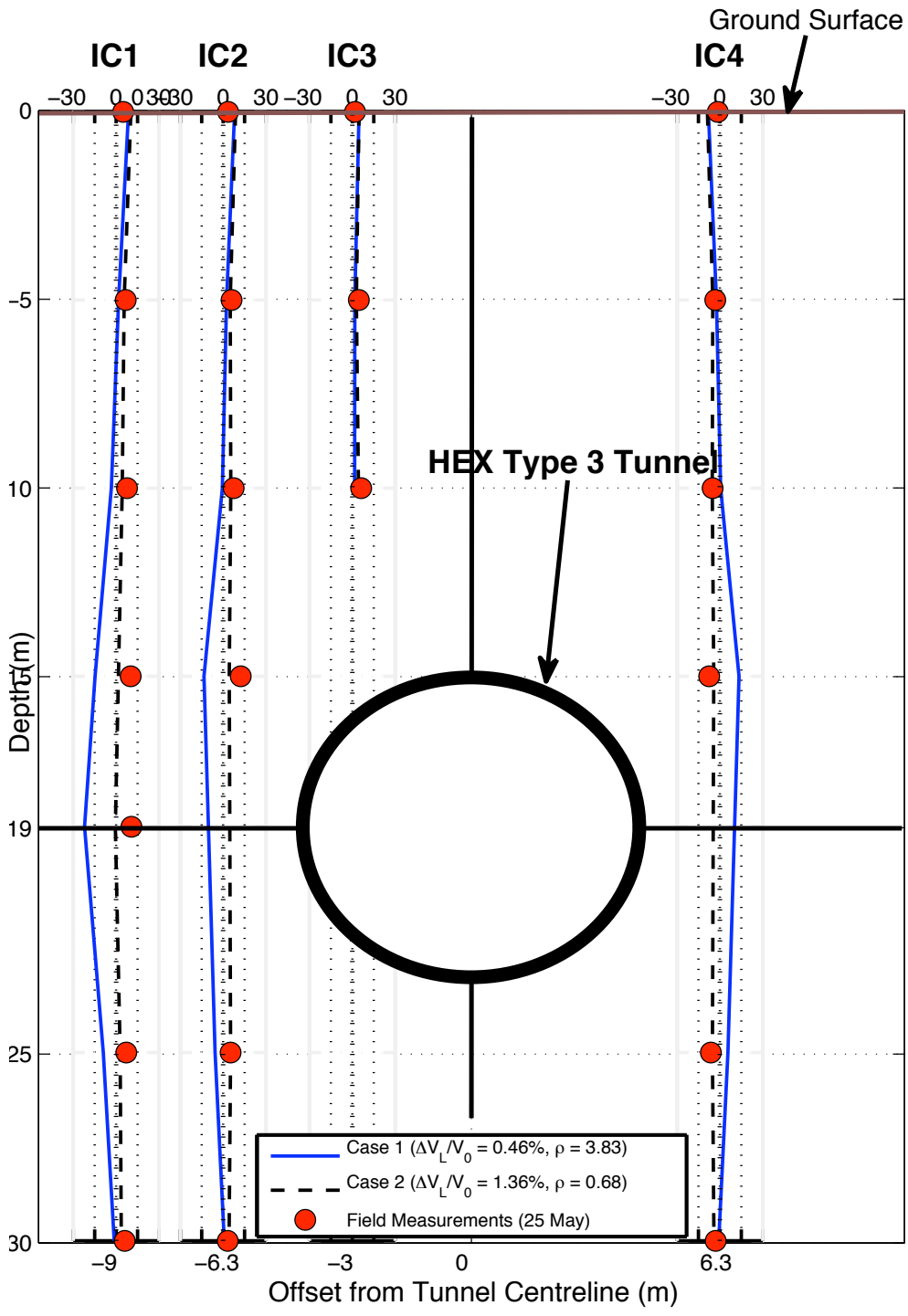

Figure 4.19: Subsurface horizontal displacements for HEX Type 3 (25 May) tunnel

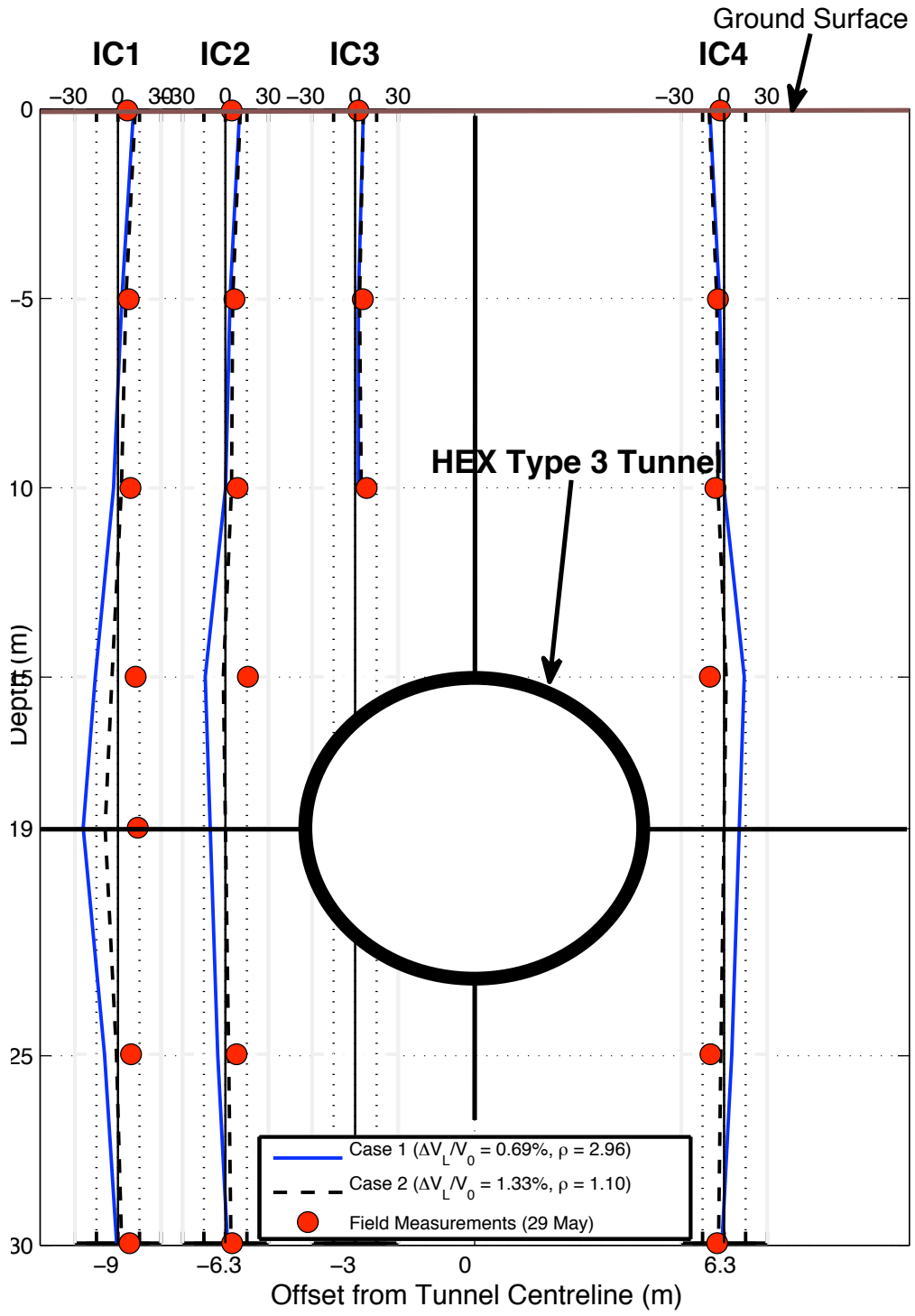

Figure 4.20: Subsurface horizontal displacements for HEX Type 3 (29 May) tunnel

Figures 4.21 and 4.22 compare the analytically computed and measured subsurface displacement vector diagrams for Types 2 and 3 (29 May) tunnels (the field measurements are extracted from the diagrams of Figure 4.7). For both tunnels, the analytical results show good agreement with the field data from the surface and up to a depth y ≈ -12m. The agreement between the computed and recorded data is also good along the tunnel centreline. However, near the tunnel springline, Case 1 deviates significantly from the field data, as it predicts outward horizontal movements instead of the recorded inward displacements. Case 2 performs better that Case 1 but still computes ground displacement vectors that deviate from the field data. The differences are larger for the Type 3 (29 May) tunnel comparing with the Type 2 tunnel.

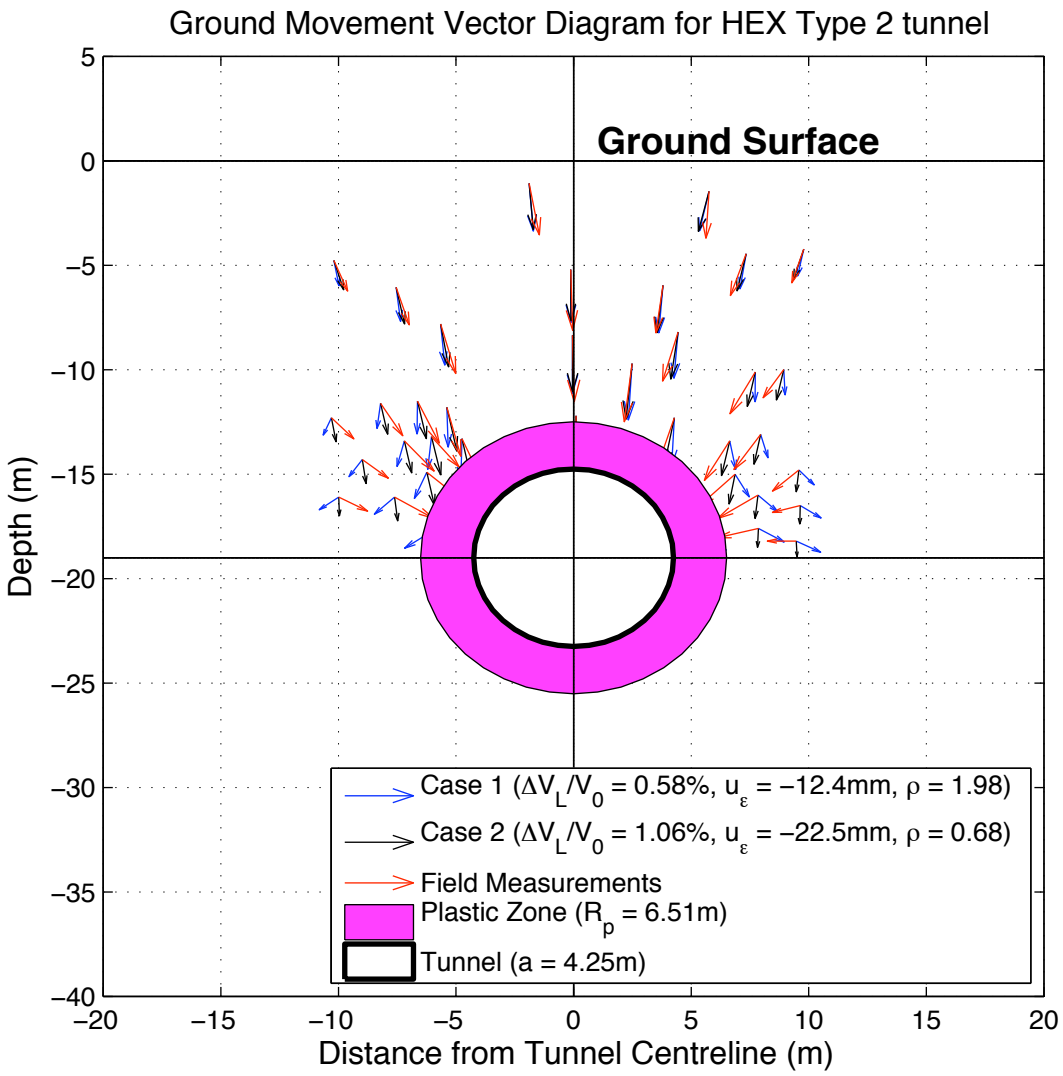

Figure 4.21: Measured and computed subsurface ground movement vector diagrams for HEX Type 2 tunnel

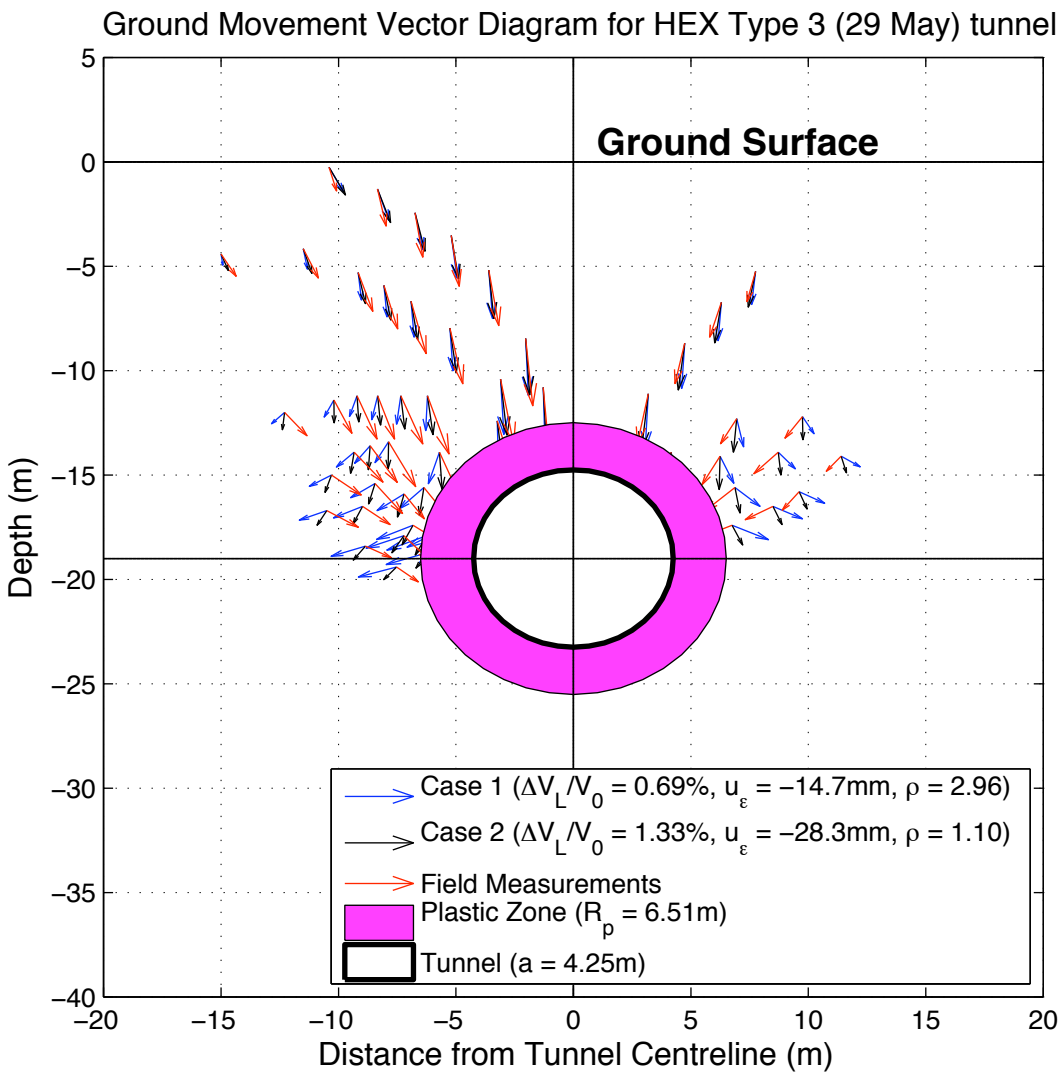

Figure 4.22: Measured and computed subsurface ground movement vector diagrams for HEX Type 3 (29 May) tunnel

4.5.1.3 Evaluation of effectiveness of isotropic analytical solutions

In order to evaluate the effectiveness of the two analyses in describing the measured surface settlements and subsurface horizontal movements on the reference grid

(Figure 4.8) and the vector diagrams (Figure 4.7), induced by the HEX Types 2 and 3 (25 and 29 May) tunnels, a least squares error method has been employed. Contour plots of the Square Solutions (SS) have been prepared covering the full range of the state space (u_ε, u_δ). Assuming that all analyses will fit the centreline settlement u_y^0, a line has been added to the figures corresponding to the (u_ε, u_δ) sets that fit u_y^0. In our analysis we consider two optimum solutions (i.e. two parameter sets that produce the minimum SS error): a global Least Squares Solution (LSS) that corresponds to the overall minimum SS, and a surface LSS that corresponds to the minimum SS along the surface settlement line (i.e. fits u_y^0). Figures 4.23 to 4.25 show the state space SS for vertical, horizontal and total displacements and Table 4.3 summarizes the results of the LSS error method for the Type 2 tunnel. The LSS surface and LSS global solutions for the settlements are closer to Case 1 and thus Case 1 is a better fit to the measured vertical movements than Case 2. The fact that the analytical solutions do not successfully predict horizontal displacements near the tunnel (Figure 4.21) caused a large difference between the LSS surface solution for horizontal displacements and the two cases. In fact, Cases 1 and 2 generate large SS errors for horizontal displacements ($SS_{1,x}$ = 9948 mm^2 and $SS_{2,x}$ = 2358 mm^2, see Table 4.4), while the corresponding LSS surface solution for horizontal displacements is LSS_x = 280. Case 2 still lies closer to the LSS surface solution for total displacements and therefore provides a better match to the measured data. However, the LSS error method suggests that the optimum solution that at the same time fits the surface centreline settlement u_y^0 (i.e. the LSS surface solution for total errors) has parameters:

$(u_\varepsilon, u_\delta)$ = (-28, 10) mm ➔$\Delta V_L/V_0$ = 1.32%, ρ = 0.36.

	Surface Solution			Global Solution		
	u_ε (mm)	u_δ (mm)	LSS (mm^2)	u_ε (mm)	u_δ (mm)	LSS (mm^2)
Vertical	-9	28	685	-14	17	403
Horizontal	-31	8	280	-23	0	240
Total	-28	10	2904	-24	3	1087
	Analytical Case 1 (u_ε=-12.4mm, u_δ=24.6mm)			Analytical Case 2 (u_ε=-22.5mm, u_δ=15.4mm)		
	SS_1 (mm^2)			SS_2 (mm^2)		
Vertical	747			1534		
Horizontal	9948			2358		
Total	10700			3891		

Table 4.3: Summary of LSS error method results for HEX Type 2 tunnel

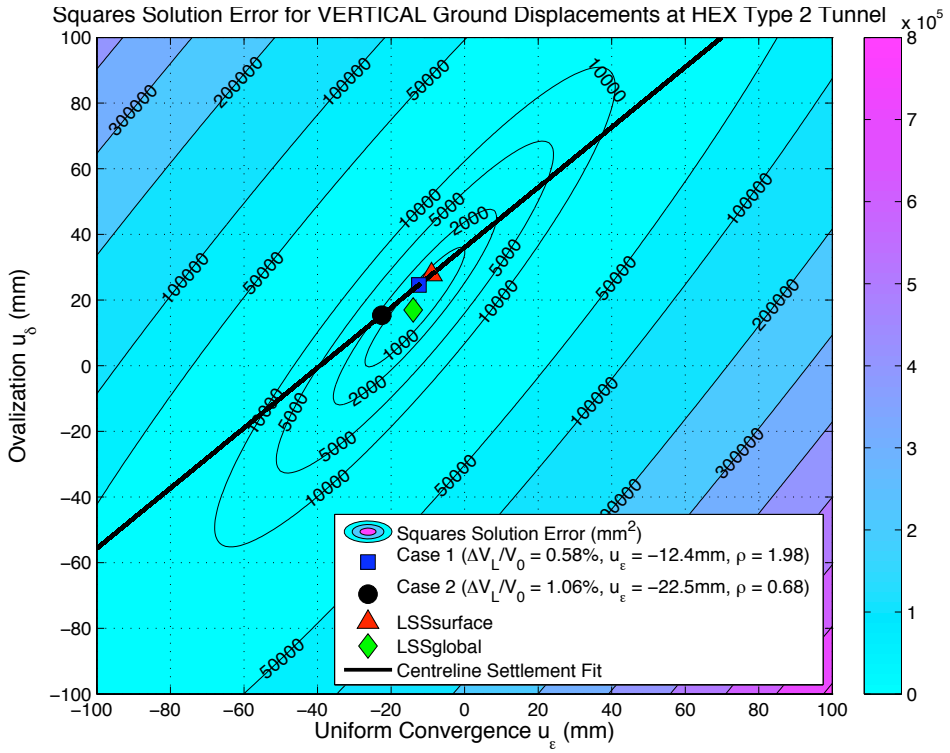

Figure 4.23: SS error for vertical displacements induced by Type 2 tunnel

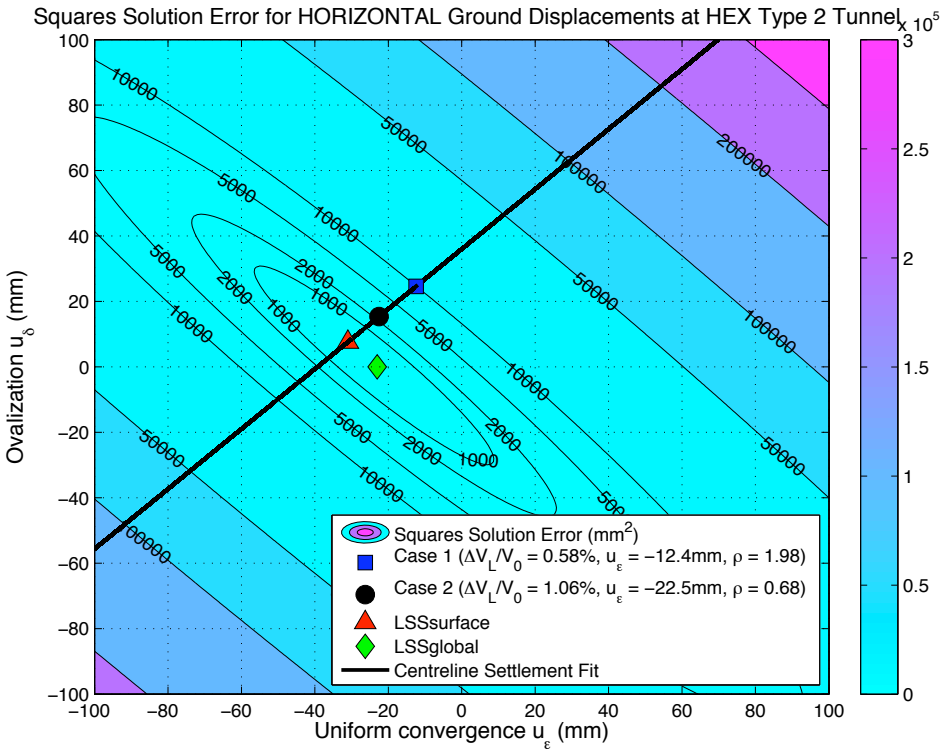

Figure 4.24: SS error for horizontal displacements induced by Type 2 tunnel

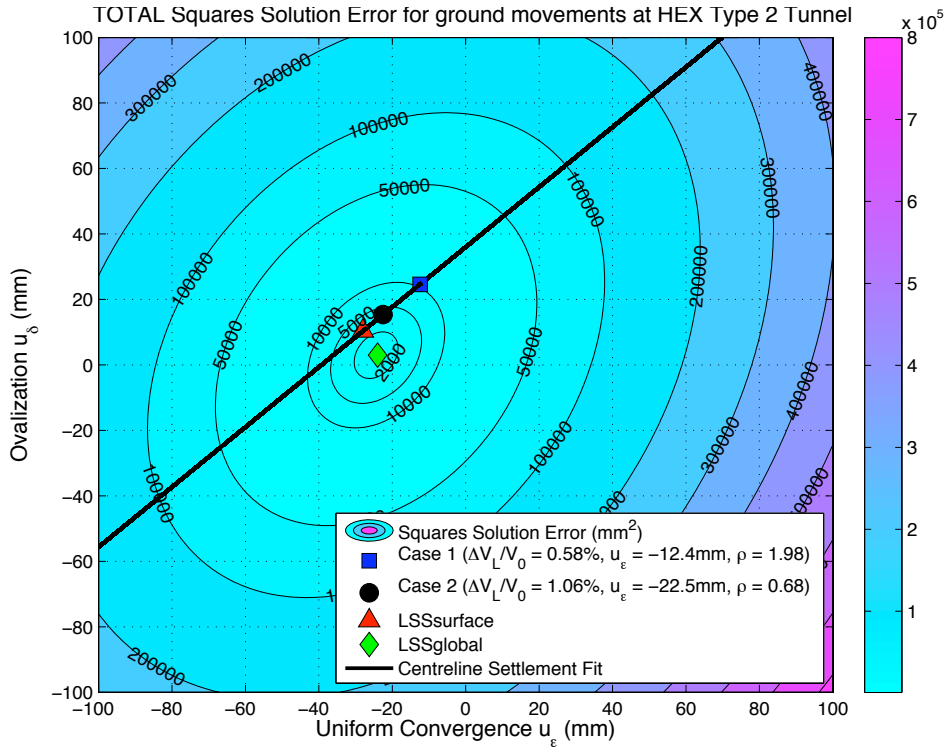

Figure 4.25: SS error for total displacements induced by Type 2 tunnel

Figures 4.26 to 4.28 show the state space SS for vertical, horizontal and total displacements and Table 4.4 summarizes the results of the LSS error method for the Type 3 (25 May) tunnel. The LSS surface and LSS global solutions for the settlements coincide with Case 1 and thus Case 1 is a better fit to the measured data than Case 2. The lack of anti-symmetry in measured horizontal displacements caused a difference in the surface and global LSS solutions. Case 2 lies closer to the LSS surface solution for horizontal displacements and therefore provides a better match to the measured inclinometer data.

In fact Case 1 generates a very large SS error in the horizontal displacements ($SS_{1,x}$ = 3763 mm^2 while $SS_{2,x}$ = 449 mm^2, see Table 4.4), which can be explained by the large discrepancies observed in Figure 4.19. Finally, Figure 4.28 suggests that Case 2 overall performs better than Case 1, since it nearly coincides with the LSS surface solution for total displacements.

	Surface Solution			Global Solution		
	u_ε (mm)	u_δ (mm)	LSS (mm^2)	u_ε (mm)	u_δ (mm)	LSS (mm^2)
Vertical	-9	38	54.2	-10	35	47.3
Horizontal	-36	13.2	216.5	-23	0	71.7
Total	-31	17.8	868.3	-28	12	621.1
	Analytical Case 1 (u_ε=-9.7mm, u_δ=37.3mm)			Analytical Case 2 (u_ε=-28.9mm, u_δ=19.8mm)		
	SS_1 (mm^2)			SS_2 (mm^2)		
Vertical	55			455		
Horizontal	3763			449		
Total	3818			905		

Table 4.4: Summary of LSS error method results for HEX Type 3 (25 May) tunnel

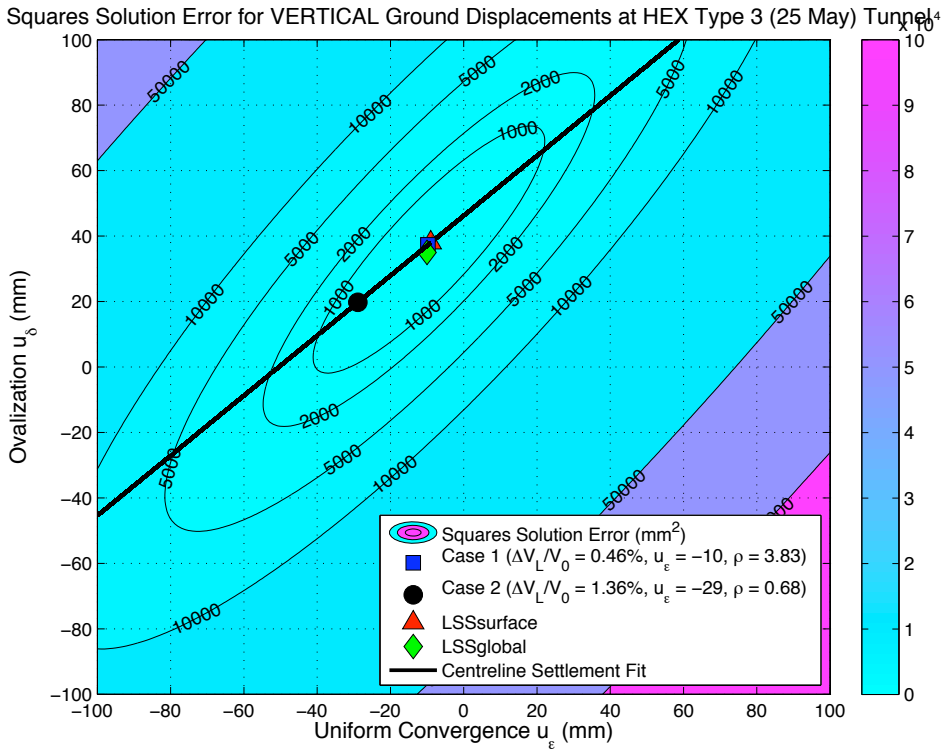

Figure 4.26: SS error for vertical displacements induced by Type 3 (25 May) tunnel

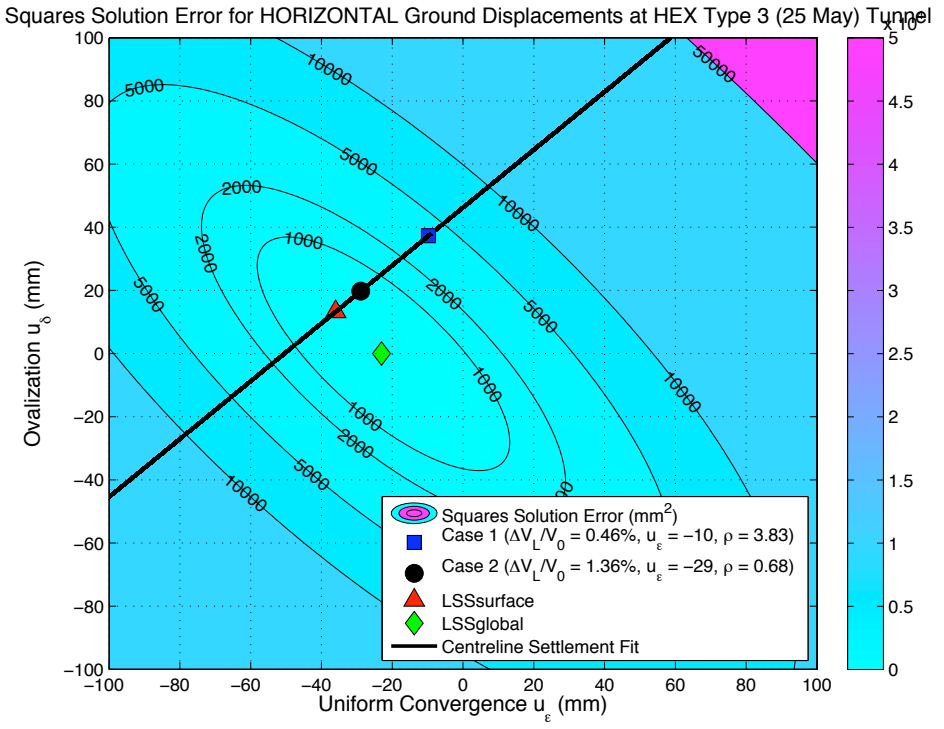

Figure 4.27: SS error for horizontal displacements induced by Type3(25 May) tunnel

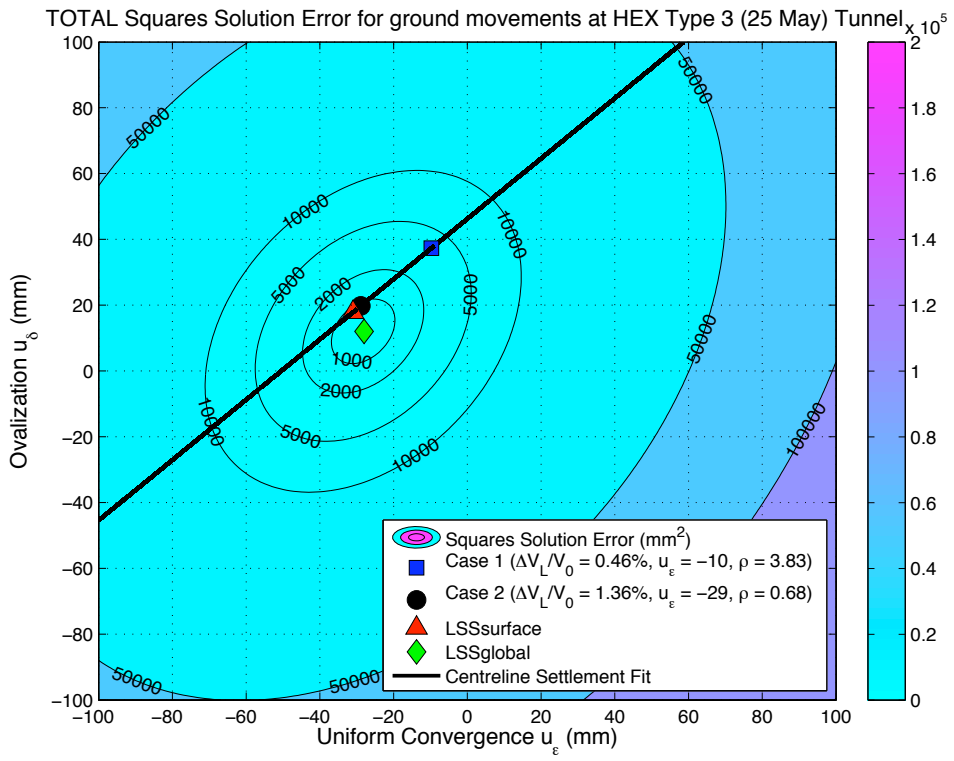

Figure 4.28: SS error for total displacements induced by Type 3 (25 May) tunnel

Figures 4.29 to 4.31 show the state space SS for vertical, horizontal and total displacements and Table 4.5 summarizes the results of the LSS error method for the Type 3 (29 May) tunnel. Figure 4.29 shows that the LSS surface solution for vertical displacements coincides with Case 1 and therefore appears to be a better fit to the data than Case 2. Both cases differ significantly from the LSS surface solution for horizontal displacements and this is due to the large discrepancies observed in Figures 4.20 and 4.22. Analytical Cases 1 and 2 produce very large SS errors for horizontal displacements ($SS_{1,x}$= 54600 mm^2 and $SS_{2,x}$ = 13150 mm^2, see Table 4.5), comparing with the LSS error for horizontal displacements (LSSx,surf = 1004 mm^2). Finally, Figure 4.31 suggests that Case 2 overall performs better than Case 1, since it is closer to the LSS surface solution for total displacements. However, the LSS error

method suggests that the optimum solution that at the same time fits the surface centreline settlement u_y^0 (i.e. the LSS surface solution for total errors) has parameters: $(u_\varepsilon, u_\delta)$ = (-42, 18.4) mm ➔$\Delta V_L/V_0$ = 1.98%, ρ = 0.44.

	Surface Solution			Global Solution		
	u_ε (mm)	u_δ (mm)	LSS (mm²)	u_ε (mm)	u_δ (mm)	LSS (mm²)
Vertical	-15	43.2	3639	-25	21	2081
Horizontal	-45	16	1004	-30	1	541
Total	-42	18	9251	-34	7	3120
	Analytical Case 1 (u_ε=-14.7mm, u_δ=43.5mm)			Analytical Case 2 (u_ε=-28.3mm, u_δ=31.0mm)		
	SS_1 (mm²)			SS_2 (mm²)		
Vertical	3832			4702		
Horizontal	54600			13150		
Total	58430			17850		

Table 4.5: Summary of LSS error method results for HEX Type 3 (29 May) tunnel

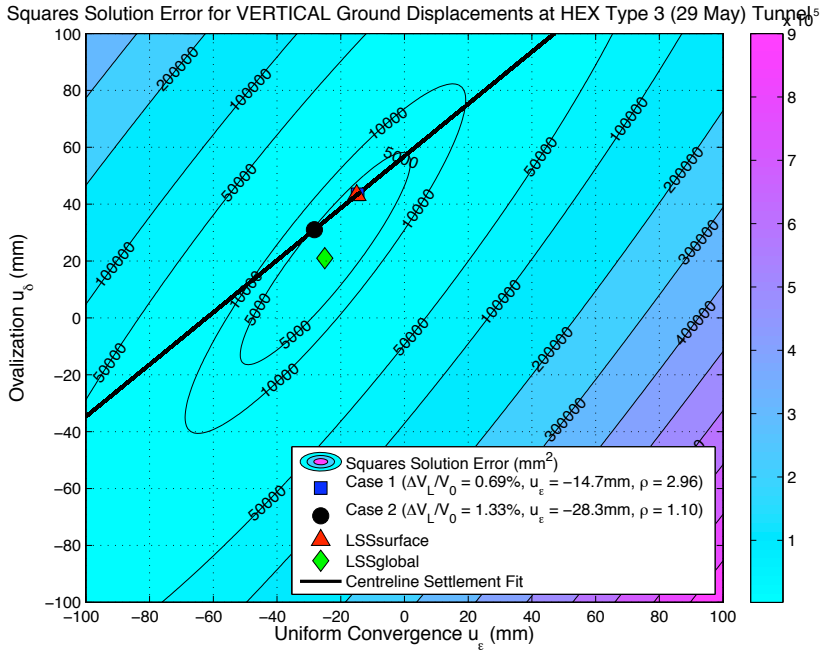

Figure 4.29: SS error for vertical displacements induced by Type 3 (29 May) tunnel

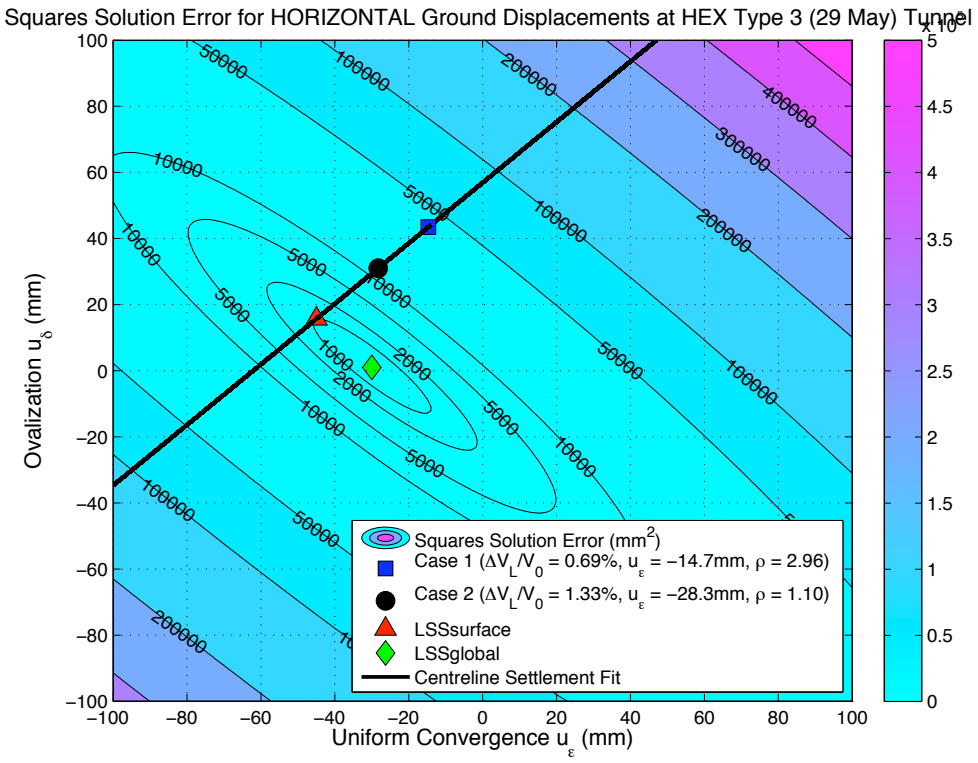

Figure 4.30: SS error for horizontal displacements induced by Type3(29 May) tunnel

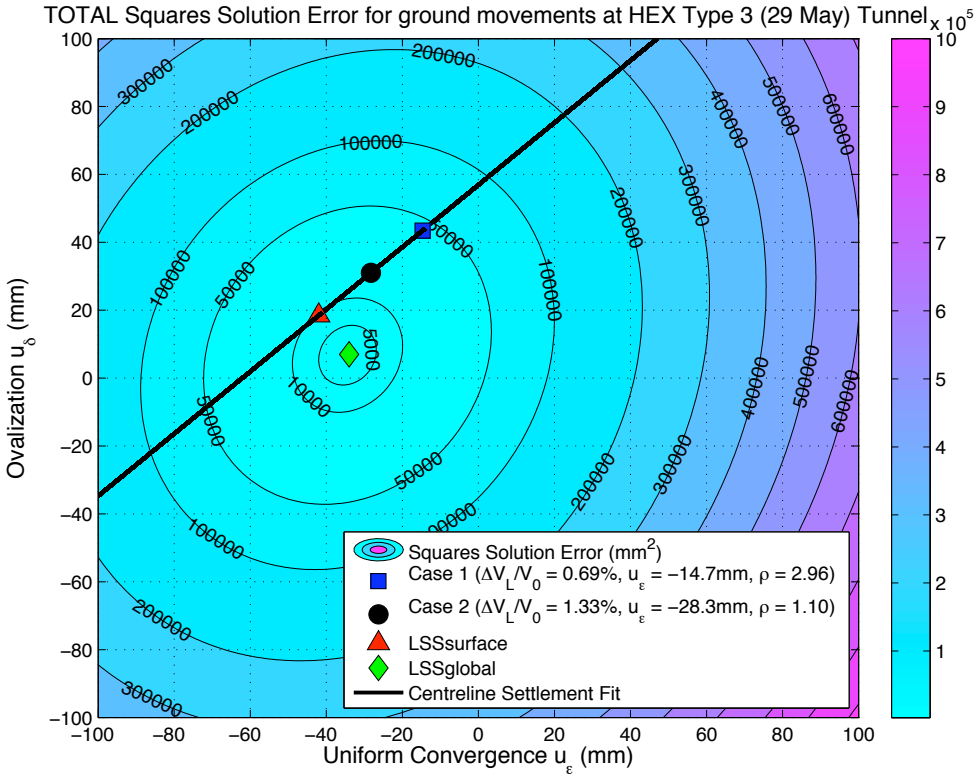

Figure 4.31: SS error for total displacements induced by Type3 (29 May) tunnel

4.6 Analytical Solutions with anisotropic stiffness

This section presents further analytical solutions of ground deformations around the HEX trial tunnel, Types 2 and 3, incorporating cross-anisotropic stiffness parameters. The analyses are based on the solutions presented by Chatzigiannelis and Whittle (2000) while stiffness parameters are based on lab test data from Heathrow T5 reported by Gasparre et al (2007) (see Table 3.10). The LSS error method was used in order to optimize the cavity parameters (u_ε, u_δ). Contour plots of the SS error for vertical, horizontal and total ground displacements were produced for the two tunnel types for cross-anisotropic stiffness parameters corresponding to four different strain levels (ε_α < 0.001%, ε_α = 0.01%, ε_α = 0.03% and ε_α = 0.1%) and the results of this procedure (i.e. the LSS surface solutions) are summarized in Tables 4.6 to 4.8.

	ε_α < 0.001%			**ε_α = 0.01%**		
	u_ε (mm)	u_δ (mm)	LSS (mm²)	u_ε (mm)	u_δ (mm)	LSS (mm²)
Vertical	-14	17	424	-12	21	459
Horizontal	-24	3	302	-24	3	263
Total	-24	3	1010	-24	3	1226
	ε_α = 0.03%			**ε_α = 0.1%**		
	u_ε (mm)	u_δ (mm)	LSS (mm²)	u_ε (mm)	u_δ (mm)	LSS (mm²)
Vertical	-8	29	574	-8	30	634
Horizontal	-24	3	222	-24	2	220
Total	-23	5	1874	-22	6	2213

Table 4.6: LSS surface solutions for 4 cross-anisotropic stiffness parameter sets for HEX Type 2 tunnel

	$\varepsilon_\alpha < 0.001\%$			$\varepsilon_\alpha = 0.01\%$		
	u_ε (mm)	u_δ (mm)	LSS (mm²)	u_ε (mm)	u_δ (mm)	LSS (mm²)
Vertical	-10	34	8	-9	37	13
Horizontal	-29	6	154	-28	8	152
Total	-26	11	498	-26	11	637
	$\varepsilon_\alpha = 0.03\%$			$\varepsilon_\alpha = 0.1\%$		
	u_ε (mm)	u_δ (mm)	LSS (mm²)	u_ε (mm)	u_δ (mm)	LSS (mm²)
Vertical	-6	44	39.6	-6	46	56
Horizontal	-28	9	172	-27	9	192
Total	-24	15	992	-23	16.2	1181

Table 4.7: LSS surface solutions for 4 cross-anisotropic stiffness parameter sets for HEX Type 3 (25 May) tunnel

	$\varepsilon_\alpha < 0.001\%$			$\varepsilon_\alpha = 0.01\%$		
	u_ε (mm)	u_δ (mm)	LSS (mm²)	u_ε (mm)	u_δ (mm)	LSS (mm²)
Vertical	-21	29	2292	-18	35	2490
Horizontal	-35	9	831	-35	9	199
Total	-34	10	3760	-30	17	3586
	$\varepsilon_\alpha = 0.03\%$			$\varepsilon_\alpha = 0.1\%$		
	u_ε (mm)	u_δ (mm)	LSS (mm²)	u_ε (mm)	u_δ (mm)	LSS (mm²)
Vertical	-13	45	2977	-12	48	3194
Horizontal	-35	10	227	-34	10	256
Total	-27	23	5037	-25	26	5694

Table 4.8: LSS surface solutions for 4 cross-anisotropic stiffness parameter sets for HEX Type 3 (29 May) tunnel

We conclude that the minimum LSS error is generated by the parameter set corresponding to the nearly elastic behavior of London Clay ($\varepsilon_\alpha < 0.001\%$) for tunnel Types 2 and 3 (25 May) while the strain level that generated the minimum LSS error for Type 3 (29 May) is $\varepsilon_\alpha = 0.01\%$. Figures 4.32 to 4.40 show the contour plots of the SS error for horizontal, vertical and total ground displacements corresponding to $\varepsilon_\alpha < 0.001\%$ for tunnel Types 2 and 3 (25 May) and also corresponding to $\varepsilon_\alpha = 0.01\%$ for Type 3 (29 May) tunnel. From Figure 4.34 we select the values of $(u_\varepsilon, u_\delta)$ that correspond to the LSS surface solution total displacements induced by the HEX Type 2 tunnel and which will be used in the anisotropic model:

Type 2: $(u_\varepsilon, u_\delta) = (-24, 3)$ mm ➔ $\Delta V_L/V_0 = 1.13\%$, $\rho = 0.12$

Similarly, from Figures 4.37 and 4.40 we select the values of $(u_\varepsilon, u_\delta)$ that correspond to the LSS surface solution for total displacements induced by the HEX Type 3 (25 and 29 May) tunnel and which will be used in the anisotropic model:

Type 3 (25 May): $(u_\varepsilon, u_\delta) = (-26, 11)$ mm ➔ $\Delta V_L/V_0 = 1.22\%$, $\rho = 0.41$

Type 3 (29 May): $(u_\varepsilon, u_\delta) = (-30, 17)$ mm ➔ $\Delta V_L/V_0 = 1.41\%$, $\rho = 0.57$

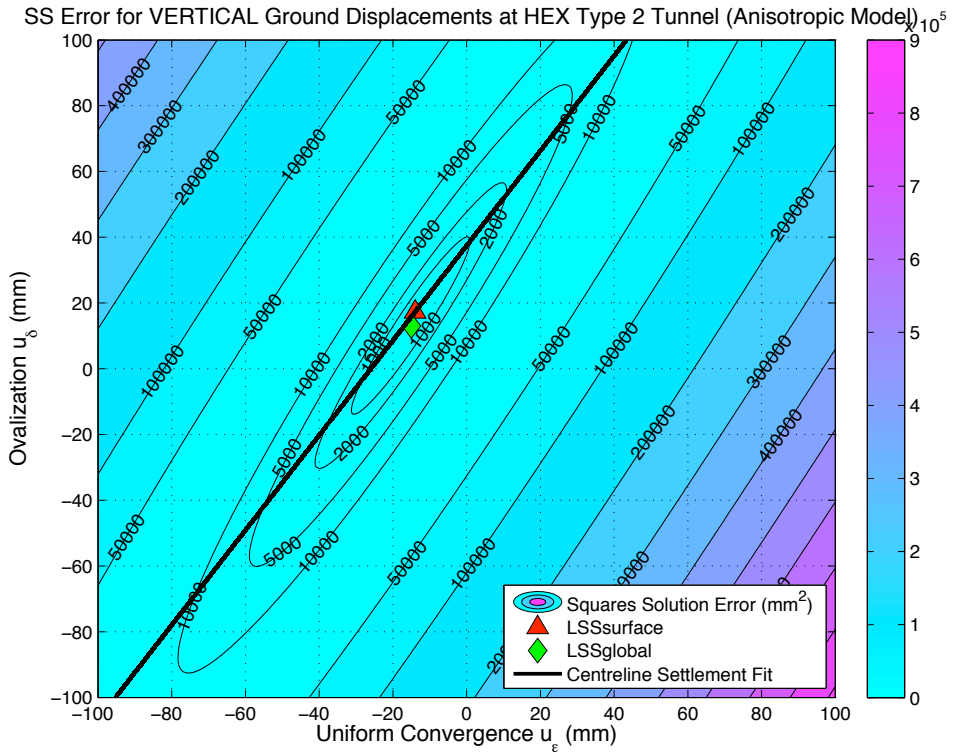

Figure 4.32: SS error for vertical displacements for HEX Type 2 tunnel using anisotropic analytical solutions

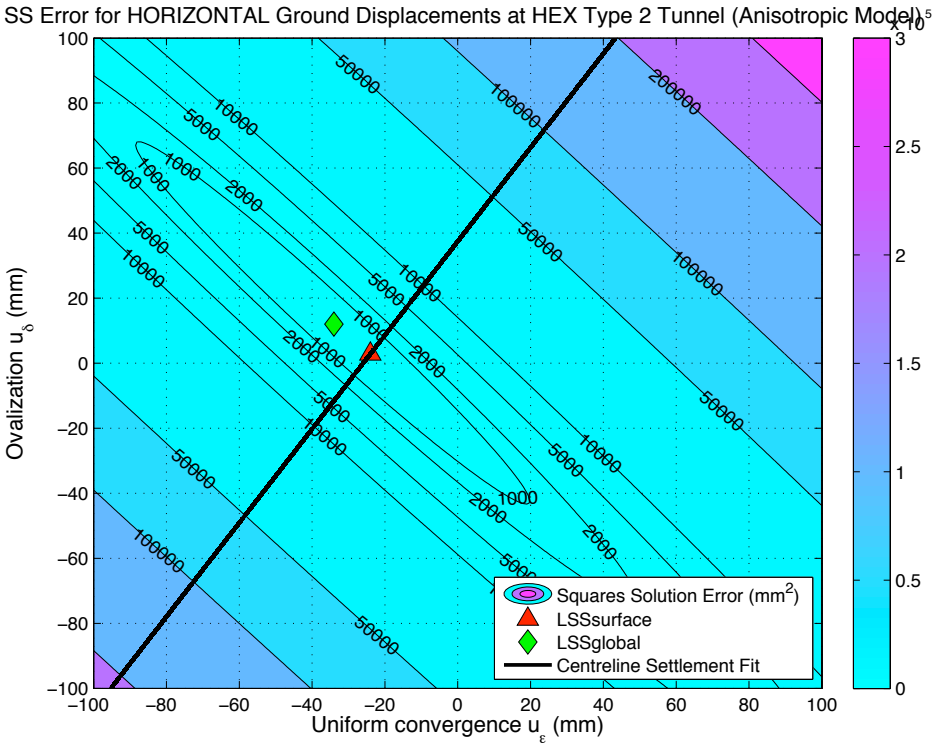

Figure 4.33: SS error for horizontal displacements for HEX Type 2 tunnel using anisotropic analytical solutions

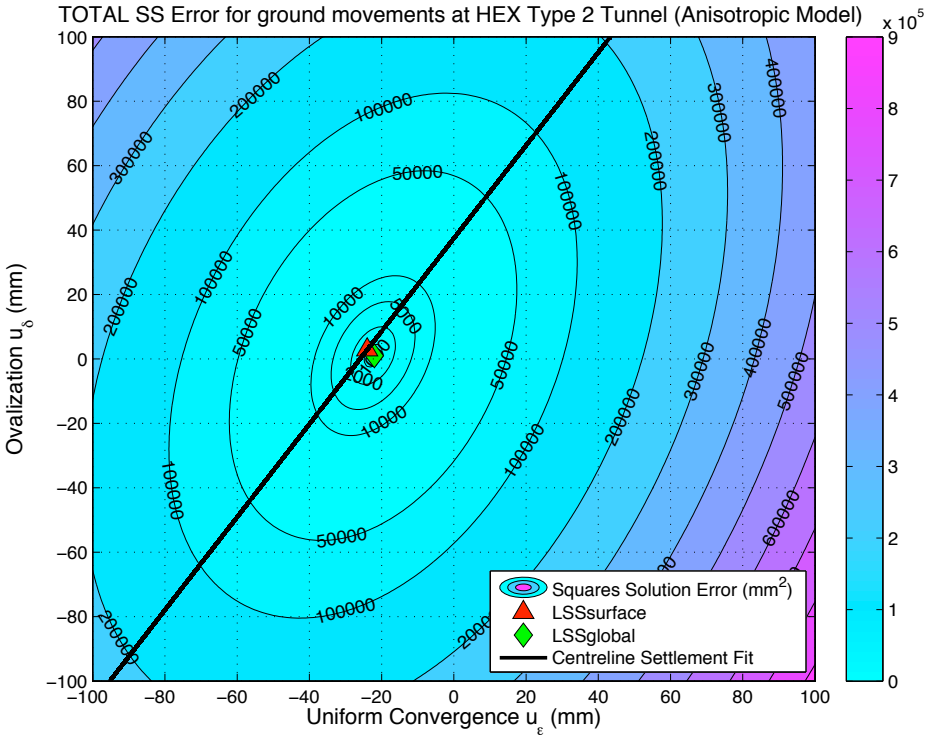

Figure 4.34: SS error for total displacements for HEX Type 2 tunnel using anisotropic analytical solutions

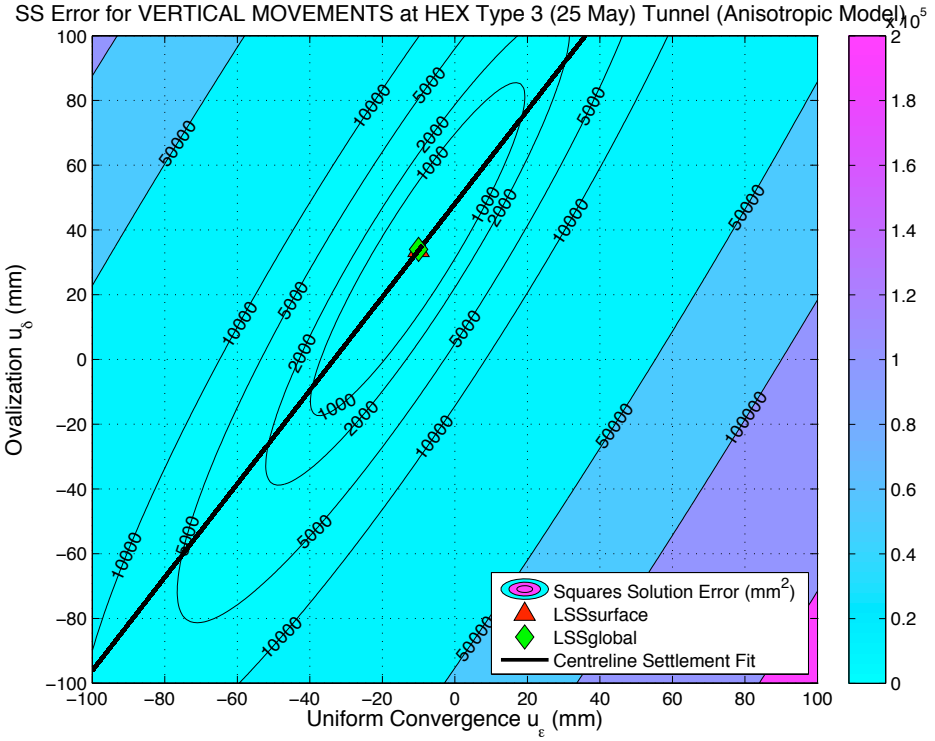

Figure 4.35: SS error for vertical displacements for HEX Type 3 (25 May) tunnel using anisotropic analytical solutions

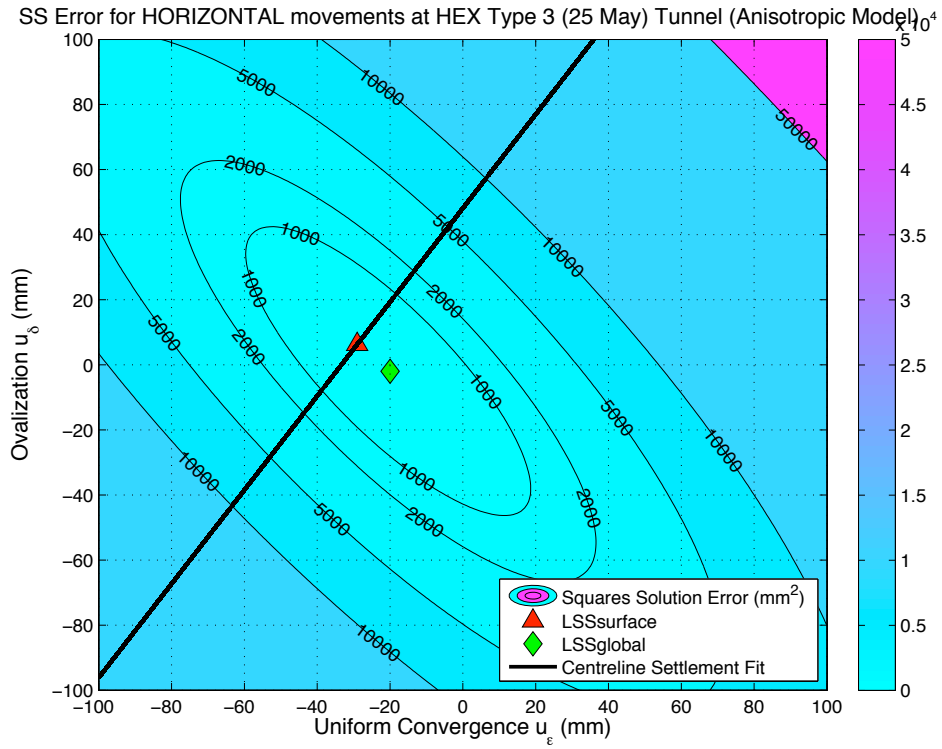

Figure 4.36: SS error for horizontal displacements for HEX Type 3 (25 May) tunnel using anisotropic analytical solutions

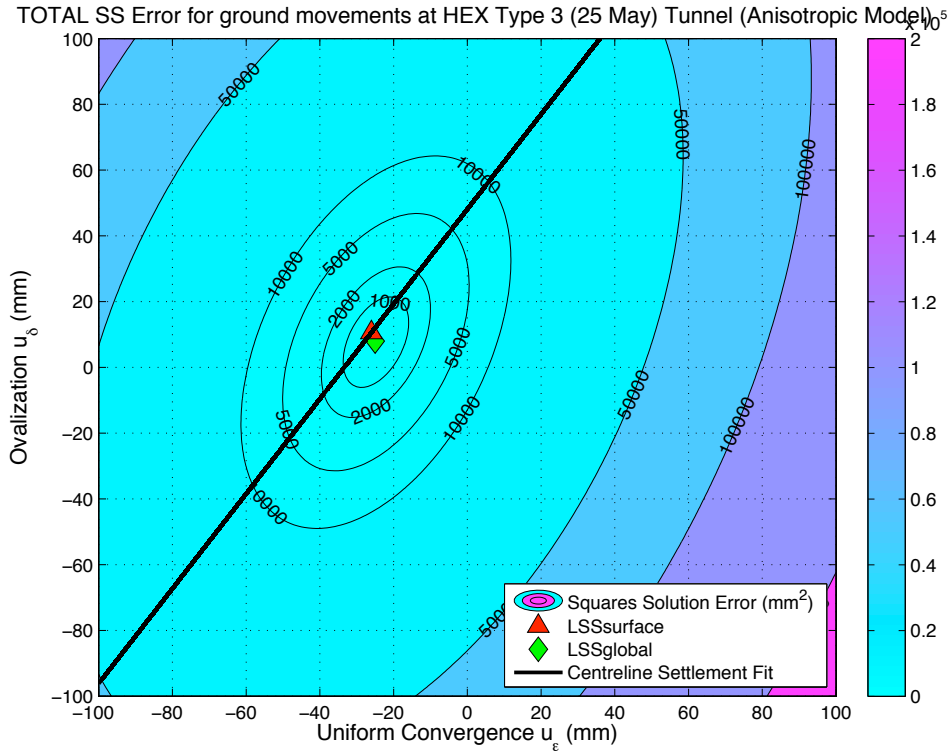

Figure 4.37: SS error for total displacements for HEX Type 3 (25 May) tunnel using anisotropic analytical solutions

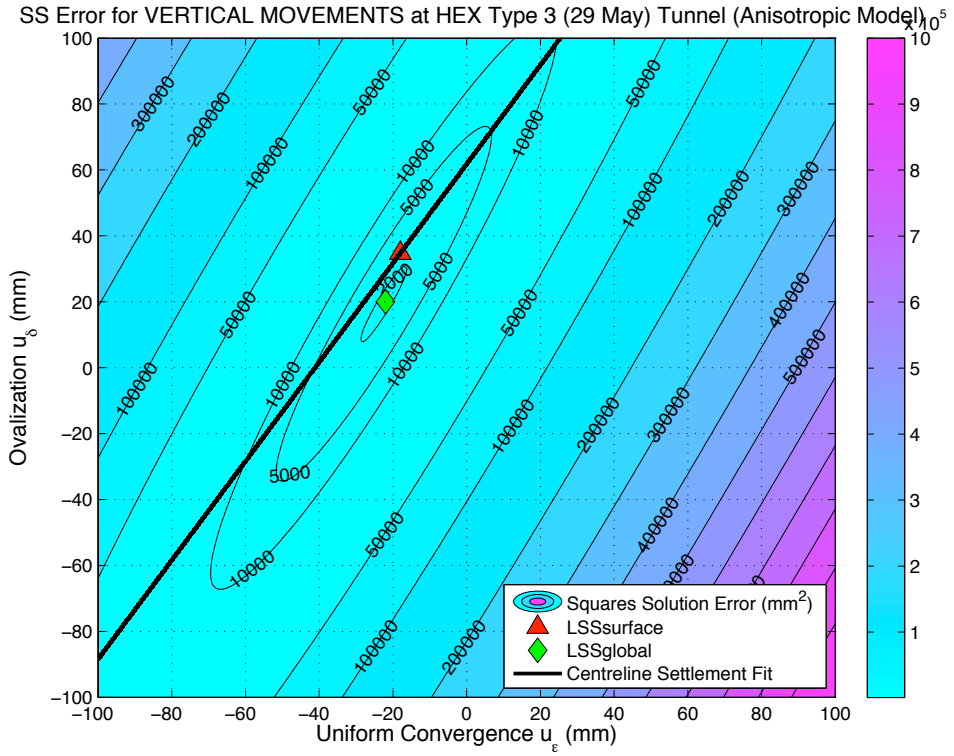

Figure 4.38: SS error for vertical displacements for HEX Type 3 (29 May) tunnel using anisotropic analytical solutions

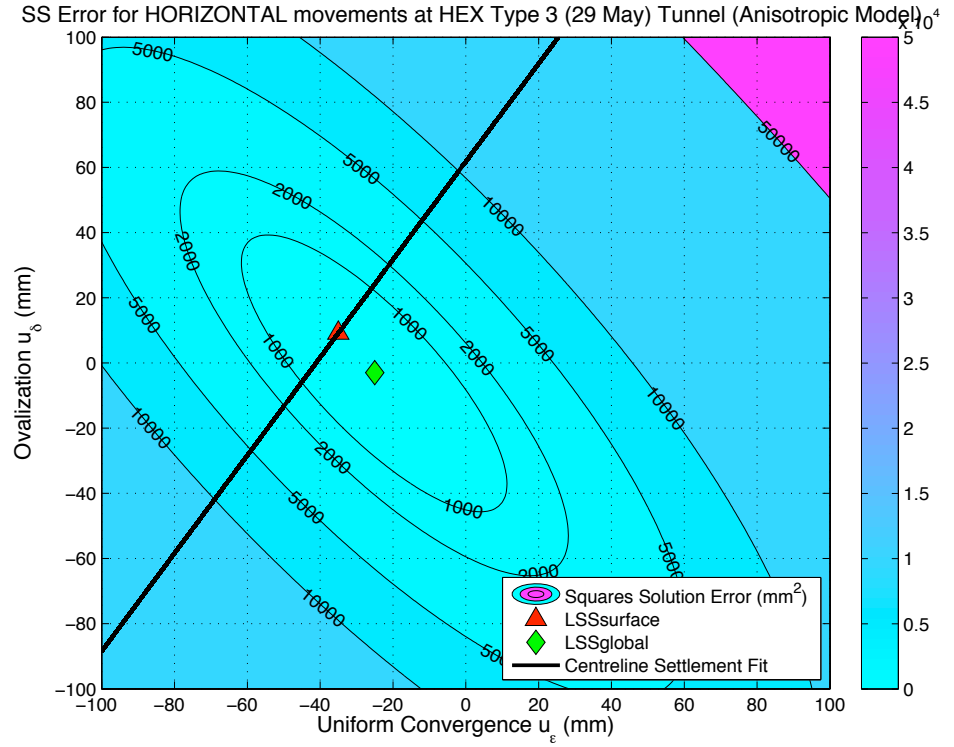

Figure 4.39: SS error for horizontal displacements for HEX Type 3 (29 May) tunnel using anisotropic analytical solutions

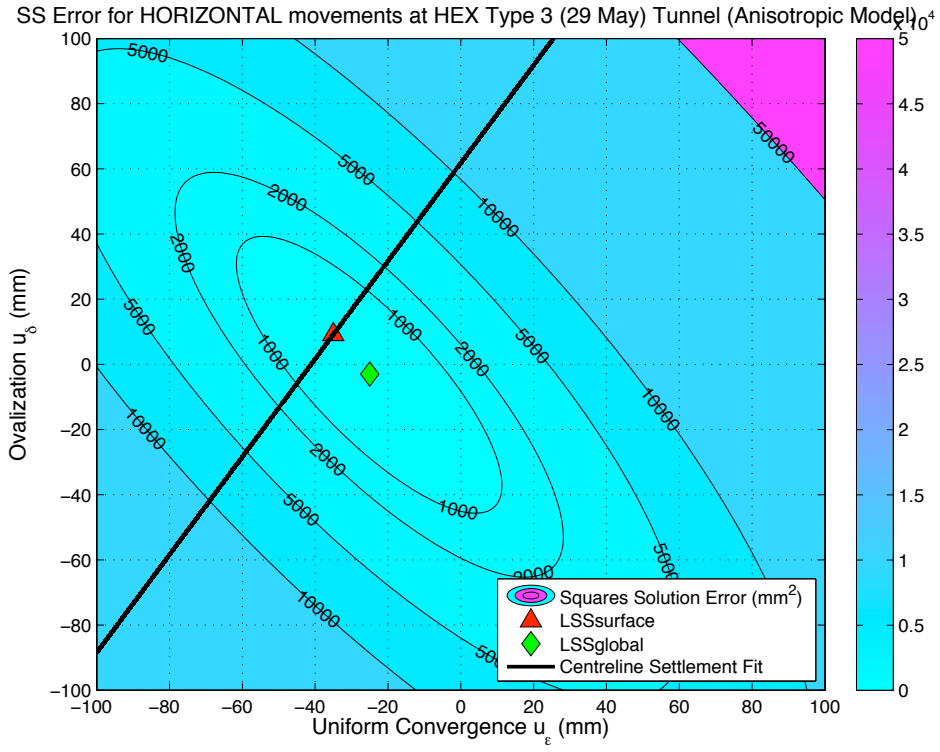

Figure 4.40: SS error for total displacements for HEX Type 3 (29 May) tunnel using anisotropic analytical solutions

The following paragraphs summarize observations on the surface settlements and subsurface horizontal displacements using analytical solutions with anisotropic and isotropic stiffness parameters for London Clay. Table 4.9 summarizes the isotropic solutions that were chosen initially as reference cases for the two tunnel types analyses, which correspond to the LSS surface solutions for total displacements estimated earlier. Moreover, Table 4.9 summarizes the cavity parameters used in the anisotropic solutions, which also coincide with the LSS surface solution for total displacements.

	Isotropic Model				Anisotropic Model			
Tunnel Type	u_ε (mm)	u_δ (mm)	$\Delta V_L/V_0$ (%)	ρ	u_ε (mm)	u_δ (mm)	$\Delta V_L/V_0$ (%)	ρ
2	-28	10	1.32	0.36	-24	2.8	1.13	0.12
3 (25 May)	-31	18	1.46	0.57	-26	11	1.22	0.42
3 (29 May)	-42	18	1.98	0.44	-30	17	1.41	0.57

Table 4.9: Cavity input parameters for isotropic and anisotropic models based on LSS surface solution for total displacements

4.6.1 Effect of anisotropic stiffness on computed distribution of subsurface ground movements

Figures 4.41 to 4.46 compare the distributions of vertical and horizontal displacements for the HEX Types 2 and 3 (25 and 29 May), as predicted by the anisotropic and isotropic models (using LSS surface solutions for total displacements as already discussed). For both tunnel types the two models predict very similar vertical displacement profiles above the tunnel springline, with the isotropic model predicting slightly wider settlement troughs. Moreover, along the centreline the isotropic model generates slightly larger displacements both above and below the tunnel cavity.

Figures 4.42, 4.44 and 4.46 show that the two models predict similar surface horizontal displacements, with the isotropic model predicting slightly larger values for tunnel Type 3. For tunnel Type 2, the isotropic model predicts significantly larger outward horizontal displacements along the tunnel centreline, comparing

with the anisotropic model which predicts small inward movements up to 5mm. For HEX Type 3 (25 and 29 May), the anisotropic model predicts some inward movements (represented by negative values) along the tunnel elevation, which have the same direction with the displacements observed in the field, while the isotropic model predicts negligible horizontal distortions. Finally, below the tunnel cavity the two models predict small horizontal movements of same outward direction for Type 2 and inward direction for Type 3 (25 and 29 May).

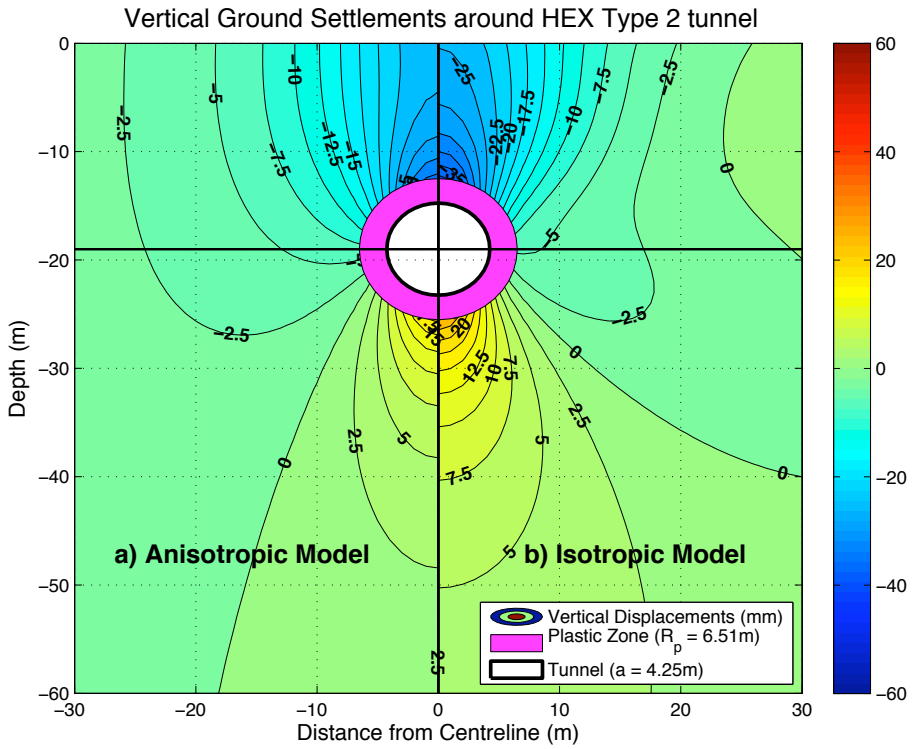

Figure 4.41: Contour Diagram of Vertical Displacements as predicted by Anisotropic and Isotropic Models for Type 2 tunnel

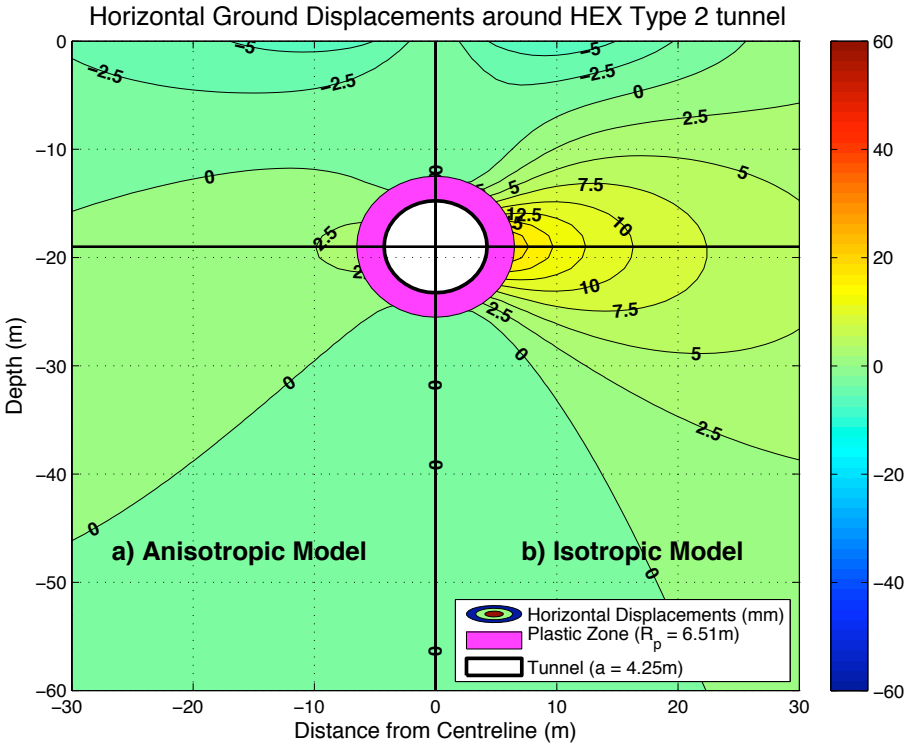

Figure 4.42: Contour Diagram of Horizontal Displacements as predicted by Anisotropic and Isotropic Models for Type 2 tunnel

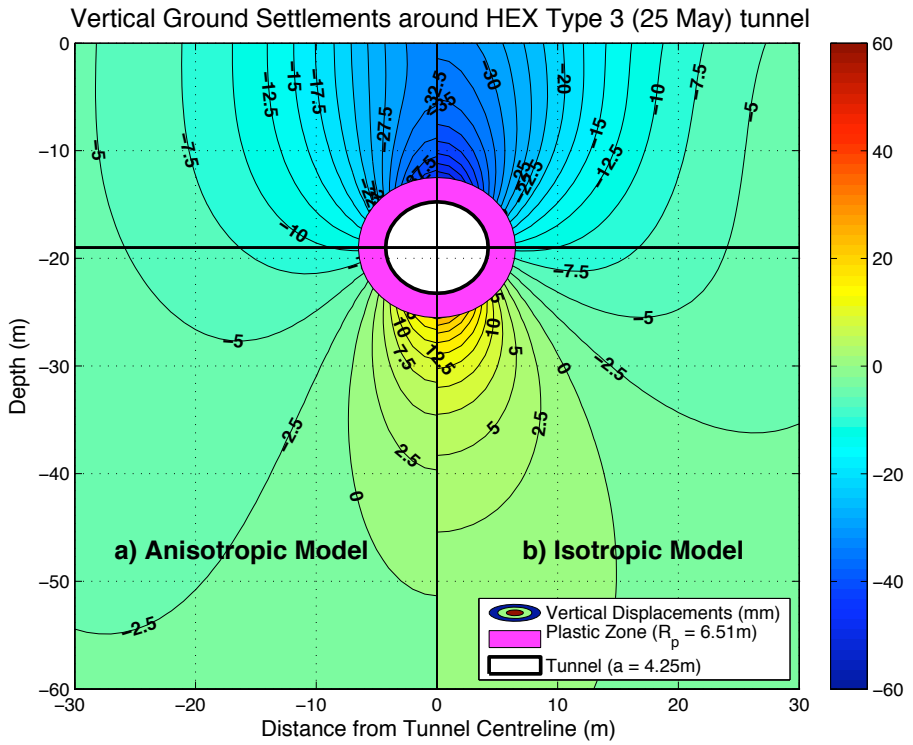

Figure 4.43: Contour Diagram of Vertical Displacements as predicted by Anisotropic and Isotropic Models for Type 3 (25 May) tunnel

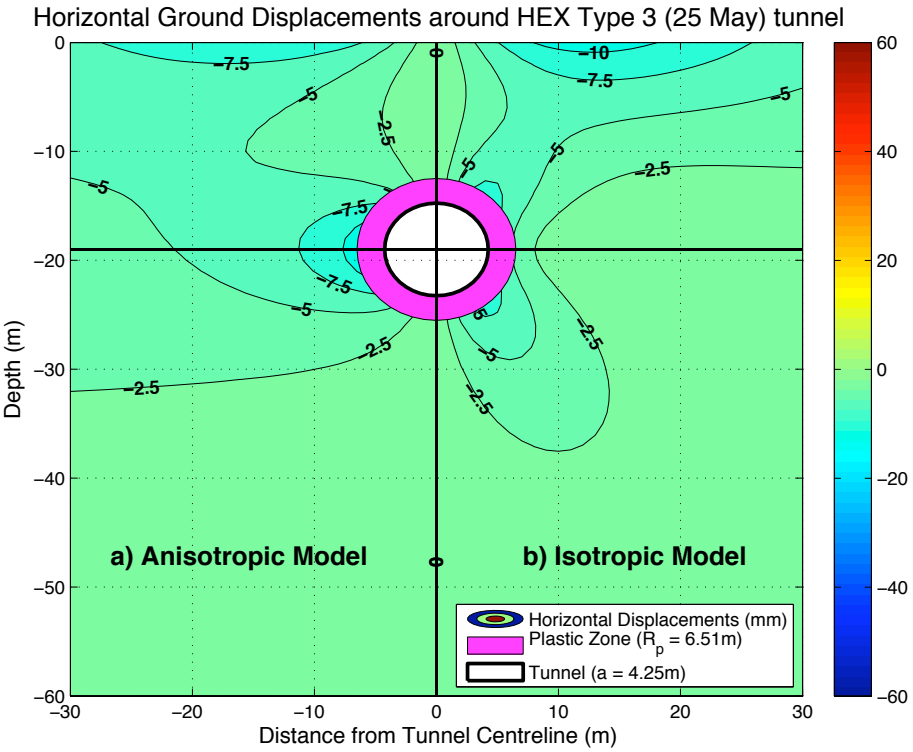

Figure 4.44: Contour Diagram of Horizontal Displacements as predicted by Anisotropic and Isotropic Models for Type 3 (25 May) tunnel

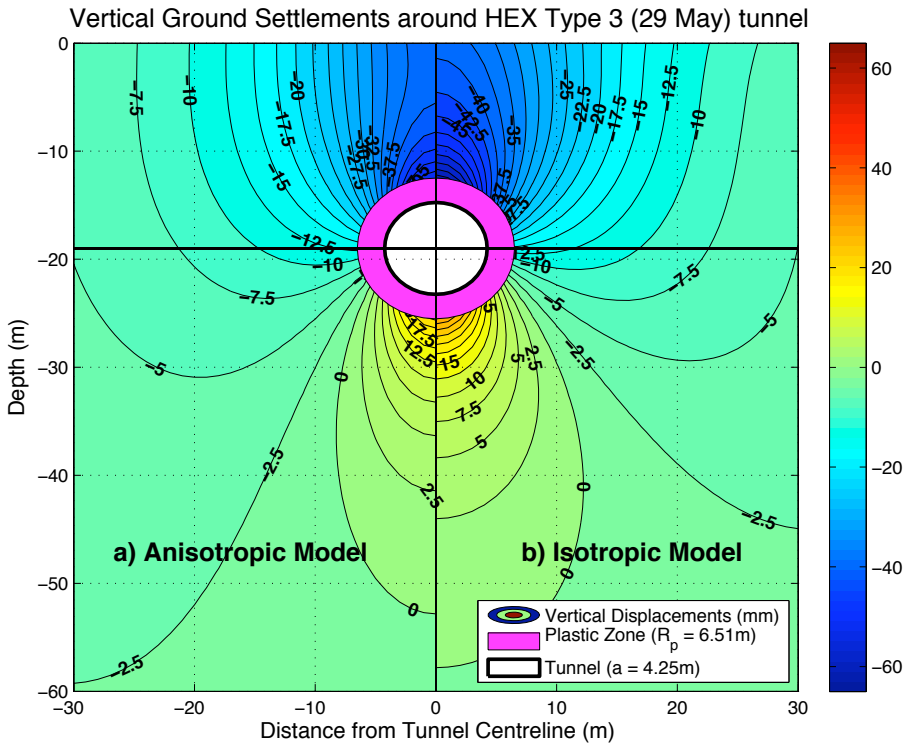

Figure 4.45: Contour Diagram of Vertical Displacements as predicted by Anisotropic and Isotropic Models for Type 3 (29 May) tunnel

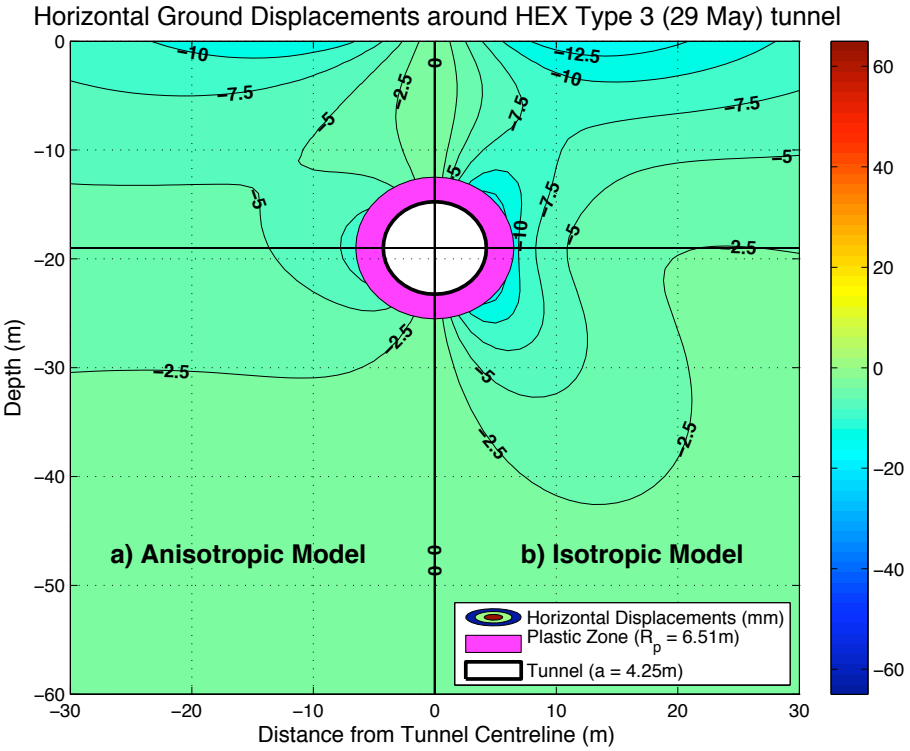

Figure 4.46: Contour Diagram of Horizontal Displacements as predicted by Anisotropic and Isotropic Models for Type 3 (29 May) tunnel

4.6.2 Effect of anisotropic stiffness on computed surface settlements

Figures 4.47, 4.49 and 4.51 compare the measured surface settlements at HEX Types 2 and 3 (25 and 29 May) tunnels with analytical solutions by assuming isotropic and anisotropic stiffness parameters. We observe that the anisotropic model is in closer agreement with the field measurements than the isotropic model. However, both models deviate significantly from the measured trough (differences up to 5mm), the reason being that as already discussed, the input cavity parameters for the two models were chosen based on the LSS surface solution for total displacements, which take into account both horizontal and vertical movements. The LSS method showed that the SS error produced due to horizontal displacements is significantly larger than the SS error for vertical displacements and therefore cavity parameters that mainly fit the horizontal displacement profile prevailed.

For comparison purposes, Figures 4.50, 4.52 and 4.54 were prepared, which compare the same surface settlement measurements with analytical solutions using input parameters that are based on LSS surface solutions for vertical displacements in the anisotropic and isotropic models (see Table 4.10). The settlement troughs produced by the new input parameters provide significantly closer fits to the measured data comparing to the analytically computed troughs presented earlier. The anisotropic model produces an excellent fit to the field data with differences up to 1.5mm for Types 2 and 3 (25 May) and slightly worse fit for Type 3 (29 May) with deviations up to 5mm. The troughs produced by the anisotropic model are narrower than those generated by the isotropic model. Moreover, for the case of Type 3 (25

May) tunnel the anisotropic model produces surface settlements that converge to zero at x ≈ 30m similar to the measured data, while the isotropic model predicts a small heave in the far field (u_y ≈ 1.5mm), which is not observed in the field. Appendix III shows the effect of these new input parameters on the distribution of subsurface ground movements for HEX Types 2 and 3 tunnels.

	Isotropic Model				Anisotropic Model			
Tunnel Type	u_ε (mm)	u_δ (mm)	$\Delta V_L/V_0$ (%)	ρ	u_ε (mm)	u_δ (mm)	$\Delta V_L/V_0$ (%)	ρ
2	-9	28	0.42	3.11	-14	17	0.66	1.24
3 (25 May)	-9	38	1.46	0.57	-26	11	1.22	0.42
3 (29 May)	-15	43	0.71	2.88	-18	35	0.85	1.94

Table 4.10: Cavity input parameters for isotropic and anisotropic models based on LSS surface solution for vertical displacements

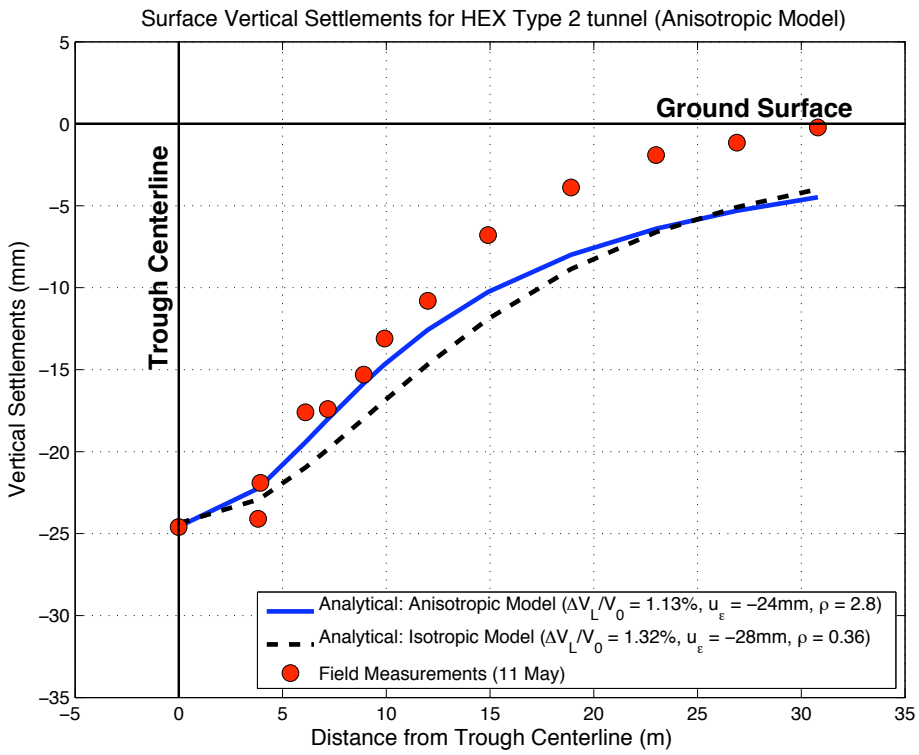

Figure 4.47: Surface settlements as predicted by Anisotropic and Isotropic Models for HEX Type 2 tunnel based on LSS surface solutions for total displacements

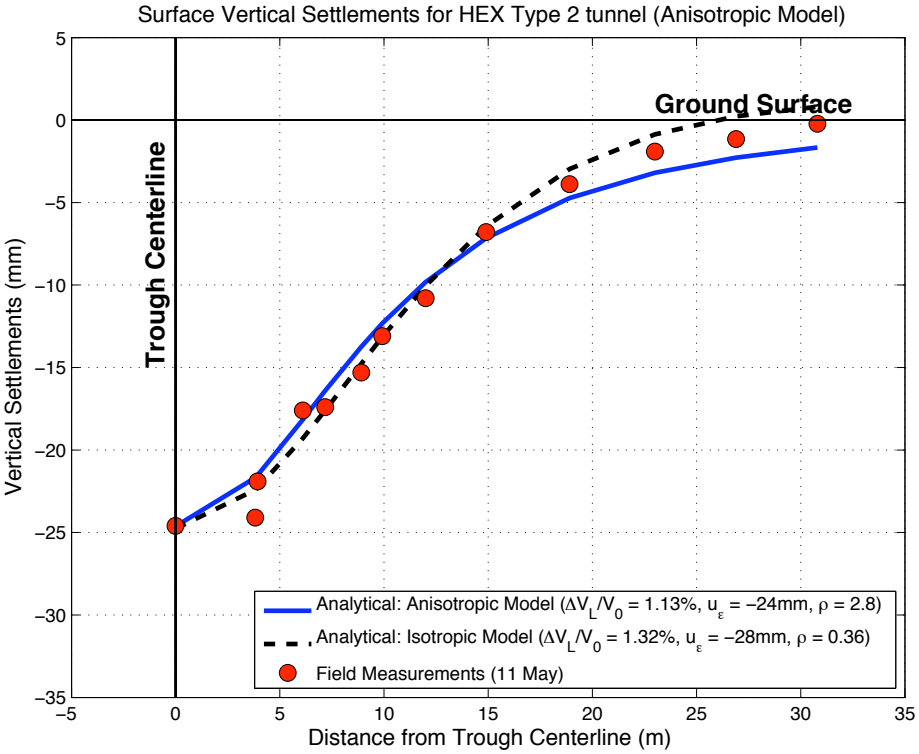

Figure 4.48: Surface settlements as predicted by Anisotropic and Isotropic Models for HEX Type 2 tunnel based on LSS surface solutions for vertical displacements

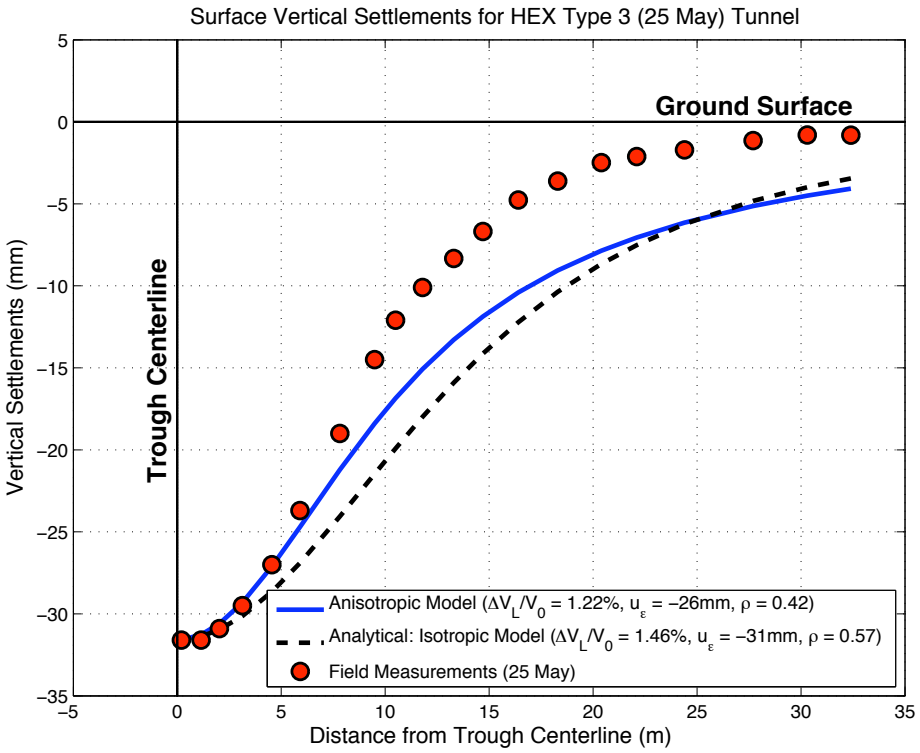

Figure 4.49: Surface settlements as predicted by Anisotropic and Isotropic Models for Type 3 (25 May) tunnel based on LSS surface solutions for total displacements

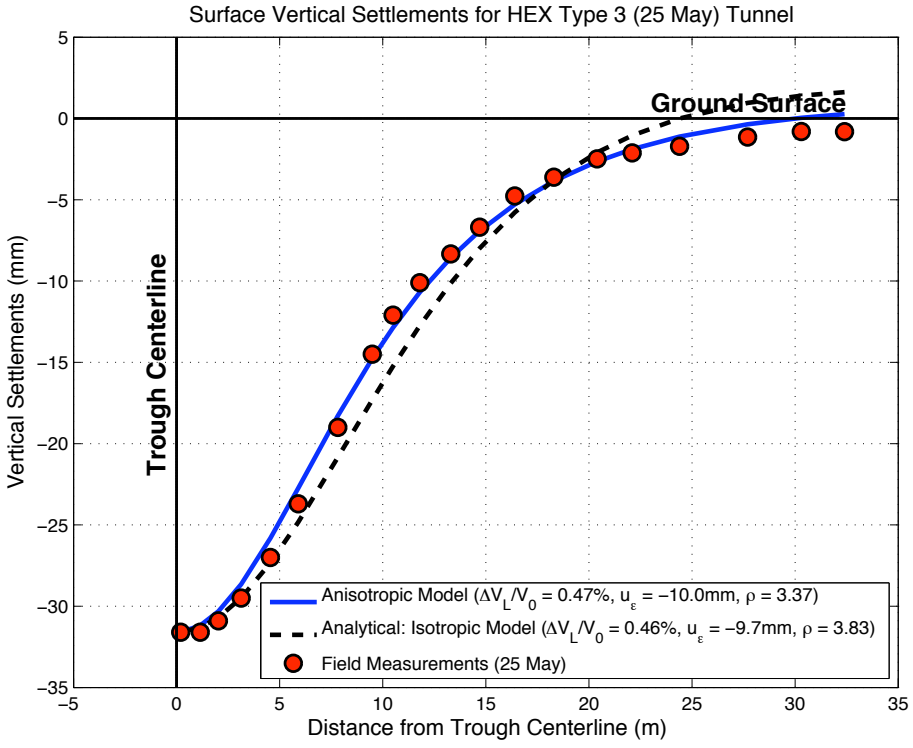

Figure 4.50: Surface settlements as predicted by Anisotropic and Isotropic Models for Type 3(25 May) tunnel based on LSS surface solutions for vertical displacements

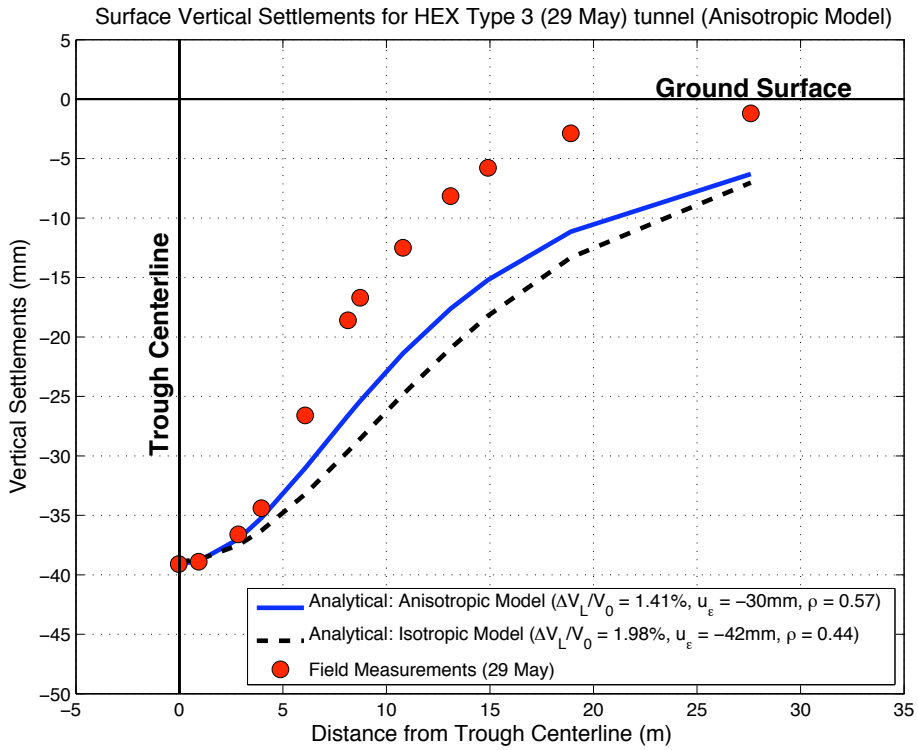

Figure 4.51: Surface settlements as predicted by Anisotropic and Isotropic Models for Type 3 (29 May) tunnel based on LSS surface solutions for total displacements

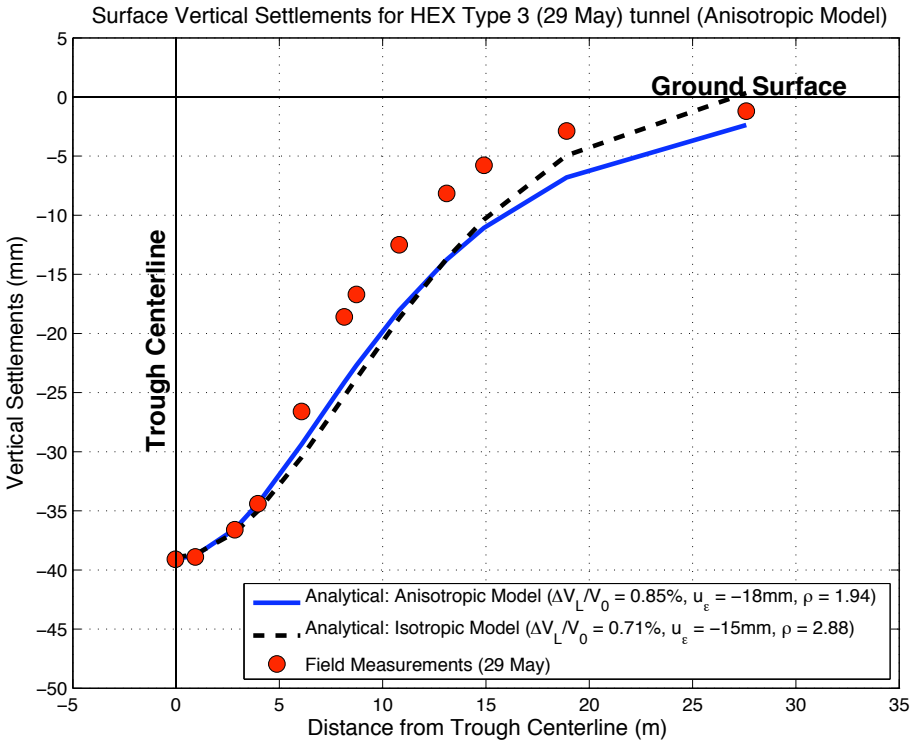

Figure 4.52: Surface settlements as predicted by Anisotropic and Isotropic Models for Type 3(29 May) tunnel based on LSS surface solutions for vertical displacements

4.6.3 Effect of anisotropic stiffness on computed subsurface horizontal displacements

Figures 4.53 and 4.54 compare the analytically computed (using anisotropic and isotropic models) and measured subsurface horizontal displacements at four inclinometer positions for the HEX type 3 (25 and 29 May) tunnels. The model input parameters are based on LSS surface solutions for total displacements and are summarized in Table 4.9. There is very good agreement between the predicted and measured data, with the anisotropic model. At inclinometer IC1, where the isotropic model predicts zero horizontal displacement, the anisotropic predicts inward movement, which agrees with what was recorded in the field. Finally the two models predict very similar horizontal displacements at the shallow subsurface and also below the tunnel cavity, which at the same time are very close to the measured data.

Figures 4.55 and 4.56 compare the measured subsurface horizontal displacements for the HEX type 3 (25 and 29 May) tunnels with analytically computed anisotropic and isotropic models, using model input parameters that are based on LSS surface solutions for vertical displacements shown in Table 4.10. The agreement between the measurement and computed displacements is not very good, especially at depths close to the tunnel. Along the tunnel springline, both models predict outward displacements, which have opposite direction to what was measured in the field. The two models predict very similar horizontal displacements throughout the soil mass, with the anisotropic model predicting slightly smaller displacements.

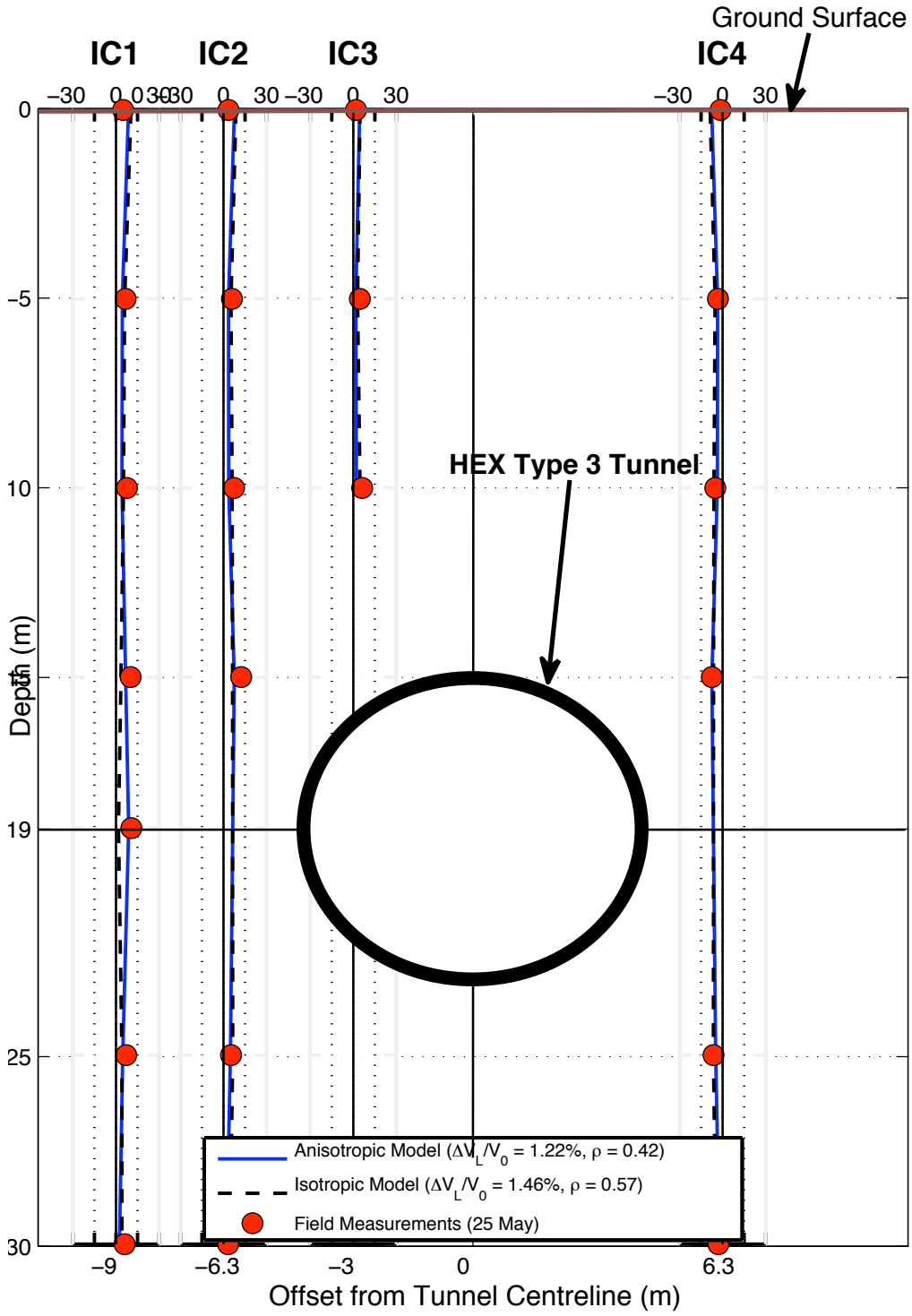

Figure 4.53: Measured and computed subsurface horizontal displacements for HEX Type 3 (25 May) tunnel using LSS surface solutions for total displacements

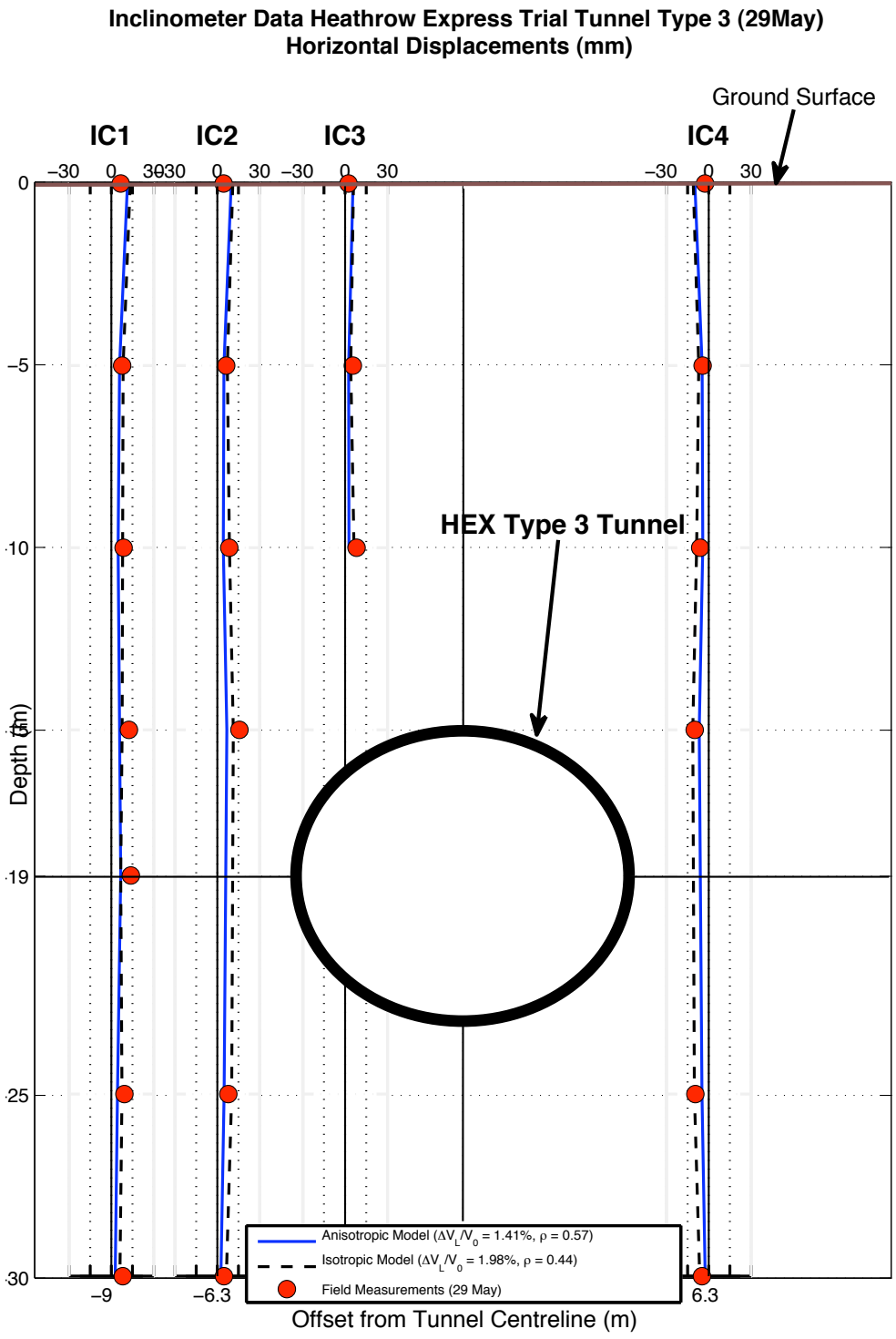

Figure 4.54: Measured and computed subsurface horizontal displacements for HEX Type 3 (29 May) tunnel using LSS surface solutions for total displacements

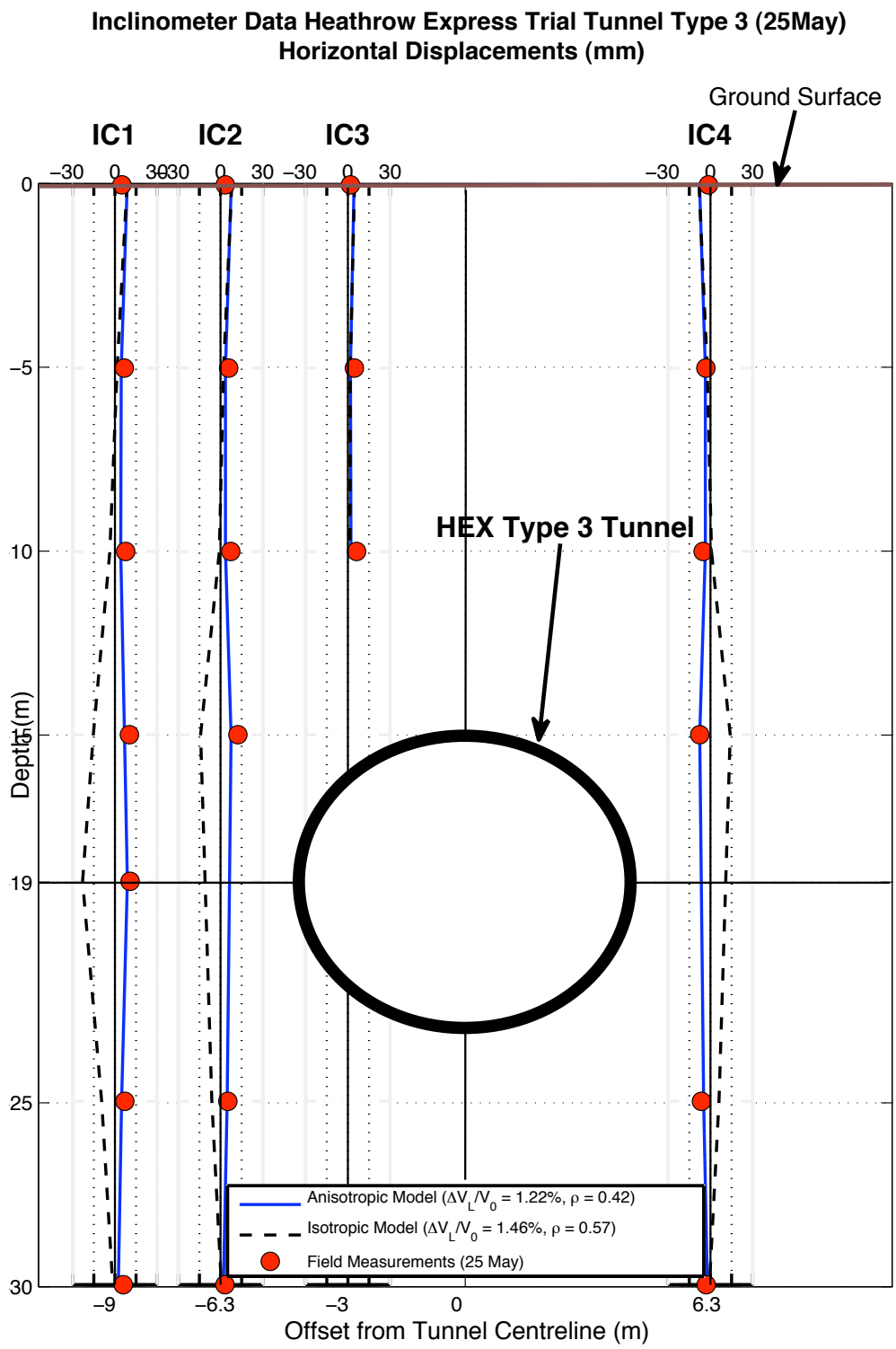

Figure 4.55: Measured and computed subsurface horizontal displacements for HEX Type 3 (25 May) tunnel using LSS surface solutions for vertical displacements

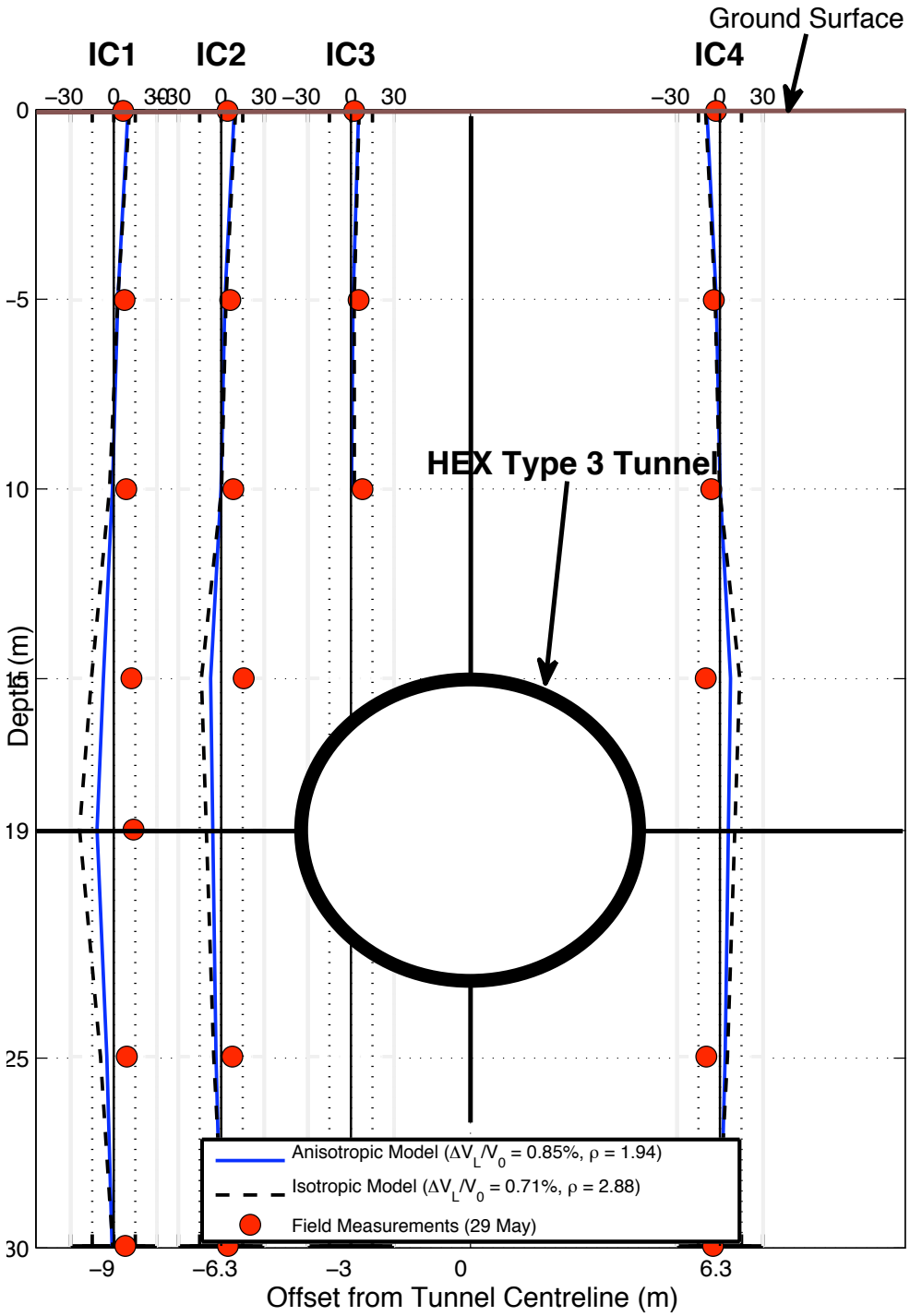

Figure 4.56: Measured and computed subsurface horizontal displacements for HEX Type 3 (29 May) tunnel using LSS surface solutions for vertical displacements

Figures 4.57 and 4.58 compare ground displacement vector diagrams for Types 2 and 3 (29 May), as measured in the field and also as computed by the anisotropic and isotropic solutions, using input parameters based on LSS surface solutions for total displacements (Table 4.9). Both computed vector diagrams provide much closer fit to the field measurements, comparing with Figures 4.21 and 4.22 which were computed using analytical Cases 1 and 2. Figure 4.57 shows that the fit to the field measurements of tunnel Type 2 is very good, even in regions close to the tunnel cavity. The anisotropic model performs better comparing to the isotropic solutions. Moreover, both analytical solutions tend to over-predict the settlement near the tunnel springline, comparing with the field data.

Figure 4.58 shows that the fit to the field data of tunnel Type 3 (29 May) is also very good, especially in the vertical component of displacement. Both solutions tend to underpredict the settlements that were measured near the tunnel springline and this is probably related to the excess settlement induced in Type 3 due to the delay in the closing of the invert discusses previously.

Appendix III shows the effect of the input parameters based on LSS surface solutions for vertical displacements, on the vector diagrams for HEX Types 2 and 3 tunnels.

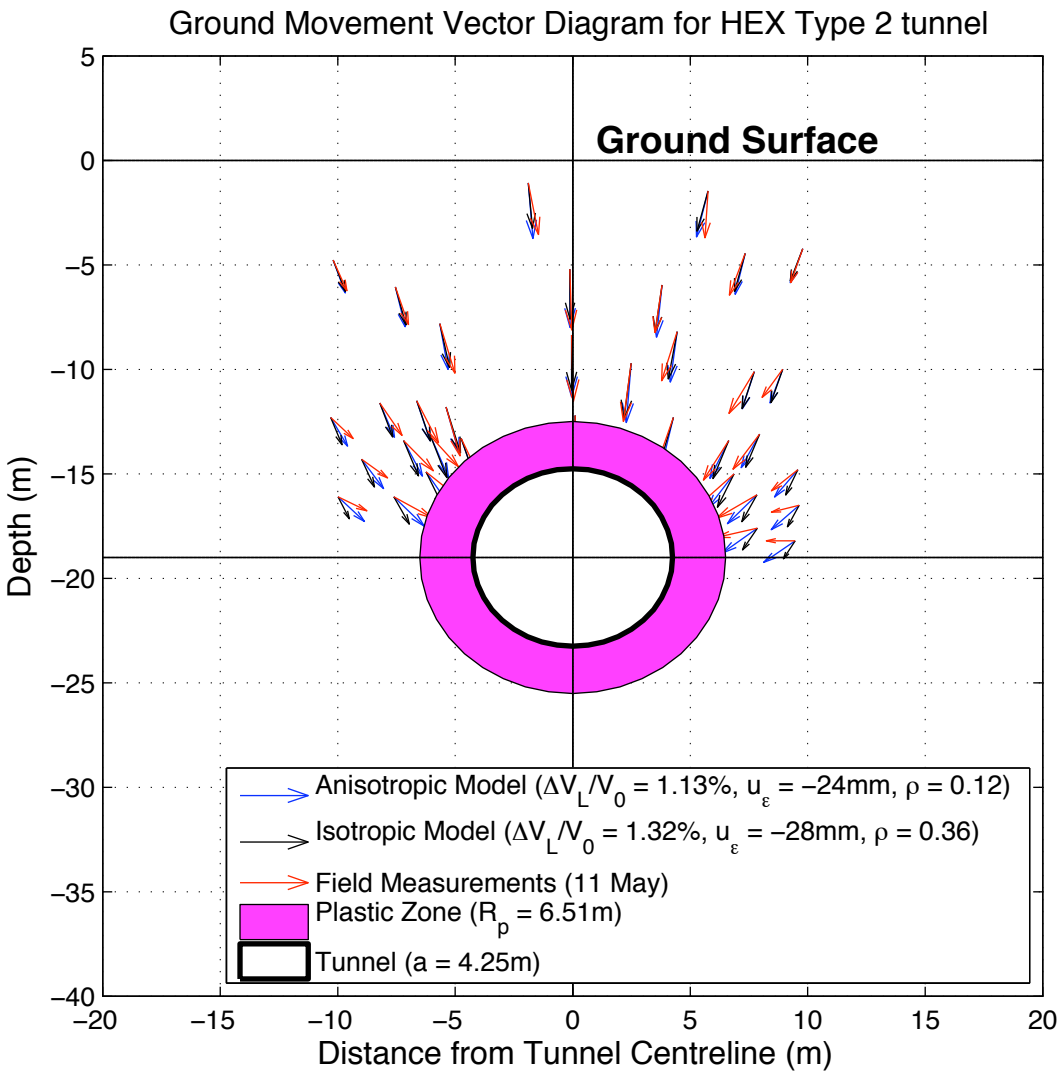

Figure 4.57: Measured and computed subsurface ground displacements for HEX Type 2 (11 May) tunnel using LSS surface solutions for total displacements

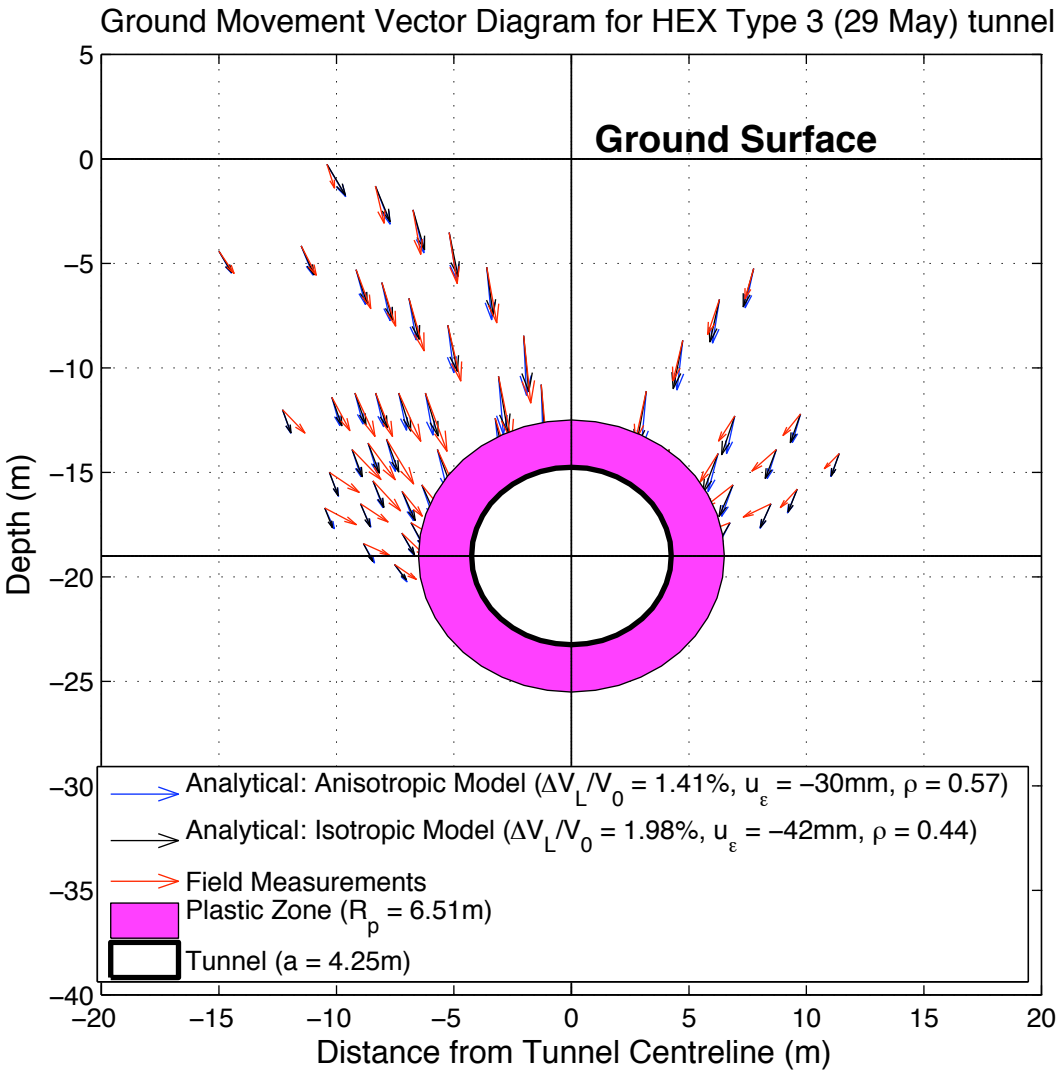

Figure 4.58: Measured and computed subsurface ground displacements for HEX Type 3 (29 May) tunnel using LSS surface solutions for total displacements

4.7 Conclusions

The analytical solutions proved to be very effective in describing the surface settlement troughs generated by all three NATM types used in the HEX trial tunnel. Isotropic Analytical Case 1 produced much closer fits to the recorded surface

settlements than Isotropic Analytical Case 2, which used the volume losses suggested by the empirical method. Analytical Case 1 suggests that Tunnel Type 3 (25 May) generated the minimum volume loss (ΔV_L = 0.46%) followed by Tunnel Type 1 that produced ΔV_L = 0.54%, while the empirical method showed that the minimum ΔV_L was caused by Tunnel Type 2. Moreover, in order to successfully fit the narrow settlement troughs that were recorded in the field, high ρ values were employed in analytical Case 1 (ρ = 2 – 3.8) and thus Pinto's (1999) suggestion that for soils with high K_0 values (such as London Clay) low ρ values should be used is not always applicable.

On the other hand, the isotropic model didn't succeed in describing subsurface horizontal displacements induced by Tunnel Type 3. Case 2 predicted smaller movements, which didn't deviate as much as the results of Case 1 from the measured data. The vector diagrams produced by analytical cases 1 and 2 for HEX tunnel types 2 and 3 (29 May) fit well the measured data up to a depth y ≈ -12m. At elevations closer to the tunnel springline, the analytical solutions predicted horizontal displacements of outward direction, opposite to the field data.

The LSS error method showed that Case 2 overall performed better than Case 1 since it was closer to the LSS surface solution for total displacements. The LSS error for horizontal displacements was significantly larger than the LSS error for vertical movements and therefore the LSS surface solution for total displacements was closer to the LSS surface solution for horizontal displacements.

Introducing anisotropy in the analytical solutions proved to be very effective. Initially, model input parameters based on LSS surface solutions for total displacements were employed. The surface settlements were not successfully described by these parameter sets, as shown in 4.47, 4.49 and 4.51 . However, the anisotropic solutions provided an excellent fit to the subsurface horizontal displacements and successfully managed to simulate the inward ground movements at the tunnel springline that were recorded in the field. They also significantly improved the ground displacement vector diagrams computed by Cases 1 and 2.

Subsequently, anisotropic solutions that were based on LSS surface solutions for vertical displacements were used, which provided excellent fits to the measured settlement troughs. However, the subsurface horizontal displacements predicted by the new parameter sets deviated significantly from the field data.

To summarize, the analytical solutions with isotropic and anisotropic stiffness parameters, were able to successfully model all ground displacements measured in the field. However, the input parameters that produced good settlement fits didn't generate realistic subsurface horizontal displacements and vice versa. The LSS method would have probably been more successful in suggesting a single optimum parameter set (i.e. LSS surface solution for total displacements) if there were more field measurements available.

Chapter 5

Further illustrative examples of tunnels

5.1 Introduction

The analytical solutions presented in Chapter 2 have been applied to three illustrative examples of tunnels taken from the literature, where there are measurements available on vertical and horizontal displacements, at the surface and the subsurface. The first case, the Madrid Metro extension project, uses open face tunneling, with hand excavation within clay. The subsequent two examples of tunnels use pressurized closed-face tunneling. Both the Mexico City sewer tunnel and also the N-2 contract tunnel for the San Francisco clean water project use E.P.B. machines and excavation takes place within clay.

5.2 Madrid metro extension

The extension plan of the Madrid Metro (1995 – 1999) included the construction of more than 30km of tunneling, 64% of which was excavated with closed face earth pressure balanced (EPB) shields, 21% with open face hand mining (Belgian method) and 21% by cut and cover (Gonzalez and Sagaseta, 2001).

The soil stratigraphy in most of the Madrid urban area includes Tertiary (Pliocene) deposits, covered by Quaternary sediments associated with the Manzanares river

and its tributaries, and also by frequent man-made fills. The Tertiary materials are very stiff, heavily overconsolidated and from top to bottom, comprise of the following layers: i) “arena de miga”, a clayey sand with the clay forming bonds between the sand particles; ii) “tosco", a stiff sandy clay; iii) “peñuela”, a stiff marly clay; and iv) gypseous marl, with some layers of gypsum rock (Gonzalez and Sagaseta, 2001).

A large monitoring plan was implemented with more than 9000 instruments installed. This system included monitoring points for surface vertical and horizontal displacements as well as inclinometers and extensometers (multiple rod type and sliding micrometers) for subsurface displacements. In some cases there were also measurements of building movements and also earth pressures and stresses in the tunnel lining (Gonzalez and Sagaseta, 2001).

The cross-section considered in the subsequent analysis was excavated by open face hand tunneling (Belgian method). The cavity has a horseshoe-shaped cross section of 62 m^2 area (equivalent radius R_{eq} = 4.44m) and the depth to tunnel springline is H = 15.2m (see Figure 5.2).

5.2.1 Field Measurements

Figure 5.1 summarizes the surface settlements measured in the field. The recorded trough appears to be asymmetric along the tunnel centreline, with the apparent

surface centrepoint $u_y^0 \approx 11.4$mm occurring at x = 1.5m. Using the empirical Gaussian fit to model the surface settlements with the trough width parameters K = 0.5 proposed by Mair and Taylor (1997) for tunnels in clay, we obtain the curve shown in Figure 5.1. We observe that the Gaussian curve produces a much narrower trough and does not provide a very good fit to the field measurements. The volume loss implied using the conventional interpretation of ground movements is 0.35% as shown:

From equation (2.2) $$V_S = u_y{}^0 i\sqrt{2\pi} = 0.0114 \times 0.5 \times 15.2 \times \sqrt{2\pi} = 0.22\,\text{m}^2$$

From equation (2.3) $$\frac{\Delta V_L}{V_0} = \frac{V_S}{\pi R^2} = \frac{0.22}{\pi \times 4.44^2} = 0.35\%$$

Figure 5.2 summarizes the horizontal displacements recorded by an inclinometer located at x = -8m from the tunnel centreline. The majority of measurements indicate inward movements towards the tunnel cavity (since the inclinometer is placed to the left of the tunnel).

Past experience of tunneling in the Madrid urban area indicates that for open face tunneling, the average volume loss is $\Delta V_L/V_0 < 1\%$, except in the presence of local weak zones, such as clean water-bearing sand lenses, quaternary sediments, man-made fills, etc (Gonzalez and Sagaseta, 2001). Thus $\Delta V_L/V_0 = 0.35\%$ deduced using the conventional method is smaller than 1% as expected by previous tunneling experience in Madrid.

Pinto (1999), using his proposed design scheme to analyze the Madrid Metro cross-section introduced earlier, concluded that the optimum parameter set for the isotropic analytical solutions is:

Pinto's Case: $(u_\varepsilon, u_\delta) = (-13.5, 3.0)$ mm ➔ $\Delta V_L/V_0 = 0.61\%$, $\rho = 0.22$ and $v = 0.48$

Therefore the volume loss $\Delta V_L/V_0 = 0.6\%$ suggested by Pinto (1999) is smaller than 1%, as expected from previous tunneling projects in the Madrid area.

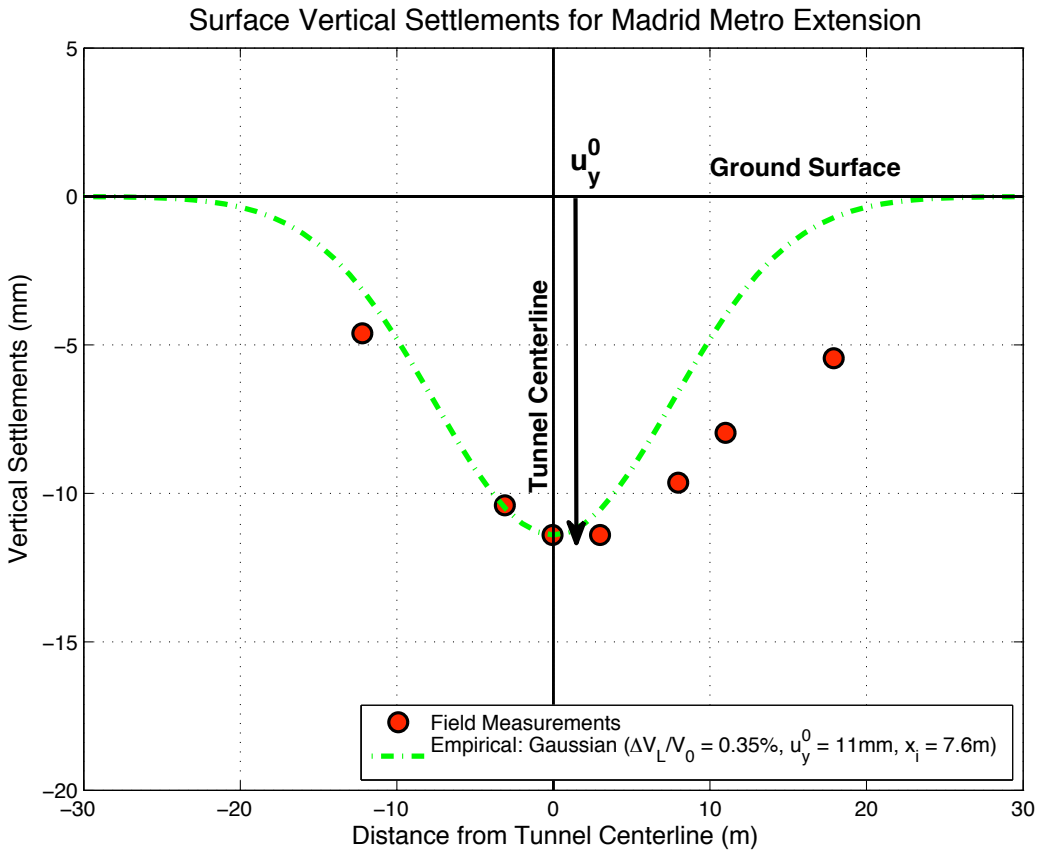

Figure 5.1: Surface Settlements measured at Madrid Metro site and modeled by empirical Gaussian curve

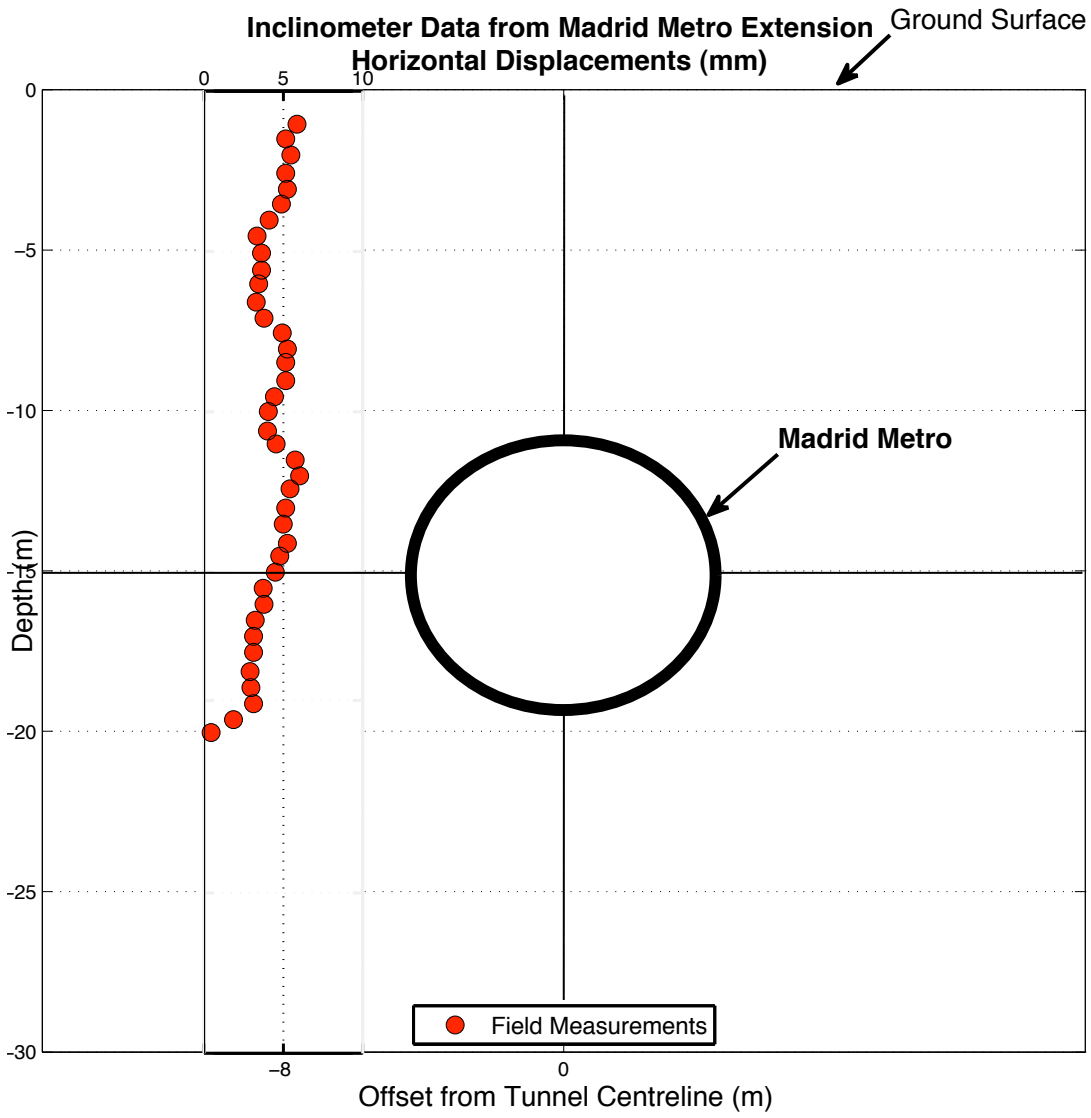

Figure 5.2: Horizontal Displacements recorded by inclinometer at x=-8m at Madrid Metro test site

5.2.2 Application of proposed analytical solutions

The key geometric parameters for the Madrid Metro extension project are:

- Depth to springline H = 15.2m

- Equivalent radius R_{eq} = 4.44m
- Ratio R/H = 0.29

Assuming undrained conditions and incompressibility of the soil (similar to Pinto's case) we employ Poisson's ratio ν = 0.5.

An LSS error method is used in order to optimize the cavity parameters (u_ε, u_δ) and at the same time evaluate Pinto's Case. The field measurements that have been considered in the LSS error analysis are the surface settlements shown in Figure 5.1 and the subsurface horizontal movements shown in Figure 5.2. Figures 5.3 – 5.5 summarize contour plots of the SS error for vertical, horizontal and total ground displacements and also Table 5.1 summarizes the results of the LSS error method (i.e. the LSS surface and global solutions and also the SS error produced by Pinto's Case). From Figure 5.5 we select the cavity parameters (u_ε, u_δ) that correspond to the LSS surface solution for total displacements and will be employed in the analysis:

LSS surface solution: (u_ε, u_δ) = (-14, 2.9) mm ➔ $\Delta V_L/V_0$ = 0.63%, ρ = 0.21

It is deduced that Pinto's Case coincides with the optimum solution and therefore Pinto's proposed design scheme proves to be very effective for the case of the Madrid Metro extension. In the subsequent analysis, Pinto's suggested input parameters will be used for the simulation of the ground movements recorded in the field.

	Surface Solution			Global Solution			Pinto's Case (u_ε, u_δ) = (-13.5, 3.0)mm
	u_ε (mm)	u_δ (mm)	LSS (mm²)	u_ε (mm)	u_δ (mm)	LSS (mm²)	SS (mm²)
Vertical	-19	0.27	6.91	-18	1	7.06	14.6
Horizontal	-14	2.88	77.12	-20	6	53	83.9
Total	-14	2.88	89.8	-15	3	82.4	98.5

Table 5.1: Summary of LSS method results for Madrid Metro extension

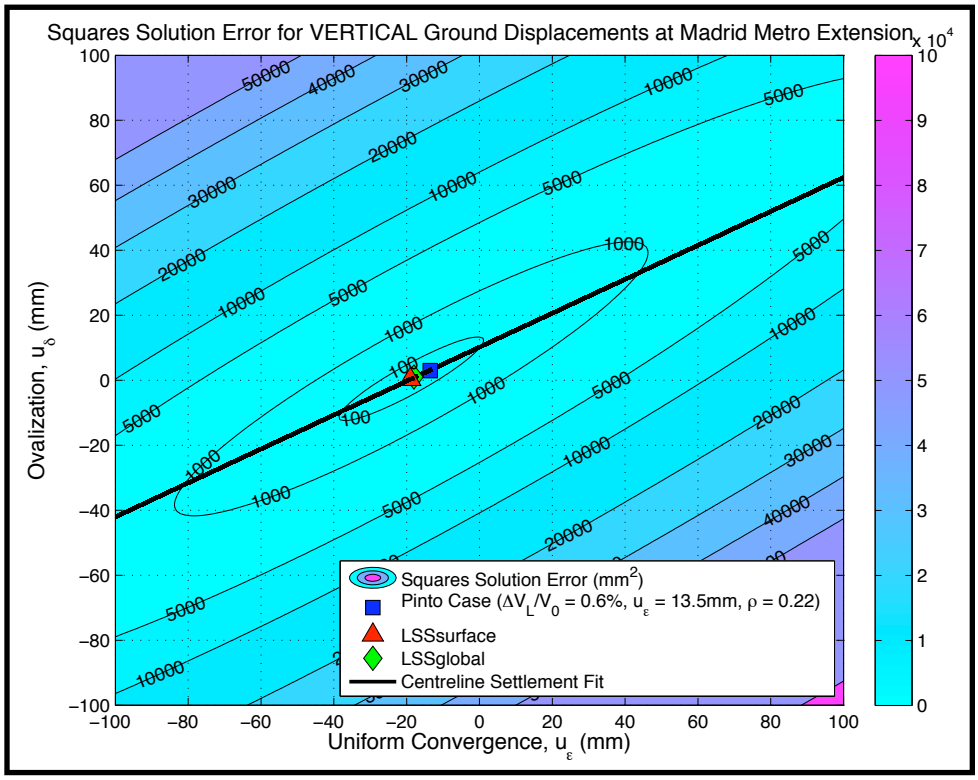

Figure 5.3: SS error for vertical displacements at Madrid Metro extension

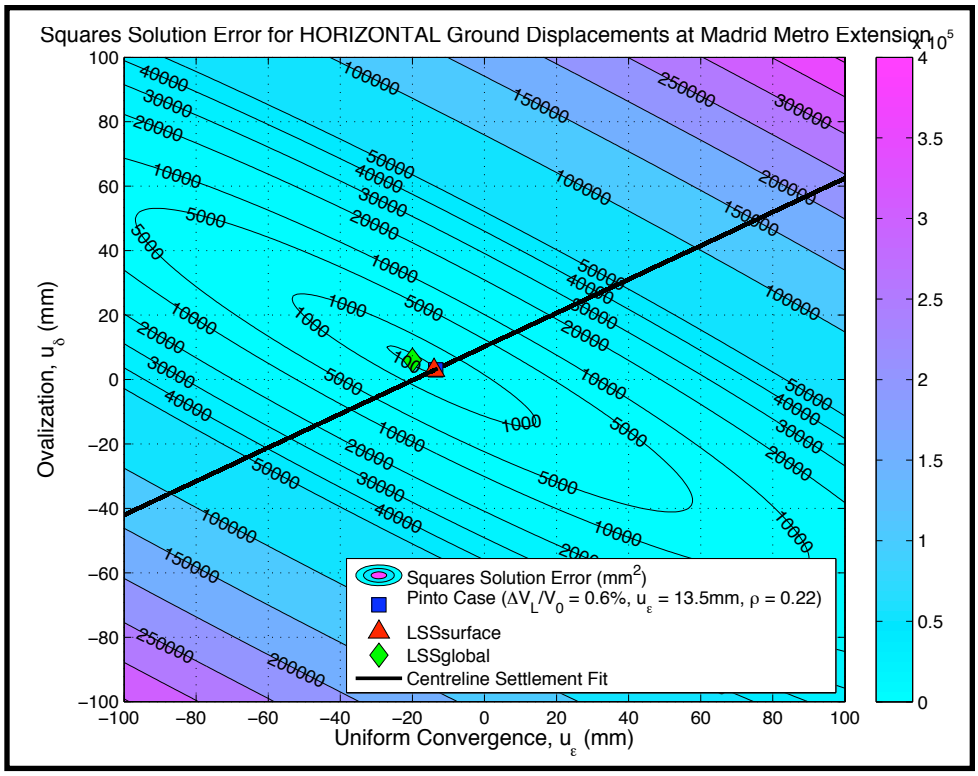

Figure 5.4: SS error for horizontal displacements at Madrid Metro extension

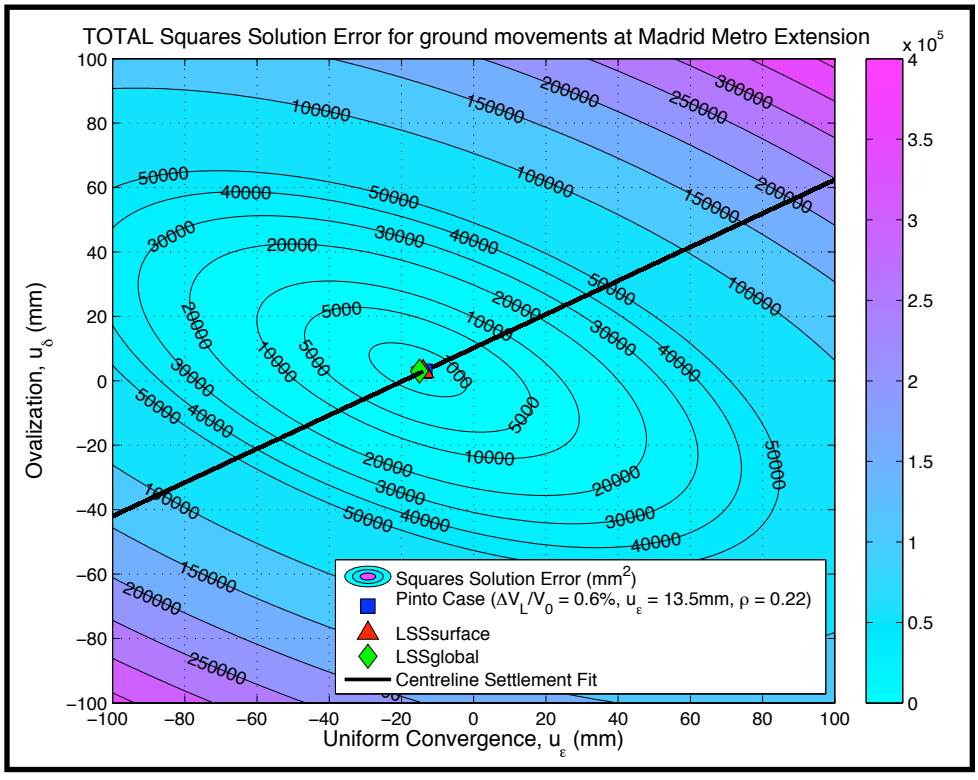

Figure 5.5: SS error for total displacements at Madrid Metro extension

5.2.2.1 Computed distribution of ground displacements

Figure 5.6 summarizes the computed distribution of vertical and horizontal ground displacements for the Madrid Metro extension project using the analytical 'Pinto case. We observe that the surface settlements are smaller compared with the previous examples of tunnels in London Clay (u_y^0 = 11mm vs. 20mm for St James's WB tunnel). Above the tunnel springline, settlements (negative vertical displacements) take place, while below the tunnel heave is generated (positive vertical displacements).

Pinto's analytical case predicts very small horizontal displacements across the soil mass (u_x < 10mm), with the surface horizontal movements being smaller than 5mm. Moreover, along the tunnel springline, the analytical solutions predict inward movements towards the tunnel cavity, represented by negative values of displacement. Finally, for most of the soil below the tunnel cavity (y < 25m) u_x = 0mm.

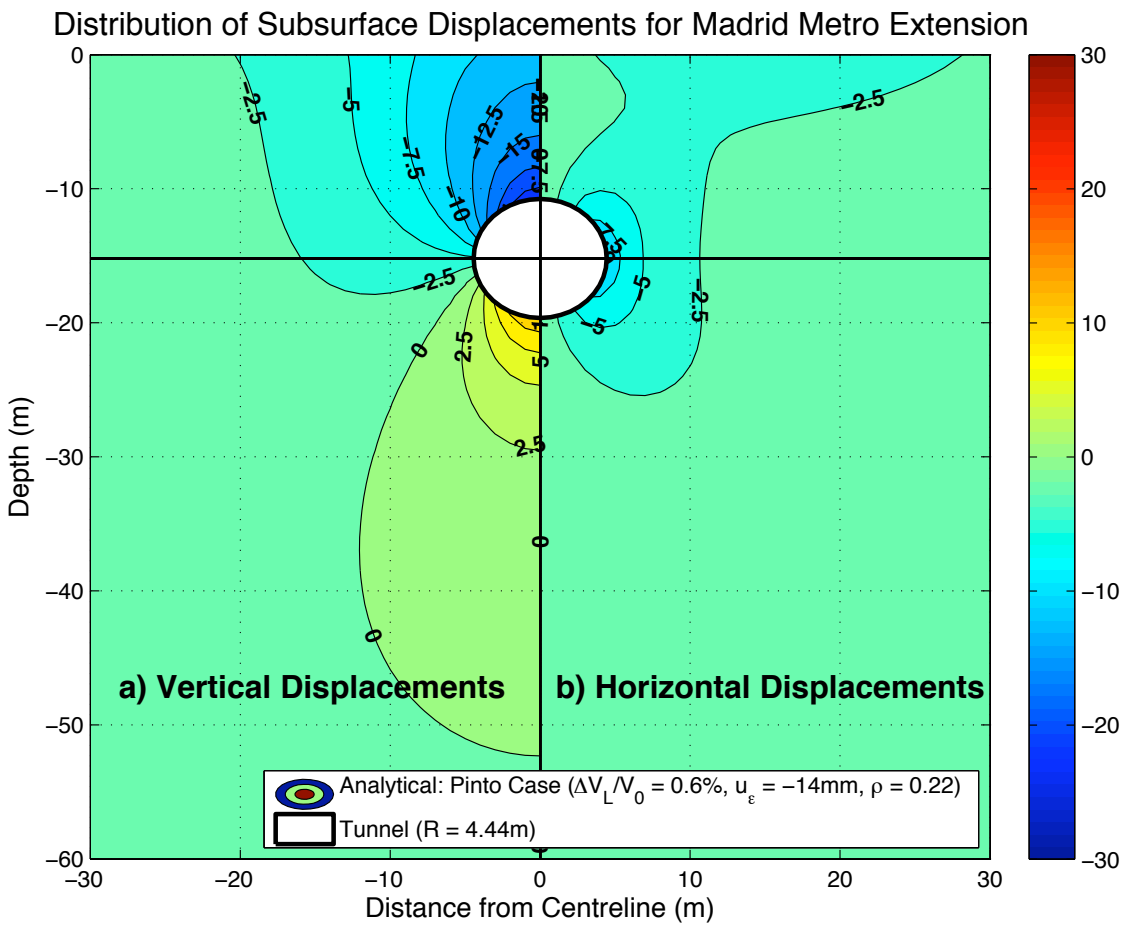

Figure 5.6: Distribution of predicted subsurface displacements for Madrid Metro using LSS method

5.2.2.2 Computed and measured surface settlements

Figure 5.7 compares the computed and measured surface settlements, along the trough centreline, by shifting the field measurements by 1.5m to the west. The trough computed by the analytical solutions is in closer agreement to the field measurements, comparing with the Gaussian trough. Asymmetry in the field measurements still exists, as data points that have the same offset from the trough

centreline, have different settlement values. The analytical model provides a better fit to the west part of the settlement trough and the largest deviation from the measurements is less than 2mm.

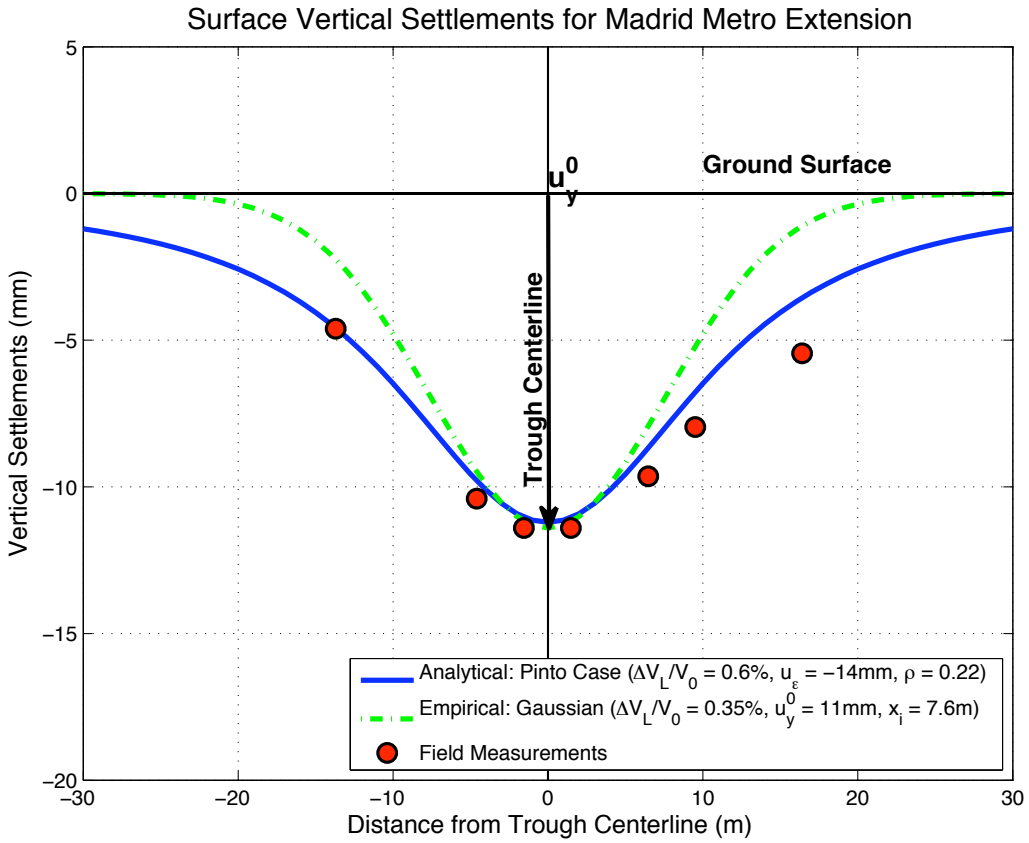

Figure 5.7: Surface settlements along trough centerline for Madrid Metro

5.2.2.3 Computed and measured subsurface horizontal displacements

Figure 5.8 compares the analytically computed and measured subsurface horizontal displacements at x = -8m from the tunnel centreline. We observe that Pinto's Case provides a very good fit to the field data, with differences up to 2mm.

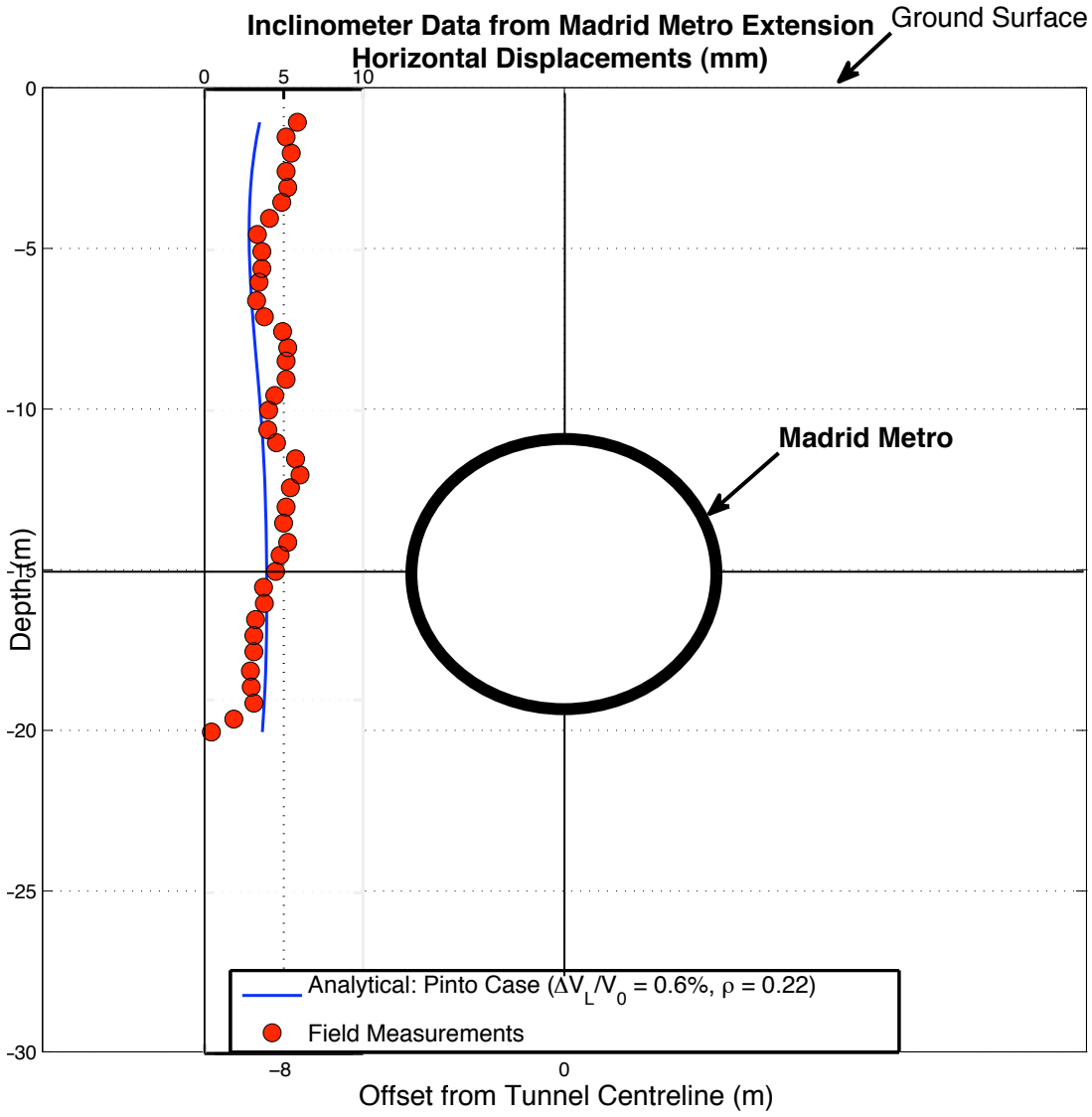

Figure 5.8: Computed and measured horizontal displacements at x = -8m at Madrid Metro test site

5.2.3 Conclusions

The analytical solutions succeeded in simulating the ground displacements measured at the Madrid Metro test site. The LSS method showed that the input

parameters suggested by Pinto (1999) coincide with the LSS surface solution for total displacements, and thus the design scheme proposed by Pinto and Whittle (2001) succeeded in selecting appropriate cavity parameters for the Madrid Metro tunnel. The surface settlement trough generated by the analytical solutions is in close agreement with the field measurements and provided a better fit than the empirical method. However, as expected, the analytical solutions and the conventional Gaussian distribution curve preserved the symmetry along the tunnel centreline and thus failed to model the asymmetry of the recorded settlement trough. Finally, the horizontal displacements measured by an inclinometer at x=-8m from the centreline were very well described by the analytical model, with deviations less than 2mm.

5.3 Sewer-Line Tunnel in Mexico City

The tunnel considered in this section is part of the sewerage system of the Mexico City Metropolitan area. The soil stratigraphy at the section considered comprises of soft clay deposits, underlying some inter-bedded silt and clay strata. The tunnel cavity was excavated by closed face earth pressure balanced (EPB) shield and pressurized slurry was used at the tunnel face in order to increase stability. Moreover, pre-cast segmental linings were placed behind the shield and the tail void was filled with pressurized grout (Romo, 1997). The tunnel has a circular cross-section of radius R = 2m and the depth to tunnel springline is H = 12.75m.

5.3.1 Field Measurements

Figure 5.9 summarizes the surface settlements measured in the field. Just the half trough has been recorded in the field (east part of the trough) and therefore we cannot draw conclusions on whether the trough is symmetric or not. The maximum surface settlement $u_y^0 \approx 28.6$mm takes place at the centreline (at x/H=0). Using the empirical Gaussian fit to model the surface settlements with the trough width parameter K = 0.5 proposed by Mair and Taylor (1997) for tunnels in clay, we obtain the curve shown in Figure 5.9. We observe that the Gaussian curve provides a good fit to the field measurements from the centreline and up to x ≈ 12m, from which point onwards the Gaussian curve underestimates the recorded movements. The volume loss implied using the conventional interpretation of ground movements is $\Delta V_L/V_0 = 3.64\%$ as shown:

From equation (2.2) $$V_S = u_y{}^0 i\sqrt{2\pi} = 0.0286 \times 0.5 \times 12.75 \times \sqrt{2\pi} = 0.46\,\text{m}^2$$

From equation (2.3) $$\frac{\Delta V_L}{V_0} = \frac{V_S}{\pi R^2} = \frac{0.46}{\pi \times 2^2} = 3.64\%$$

Figure 5.10 summarizes settlement measurements at three depths, y=0, -5 and -10.15m. Moreover, Figure 5.11 shows horizontal displacements recorded by an inclinometer located at x = 4.5m from the tunnel centreline. The measurements show outward movement (away from the tunnel cavity) and the maximum horizontal displacement taking place 1.5m above the tunnel springline.

Pinto (1999), using his proposed design scheme to analyze the sewer-line tunnel in Mexico, concluded that the optimum parameter set for the isotropic analytical solutions is:

Pinto's Case: $(u_\varepsilon, u_\delta) = (-22, 34)$ mm➔$\Delta V_L/V_0 = 1.1\%$, $\rho = 1.53$ and $v = 0.12$

Therefore the volume loss $\Delta V_L/V_0 = 1.1\%$ suggested by Pinto (1999) is smaller than that implied by the empirical method, due to the large effect of tunnel cavity distortion.

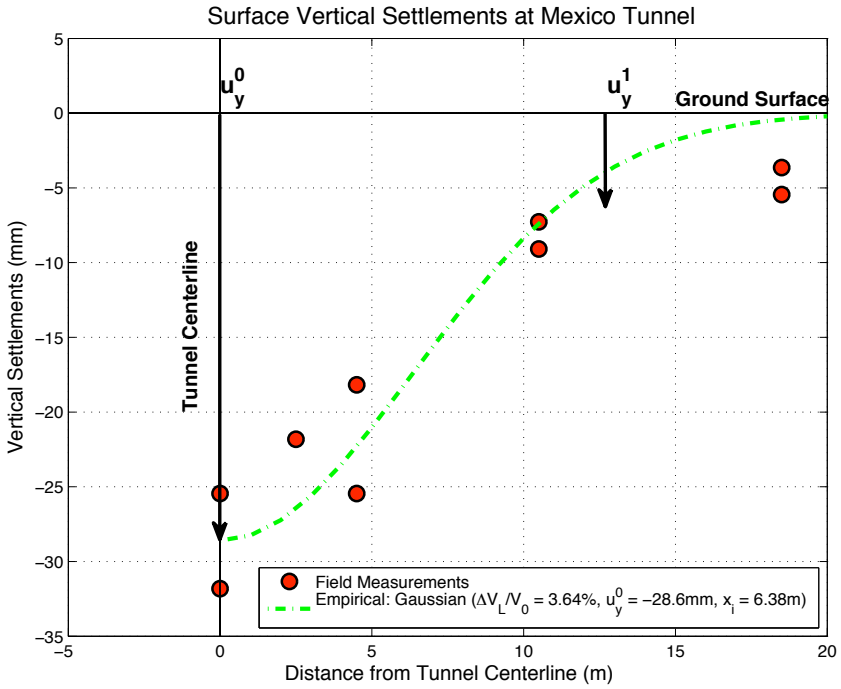

Figure 5.9: Surface Settlements measured at Mexico tunnel site and modeled by empirical Gaussian curve

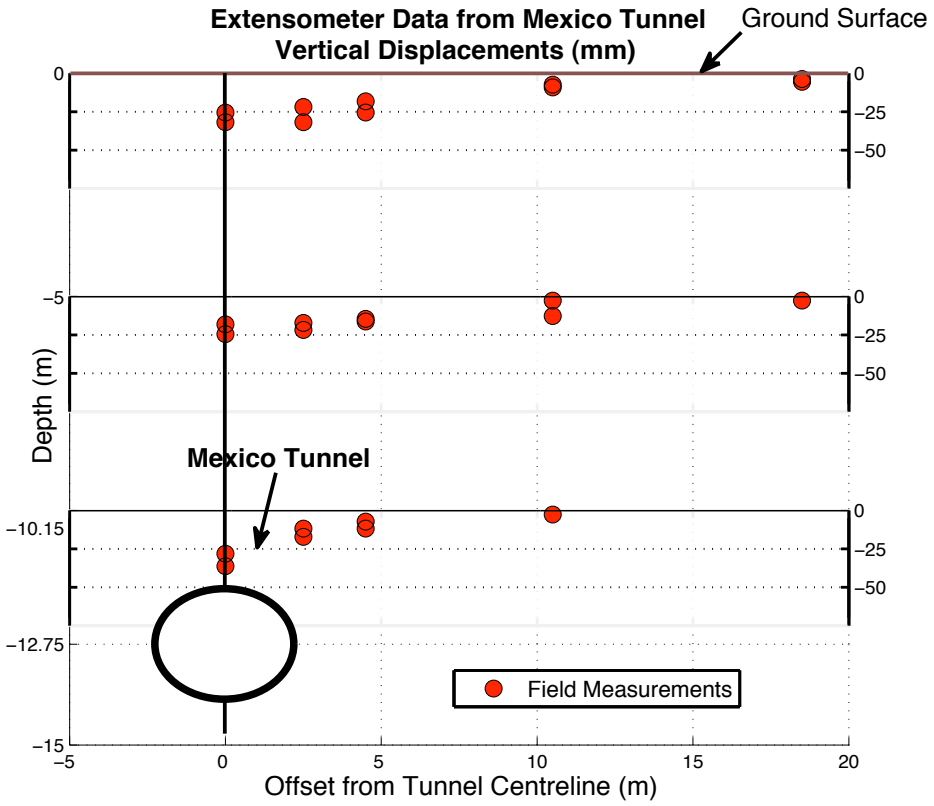

Figure 5.10: Subsurface Settlements measured at 3 depths at Mexico tunnel site

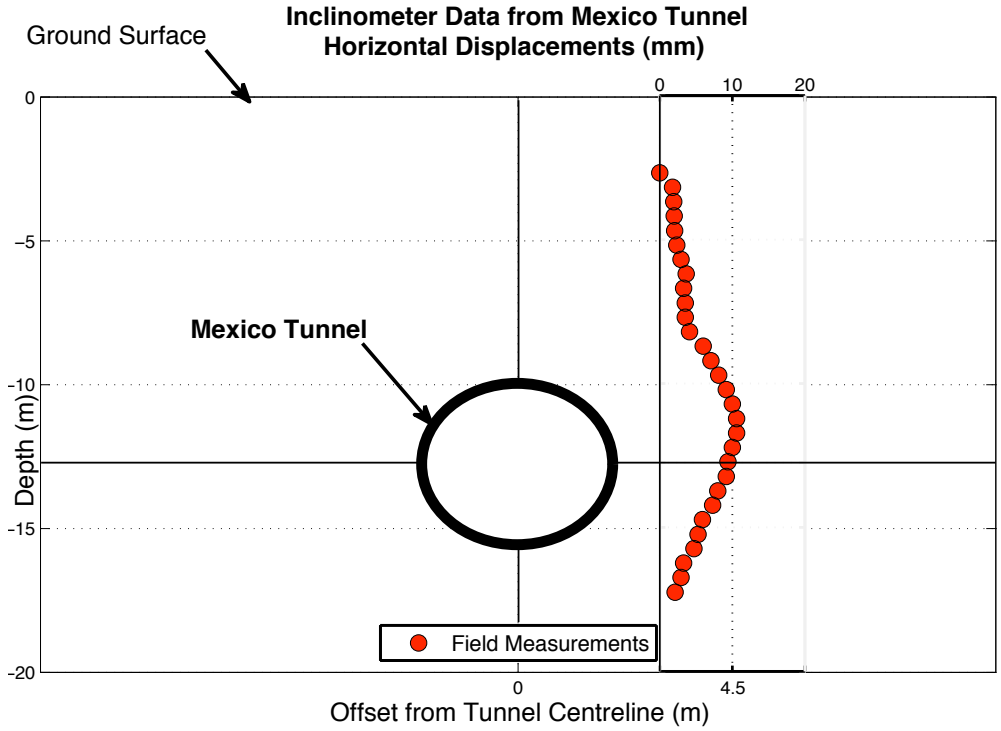

Figure 5.11: Horizontal Displacements recorded by inclinometer at x = 4.5m at Mexico Tunnel site

5.3.2 Application of proposed analytical solutions

The key geometric parameters for the sewer-line tunnel in Mexico City are:

- Depth to springline H = 12.75m
- Diameter 2R = 4m ➔ R = 2m
- Ratio R/H = 0.157

Assuming undrained condition and incompressibility of the soil we use Poisson's ratio $\nu = 0.5$. Note that this is different to the value used by Pinto (1999), $\nu = 0.12$.

An LSS error method is employed in order to optimize the cavity parameters (u_ε, u_δ) and at the same time evaluate Pinto's Case. The field measurements used in the LSS method include the surface and subsurface settlements and horizontal displacements at inclinometer position x = 4.5m (shown in Figures 5.9 to 5.11). Figures 5.12 – 5.14 summarize contour plots of the SS error for vertical, horizontal and total ground displacements and also Table 5.2 summarizes the results of the LSS error method (i.e. the LSS surface and global solutions and also the SS error produced by Pinto's Case). From Figure 5.14 we select the cavity parameters (u_ε, u_δ) that correspond to the LSS surface solution for total displacements and will be employed in the analysis:

LSS surface solution: (u_ε, u_δ) = (-22, 35) mm➔$\Delta V_L/V_0 = 2.2\%$, $\rho = 1.59$

In all three contour plots we observe that the LSS surface solution deviates from the LSS global solution for the Mexico Tunnel case as opposed to the Madrid Metro

analysis where the two LSS solutions coincided. Moreover, although Pinto's Case is very close to the LSS surface solution for total displacements, it doesn't lie exactly on the centreline settlement fit line, since it slightly underestimates the value of u_y^0 = 28.6mm recorded in the field. However, Pinto's proposed design scheme proved to be very effective in selecting appropriate cavity parameters for the Mexico tunnel case, since it lies very close to the optimum surface solution in the (u_ε, u_δ) state space. In the subsequent analysis, the parameters suggested by the LSS surface solution will be used for the simulation of the ground movements recorded in the field.

	Surface Solution			Global Solution			Pinto's Case (u_ε, u_δ) = (-22, 34)mm
	u_ε (mm)	u_δ (mm)	LSS (mm²)	u_ε (mm)	u_δ (mm)	LSS (mm²)	SS (mm²)
Vertical	3	48	2812	-17	21	1169	3260
Horizontal	-26	33	973	19	2	53	1019
Total	-22	35	4597	-13	23	1683	4279

Table 5.2: Summary of LSS method results for Mexico sewer tunnel

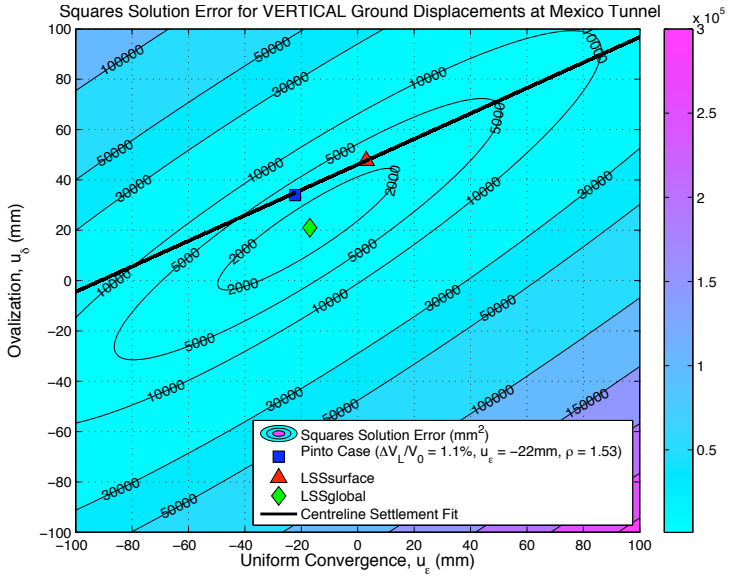

Figure 5.12: SS error for vertical displacements at Mexico Tunnel

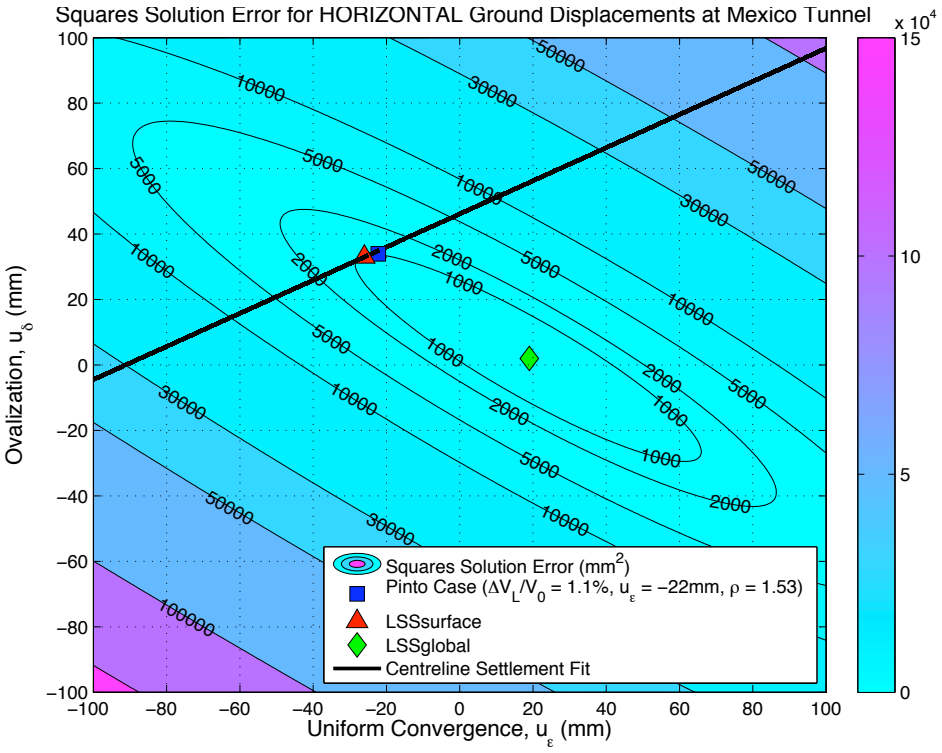

Figure 5.13: SS error for horizontal displacements at Mexico Tunnel

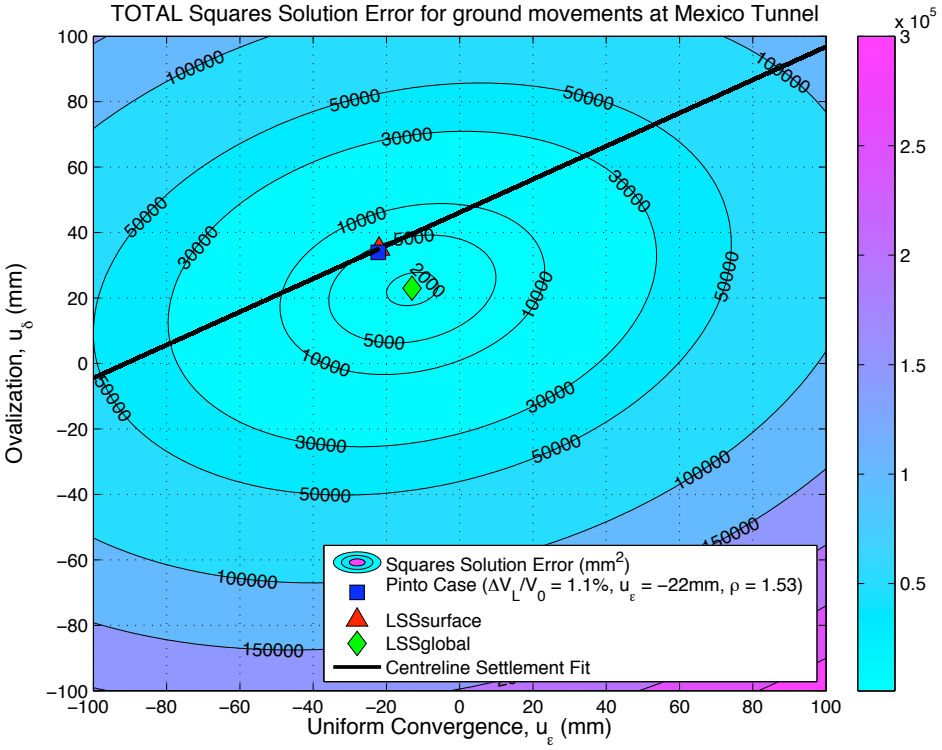

Figure 5.14: SS error for total displacements at Mexico Tunnel

5.3.2.1 Computed distribution of ground displacements

Figure 5.15 summarizes the computed distribution of vertical and horizontal ground displacements for the sewer line tunnel in Mexico City using the analytical LSS surface solution for total displacements. Surface settlements become smaller than 5mm at x/H ≈ 1. Right above the tunnel crown, the analytical solutions generate very large settlements (up to 70mm). Finally, below the tunnel cavity, heave up to 45mm is generated. Figure 5.15b shows that the analytical model predicts negative horizontal displacements at the surface that translate into inward movements towards the tunnel. Along the tunnel springline the analytical solutions generate positive horizontal displacements (i.e. outward) up to 25mm. Finally, below the tunnel cavity horizontal displacements of less than 5mm are computed.

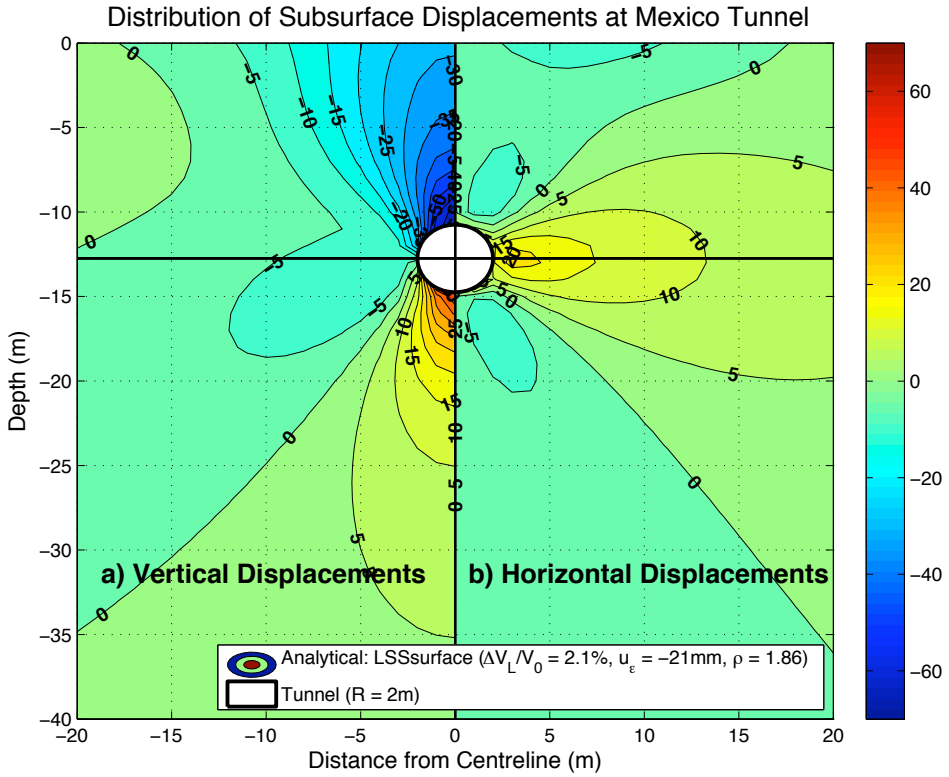

Figure 5.15: Contour Diagram of Subsurface Displacements for Mexico Tunnel

5.3.2.2 Computed and measured surface settlements

Figure 5.16 compares the computed and measured surface settlements for the Madrid Metro with the empirical Gaussian distribution (K = 0.5 ➔x_i = 6.4m). The analytical solutions and the Gaussian distribution produce very similar settlement troughs that have an excellent agreement with the field measurements. The analytical model produces a slightly narrower settlement trough comparing with the Gaussian fit and predicts a small heave ($u_y \approx 0.5$mm) in the far-field. Both models underestimate the recorded displacements for x> 15m, with a maximum deviation from the field data of less than 5mm.

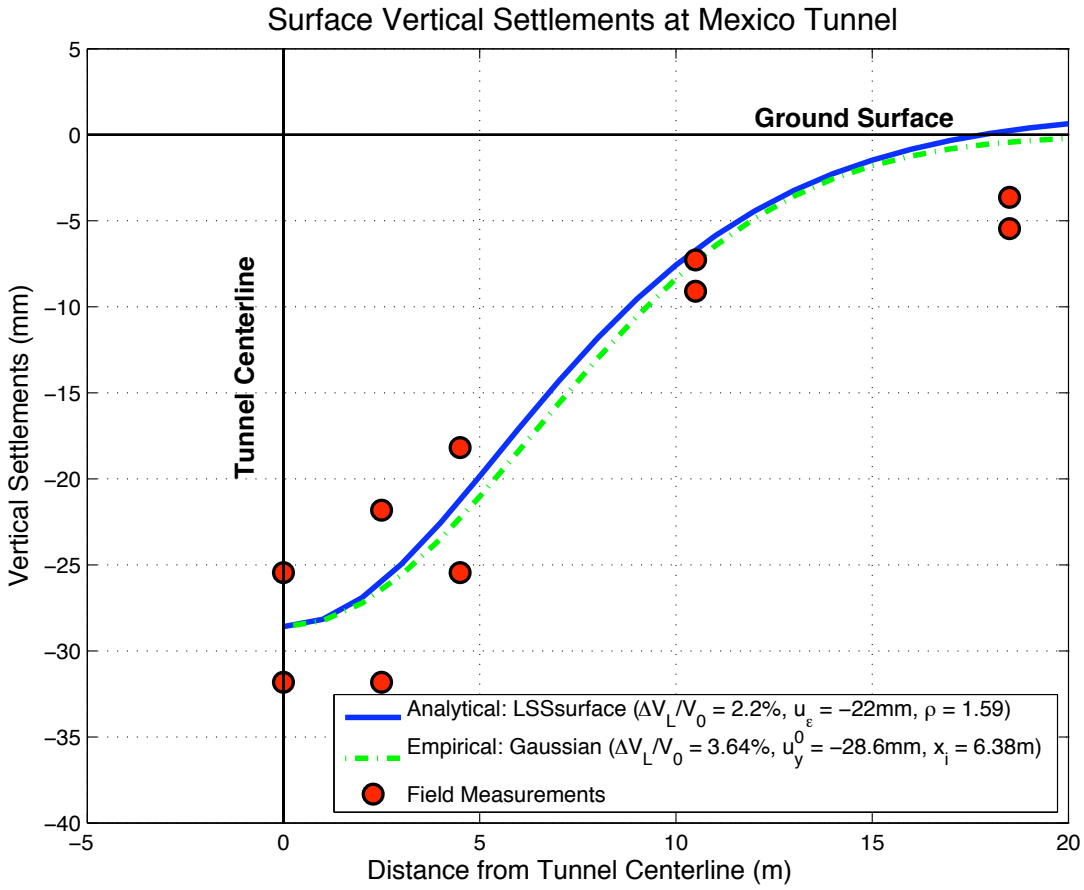

Figure 5.16: Measured and computed surface settlements for Mexico Tunnel

5.3.2.3 Computed and measured subsurface displacements

Figure 5.17 compares the analytically computed and measured settlement troughs at three elevations (y = 0, -5 and -10.15m) within the overlying clay layer. As already discussed, the results show excellent agreement between the computed and measured settlements at the surface. However, the analytical solutions tend to overestimate the measured movements along the tunnel centreline at y = -5m (by 10 - 20%) and gives a substantial overestimate (up to 70 – 100 %) at y = -10.15m. However, this latter result can be largely affected by the very close proximity of the measurement to the tunnel lining (60 cm distance), where soil plasticity most probably takes place.

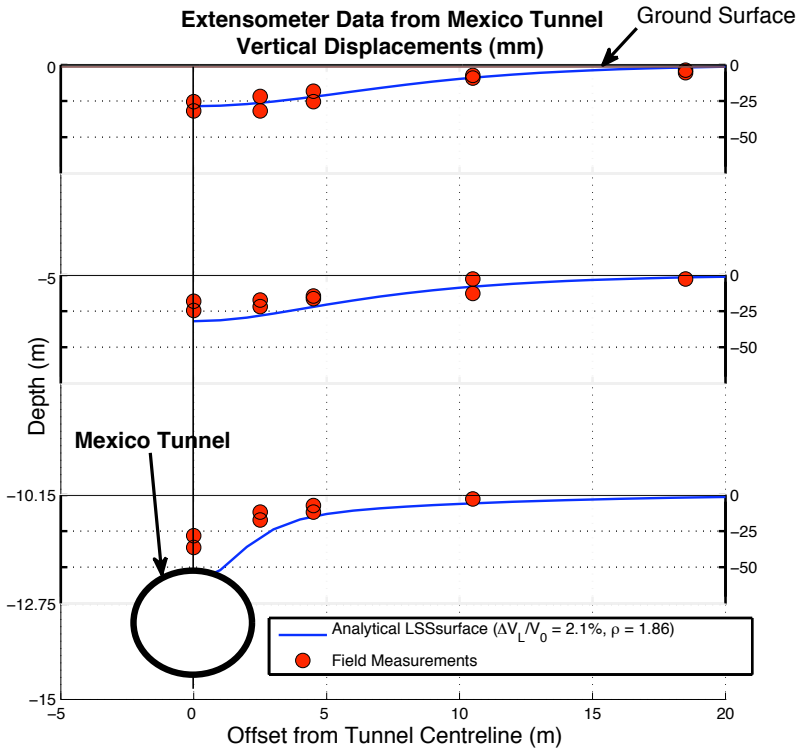

Figure 5.17: Computed and measured subsurface settlements at Mexico tunnel site

Figure 5.18 compares the analytically computed and measured lateral displacements at the inclinometer position x = 4.5m. Both the model predictions and the field data show outward movements near the tunnel elevation. However, in the shallow subsurface (y > -8m) the analytical solutions predict inward horizontal movements (towards the tunnel cavity) while the field data show small outward movements. The maximum horizontal displacement is predicted by the analytical solutions at the tunnel springline (y = -12.75m), while the maximum lateral movement was recorded at y ≈ -11.5m. Finally, the computed maximum horizontal displacement is slightly larger than the measured data (by less than 3mm).

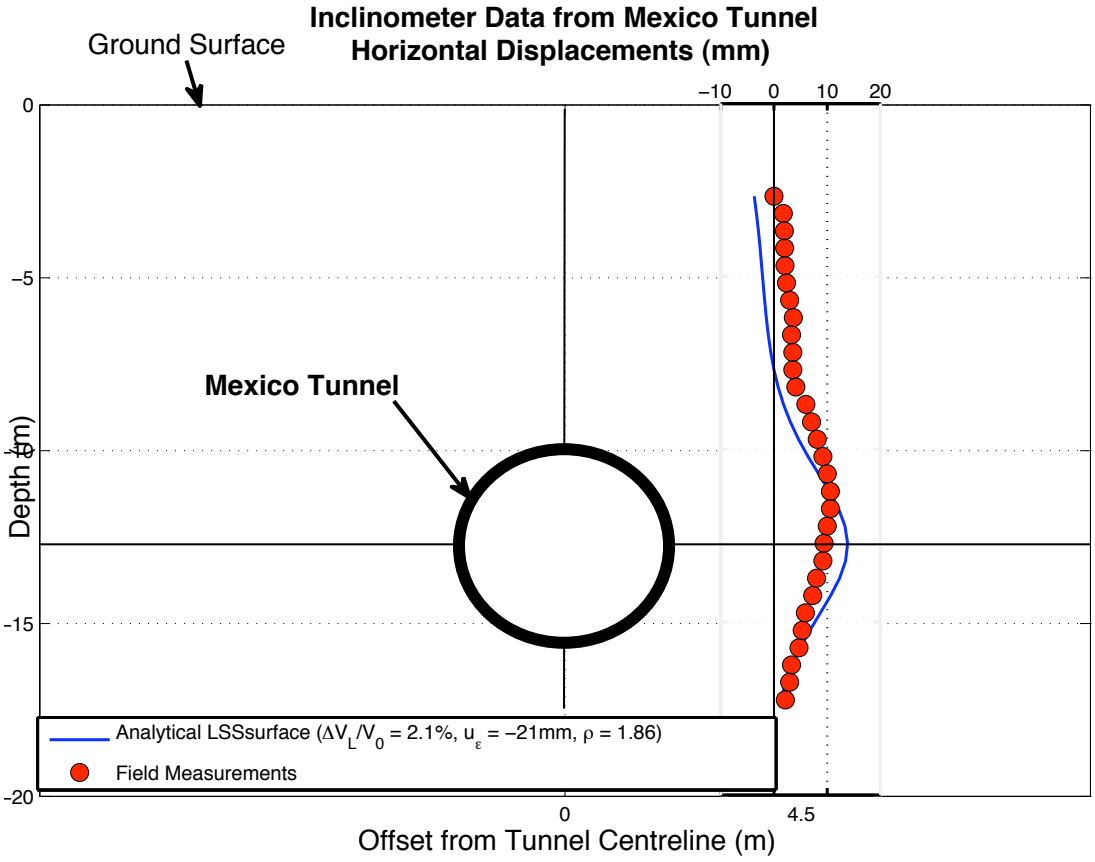

Figure 5.18: Computed and measured horizontal displacements at x = 4.5m at Mexico tunnel test site

5.3.3 Conclusions

The analytical solutions succeeded in simulating the ground displacements measured at the sewer-line tunnel in Mexico City. The LSS method showed that the input parameters suggested by Pinto (1999) coincide with the LSS surface solution for total displacements, and thus the design scheme proposed by Pinto and Whittle (2001) succeeded in selecting appropriate cavity parameters for the Mexico sewer tunnel. The surface settlement trough generated by the analytical solutions is very similar to the Gaussian fit and is in close agreement with the field measurements. However, the analytically computed subsurface settlements are larger than the measured data, especially at depth y = -10.15m which is probably within the zone of plasticity. Finally, the horizontal displacements measured by an inclinometer at x = 4.5m were very well described by the analytical model, with deviations from the field data less than 5mm.

5.4 N-2 contract tunnel for the San Francisco Clean Water Project

The construction of the N-2 contract tunnel for the San Francisco clean water project involved the use of an Earth Pressure Balance (EPB) tunnel boring machine for the first time in the US (Clough et al., 1983). Figure 2.11 shows a typical cross-section of the tunnel with radius, R = 1.78m located at a depth to springline, H = 9.6m. The soil profile at the tunnel cross-section considered herein comprises 6.6m of rubble fill underlain by a 7.1m layer of Recent Bay Mud, containing the tunnel and

underlain by colluvium and residual sandy clay. The current analysis considers the settlements and lateral deflections measured at one line of instrumentation (line 4; Clough et al., 1983) 15 days after the passage of the tunnel shield.

5.4.1 Field Measurements

Figure 5.19 summarizes the surface settlements measured in the field. The trough appears to be symmetric, with a maximum surface settlement u_y^0 = 30.6mm that takes place at the centreline (at x/H=0). Using the empirical Gaussian fit to model the surface settlements, with the trough width parameter K = 0.42 suggested by Clough et al. (1983), we obtain the curve shown in Figure 5.19. We observe that the field data are well matched by the Gaussian curve. The volume loss implied using the conventional interpretation of ground movements is $\Delta V_L/V_0$ = 3.70% as shown:

From equation (2.2) $$V_S = u_y{}^0 i\sqrt{2\pi} = 0.0306 \times 0.5 \times 9.6 \times \sqrt{2\pi} = 0.37\,\text{m}^2$$

From equation (2.3) $$\frac{\Delta V_L}{V_0} = \frac{V_S}{\pi R^2} = \frac{0.37}{\pi \times 1.78^2} = 3.70\%$$

Figure 5.20 summarizes the horizontal displacements recorded by an inclinometer located at x = -3.6m from the tunnel centreline. The measurements show outward movement away from the tunnel cavity. Moreover, the maximum horizontal displacement takes place 1m above the tunnel springline.

Pinto (1999), using his proposed design scheme to analyze the N-2 contract tunnel for the San Francisco clean water project, concluded that the optimum parameter set for the isotropic analytical solutions is:

Pinto's Case: $(u_\varepsilon, u_\delta) = (-20, 33)$ mm➔$\Delta V_L/V_0 = 2.2\%$, $\rho = 1.66$ and $v=0.5$

Therefore the volume loss $\Delta V_L/V_0 = 2.2\%$ suggested by Pinto (1999) is smaller than $\Delta V_L/V_0 = 3.70\%$ implied by the empirical method.

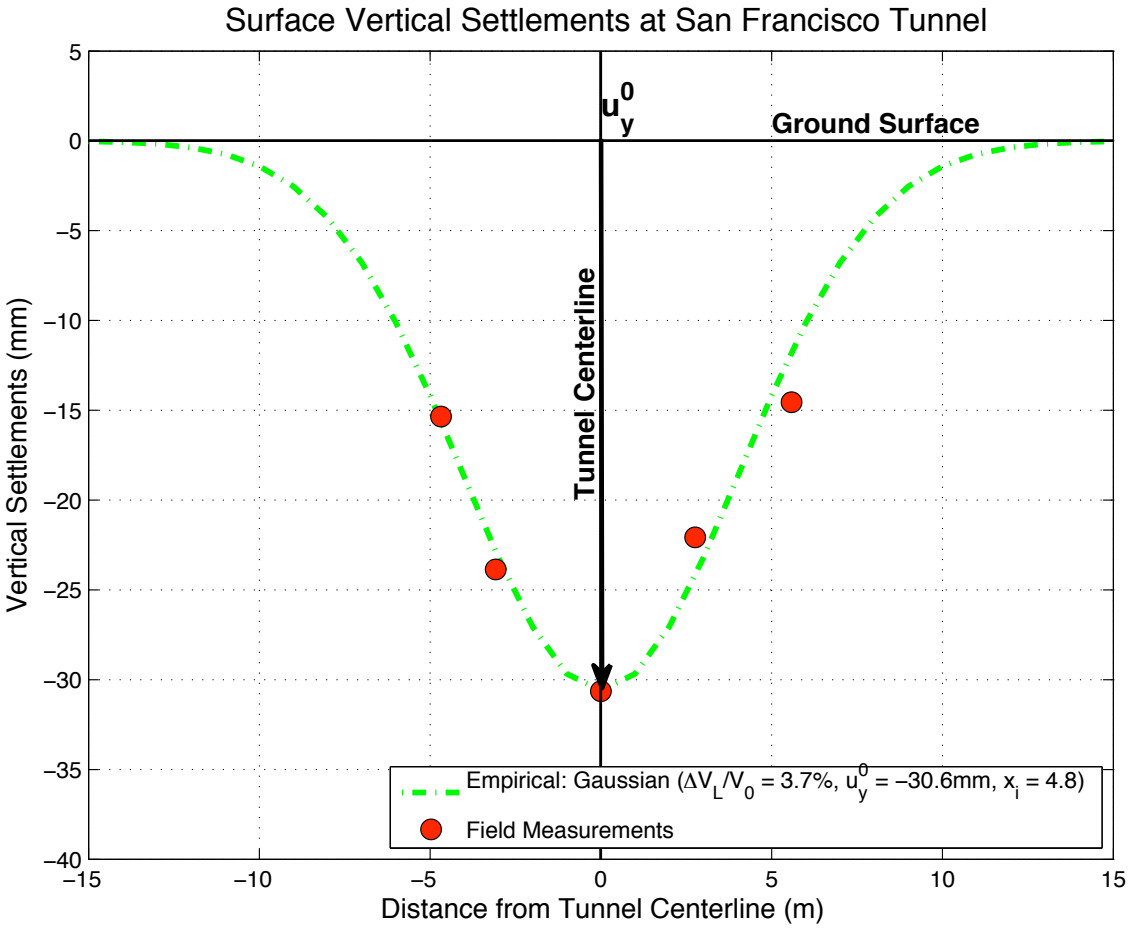

Figure 5.19: Surface Settlements measured at Mexico tunnel site and modeled by empirical Gaussian curve

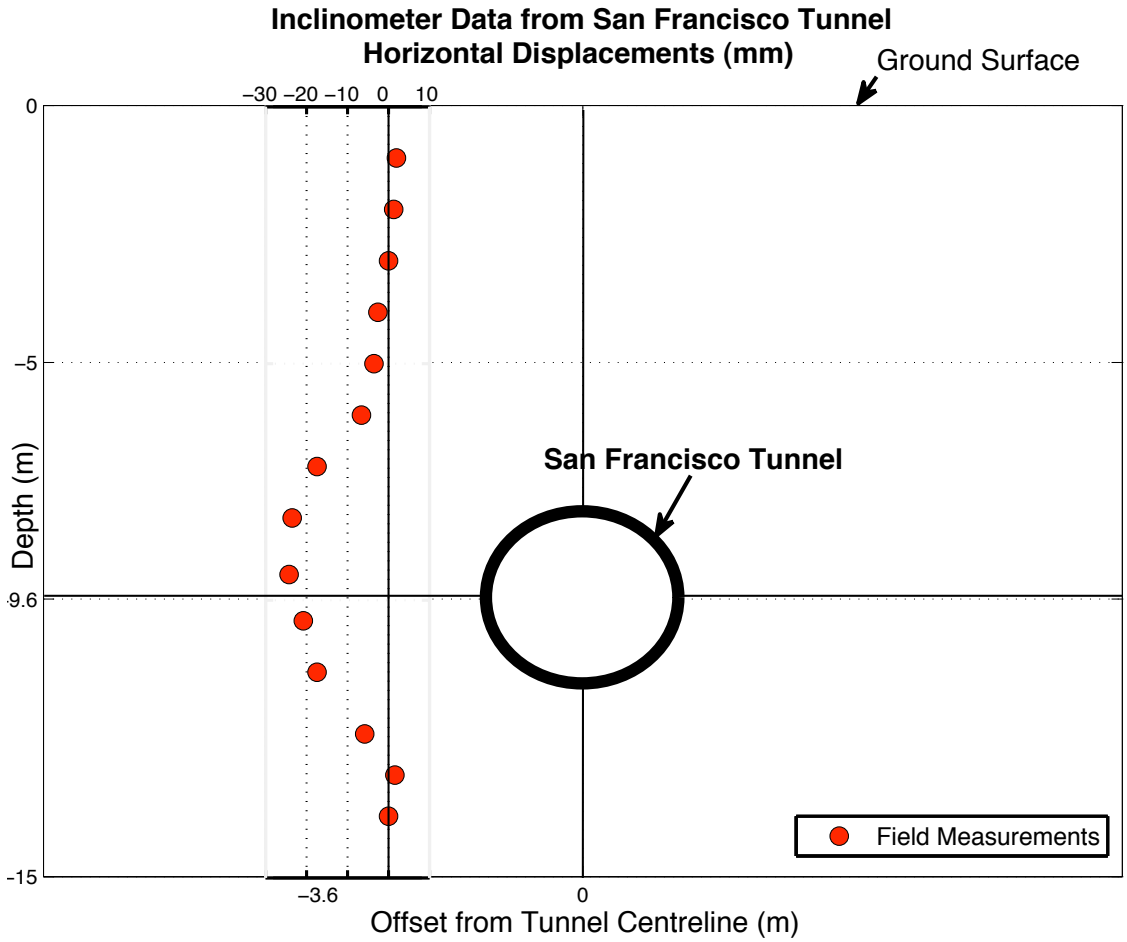

Figure 5.20: Horizontal Displacements recorded by inclinometer at x = -6.3m at San Francisco Tunnel site

5.4.2 Application of proposed analytical solutions

The key geometric parameters for the San Francisco Tunnel are:

- Depth to springline H = 9.6m
- Diameter 2R = 3.56m ➔ R = 1.78m
- Ratio R/H = 0.185

We assume that Poisson's ratio ν = 0.5, which is the value used by Pinto (1999).

An LSS error method is used in order to optimize the cavity parameters (u_ε, u_δ) and at the same time evaluate Pinto's Case. The field measurements used in the LSS method include the surface settlements and horizontal displacements at inclinometer position x = -6.3m (shown in Figures 5.19 and 5.20 respectively). Figures 5.21 to 5.23 summarize contour plots of the SS error for vertical, horizontal and total ground displacements and also Table 5.3 summarizes the results of the LSS error method (i.e. the LSS surface and global solutions and also the SS error produced by Pinto's Case). From Figure 5.23 we select the cavity parameters (u_ε, u_δ) that correspond to the LSS surface solution for total displacements and which will be employed in the analysis:

LSS surface solution: $(u_\varepsilon, u_\delta) = (-10, 37)$ mm➔$\Delta V_L/V_0 = 1.12\%$, $\rho = 3.7$

In the contour plots for vertical and total displacements the LSS surface solution nearly coincides with the LSS global solution. However, in the contour plot for horizontal displacements the two LSS solutions do not overlap, suggesting that the fit of the LSS surface solution will not be as good in the horizontal displacements as in the vertical distortions. Moreover, Pinto's Case is very close to the LSS surface solution for total displacements, and thus the LSS method suggests that Pinto's proposed design scheme is effective in selecting appropriate cavity parameters for the San Francisco tunnel case. In the subsequent analysis, both the parameters suggested by Pinto's Case and the LSS surface solution for total displacements will be used for the simulation of the ground movements recorded in the field, and their performances will be compared.

	Surface Solution			Global Solution			Pinto's Case (u_ε,u_δ) = (-20, 33)mm
	u_ε (mm)	u_δ (mm)	LSS (mm²)	u_ε (mm)	u_δ (mm)	LSS (mm²)	SS (mm²)
Vertical	-10	37	11	-15	33	9	24
Horizontal	-10	37	300	9	23	179	556
Total	-10	37	311	-8	35	290	580

Table 5.3: Summary of LSS method results for San Francisco N-2 Contract tunnel

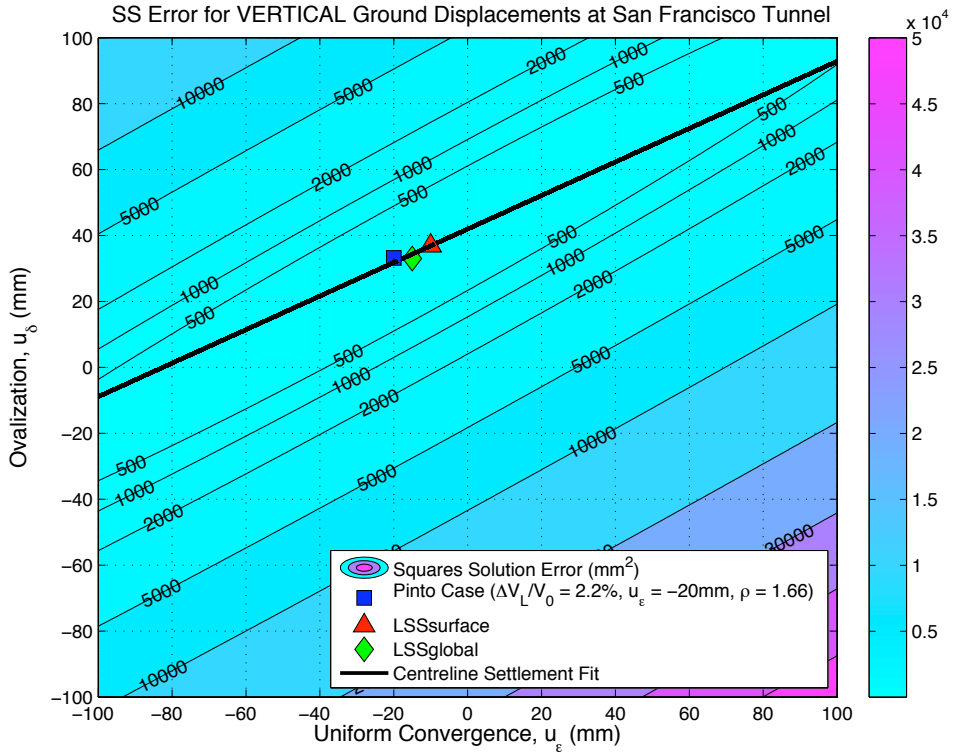

Figure 5.21: SS error for vertical displacements at San Francisco Tunnel

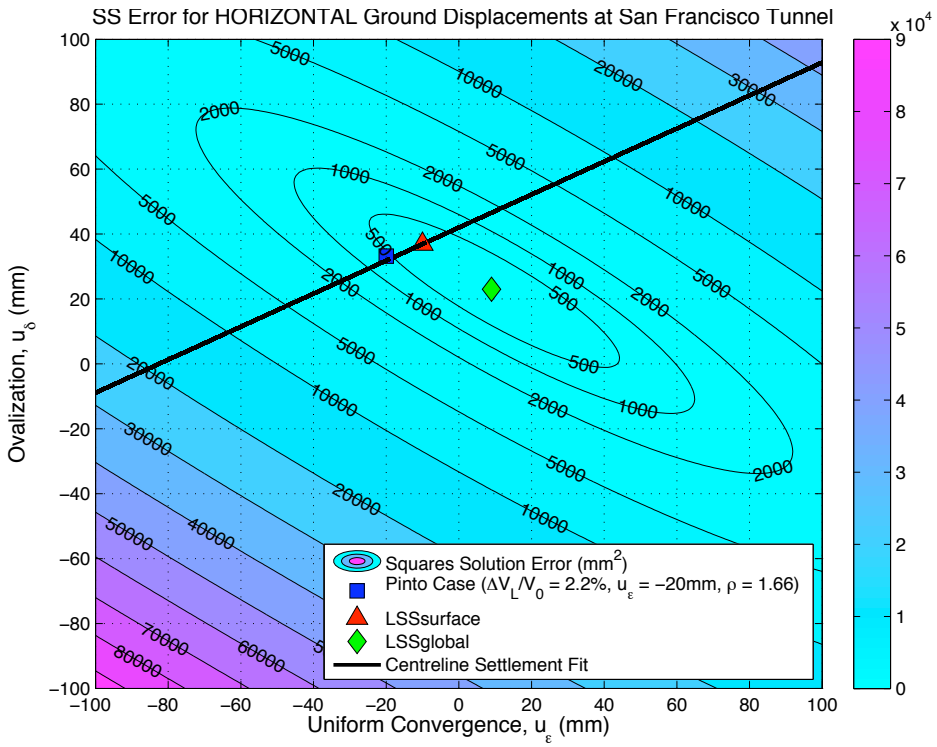

Figure 5.22: SS error for horizontal displacements at San Francisco Tunnel

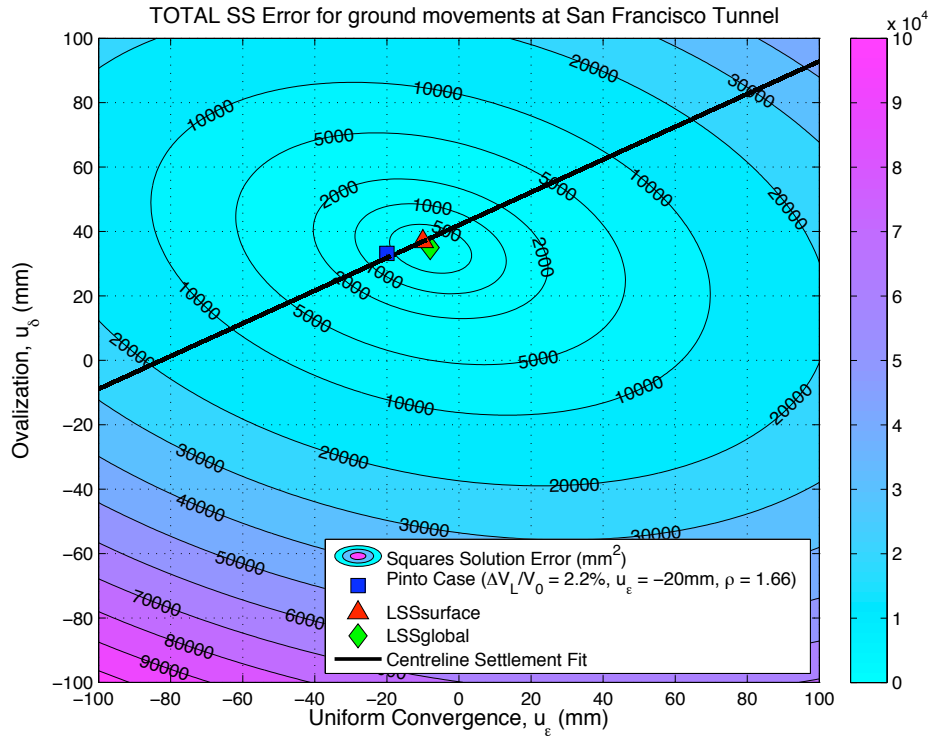

Figure 5.23: SS error for total displacements at San Francisco Tunnel

5.4.2.1 Computed distribution of ground displacements

Figures 5.24 and 5.25 summarize the computed distribution of vertical and horizontal ground displacements for the N-2 contract tunnel for the San Francisco clean water project, using two analytical parameters sets given by Pinto's Case and the LSS surface solution for total displacements. Above the tunnel springline the two models predict very similar distortions, with the LSS surface solution predicting slightly narrower settlement troughs. Along the tunnel centreline and above the tunnel cavity, Pinto's Case predicts slightly higher values. Below the tunnel cavity both models predict very small heave and the LSS surface solution predicts slightly higher displacements along the centreline (and below the cavity).

Figure 5.25 shows that the two analytical cases predict very similar movements at the surface. Moreover, along the tunnel springline, the analytical solutions predict outward movements away from the tunnel cavity, with the LSS surface solution predicting larger values (differences up to 3mm). Finally, below the tunnel, the two solutions predict similar lateral displacements that of very small magnitude.

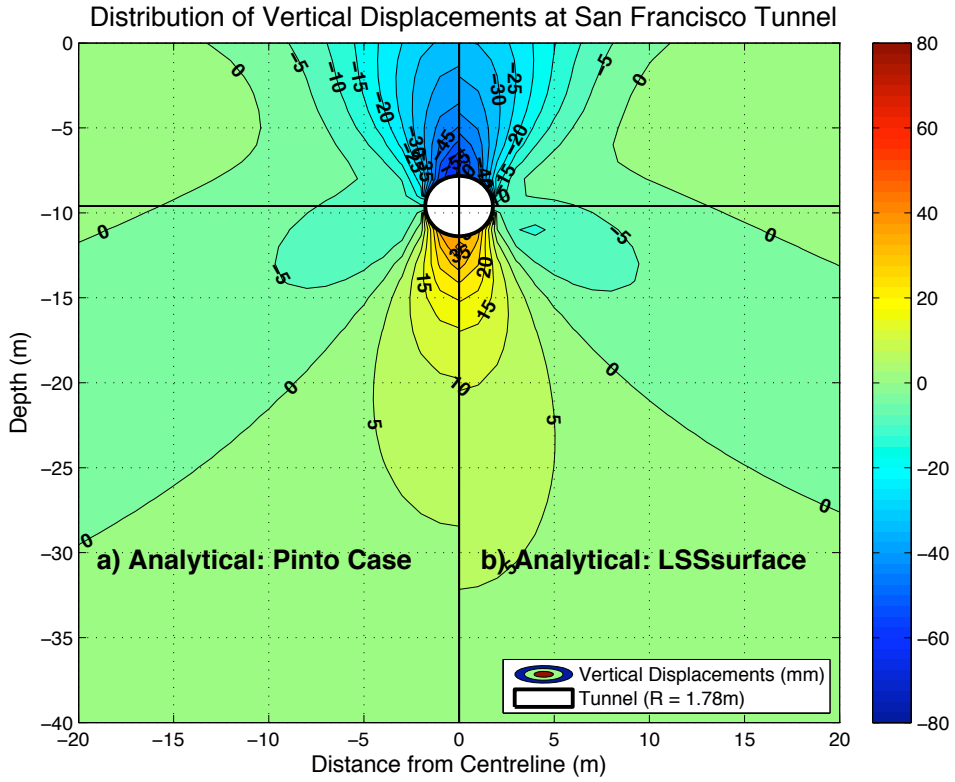

Figure 5.24: Contour Diagram of Vertical Displacements at San Francisco Tunnel

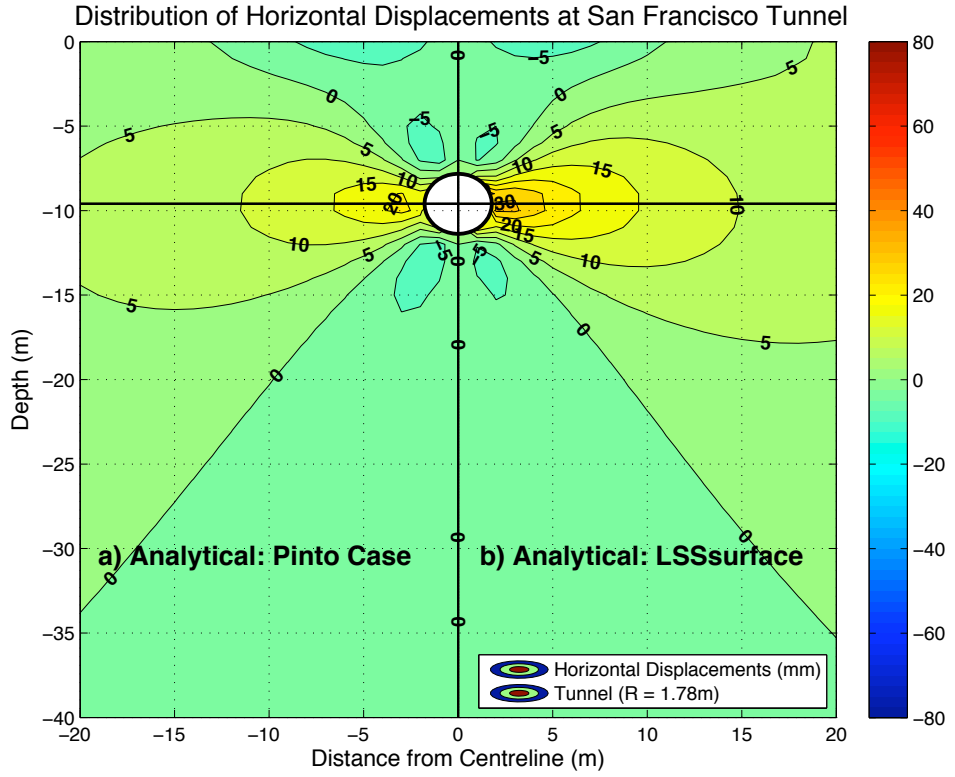

Figure 5.25: Contour Diagram of Horizontal Displacements at San Francisco Tunnel

5.4.2.2 Computed and measured surface settlements

Figure 5.26 compares the analytically computed and measured surface settlements for the San Francisco tunnel, with the empirical Gaussian distribution (K = 0.42). From the centreline and up to x ≈ 10m, the analytical solutions and the Gaussian distribution produce very similar settlements, which are in very good agreement with the measured data (differences less than 3mm). The LSS surface solution produces a settlement trough that is slightly narrower than Pinto's Case, and provides a closer fit to the field data. Moreover, Pinto's Case slightly overestimates the surface centerline settlement u_y^0. Both analytical solutions predict a small heave in the far-field (u_y ≈ 2mm for Pinto's Case and 3mm for the LSS surface solution), as opposed to the Gaussian curve that converges to zero settlement for x > 10m.

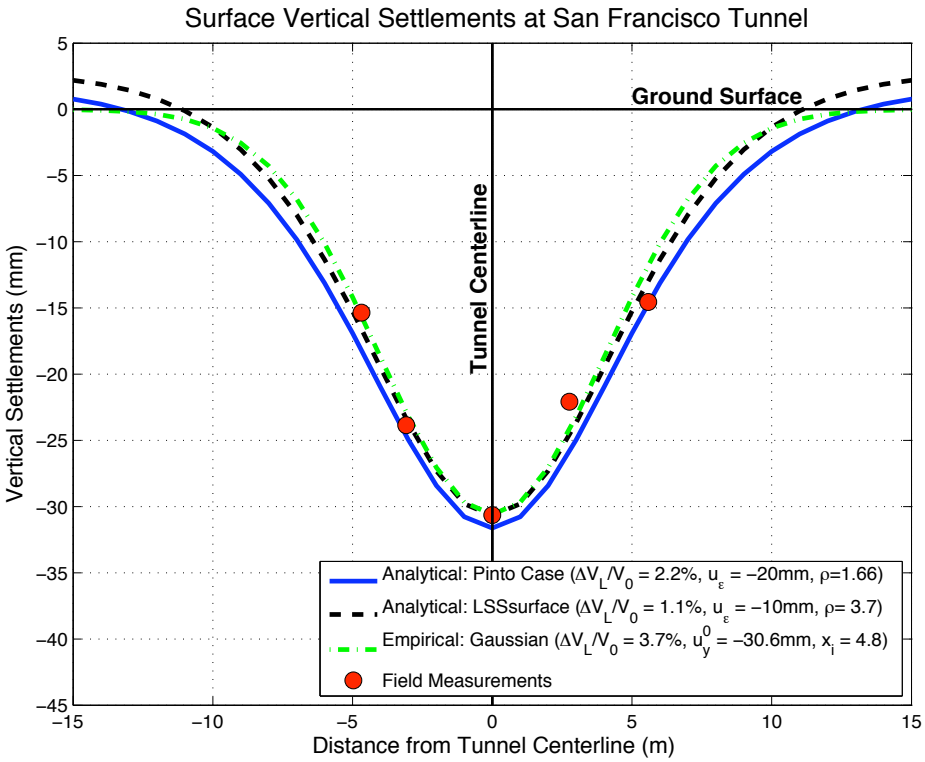

Figure 5.26: Measured and computed surface settlements at San Francisco Tunnel

5.4.2.3 Computed and measured subsurface horizontal displacements

Figure 5.27 compares the analytically computed and measured lateral displacements at the inclinometer position x = -3.6m. The two sets of analytical solutions predict very similar horizontal movements at the shallow subsurface (y > -5m) and at large depths (y < -13m), which successfully match the measured displacements. The field data show that maximum horizontal movement $u_{x,max}$ took place 1m above the springline while the analytical solutions predict $u_{x,max}$ along the tunnel springline. The LSS surface solution predicts a larger $u_{x,max}$ than Pinto's Case (5 mm difference), which is closer to the recorded value, while at the same time it provides a better fit to the measured displacements from the springline and up to y = -5m. The reason why Pinto's Case underpredicts $u_{x,max}$ is because, the proposed reference field measurements used in his analysis restricts the analytical solutions to fit the horizontal displacement measured at the springline, which corresponds to the maximum lateral displacement in the analytical solutions. However, as we already saw in the Mexico and San Francisco tunnels, $u_{x,max}$ does not always take place along the tunnel elevation and therefore the hypothesis used in Pinto's proposed scheme (maximum lateral displacement taking place along the tunnel springline) is not always true.

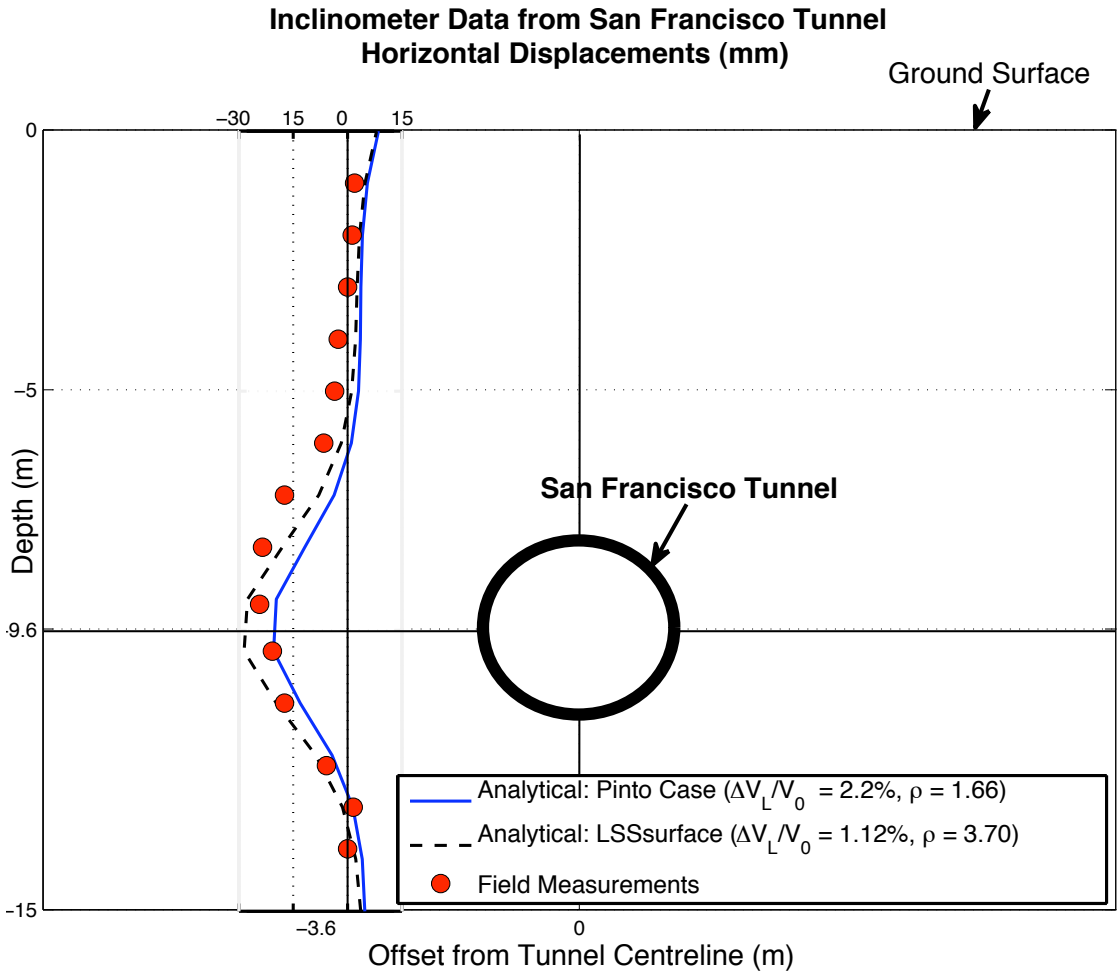

Figure 5.27: Computed and measured horizontal displacements at x = -3.6m at San Francisco Tunnel

5.4.3 Conclusions

The analytical solutions succeeded in simulating the ground displacements measured at the N-2 contract tunnel for the San Francisco clean water project. The LSS method showed that the input parameters suggested by Pinto (1999) are close to the LSS surface solution for total displacements, and thus the design scheme proposed by Pinto and Whittle (2001) succeeded in selecting appropriate cavity

parameters for the San Francisco tunnel. Comparisons of the ground displacements produced by Pinto's Case and the LSS surface solution with the movements measured in the field showed that the analytical solutions succeeded in simulating the ground distortions induced by the San Francisco tunnel. The two analytical cases produced very similar results, with the LSS surface solution performing slightly better than Pinto's Case. The surface settlement trough produced by the LSS surface solution was slightly narrower and closer to the field data, comparing to the trough produced by Pinto's Case. Both analytical solutions generated a small heave in the far field, with the LSS surface solution producing a slightly larger leave than Pinto's Case (~1mm difference). Finally, the analytical solutions successfully described the lateral displacements recorded at an inclinometer positioned at x = -3.6m. However, they predicted maximum horizontal displacement taking place along the tunnel springline, while the field data showed the same value taking place 1m above the tunnel elevation.

Pinto's Case underpredicted the value of $u_{x,max}$ and was probably due to his proposed 'reference field measurements', that set $u_{x,max}$ equal to the lateral displacement that was measured at the springline.

5.5 Conclusions from Chapter 5

The analytical solutions succeeded in simulating the vertical and horizontal ground displacements measured at three tunnel sites: 1) Madrid Metro extension project, 2) Mexico City sewer-line tunnel and 3) N-2 contract tunnel for the San Francisco clean water project. The LSS method showed that the input parameters suggested by Pinto (1999) for the three tunnel cases nearly coincide with the LSS surface solution for total displacements and thus the design scheme proposed by Pinto and Whittle (2001) succeeded in selecting appropriate cavity parameters. The largest discrepancy between the computed movements and field measurements was observed in the subsurface settlements induced by the Mexico sewer tunnel excavation. However, the close proximity of the tunnel to the measurement elevation (less than 60cm distance) suggests that this large difference was probably caused due to soil plasticity.

Chapter 6

Summary, Conclusions and Recommendations for future work

6.1 Summary

The goal of this study was to evaluate the effectiveness of analytical solutions in modeling ground deformations induced by the construction of tunnels. Two sets of analytical solutions were considered: 1) Analytical solutions, proposed by Pinto and Whittle (1999), which assume isotropic soil stiffness parameters and; 2) analytical solutions developed by Chatzigiannelis and Whittle (2001), that assume cross-anisotropic soil stiffness parameters.

The analytical solutions were applied to five tunnel cases that used different construction techniques and were excavated in varying soil types. The control study of the thesis was the westbound tunnel of the Jubilee Line Extension (JLE) project in London, were extensive field monitoring had taken place (Nyren et al, 1997). Other tunnels that were analyzed include the Heathrow Express (HEX) trial tunnel, the Madrid Metro extension project, a sewer line tunnel in Mexico Cityand the N-2 contract tunnel for the San Francisco clean water project.

The performance of the analytical solutions was evaluated by using a Least Squares Solution (LSS) method that measured the difference between the computed and measured displacements. Moreover, this LSS procedure optimized the selection of model input parameters that best matched the field data.

6.2 Conclusions

The analytical solutions proved to be very effective in describing ground deformations induced by different tunneling techniques and in various site conditions. For the cases of the tunnels in London Clay (westbound JLE tunnel and HEX trial tunnel), the isotropic solutions succeeded in modeling settlements that were recorded in the field but didn't produce very close fits to the measured lateral displacements. Incorporating anisotropic stiffness parameters significantly improved the results and this is one of the major findings of this work.

For the cases of the Madrid Metro extension project, Mexico City sewer-line tunnel and the N-2 contract tunnel in San Francisco, the LSS method was employed for checking Pinto's (1999) proposed parameter optimization. The LSS method showed that Pinto's design methodology was successful in selecting appropriate cavity input parameters for the isotropic solutions.

Table 6.1 summarizes best estimates of cavity input parameters used in the modeling of the five tunnels using isotropic analytical solutions. The volume losses generated by the five tunnel excavations range from $\Delta V_L/V_0$ = 0.54 – 2.10, with the smallest volume loss generated by HEX Type 1 tunnel and the largest $\Delta V_L/V_0$ induced by the Mexico City sewer line tunnel. Moreover, the relative distortions estimated for the five tunnel cases range from ρ = 0.21 – 3.70, with the smallest relative distortion induced by HEX Type 2 tunnel while the largest was generated by the San Francisco N-2 contract tunnel. The number of tunnels analyzed is not

sufficient in order to draw generalized conclusions regarding the influence of contruction method and clay type on the analytical model input parameters.

Tunnel	Construction Method	$\Delta V_L/V_0$ (%)	ρ
JLE WB	Open Face	1.80	2.51
HEX Type 1	Open Face	0.54	2.69
HEX Type 2	Open Face	1.32	0.36
HEX Type 3 (25 May)	Open Face	1.46	0.57
HEX Type 3 (29 May)	Open Face	1.98	0.44
Madrid Metro	Open Face	0.63	0.21
Mexico sewer-line	Closed Face	2.10	1.86
San Francisco N-2	Closed Face	1.12	3.70
All tunnels were excavated through clay and Poisson's ratio ν = 0.5 was assumed throughout			

Table 6.1: Summary of input parameters used in isotropic analytical solutions for 5 tunnel examples

6.3 Recommendations for future work

The current study could be further advanced by applying the analytical solutions to a large number of tunnels around the world, of different construction methods and soil properties. Using the LSS method to obtain optimum cavity parameters, a database could be created, that would indicate the relative distortion, ρ and volume loss, $\Delta V_L/V_0$ corresponding to specific soil types and tunneling methods. This database will be useful during the design phase of a new tunnel, as it will enable the selection of appropriate input parameters, corresponding to the particular construction method and soil properties of the tunnel. This will subsequently transform the analytical solutions to a powerful tool for predicting ground distortions, prior to construction of the tunnel and before any field measurements have been undertaken. This will be a significant improvement and will benefit the tunneling design process, since ground movements and their potential influence on surrounding structures will be assessed well in advance.

References

Attewell, P. B., Glossop, N. H. & Farmer, I. W. (1978) "Ground deformations caused by tunneling in a silty alluvial clay," *Ground Engineering,* Vol. 11, No 8, 32-41.

Chatzigiannelis, Y. & Whittle, A.J. (2001) "Analysis of ground deformations caused by shallow tunneling in cross-anisotropic soil," *submitted for publication.*

Clough, G. W., Sweeny, B. P. & Finno, R. J. (1983) "Measured soil response to EPB shield tunneling," *Journal of Geotechnical Engineering, ASCE,* 109 (2), February, 131-149.

Clough, G. W. & Leca, E. (1989) "With focus on use of finite element methods for soft ground tunneling," *Review paper in Tunnels et Micro-Tunnels en Terrain Meuble-du Chantier a la Theorie*, Presse de l'Ecole Nationale des Ponts et Chaussees, Paris, 531-573.

Cording, E. J. & Hansmire, W. H. (1975) "Displacements around soft ground tunnels," *General Report 5th Pan American Conference on Soil Mechanics and Foundation Engineering Buenos Aires*, Session IV, 571-632.

Cuccovillo, T. & Coop, M. R. (1997), "The measurement of local axial strains in triaxial tests using LVDTs," *Géotechnique,* 47(1), 167-171.

Deane, A. P. & Bassett, R. H. (1995), "The Heathrow Express trial tunnel," *Proc. Inst. Civ. Engrs Geotechnical Engng,* 113, July, 144-156

Franzius, J. N., Potts, D. M. & Burland, J. B. (2005) "The influence of soil anisotropy and K0 on ground movements resulting from tunnel excavation," *Géotechnique,* 55(3), 189-199.

Gasparre, A., Nishimura, S., Minh, N. A., Coop, M. R. & Jardine, R. J. (2007), "The stiffness of natural London Clay," *Géotechnique,* 57(1), 33-47.

Graham, J. & Houlsby, G. T. (1983) "Anisotropic elasticity of a natural clay," *Géotechnique,* 33(2), 165-180.

Lee, K. M. & Rowe, R. K. (1989) "Deformations caused by surface loading and tunneling: the role of elastic anisotropy," *Géotechnique,* 39(1), 125-140.

Mair, R. J., Gunn, M. J. & O'Reilly, M. P. (1981) "Ground movements around shallow tunnels in soft clay," *10th International Conference on Soil Meachnics and Foundation Engineering,* Stockholm, (1), 323-328.

Mair, R. J., Taylor, R. N. & Bracegirdle, A. (1993), "Subsurface settlement profiled above tunnels in clay," *Géotechnique,* 43(2), 315-320.

Mair, R.J. & Taylor, R.N. (1997) "Bored tunnelling in the urban environment," *Proc. 14th Intl. Conf. Soil Mechs. & Found. Engrg*, Hamburg, (4), 2353-2385.

Moller, S. (2006), "Tunnel induced settlements and structural forces in linings," *PhD thesis*, Institut fur Geotechnik der Universitat Stuttgart.

Nyren, R. J. (1998), "Field measurements above twin tunnels in London Clay," *PhD thesis*, Imperial College, University of London.

O'Really, M. P. & New, B. M. (1982) "Settlements above tunnels in the United Kingdom – their magnitude and prediction," *Tunnelling 82,* London, IMM, 173-181.

Peck, R. B. (1969) "Deep excavations and tunneling in soft ground," *Proc. 7th International Conference Soil Mechanics and Foundation Engineering,* Mexico City, State of the Art Volume, 225-290.

Pennington, D. S., Nash, D. F. T. & Lings, M. L. (1997) "Anisotropy of G_0 shear stiffness of Gault clay," *Géotechnique,* 47(3), 391-398.

Pinto, F. (1999) "Analytical methods to interpret ground deformations due to soft ground tunneling," *S.M Thesis*, Dept. of Civil and Environmental Engineering, MIT, Cambridge, MA.

Pinto, F. & Whittle, A.J. (2001) "Evaluation of analytical solutions for predicting deformations around shallow tunnels in soft ground," *submitted for publication.*

Romo, M. P. (1997) "Soil movements induced by slurry shield tunneling," *Proceedings of the 14th International Conference on Soil Mechanics and Foundation Engineering*, Hambourg, 3, 1473-1481.

Sagaseta, C. (1987) "Analysis of undrained soil deformation due to ground loss," *Géotechnique,* 37(3), 301-320.

Sagaseta, C. & González, C. (2000) "Predicción teórica de subsidencias," *Chapter 6.2 Aspectors Geotécnicos de la Ampliación del Metro de Madrid.*

Schmidt, B. (1969) "Settlements and ground movements associated with tunneling in soils," *PhD Thesis,* University of Illinois, Urbana.

Simpson, B., Atkinson, J. H. & Jovicic, V. (1996) "The influence of anisotropy on calculations of ground settlements above tunnels," Proc. International Symposium on *Geotechnical Aspects of Underground Construction in Soft Ground*, London (eds. R. J. Mair & R. N. Taylor) Balkema, 591-595.

Skempton, A. W. & Henkel, D. J. (1957), "Tests on London Clay from deep borings at Paddington, Victoria and the South Bank," *Proc. 4th Int. Conf. Soil Mech. Found. Engng,* London (1), 100-106.

Standing, J. R. & Burland, J. B. (2006), "Unexpected tunnelling volume losses in the Westminster area, London," *Géotechnique,* 56(1), 11-26.

Verruijt, A. and Booker, J.R. (1996) "Surface settlements due to deformation of a tunnel in an elastic half plane," *Géotechnique,* 46(4), 753-756.

Verruijt, A. (1997) "A Complex Variable Solution for a Deforming Tunnel in an Elastic Half-Plane," *International Journal for Numerical and Analytical Methods in Geomechanics*, 21, 77-89.

Whittle, A.J. & Sagaseta, C. (2001) "Analyzing the effects of gaining and losing ground," *ASCE Journal of Geotechnical & Geoenvironmental Engineering*, 255-290, (doi 10.1061/40659(2003)9).

Wongsaroj, J. (2005), "Three-dimensional finite element analysis of short and long-term ground response to open-face tunneling in stiff clay," *PhD thesis*, Hughes Hall, University of Cambridge.

Appendix I

- **Derivation of Analytical Solutions for tunnel in Cross-Anisotropic half-plane (Chatzigiannelis and Whittle, 2001)**

In cross-anisotropic media, with x-y being the plane of anisotropy, the linear relation that relates the strains to the stresses (commonly known as Hooke Law) is:

$$\begin{Bmatrix} \varepsilon_x \\ \varepsilon_y \\ \varepsilon_z \\ \gamma_{yz} \\ \gamma_{zx} \\ \gamma_{xy} \end{Bmatrix} = \begin{bmatrix} \frac{1}{E_h} & -\frac{\nu_{hh}}{E_h} & -\frac{\nu_{vh}}{E_v} & 0 & 0 & 0 \\ -\frac{\nu_{hh}}{E_h} & \frac{1}{E_h} & -\frac{\nu_{vh}}{E_v} & 0 & 0 & 0 \\ -\frac{\nu_{hv}}{E_h} & -\frac{\nu_{hv}}{E_h} & \frac{1}{E_v} & 0 & 0 & 0 \\ 0 & 0 & 0 & \frac{1}{G_{vh}} & 0 & 0 \\ 0 & 0 & 0 & 0 & \frac{1}{G_{vh}} & 0 \\ 0 & 0 & 0 & 0 & 0 & \frac{1}{G_{hh}} \end{bmatrix} \begin{Bmatrix} \sigma_x \\ \sigma_y \\ \sigma_z \\ \tau_{yz} \\ \tau_{zx} \\ \tau_{xy} \end{Bmatrix} \qquad \text{(I.1a)}$$

where

E_v Young's modulus in the vertical direction

E_h Young's modulus in (any) horizontal direction

ν_{vh} Poisson's ratio for the effect of vertical strain on horizontal strain

ν_{hh} Poisson's ratio for the effect of horizontal strain on complementary horizontal strain

ν_{hv} Poisson's ratio for the effect of horizontal on vertical strain

G_{vh}= G_{hv} Shear modulus for strain in (any) vertical plane (planes of anisotropy)

G_{hh} Shear modulus for strain in the horizontal plane (plane of isotropy)

Of these 7 engineering properties only 5 are independent for an elastic body: E_v, E_h, ν_{vh}, ν_{hh} and G_{vh}. For the remaining 2 the following relations are valid:

$$\nu_{hv} = \nu_{vh} \frac{E_h}{E_v} \tag{I.2}$$

$$G_{hh} = \frac{E_h}{2(1+\nu_{hh})} \tag{I.3}$$

Two commonly used ratios that measure the degree of anisotropy of a soil are:

$$n = \frac{E_h}{E_v}; \quad m = \frac{G_{vh}}{E_v}$$

Note that equation 2A.1a can be rewritten as follows:

$$\begin{Bmatrix} \varepsilon_x \\ \varepsilon_y \\ \varepsilon_z \\ \gamma_{yz} \\ \gamma_{zx} \\ \gamma_{xy} \end{Bmatrix} = \begin{bmatrix} \alpha_{11} & \alpha_{12} & \alpha_{13} & 0 & 0 & 0 \\ \alpha_{21} & \alpha_{22} & \alpha_{23} & 0 & 0 & 0 \\ \alpha_{31} & \alpha_{32} & \alpha_{33} & 0 & 0 & 0 \\ 0 & 0 & 0 & \alpha_{44} & 0 & 0 \\ 0 & 0 & 0 & 0 & \alpha_{55} & 0 \\ 0 & 0 & 0 & 0 & 0 & \alpha_{66} \end{bmatrix} \begin{Bmatrix} \sigma_x \\ \sigma_y \\ \sigma_z \\ \tau_{yz} \\ \tau_{zx} \\ \tau_{xy} \end{Bmatrix} \tag{I.1b}$$

Taking into account thermodynamic considerations (such as always positive strain energy), there are certain restrictions posed to the possible values of the elastic constants (Barden 1963, Pickering 1970, Lekhnitskii 1977):

G_{hv}, E_v, E_h >0

$0 < n < 4$

$-1 < \nu_{hh} < 1$

$\nu_{hh} + 2\,\nu_{hv}\,\nu_{vh} < 1$

Barden (1963), who presented the solution to the Boussinesq problem for the plane strain cross-anisotropic case, concludes that vertical stresses σ_z and shear stresses τ_{zx}, do not depend much on the three Poisson's ratios. However, the magnitude and the spatial distribution of the horizontal stresses are affected by the values of the Poisson's ratios.

Gazetas (1982) who studied the loading of cross-anisotropic soil under axisymmetric parabolic load showed that surface displacements and stress distributions depend much on the cross-anisotropic elastic parameters, and especially on moduli ratio m and Poisson's ratio ν_{vh}. Lee and Rowe (1989) and Simpson et al (1996) addressed the problem of surface settlement due to tunneling construction activities in soft ground and the effect of soil anisotropy. Both concluded that the settlement trough (shape and magnitude) seemed to be highly dependent on m.

Plane-strain cross-anisotropic soils

Plane-strain deformation is a 2D elasticity problem that assumes w=0 and also that no changes occur in any stress or strain with respect to z-axis $\left(\frac{\partial}{\partial z}=0\right)$ (Milne-Thompson, 1960). As a result only u, v, ε_x, ε_y, γ_{xy}, σ_x, σ_y, τ_{xy} are non-zero. From equation (2A.1b) we thus obtain

$$\begin{Bmatrix}\varepsilon_x\\ \varepsilon_y\\ 0\\ 0\\ 0\\ \gamma_{xy}\end{Bmatrix}=\begin{bmatrix}\alpha_{11} & \alpha_{12} & \alpha_{13} & 0 & 0 & 0\\ \alpha_{21} & \alpha_{22} & \alpha_{23} & 0 & 0 & 0\\ \alpha_{31} & \alpha_{32} & \alpha_{33} & 0 & 0 & 0\\ 0 & 0 & 0 & \alpha_{44} & 0 & 0\\ 0 & 0 & 0 & 0 & \alpha_{55} & 0\\ 0 & 0 & 0 & 0 & 0 & \alpha_{66}\end{bmatrix}\begin{Bmatrix}\sigma_x\\ \sigma_y\\ 0\\ 0\\ 0\\ \tau_{xy}\end{Bmatrix} \tag{I.4a}$$

$$\therefore \quad \begin{Bmatrix}\varepsilon_x\\ \varepsilon_y\\ \gamma_{xy}\end{Bmatrix}=\begin{bmatrix}\alpha_{11}-\frac{a_{13}^{\,2}}{\alpha_{33}} & \alpha_{12}-\frac{a_{13}a_{23}}{\alpha_{33}} & 0\\ \alpha_{12}-\frac{a_{13}a_{23}}{\alpha_{33}} & \alpha_{22}-\frac{a_{23}^{\,2}}{\alpha_{33}} & 0\\ 0 & 0 & \alpha_{66}\end{bmatrix}\begin{Bmatrix}\sigma_x\\ \sigma_y\\ \tau_{xy}\end{Bmatrix}=\begin{bmatrix}\beta_{11} & \beta_{12} & 0\\ \beta_{21} & \beta_{22} & 0\\ 0 & 0 & \beta_{66}\end{bmatrix}\begin{Bmatrix}\sigma_x\\ \sigma_y\\ \tau_{xy}\end{Bmatrix} \tag{I.4b}$$

The remaining strains ε_x, ε_y, and γ_{xy} are thus related to stresses σ_x, σ_y, τ_{xy} through the coefficients of deformation: β_{11}, β_{12}, β_{22} and β_{66}.

The compatibility equation that corresponds to plane strain conditions is:

$$\frac{\partial^2\varepsilon_x}{\partial y^2}+\frac{\partial^2\varepsilon_y}{\partial x^2}=\frac{\partial^2\gamma_{xy}}{\partial x\partial y} \tag{I.5}$$

It is useful to introduce the Airy stress function Φ(x,y). In the absence of body forces the stresses are expressed using the following stress functions:

$$\sigma_x = \frac{\partial^2 \Phi}{\partial y^2}$$
$$\sigma_y = \frac{\partial^2 \Phi}{\partial x^2} \qquad \text{(I.6)}$$
$$\tau_{xy} = \frac{\partial^2 \Phi}{\partial x \partial y}$$

Substituting equations (2A.1b) and (2A.6) into (2A.5) we get:

$$\beta_{22} \frac{\partial^4 \Phi}{\partial x^4} + (2\beta_{12} + \beta_{66}) \frac{\partial^4 \Phi}{\partial x^2 \partial y^2} + \beta_{11} \frac{\partial^4 \Phi}{\partial y^4} = 0 \qquad \text{(I.7)}$$

To solve equation (2A.7) we need to solve the characteristic equation:

$$f(\lambda) = \beta_{11} \lambda^4 + (2\beta_{12} + \beta_{66}) \lambda^2 + \beta_{22} \qquad \text{(I.8)}$$

that has roots of the form: $\lambda_1, \overline{\lambda}_1, \lambda_2, \overline{\lambda_2}$

and without loss of generality let's assume: $\lambda_1 = a_1 + i\, b_1$, $\lambda_2 = a_2 + i\, b_2$, $b_1 > b_2 > 0$

Any arbitrary function of $g(x + \lambda y)$ satisfies (I.7) as long as λ is a solution to (I.8). The general solution of (I.7) is expressed using complex numbers z_1, z_2 and their conjugates:

$z_1 = x + \lambda_1 y$ and $z_2 = x + \lambda_2 y$

Since the resulting stress function must be real, the solution is given by the following expression:

$$\Phi(x,y) = 2\mathrm{Re}\{\Phi_1(z_1) + \Phi_2(z_2)\} = \Phi_1(z_1) + \overline{\Phi_1(z_1)} + \Phi_2(z_2) + \overline{\Phi_2(z_2)} \qquad \text{(I.9a)}$$

For the case that the roots of the characteristic equation are the same ($\lambda_1 = \lambda_2$), the problem reduces to an equivalent isotropic (Lekhnitskii, 1977) and the solution becomes:

$$\Phi(x,y) = 2\mathrm{Re}\left\{\overline{z_1}\,\Phi_1(z_1) + \Phi_2(z_1)\right\} \tag{I.9b}$$

The stresses are found to be:

$$\begin{aligned}
\sigma_x &= 2\mathrm{Re}\left\{\lambda_1^{\,2}\Phi_1'(z_1) + \lambda_2^{\,2}\Phi_2'(z_2)\right\} \\
\sigma_y &= 2\mathrm{Re}\left\{\Phi_1'(z_1) + \Phi_2'(z_2)\right\} \\
\tau_{xy} &= -2\mathrm{Re}\left\{\lambda_1\Phi_1'(z_1) + \lambda_2\Phi_2'(z_2)\right\}
\end{aligned} \tag{I.10}$$

The displacements u(x,y) and v(x,y) are subsequently determined after computing strains in terms of these stresses and integrating, and are equal to:

$$\begin{aligned}
u &= 2\mathrm{Re}\left\{p_1\Phi_1(z_1) + p_2\Phi_2(z_2)\right\} \\
v &= 2\mathrm{Re}\left\{q_1\Phi_1(z_1) + q_2\Phi_2(z_2)\right\}
\end{aligned} \tag{I.11}$$

where

$$p_k = \beta_{12} + \beta_{11}\lambda_k^2$$

$$q_k = \frac{\beta_{22}}{\lambda_k} + \beta_{12}\lambda_k \qquad , \qquad k = 1, 2$$

The analytic functions Φ_1 and Φ_2 are finally determined using the boundary conditions of the problem that we want to solve.

Deforming circular tunnel in a cross-anisotropic infinite plane

Let's assume a circular tunnel in an elastic cross-anisotropic material that extends to infinity (with horizontal planes of isotropy). Let the tunnel have radius R and the elastic material be described by 5 anisotropic parameters, namely E_v, E_h, ν_{vh}, ν_{hh}, G_{vh}. For prescribed tunnel wall displacements (u_ε, u_δ) the displacement field around the tunnel will be determined.

1) Uniform Convergence of a tunnel in an infinite plane

In the case of **uniform convergence** of magnitude u_ε, with outward displacement defined as positive, the displacements of the tunnel wall are (see Figure I.1):

$$u_E(\theta) = u_\varepsilon \cos\theta = u_\varepsilon \frac{e^{i\theta} + e^{-i\theta}}{2} = u_\varepsilon \frac{\sigma + \sigma^{-1}}{2}$$
$$v_E(\theta) = u_\varepsilon \sin\theta = u_\varepsilon \frac{e^{i\theta} - e^{-i\theta}}{2i} = u_\varepsilon \frac{\sigma - \sigma^{-1}}{2i} \qquad \text{(I.12)}$$

where θ is the angle from the origin.

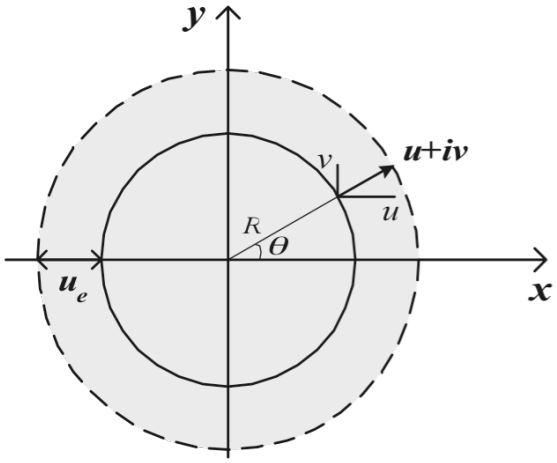

Figure I.1: Prescribed displacements at tunnel wall for uniform convergence case

The boundary (tunnel wall) is a circle of radius R in the x-y plane and thus described by $z(x,y) = x + i\,y = R\,e^{i\theta} = R\,\sigma$. But since

$$z_1 = x + \lambda_1 y = x + \mathrm{Re}\{\lambda_1\}\,y + i\,\mathrm{Im}\{\lambda_1\}\,y = x_1 + i\,y_1,$$

$$z_2 = x + \lambda_2 y = x + \mathrm{Re}\{\lambda_2\}\,y + i\,\mathrm{Im}\{\lambda_2\}\,y = x_2 + i\,y_2,$$

the boundary is an inclined ellipse in the domains $S_1(x_1\text{-}y_1)$, $S_2(x_2\text{-}y_2)$ in the general case. In order to apply the boundary conditions to find the analytic functions Φ_1 and Φ_2 the boundaries need to be mapped into surfaces that can be described using a single parameter. Using the transformations:

$$z_k = R\left(\frac{1 - i\,\lambda_k}{2}\,\zeta_k + \frac{1 + i\,\lambda_k}{2}\cdot\frac{1}{\zeta_k}\right) \Leftrightarrow \zeta_k = \frac{z_k + \left\{z_k^{\,2} - R^2\left(1 + \lambda_k^{\,2}\right)\right\}^{1/2}}{R\left(1 - i\lambda_k\right)}, \quad k = 1,2 \qquad \text{(I.13)}$$

$$|\zeta_k| > 1$$

the boundary is mapped analytically into a circle of unit radius, in the mapped domain (see Figure I.2).

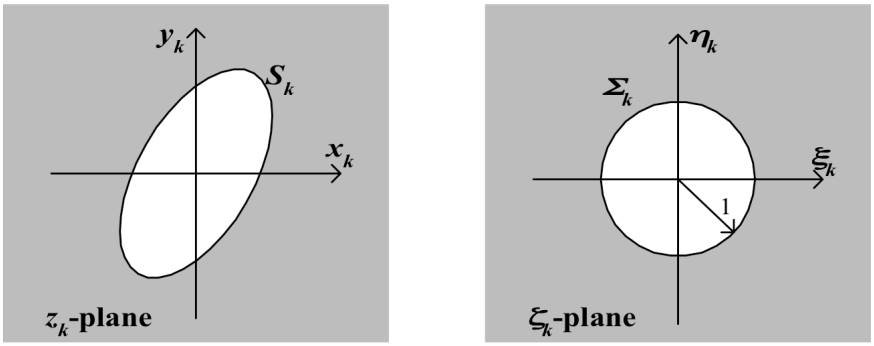

Figure I.2: Problem's boundaries in z_k-plane and in transformed ζ_k-plane

The analytic functions $\Phi_k(z_k)$ can be expressed using the conformed variables ζ_k. Since an analytic expression ζ_k is used for the transformation, functions $\Phi_k(z_k)$ will remain analytical and will be expressed as Laurent series of the conformed variable ζ_k:

$$\Phi_1(z_1) = \Phi_1(z_1(\zeta_1)) = \Phi_1(\zeta_1) = \sum_{n=0}^{\infty} a_n \zeta_1^{-n}$$
$$\Phi_2(z_2) = \Phi_2(z_2(\zeta_2)) = \Phi_2(\zeta_2) = \sum_{n=0}^{\infty} b_n \zeta_2^{-n} \qquad \text{(I.14)}$$

The series are truncated to negative powers of ζ_k so as to ensure boundness of the functions Φ_1, Φ_2 as ζ_k approaches infinity. The boundary conditions are now applied:

At tunnel wall: $|z| = R \leftrightarrow \zeta_1 = \zeta_2 = e^{i\theta} = \sigma$

Horizontal displacements

$$u(x,y)\big|_{|z|=R} = u_B(\sigma) \qquad \Leftrightarrow$$

$$p_1\,\Phi_1(\sigma) + \overline{p_1\,\Phi_1(\sigma)} + p_2\,\Phi_2(\sigma) + \overline{p_2\,\Phi_2(\sigma)} = u_e\,\frac{\sigma+\sigma^{-1}}{2} \qquad \Leftrightarrow$$

$$p_1\sum_0^\infty a_n\sigma^{-n} + \bar{p}_1\sum_0^\infty \bar{a}_n\sigma^{n} + p_2\sum_0^\infty b_n\sigma^{-n} + \bar{p}_2\sum_0^\infty \bar{b}_n\sigma^{n} = u_e\,\frac{\sigma+\sigma^{-1}}{2} \qquad \Leftrightarrow$$

equating the coefficients for all powers of σ we get

$$p_1\,a_n + p_2 b_n = 0 \qquad , \qquad n \neq 1$$

$$p_1\,a_1 + p_2 b_1 = \frac{u_e}{2} \qquad , \qquad n = 1$$

Vertical displacements

$$v(x,y)\big|_{|z|=R} = v_B(\sigma) \qquad \Leftrightarrow$$

$$q_1\,\Phi_1(\sigma) + \overline{q_1\,\Phi_1(\sigma)} + q_2\,\Phi_2(\sigma) + \overline{q_2\,\Phi_2(\sigma)} = u_e\,\frac{\sigma-\sigma^{-1}}{2i} \qquad \Leftrightarrow$$

$$q_1\sum_0^\infty a_n\sigma^{-n} + \bar{q}_1\sum_0^\infty \bar{a}_n\sigma^{n} + q_2\sum_0^\infty b_n\sigma^{-n} + \bar{q}_2\sum_0^\infty \bar{b}_n\sigma^{n} = u_e\,\frac{\sigma-\sigma^{-1}}{2i} \qquad \Leftrightarrow$$

so we get

$$q_1\,a_n + q_2 b_n = 0 \qquad , \qquad n \neq 1$$

$$q_1\,a_1 + q_2 b_1 = -\frac{u_e}{2i} = \frac{u_e\,i}{2} \qquad , \qquad n = 1$$

Solving for the series coefficients a_n, b_n we get:

$$a_1 = \frac{u_e}{2}\,\frac{q_2 - i\,p_2}{p_1 q_2 - q_1 p_2},$$

$$b_1 = \frac{u_e}{2}\,\frac{-q_1 + i\,p_1}{p_1 q_2 - q_1 p_2} \text{ and}$$

$$a_n = b_n = 0 \qquad \text{for n} \neq 1$$

The displacements caused by a contracting circular tunnel in an infinite medium are thus given by:

$$U(x,y) = 2\mathrm{Re}\left\{\frac{u_\varepsilon}{2} p_1 \frac{q_2 - ip_2}{p_1 q_2 - q_1 p_2} \cdot \frac{1}{\zeta_1(x,y)} + \frac{u_\varepsilon}{2} p_2 \frac{-q_1 + ip_1}{p_1 q_2 - q_1 p_2} \cdot \frac{1}{\zeta_2(x,y)}\right\} \tag{I.15a}$$

$$V(x,y) = 2\mathrm{Re}\left\{\frac{u_\varepsilon}{2} q_1 \frac{q_2 - ip_2}{p_1 q_2 - q_1 p_2} \cdot \frac{1}{\zeta_1(x,y)} + \frac{u_\varepsilon}{2} q_2 \frac{-q_1 + ip_1}{p_1 q_2 - q_1 p_2} \cdot \frac{1}{\zeta_2(x,y)}\right\} \tag{I.15b}$$

2) Pure Distortion of a tunnel in an infinite plane

In the case of pure distortion of magnitude u_δ, the displacements at the tunnel wall are (see Fig. I.3):

$$\begin{aligned} u_D(\theta) &= u_\delta \cos\theta = u_\delta \frac{e^{i\theta} + e^{-i\theta}}{2} = u_\delta \frac{\sigma + \sigma^{-1}}{2} \\ v_D(\theta) &= -u_\delta \sin\theta = -u_\delta \frac{e^{i\theta} - e^{-i\theta}}{2i} = -u_\delta \frac{\sigma - \sigma^{-1}}{2i} \end{aligned} \tag{I.16}$$

where θ is the angle from the origin.

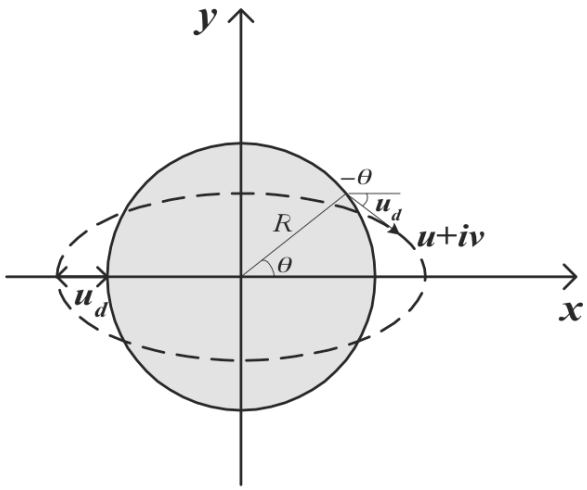

Figure I.3: Prescribed displacements of tunnel wall for pure distortion case

Once again the transformation shown in eq. I.13 is employed, which transforms the inclined ellipses into unit circles in the mapped domain, is used. Writing the analytic functions as Laurent series with negative exponents

$$\Phi_1(z_1) = \Phi_1(z_1(\zeta_1)) = \Phi_1(\zeta_1) = \sum_{n=0}^{\infty} a_n \zeta_1^{-n}$$

$$\Phi_2(z_2) = \Phi_2(z_2(\zeta_2)) = \Phi_2(\zeta_2) = \sum_{n=0}^{\infty} b_n \zeta_2^{-n}$$

The boundary conditions are subsequently applied:

<u>Horizontal displacements</u>

$$u(x,y)\big|_{|z|=R} = u_B(\sigma) \qquad \Leftrightarrow$$

$$p_1 \Phi_1(\sigma) + \overline{p_1 \Phi_1(\sigma)} + p_2 \Phi_2(\sigma) + \overline{p_2 \Phi_2(\sigma)} = u_d \frac{\sigma + \sigma^{-1}}{2} \qquad \Leftrightarrow$$

$$p_1 \sum_0^{\infty} a_n \sigma^{-n} + \overline{p}_1 \sum_0^{\infty} \overline{a}_n \sigma^n + p_2 \sum_0^{\infty} b_n \sigma^{-n} + \overline{p}_2 \sum_0^{\infty} \overline{b}_n \sigma^n = u_d \frac{\sigma + \sigma^{-1}}{2} \qquad \Leftrightarrow$$

equating the coefficients for all powers of σ we get

$$p_1 a_n + p_2 b_n = 0 \qquad , \qquad n \neq 1$$

$$p_1 a_1 + p_2 b_1 = \frac{u_d}{2} \qquad , \qquad n = 1$$

<u>Vertical displacements</u>

$$v(x,y)\big|_{|z|=R} = v_B(\sigma) \qquad \Leftrightarrow$$

$$q_1 \Phi_1(\sigma) + \overline{q_1 \Phi_1(\sigma)} + q_2 \Phi_2(\sigma) + \overline{q_2 \Phi_2(\sigma)} = -u_d \frac{\sigma - \sigma^{-1}}{2i} \qquad \Leftrightarrow$$

$$q_1 \sum_0^{\infty} a_n \sigma^{-n} + \overline{q}_1 \sum_0^{\infty} \overline{a}_n \sigma^n + q_2 \sum_0^{\infty} b_n \sigma^{-n} + \overline{q}_2 \sum_0^{\infty} \overline{b}_n \sigma^n = -u_d \frac{\sigma - \sigma^{-1}}{2i} \qquad \Leftrightarrow$$

so we get

$$q_1 a_n + q_2 b_n = 0 \qquad , \qquad n \neq 1$$

$$q_1 a_1 + q_2 b_1 = \frac{u_\delta}{2i} = -\frac{u_\delta i}{2} \qquad , \qquad n = 1$$

Solving for the series coefficients a_n, b_n we get:

$$a_1 = \frac{u_\delta}{2} \frac{q_2 + i p_2}{p_1 q_2 - q_1 p_2},$$

$$b_1 = \frac{u_\delta}{2} \frac{-q_1 - i p_1}{p_1 q_2 - q_1 p_2} \text{ and}$$

$$a_n = b_n = 0 \qquad \text{for n} \neq 1$$

The displacements caused by a purely distorting circular tunnel in an infinite medium are given by:

$$U(x,y) = 2\mathrm{Re}\left\{ \frac{u_\delta}{2} p_1 \frac{q_2 + i p_2}{p_1 q_2 - q_1 p_2} \cdot \frac{1}{\zeta_1(x,y)} + \frac{u_\delta}{2} p_2 \frac{-q_1 - i p_1}{p_1 q_2 - q_1 p_2} \cdot \frac{1}{\zeta_2(x,y)} \right\} \qquad \text{(I.17a)}$$

$$V(x,y) = 2\mathrm{Re}\left\{ \frac{u_\delta}{2} q_1 \frac{q_2 + i p_2}{p_1 q_2 - q_1 p_2} \cdot \frac{1}{\zeta_1(x,y)} + \frac{u_\delta}{2} q_2 \frac{-q_1 - i p_1}{p_1 q_2 - q_1 p_2} \cdot \frac{1}{\zeta_2(x,y)} \right\} \qquad \text{(I.17b)}$$

Deforming circular tunnel in a cross-anisotropic half-plane

In order to derive the displacement field caused by a deforming circular tunnel in a cross-anisotropic half-plane the mirror image technique will be implemented. Two tunnels at points (0, H) and (0, -H) are considered while the first one is contracting and the second is expanding (negative mirror image technique). The final displacement field will be the direct superposition of the two opposite deforming cavities plus the displacement field caused by the corrective shear stresses in the free surface (see Figure I.4). It is noted that although superimposing solutions is absolutely correct within linear elasticity assumptions, the solution is only an approximate one, since the dimensions of the tunnel cavity are not taken into account in the analysis. Pinto and Whittle (2001) concluded that for the isotropic case the results of the approximate solution are very close to those of the exact solution for $R/H < 0.45$.

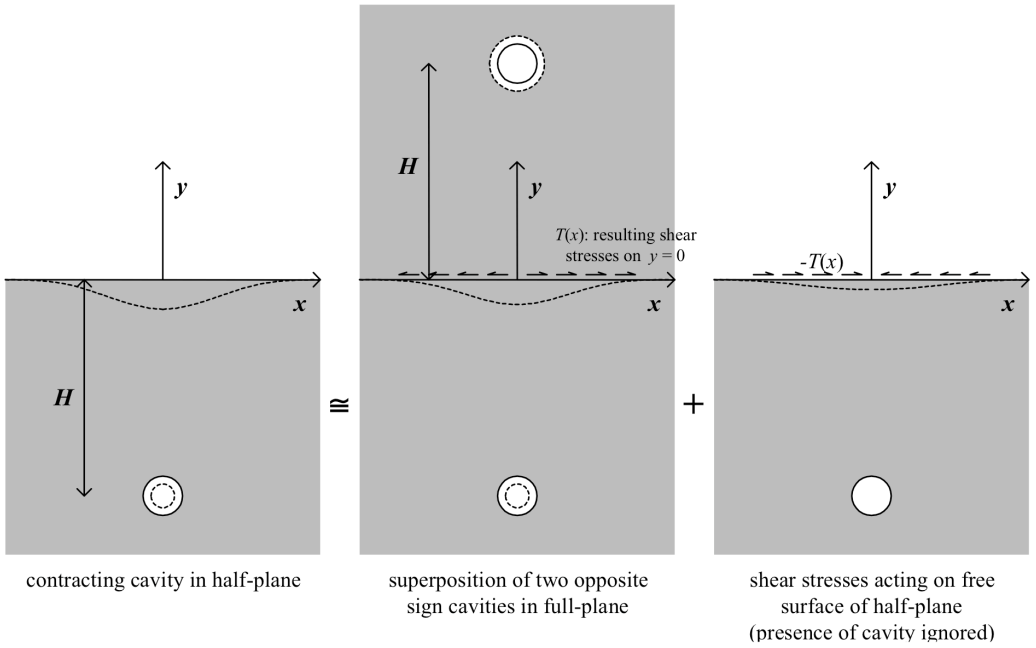

Figure I.4: Negative mirror image technique used in half-plane solutions

1. Displacement field caused by **expanding** (magnitude $u_\varepsilon>0$, $u_\delta>0$) cavity at (0, -H)

$u^+(x, y) = U(x, y + H)$ (I.18a)

$v^+(x, y) = V(x, y + H)$ (I.18b)

2. Displacement field caused by **contracting** (magnitude $-u_\varepsilon<0$, $-u_\delta<0$) cavity at (0,H)

$u^-(x, y) = -U(x, y - H)$ (I.19a)

$v^-(x, y) = -V(x, y - H)$ (I.19b)

The resulting stresses at the surface (from the two cavities of opposite sign) are:

$\sigma_y(x, 0) = 0$ due to antisymmetry

$\tau^c_{xy}(x, 0) = 2\,\tau_{xy}^-|_y = -H$

the shear stresses due to a deforming tunnel cavity are

$$\begin{aligned}\tau_{xy}(x,y) &= -2\,\mathrm{Re}\left\{\lambda_1\,\Phi_1'(z_1) + \lambda_2\,\Phi_2'(z_2)\right\} = \\ &= -2\,\mathrm{Re}\left\{\lambda_1\,\Phi_1'(\zeta_1)\,\zeta_1'(z_1) + \lambda_2\,\Phi_2'(\zeta_2)\,\zeta_2'(z_2)\right\} \\ &= -2\,\mathrm{Re}\left\{-\frac{\lambda_1\,a_1}{\zeta_1\left\{z_1^2 - R^2(1+\lambda_1^2)\right\}^{1/2}} - \frac{\lambda_2\,b_1}{\zeta_2\left\{z_2^2 - R^2(1+\lambda_2^2)\right\}^{1/2}}\right\}\end{aligned}$$

so the resulting stresses at the free surface of the half-plane are

$$T^c(x) = -2\,\tau_{xy}(x,-H)$$

The corrective displacements result when we apply shear stresses opposite to $T^c(x)$ to the free surface. For surface loading of a half-plane the resulting displacements are

$U^c = 2\mathrm{Re}\{p_1\,\Phi_1^c(z_1) + p_2\,\Phi_2^c(z_2)\}$

$V^c = 2\mathrm{Re}\{q_1\,\Phi_1^c(z_1) + q_2\,\Phi_2^c(z_2)\}$

where the analytic functions Φ_1^c, Φ_2^c are obtained through integration

$$\Phi_1^c(z_1) = \frac{1}{\lambda_1 - \lambda_2}\frac{1}{2\pi i}\int_{-\infty}^{\infty}\frac{\lambda_2 f_1(\xi) + f_2(\xi)}{\xi - z_1}d\xi$$

$$\Phi_2^c(z_2) = -\frac{1}{\lambda_1 - \lambda_2}\frac{1}{2\pi i}\int_{-\infty}^{\infty}\frac{\lambda_1 f_1(\xi) + f_2(\xi)}{\xi - z_2}d\xi$$

where

$$f_1(s) = -\int_{\infty}^{s} N(x)dx = 0 \qquad \text{(integral of normal traction along boundary)}$$

$$f_2(s) = \int_{\infty}^{s} T(x)dx = \int_{s}^{\infty} T^c(x)dx \qquad \text{(integral of shear traction along boundary)}$$

in our case the function f_2 is calculated to be (see 'integral of horizontal traction' section):

$f^c_2(s) = -4\mathrm{Re}\{\lambda_1\,\Phi_1(s-\lambda_1 H) + \lambda_2\,\Phi_2(s-\lambda_2 H)\}$

Therefore the analytic functions Φ_k^c are calculated to be (see 'Infinite integral of shear stresses' section):

$$\Phi_1^c(z) = \frac{1}{\lambda_1 - \lambda_2}\frac{1}{2\pi i}\int_{-\infty}^{\infty}\frac{f_2(\xi)}{\xi - z}d\xi =$$

$$= \frac{1}{\lambda_1 - \lambda_2}\frac{1}{2\pi i}(-2)\int_{-\infty}^{\infty}\frac{\lambda_1\Phi_1(\xi-\lambda_1 H) + \overline{\lambda_1\Phi_1(\xi-\lambda_1 H)} + \lambda_2\Phi_2(\xi-\lambda_2 H) + \overline{\lambda_2\Phi_2(\xi-\lambda_2 H)}}{\xi - z}d\xi =$$

$$= \frac{1}{\lambda_1 - \lambda_2}2\left[\lambda_1\Phi_1(z-\lambda_1 H) + \lambda_2\Phi_2(z-\lambda_2 H)\right] =$$

$$= \frac{2}{\lambda_1 - \lambda_2}\left[\frac{\lambda_1 a_1 R(1 - i\lambda_1)}{z - \lambda_1 H + \left\{(z-\lambda_1 H)^2 - R^2(1+\lambda_1^2)\right\}^{1/2}} + \frac{\lambda_2 b_1 R(1 - i\lambda_2)}{z - \lambda_2 H + \left\{(z-\lambda_2 H)^2 - R^2(1+\lambda_2^2)\right\}^{1/2}}\right]$$

and $\Phi_2^c(z) = -\Phi_1^c(z)$

3. The final result for the displacements due to **corrective stresses** is written

$$u^c(x,y) = 2\mathrm{Re}\left\{p_1\Phi_1^{\,c}(z_1) - p_2\Phi_1^{\,c}(z_2)\right\} \tag{I.20a}$$

$$v^c(x,y) = 2\mathrm{Re}\left\{q_1\Phi_1^{\,c}(z_1) - q_2\Phi_1^{\,c}(z_2)\right\} \tag{I.20b}$$

The displacement field of a deforming circular tunnel in a cross-anisotropic half-plane is given by superimposing the derived results:

$$u(x,y) = u^+(x,y) + u^-(x,y) + u^c(x,y) \tag{I.21a}$$

$$v(x,y) = v^+(x,y) + v^-(x,y) + v^c(x,y) \tag{I.21b}$$

- **Integral of horizontal traction**

The shear stress distribution caused by the two mirror tunnels can be written in shorthand as

$$T^c(x) = -2\tau_{xy}(x,-H) = 4\,\mathrm{Re}\left\{\sum_{k=1}^{2}\frac{-\lambda_k\, a_{1k}}{\zeta_k(x,-H)\sqrt{(x-\lambda_k H)^2 - R^2(1+\lambda_k^2)}}\right\}$$

where $a_1 = a_{11}$ and $b_1 = a_{12}$

So the integral of surface horizontal traction is

$$f_2(s) = \int_s^\infty T^c(x)dx = 4\,\mathrm{Re}\left\{\sum_{k=1}^{2}\int_s^\infty \frac{-\lambda_k\, a_{1k}}{\zeta_k(x,-H)\sqrt{(x-\lambda_k H)^2 - R^2(1+\lambda_k^2)}}dx\right\}$$

But

$$\zeta_k(x,-H) = \frac{x - \lambda_k H + \sqrt{(x-\lambda_k H)^2 - R^2(1+\lambda_k^2)}}{R(1 - i\,\lambda_k)}$$

$$d\zeta_k(x,-H) = \left(1 + \frac{x - \lambda_k H}{\sqrt{(x-\lambda_k H)^2 - R^2(1+\lambda_k^2)}}\right)\frac{dx}{R(1 - i\,\lambda_k)}$$

$$\frac{1}{\zeta_k(x,-H)}\, d\zeta_k(x,-H) = \frac{dx}{\sqrt{(x-\lambda_k H)^2 - R^2(1+\lambda_k^2)}}$$

$$f_2(s) = 4\,\mathrm{Re}\left\{\sum_{k=1}^{2}\int_s^{\infty} \frac{-\lambda_k\, a_{1k}}{\zeta_k^2(s,-H)}\, d\zeta_k(s,-H)\right\} = 4\,\mathrm{Re}\left\{\sum_{k=1}^{2} \frac{\lambda_k\, a_{1k}}{\zeta_k(s,-H)}\Bigg|_s^{\infty}\right\} =$$

$$= -4\,\mathrm{Re}\left\{\sum_{k=1}^{2} \lambda_k\, \Phi_k(s - \lambda_k H)\right\}$$

So $\quad f'_2(s) = -4\ \mathrm{Re}\{\lambda_1\, \Phi_1(s-\lambda_1 H) + \lambda_2\, \Phi_2(s-\lambda_2 H)\}$

- **Infinite integral of shear stresses**

When calculating the analytic function for the displacements due to corrective stresses we end up with

$$\Phi_1^{c}(z) = \frac{1}{\lambda_1 - \lambda_2}\,\frac{-2}{2\pi i}\int_{-\infty}^{\infty} \frac{\lambda_1 \Phi_1(\xi - \lambda_1 H) + \overline{\lambda_1 \Phi_1(\xi - \lambda_1 H)} + \lambda_2 \Phi_2(\xi - \lambda_2 H) + \overline{\lambda_2 \Phi_2(\xi - \lambda_2 H)}}{\xi - z}\, d\xi$$

For the infinite integral calculation we integrated complex argument function $\varphi(w)$ along the integration path shown in the following figure:

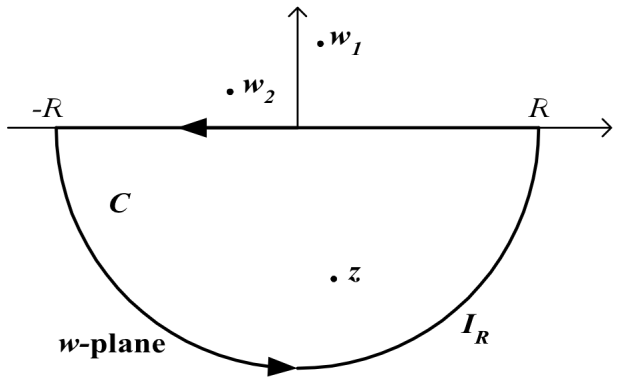

Figure I.1: Integration path for complex function ϕ(w)

function $\phi(w)$ is $\Phi_k(w-\lambda_k H)$ and $\overline{\phi(w)}$ is $\overline{\Phi_k(w-\lambda_k H)}$

function $\phi(w) = \dfrac{a_{1k} R(1 - i\lambda_k)}{w - \lambda_k H + \left\{(w-\lambda_k H)^2 - R^2(1+\lambda_k^2)\right\}^{1/2}}$ has two branch points, namely

$w_{1,2} = \lambda_k H \pm R\sqrt{1+\lambda_k^2}$

It can be seen that for small ratios R/H, and usual degrees of anisotropy these branch points will lie in the upper plane (i.e. outside the integration path). Therefore the function is analytic inside the integration contour and the integral assumes the value:

$$\oint_C \frac{\phi(w)\,dw}{w-z} = 2\pi i\phi(z)$$

$$\oint_C \frac{\overline{\phi(w)}\,dw}{w-z} = 0 \qquad \text{[Cauchy type integrals]}$$

But $\oint_C \frac{\phi(w)\,dw}{w-z} = \lim_{R\to\infty}\left[\int_R^{-R}\frac{\phi(\xi)\,d\xi}{\xi-z} + \int_{I_R}\frac{\phi(w)\,dw}{w-z}\right] = -\int_{-\infty}^{\infty}\frac{\phi(\xi)\,d\xi}{\xi-z}$

and $\oint_C \frac{\overline{\phi(w)}\,dw}{w-z} = -\int_{-\infty}^{\infty}\frac{\overline{\phi(\xi)}\,d\xi}{\xi-z}$

so the final result is

$$\Phi_1^c(z) = \frac{2}{\lambda_1-\lambda_2}\left[\lambda_1\Phi_1(z-\lambda_1 H) + \lambda_2\Phi_2(z-\lambda_2 H)\right]$$

Appendix II

1) Instrumentation used at St James's Park test site (Nyren et al, 1998)

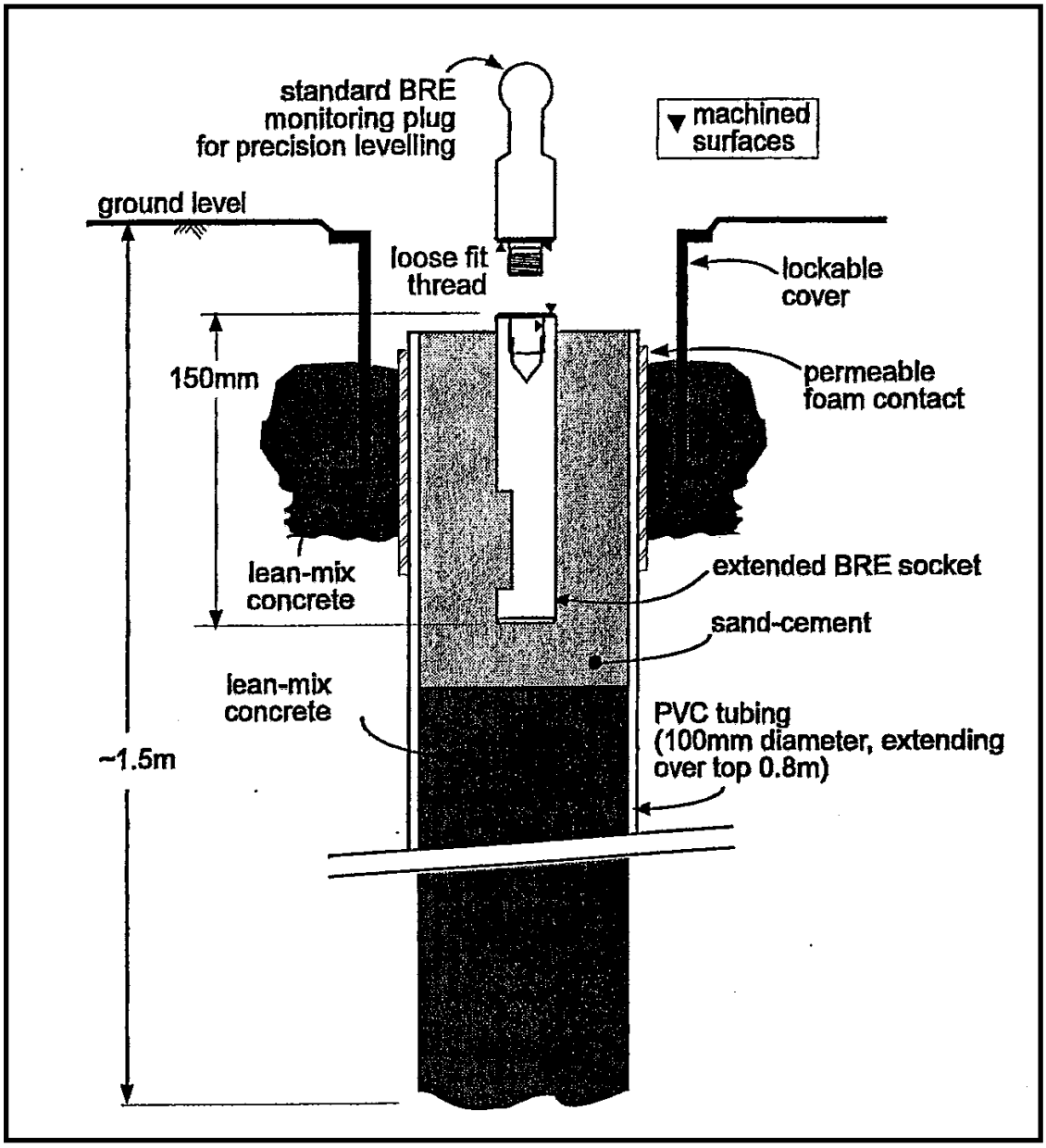

Figure II.1: Surface Monitoring Point (SMP) details (Nyren, 1998)

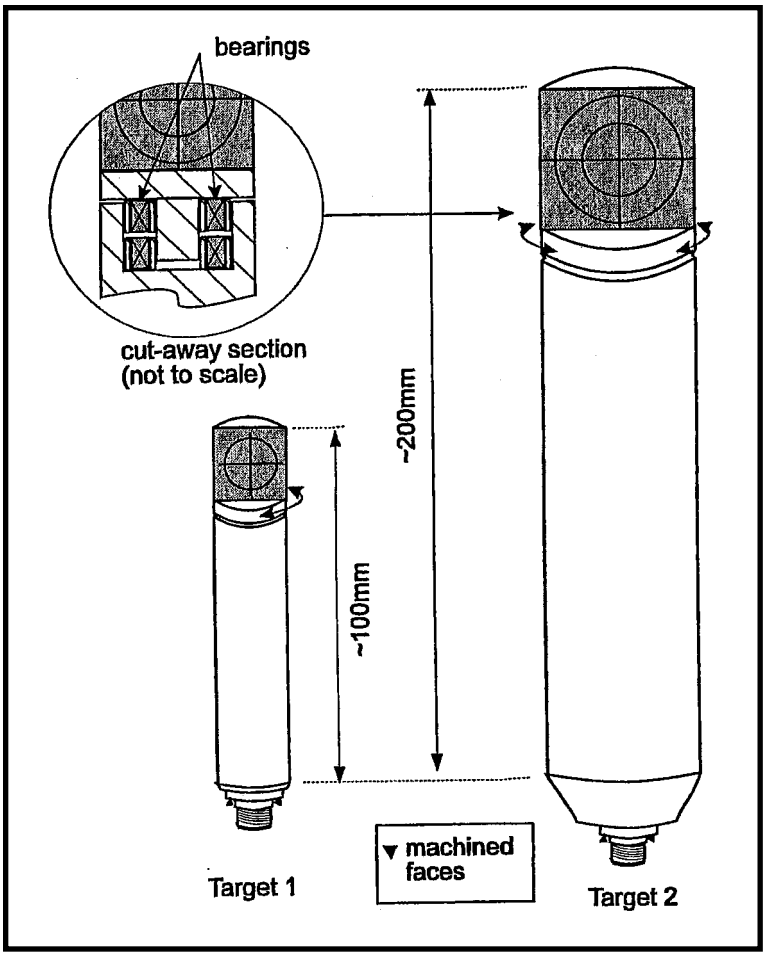

Figure II.2: Total station surveying targets used at St James's Park (Nyren, 1998)

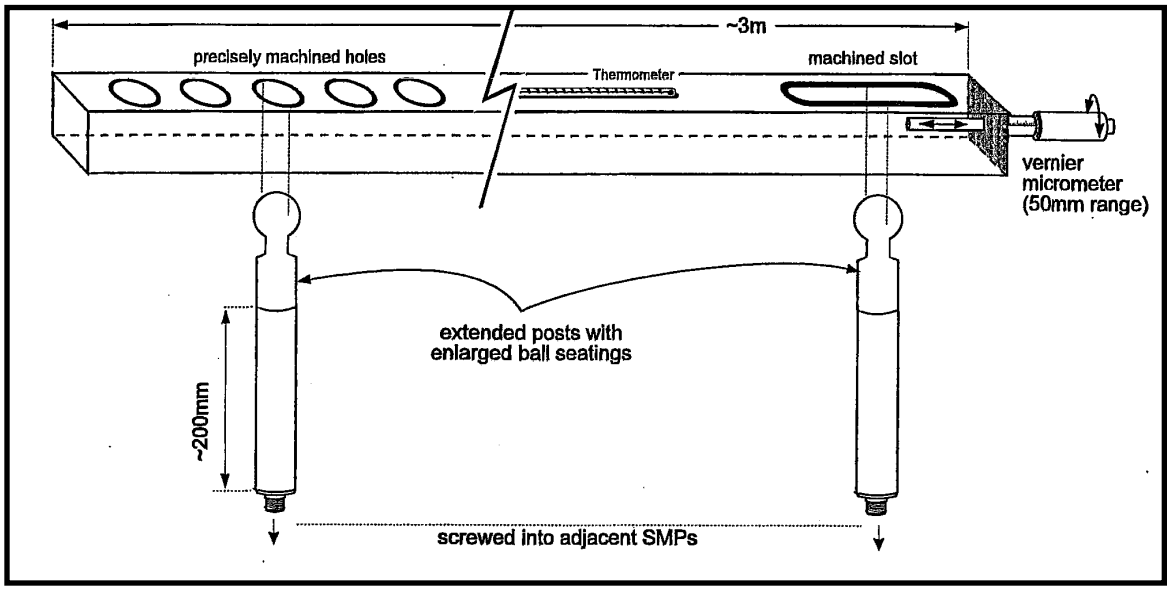

Figure II.3: The micrometer stick used for horizontal strain measurements (Nyren, 1998)

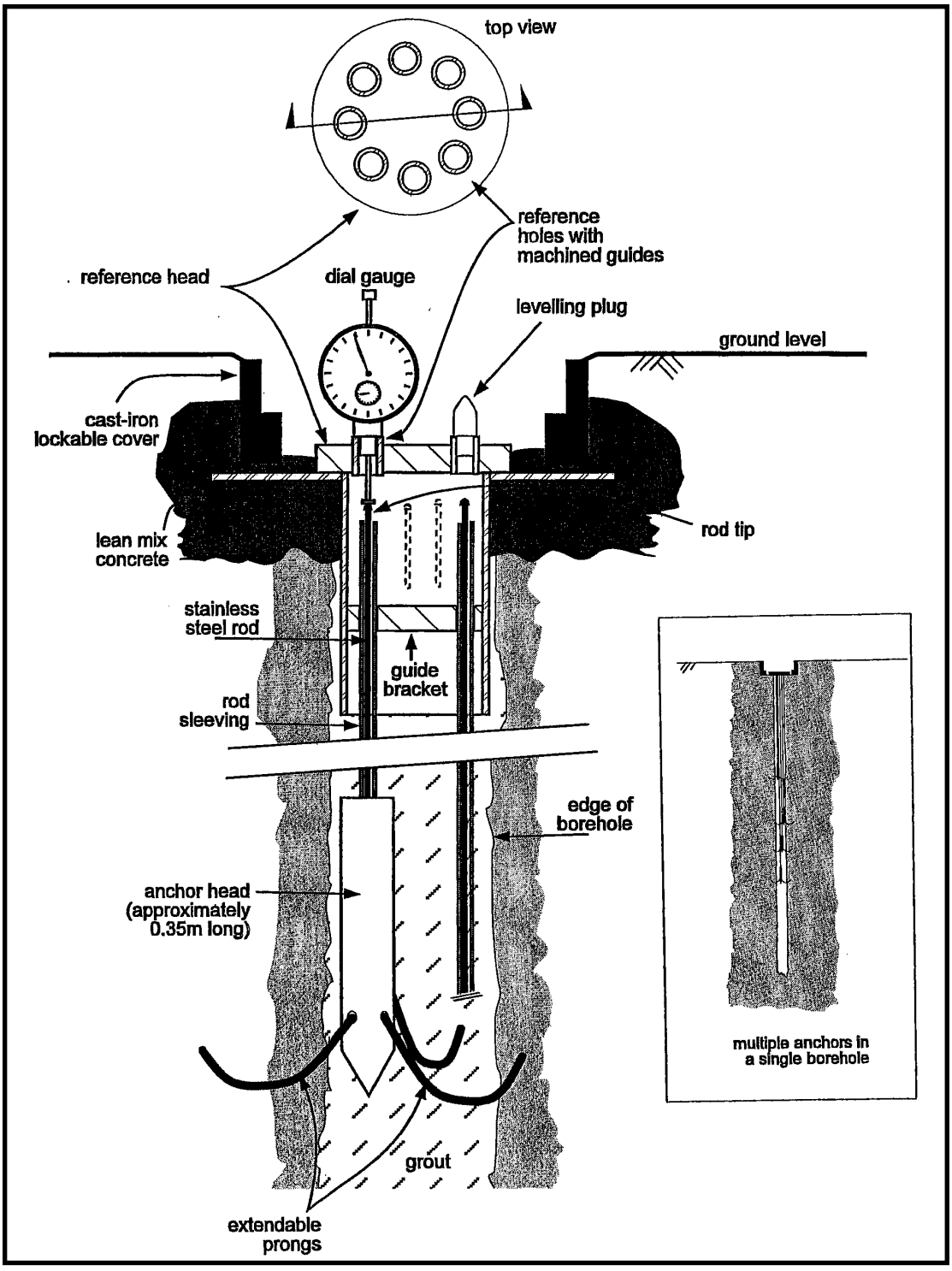

Figure II.4: Rod Extensometer hole and reference head (Nyren, 1998)

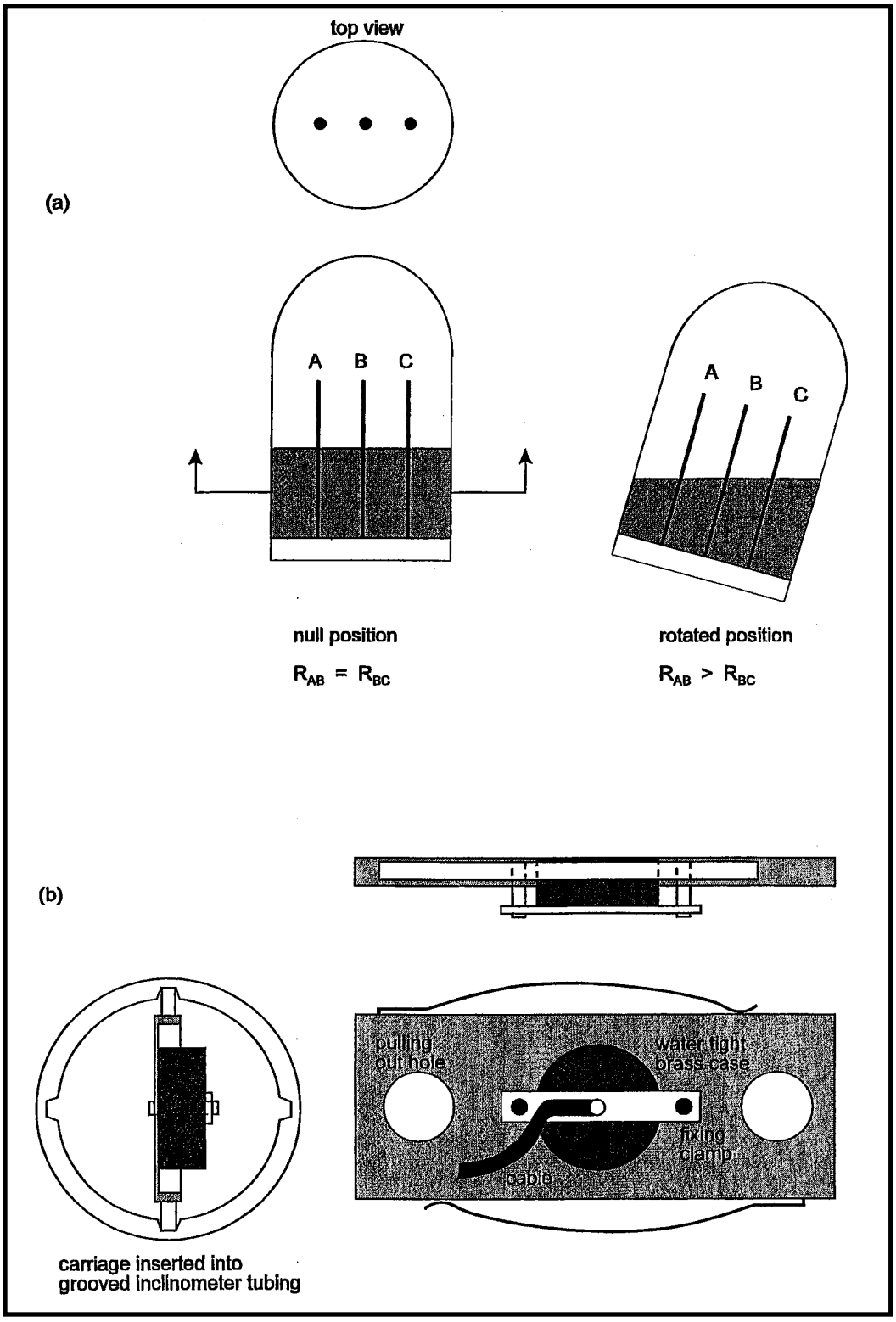

Figure II.5: Schematic diagram of electrolevel showing (a) the basic operating principle and (b) details of the electrolevel carriages used in the instrumentation tubes

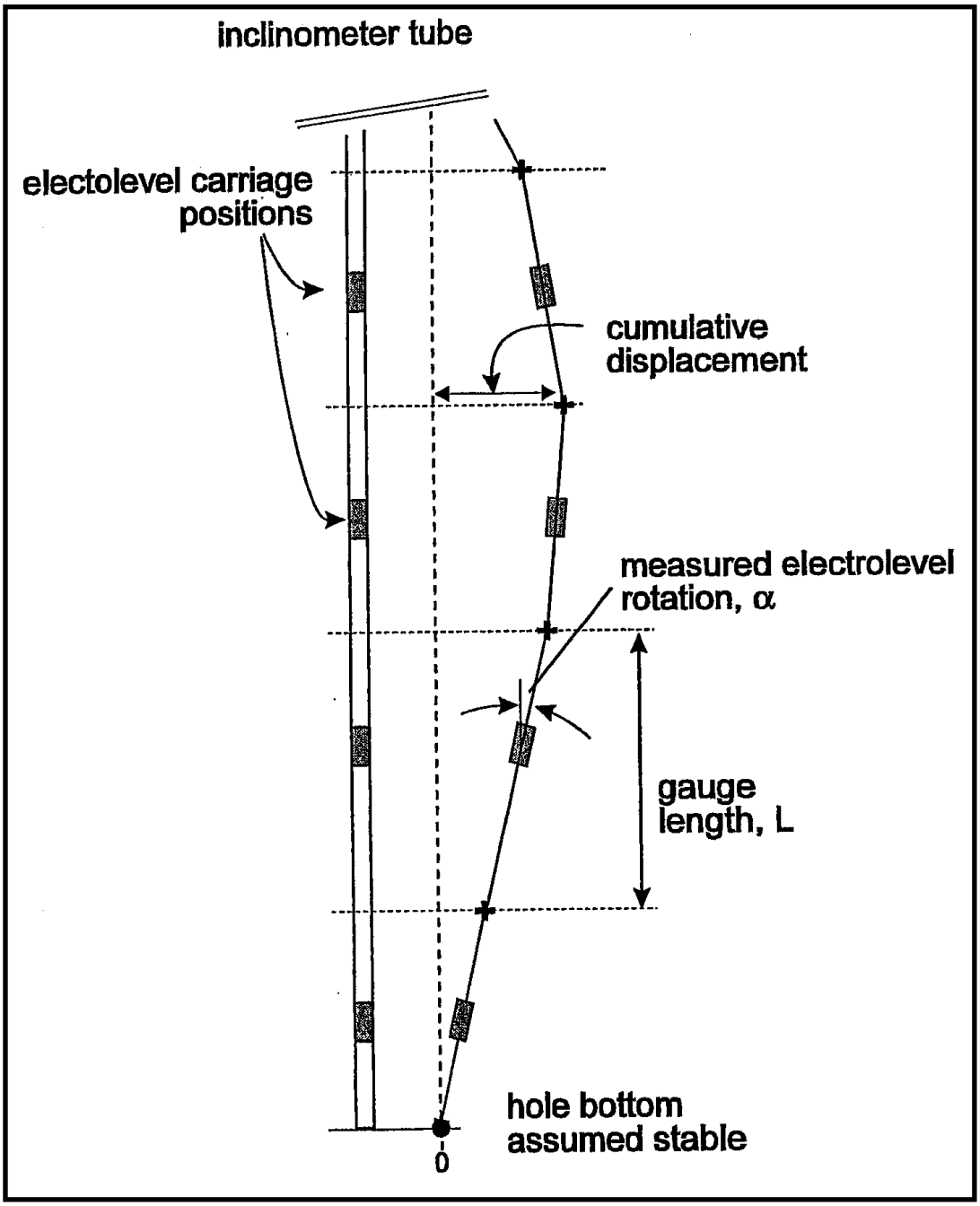

Figure II.6: Method for determining vertical profiles of horizontal displacements from discrete measurements of tilt in electrolevel inclinometers (Nyren, 1998)

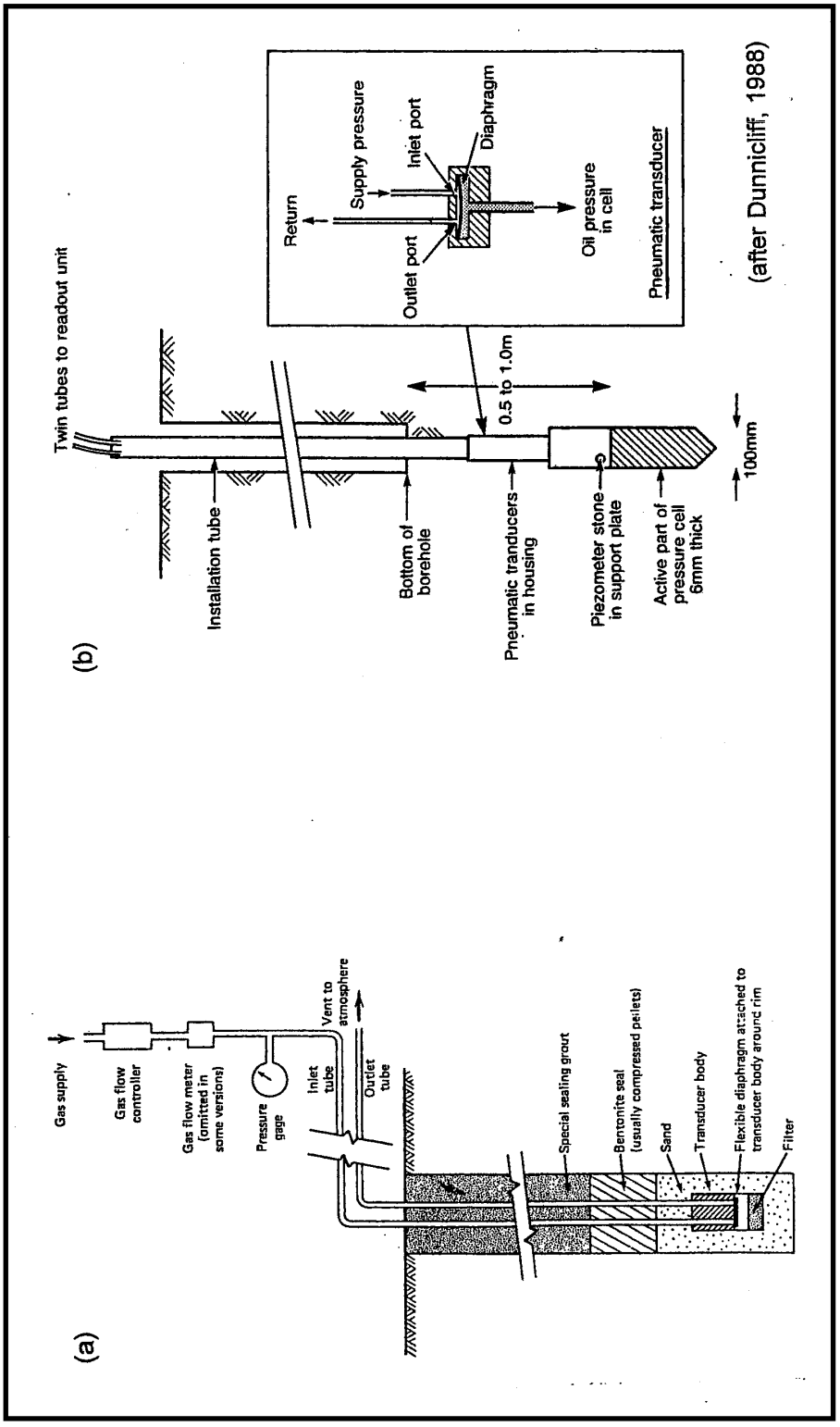

Figure II.7: Schematic diagrams of (a) a pneumatic piezometer installed in a borehole and (b) a push-in spade-shaped pressure cell

2) The physical meanings of the advanced soil model input parameters used by Wongsaroj (2005) are:

- M is the gradient of the critical state line in q - p' space
- e is the current void ratio of the soil
- ν' is the material drained Poisson's ratio (ν'_{vh}, ν'_{hv} and ν'_{hh} for anisotropic materials)
- u_1 and m are the coefficients for dR, which is used to control the amount of the plastic strains within the normal yield surface. The plastic strain becomes bigger as u_1 increases and m decreases.
- C_b is the material constant which determines the initial gradient of the isotropic swelling line at load reversal.
- ω_s is the material constant which controls the non-linearity of the swelling line
- D and r are the parameters that control the non-linearity during isotropic loading and unloading.
- p_0' is the soil mean effective preconsolidation pressure.
- ρ_c is the gradient of the normal consolidation line in $\log_{10}$e – $\log_{10}$p' space.

3) Surface Ground displacements at JLE WB tunnel, as predicted with different anisotropic stiffness parameters:

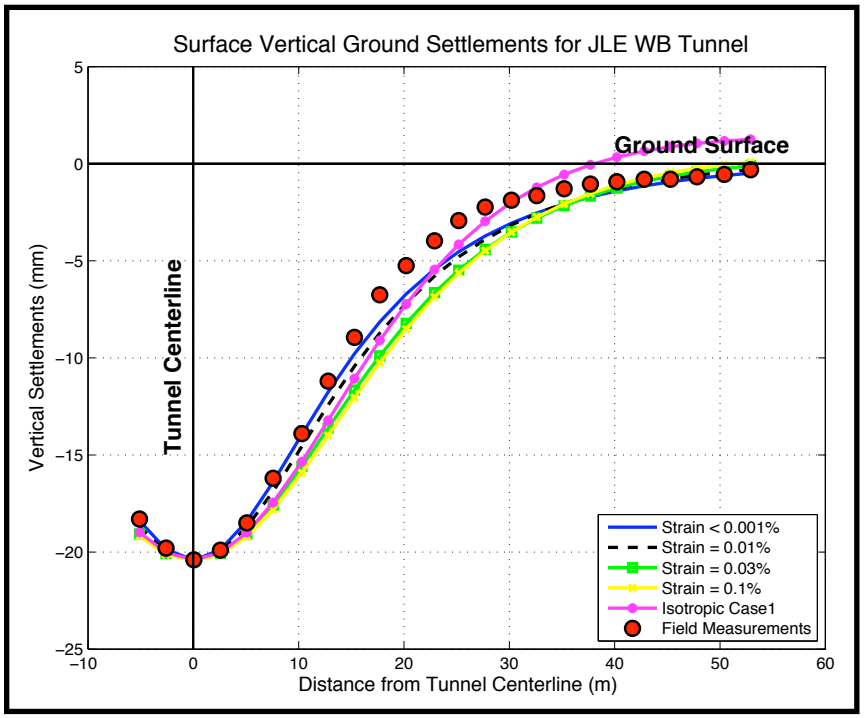

Fig II.8: Surface Vertical Settlements predicted by anisotropic and isotropic models

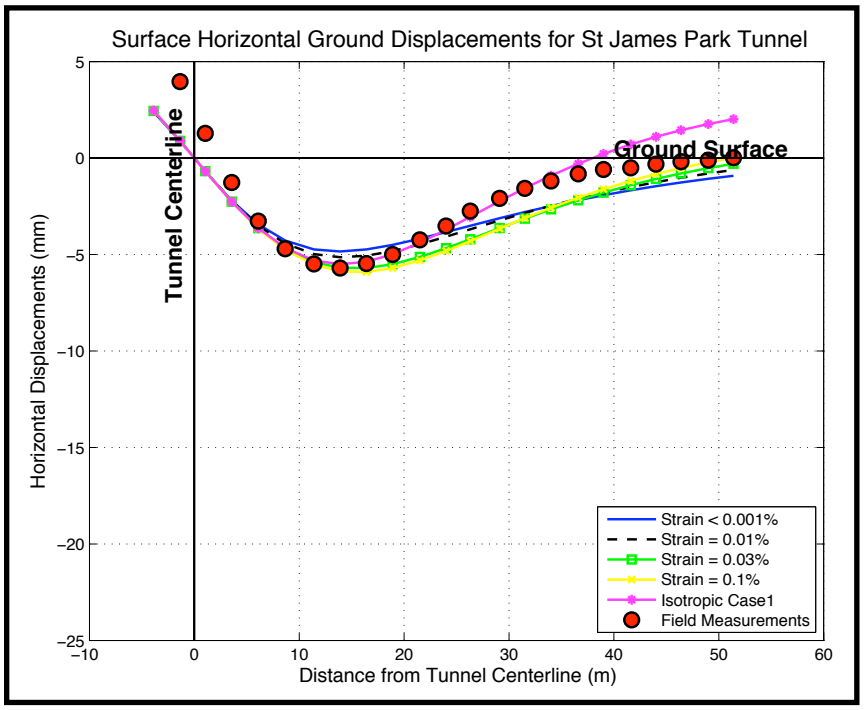

Fig II.9: Surface Horizontal Displacements predicted by anisotropic and isotropic models

Appendix III

- Effect of anisotropic stiffness on computed distribution of subsurface ground movements at HEX trial tunnel, using input parameters from LSS surface solution for vertical displacements (shown in Table 4.10):

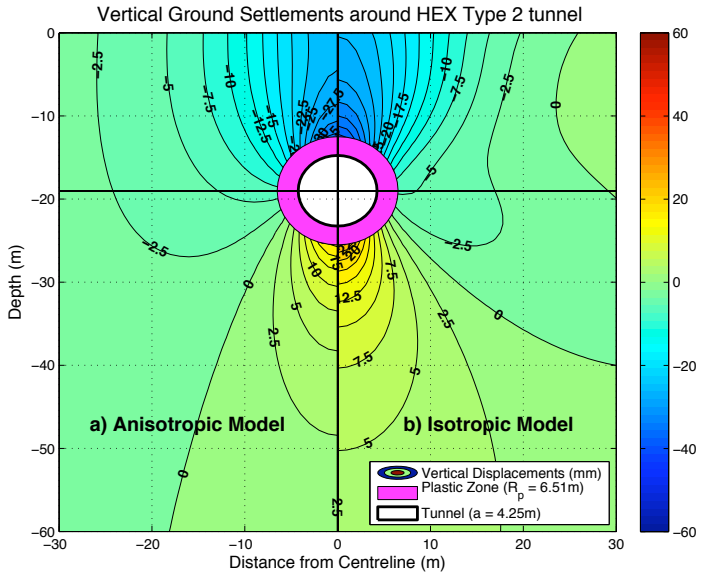

Figure III.1: Vertical Displacements as predicted by Isotropic and Anisotropic Models for the Type 2 tunnel, based on LSS surface solutions for vertical displacements

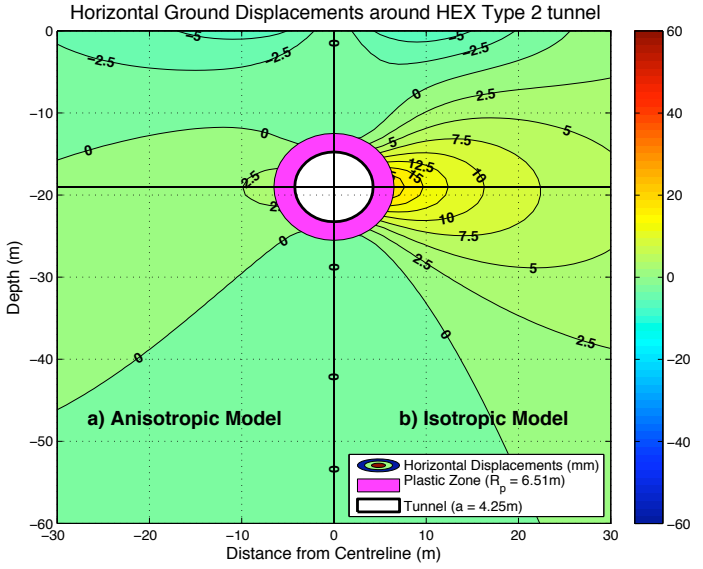

Figure III.2: Horizontal Displacements as predicted by Isotropic and Anisotropic Models for the Type 2 tunnel, based on LSS surface solutions for vertical displacements

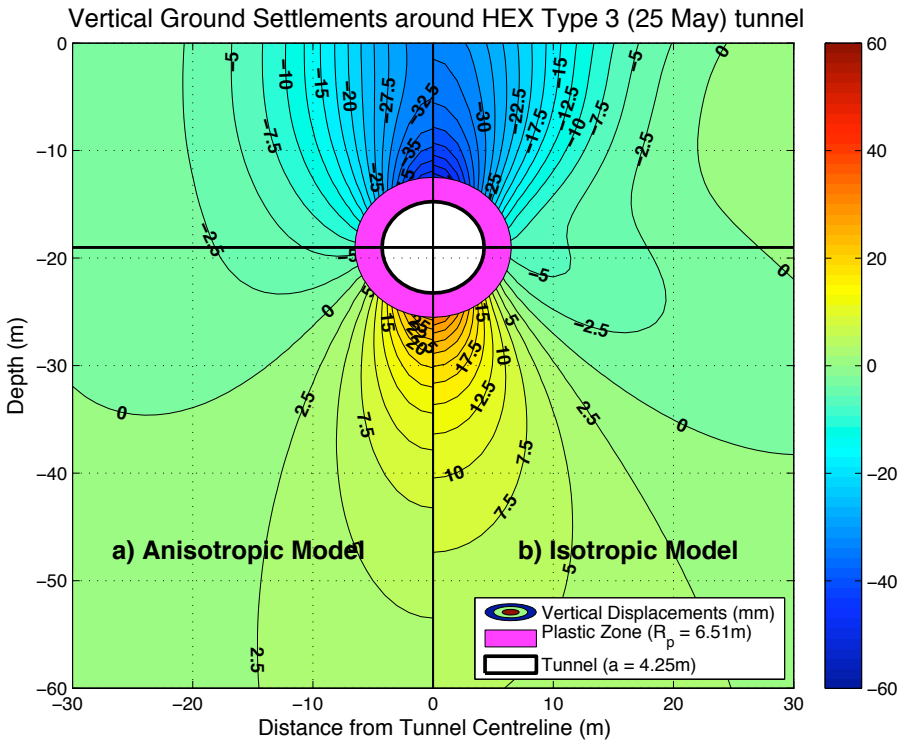

Figure III.3: Vertical Displacements as predicted by Isotropic and Anisotropic Models for the Type 3 (25 May) tunnel, based on LSS surface solutions for vertical displacements

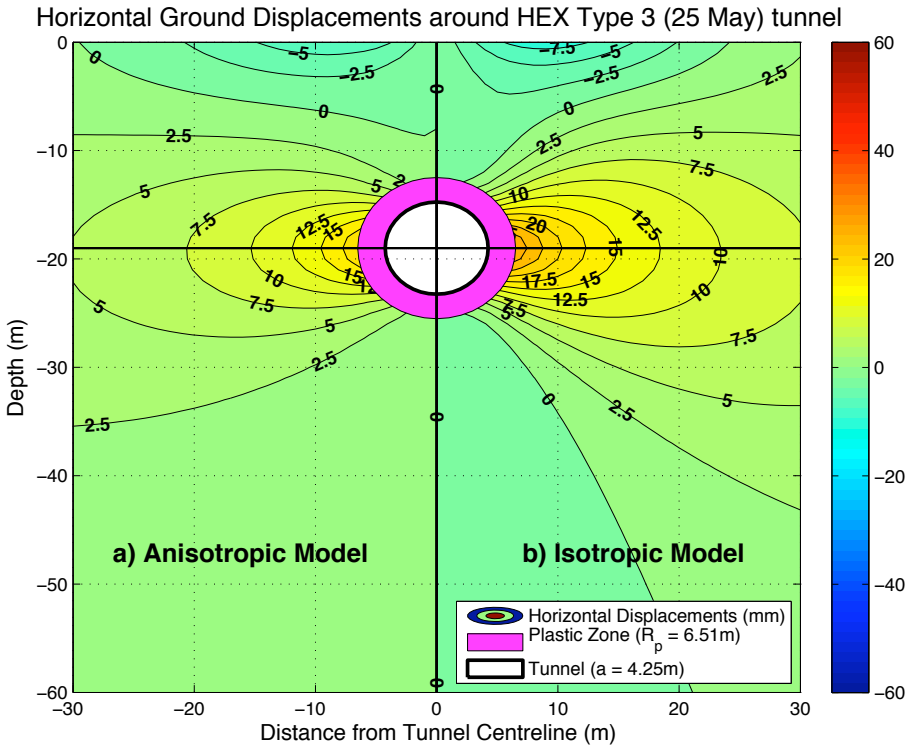

Figure III.4: Horizontal Displacements as predicted by Isotropic and Anisotropic Models for the Type 3 (25 May) tunnel, based on LSS surface solutions for vertical displacements

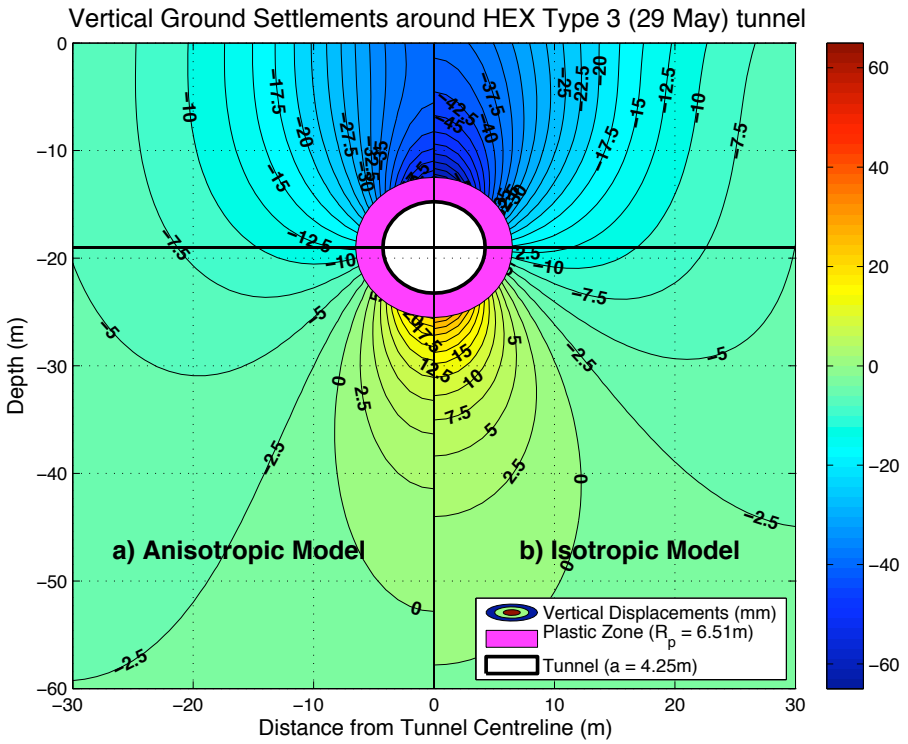

Figure III.5: Vertical Displacements as predicted by Isotropic and Anisotropic Models for the Type 3 (29 May) tunnel, based on LSS surface solutions for vertical displacements

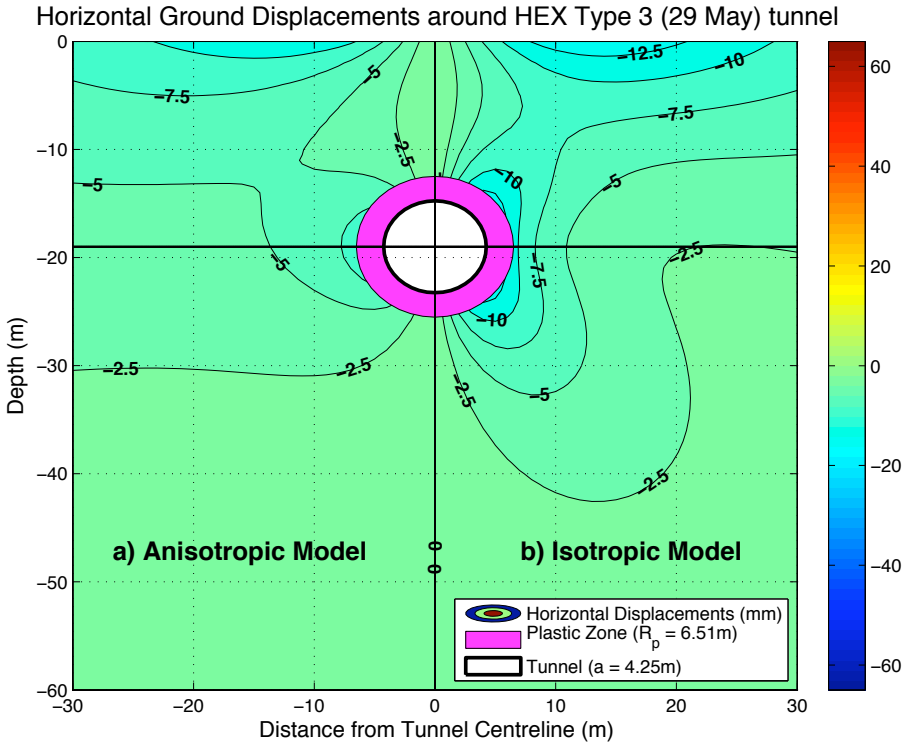

Figure III.6: Horizontal Displacements as predicted by Isotropic and Anisotropic Models for the Type 3 (29 May) tunnel, based on LSS surface solutions for vertical displacements

- Effect of anisotropic stiffness on computed distribution of subsurface ground movements at HEX trial tunnel, using input parameters from LSS surface solution for vertical displacements (see Table 4.10):

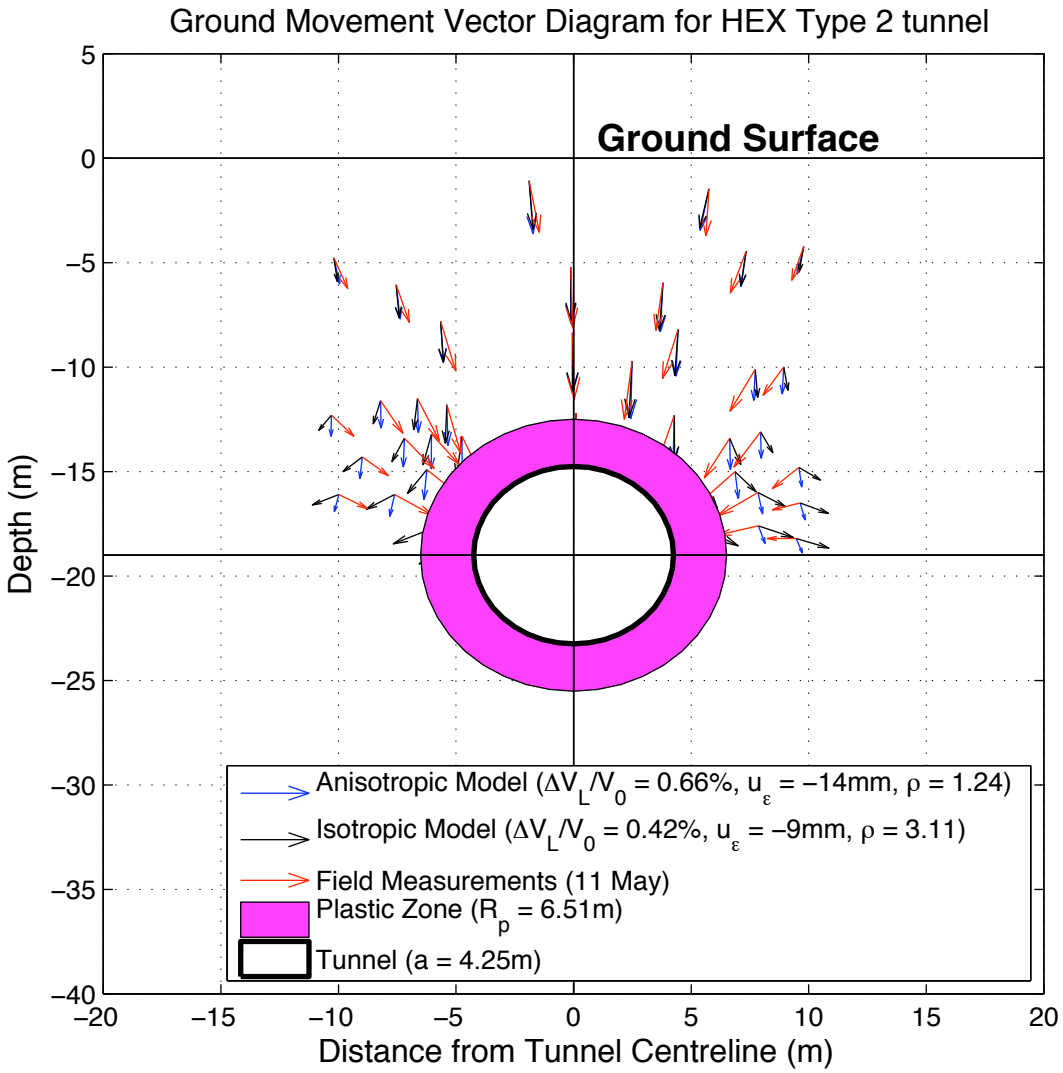

Figure III.7: Ground movement vector diagram as predicted by Isotropic and Anisotropic Models for the Type 2 tunnel, based on LSS surface solutions for vertical displacements

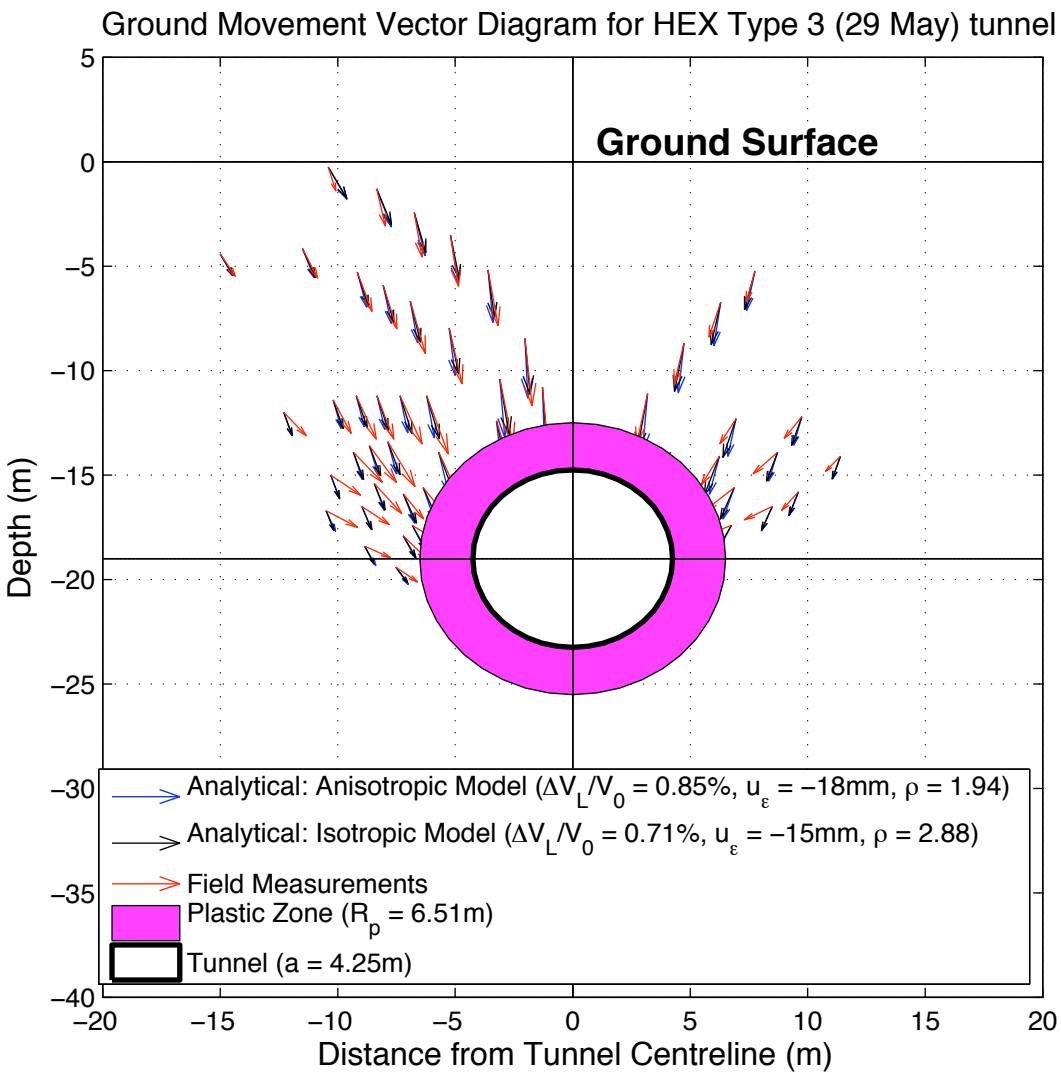

Figure III.8: Ground movement vector diagram as predicted by Isotropic and Anisotropic Models for the Type 3(29 May) tunnel, based on LSS surface solutions for vertical displacements